Drone swarm for wind turbine de-icing

DICE: Drone-based Intelligent De-Icing System

Group 30

Gavin Sun	4412249	Likun Zhao	5699223
Josephine van der Hage	5532590	Mike Kuijper	5701082
Leonardo Peralta Tapia	5532868	Edlyn Santha Kumaran	5730937
Michal Pavol Podolinský	5537169	Max Cárdenas Cruz	5734711
Patryk Prochacki	5695228	Hew Wei Qing	5739756

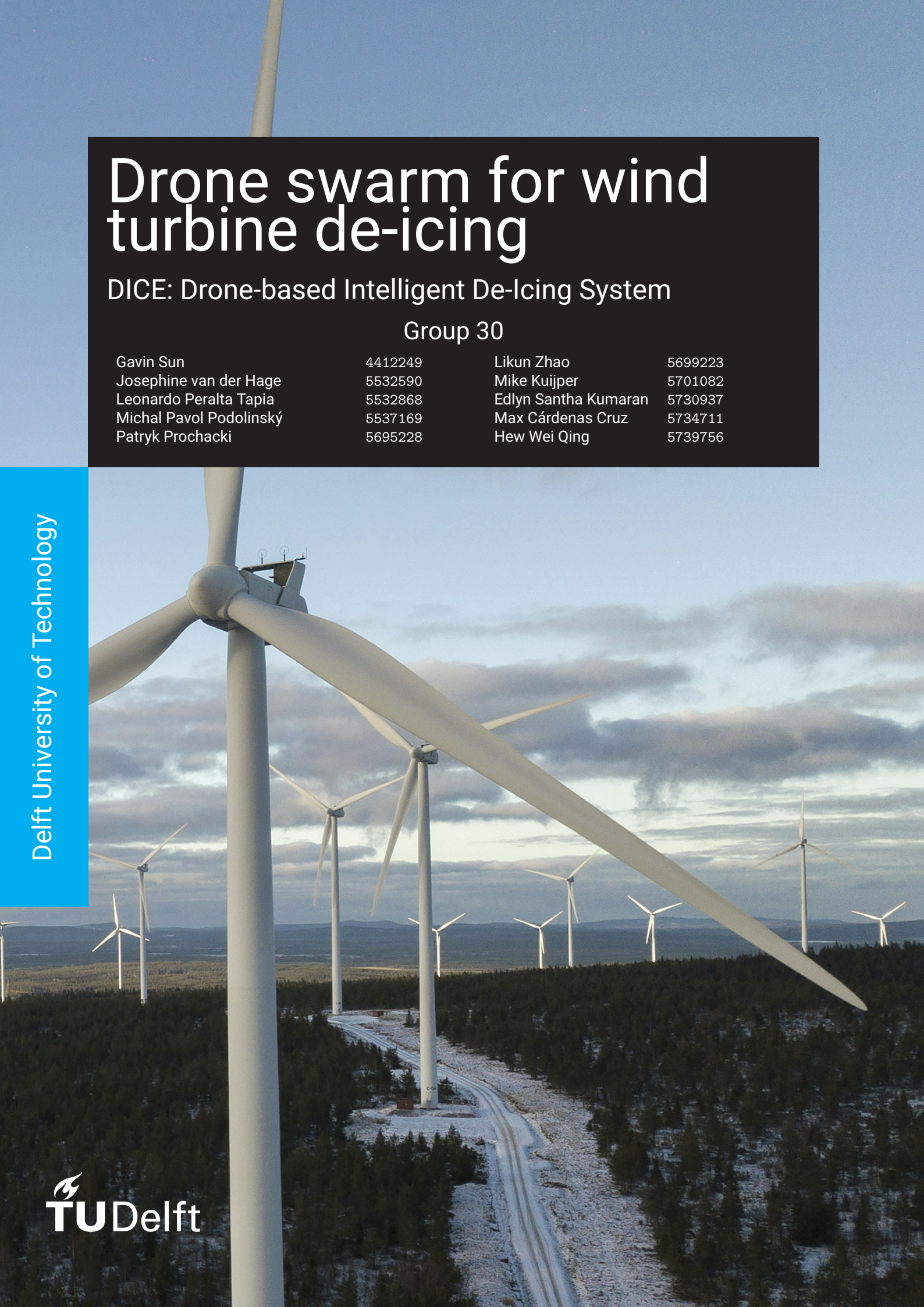

Delft University of Technology

TU Delft

Drone swarm for wind turbine de-icing

DICE: Drone-based Intelligent De-Icing System

Delft University of Technology

AE3200 Design Synthesis Exercise

Tutor:
Dr. Xuerui Wang (PhD)

Coaches:
Direnc Atmaca (MSc.)
Hafiz Ghazali Bin Muhammad Amri (MEng.)

June 24, 2025

by

Gavin Sun	4412249	Likun Zhao	5699223
Josephine van der Hage	5532590	Mike Kuijper	5701082
Leonardo Peralta Tapia	5532868	Edlyn Santha Kumaran	5730937
Michal Pavol Podolinský	5537169	Max Cárdenas Cruz	5734711
Patryk Prochacki	5695228	Hew Wei Qing	5739756

Image credit:
Vattenfall, Stor-Rotliden Wind Farm.

TU Delft

Executive overview

Likun, Patryk, Josephine

Following an extensive evaluation of subsystem options outlined in the mid-term report, the multi-rotor swarm configuration was selected as the final design, accompanied by a preliminary operational strategy. This decision has guided the project into its final detailed design phase. This report demonstrates how the design proceeds using the selected analytical methods. A series of detailed analyses further illustrates how the design meets the updated performance requirements, supported by numerical results and visualisations. Finally, post-project actions and future plans are outlined to ensure the project's continued development and success.

Context, project justification, and problem statement

Ice accumulation on wind turbine blades poses a significant challenge to energy production in cold climates, causing annual output losses of up to 12% (Stoyanov et al., 2021) and introducing substantial structural risks. Current mitigation strategies, which are primarily passive measures such as turbine shutdowns, can lead to prolonged operational downtime and significant revenue losses. For instance, the 40 turbines at the Stor-Rotliden wind farm in Sweden experienced approximately ten severe icing events per year, resulting in an estimated €1.5 million in annual revenue loss (Vattenfall et al., 2016). These figures underscore the urgent need for more effective, proactive de-icing solutions.

To address this critical icing issue, a team of 10 students from TU Delft undertook the challenge of designing an autonomous drone equipped with computer vision capabilities for de-icing operations on wind turbines. The project was completed within a 10-week time frame for the detailed design phase and included discussions on post-project implementation and future developments.

Before starting the actual design, it is important to clarify the challenges the team will face. Therefore, it is established that ice on turbine blades takes on several distinct forms, such as rime at the tip during high-speed rotation under cold, high-humidity conditions, glaze near the hub under drizzle, the rarer hoar frost and white dew. These forms indicate where and how aggressively de-icing must be applied. Icing proceeds in three clear phases, meaning the most effective mitigation should be taken immediately after the accretion phase ends, before the ice can significantly degrade performance. Additionally, the de-icing mechanism is discussed and should be evaluated from three aspects: freeze point depression, heat, and kinetic energy.

The de-icing fluid chapter evaluates four leading de-icing candidates, propylene glycol, ethanol, potassium acetate and potassium formate, by first comparing their lowest achievable freeze points when mixed at eutectic ratios with de-ionised water. The environmental impact is analysed via BOD_5, COD and biodegradation fractions, showing that propylene glycol, potassium acetate, and potassium formate are readily biodegradable. Despite a lower biodegradation ratio, it has minimal oxygen demand. Logistics and cost analyses reveal that the dense potassium salts exceed drone payload limits and that ethanol's high concentration and transport cost make it infeasible as the final option. All the evidence pointed to propylene glycol as the optimal fluid based on eutectic performance, biodegradability, and financial considerations.

The market analysis chapter presents a gain-sharing financial model based on Vattenfall's Stor-Rotliden case to evaluate a drone-based de-icing service (Vattenfall et al., 2016). With the farm's return on investment fixed at 33 per cent and a total of €1.12 million allocated to service costs and drone operator profit, the model establishes relationships between energy prices, icing frequency, and drone characteristics. Iterative elbow analysis and sensitivity tests confirm an operator margin of approximately 8.6 %, supporting the technical and commercial feasibility of the drone setup.

Design & engineering development

The drone design process implements a custom iterative sizing tool to select optimal components. These components include propellers, motors, and batteries. Based on mission constraints, primarily a payload mass of 27 kilograms and an endurance of 14 minutes, the optimal configuration identified from the available databases consists of 14 coaxial rotors with 22×10E propellers and T-Motor F20II 2800 kV motors, powered by a 128,748 mAh 14S Li-ion battery pack. The sensitivity analysis indicates that the drone operates near the limits of feasible payload and endurance, reflecting an efficient design tailored specifically to the requirements of the de-icing mission.

As the primary objective is to successfully complete the de-icing mission, the necessary de-icing components are identified. Following an assessment of commercial solutions and their elimination due to cost and complexity, a system is developed using integrated off-the-shelf components. The design process includes selecting an optimal flat fan nozzle for effective spray coverage, a high-pressure pump for reliable fluid delivery, and a standard 20-litre tank with thermal insulation. Key considerations are evaluated based on fluid compatibility, structural integration, flexibility through a boom orientation mechanism, and placement configuration to maintain weight balance and control. The final design achieves a balance of efficiency, cost, and operational flexibility to meet the de-icing performance requirements.

The structural characteristic analysis focuses first on the configuration choice, followed by material selection, component sizing, and the production plan. A U-shaped coaxial configuration is selected for its optimal spray coverage, structural symmetry, and ease of transport. The structure is constructed from aerospace-grade carbon fibre and includes key elements such as arms, joints, bolts, and landing gear. These components are sized based on critical loading cases. The structural design is validated using shear and composite failure criteria. A modular production plan is also proposed, incorporating off-the-shelf components and outsourced fabrication.

The aerodynamic characteristics primarily cover a moderate aeroacoustic analysis of the final design using an open-source program. This analysis is validated through a lower-fidelity method known as far-field theory. Since the program can only estimate the noise level of an isolated rotor, additional analyses are performed to determine correction factors for the coaxial layout, providing a more robust noise prediction for the complete design configuration.

System Integration

The stability and control chapter covers the modelling of a simplified aircraft dynamics model and the control techniques used to ensure mission operation within the defined operational profile. The drone dynamics are modelled as linearised equations of motion based on Newtonian mechanics and Euler's law of rotation. This system of equations is run as a state-space model through an LQR controller paired with a Kalman filter that serves as a tool for correcting system measurements using sensor data. Sensors employed include RTK-GNSS and a 9DOF-IMU, integrated via sensor fusion with an additional Kalman filter. The stability of the resulting control loop and the overall system control characteristics are then discussed.

As noted in the project objective statement, computer vision for ice detection is a key feature of the drone system. The design describes the flow of data from image capture through ground transmission and covers data integrity, model architecture, and integration with control data for three-class ice mapping. The software runs on an NVIDIA Jetson platform optimised for parallel AI computing. Details of the final design's key hardware components follow, including the camera, lighting, and onboard computer.

After explaining different characteristics of the system, it is essential to specify how different components are integrated. A preliminary prototype configuration outlook is performed by

generating a CAD model, as shown in Figure 1. Another good way to show this is by means of block diagrams. The first diagram that is constructed is a hardware diagram, showing the different components that the drone is made of and how they are related, either by means of a physical connection, a data connection or a power connection. The second is a software diagram, it how different software modules interact with each other to perform the mission autonomously. Third, the electrical diagram is constructed, specifying the logical structure of how the power is distributed within the drone's components. Lastly, a communication and data handling diagram is created, representing the flow of information through different software elements in the drone's system.

Before detailing component integration, a preliminary prototype configuration is visualised by generating a CAD model, as shown in Figure 1. Block diagrams offer another clear representation. The first diagram presents hardware, illustrating each component and its physical, data, or power connections. The second diagram depicts software, illustrating how modules interact autonomously to execute the mission. The third diagram specifies the electrical architecture, showing how power is distributed among components. The final diagram covers communication and data handling, tracing information flow through the system's software elements.

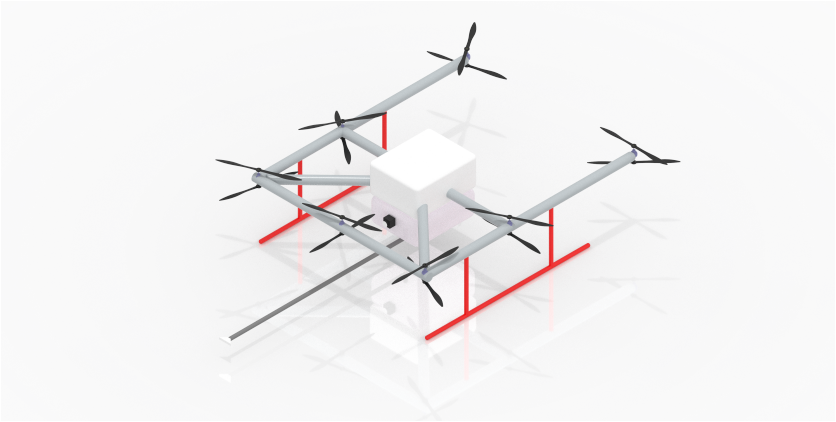

Figure 1: *ISO view of the drone*

Furthermore, the operations and logistics of the drone's mission are detailed. It starts by giving an operational flow of all the stages of the drone's mission, which is summarised in Figure 2.

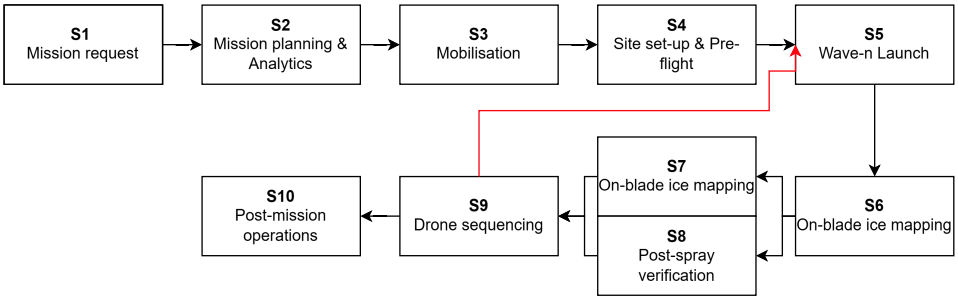

Figure 2: *Mission operation block diagram*

Logistics are outlined from multiple perspectives. The detailed transportation setup is analysed and specifies a main truck for operational components and secondary vehicles for de-icing chemical transport. The ground station layout is optimised for rapid deployment at the Stor-Rotliden wind farm. For navigation logistics, the RTK-GNSS combined with the

9DOF IMU provides centimetre-level position accuracy and precise attitude measurement. Moreover, swarm operation requires inter-drone communication planning. Two architectures were evaluated, infrastructure-based and FANET. The FANET architecture was chosen for its scalability and redundancy. The chapter concludes with a functional flow representation and a functional breakdown structure of the drone's operations.

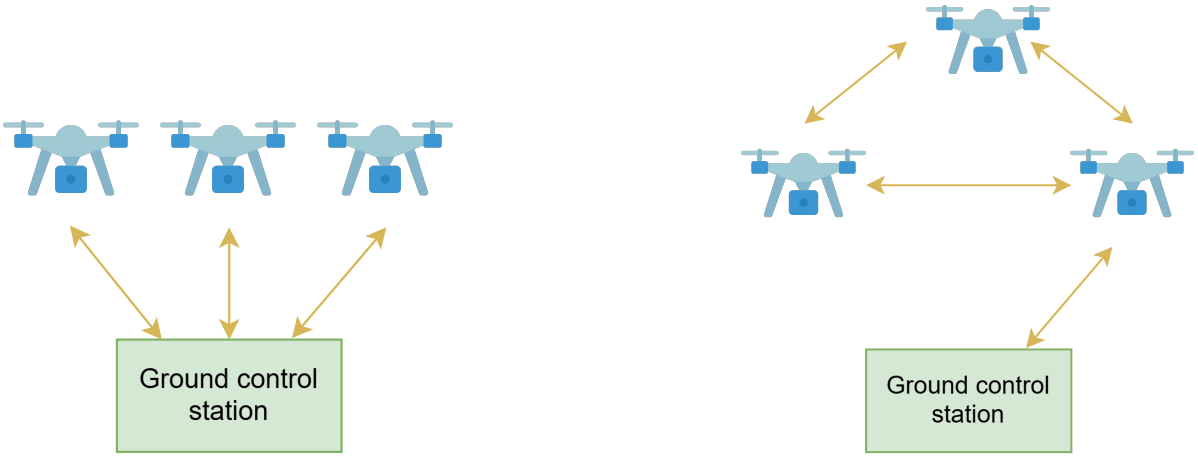

(a) *Infrastructure based architecture* **(b)** *FANET based architecture*

Figure 3: *Two situations for the communication architecture of a drone swarm*

Performance, testing and verification

After finalising the design configuration for the entire system, verification and validation of the tools and analytical methods used in the detailed design phase become essential. This process provides a crucial validity check for the designer. A series of verification and validation activities was therefore conducted across different subsystems, requirements and the final product to demonstrate robust and reliable design outcomes.

Based on the risk list presented in the mid-term report, this chapter provides an updated, more structured risk assessment. It begins with the definition of assessment criteria to ensure a standardised evaluation for the subsequent analysis. Next brings out a breakdown of key risk statements, mitigation strategies, contingency plans, and design impacts across subsystems, accompanied by an evaluation of risk levels before and after mitigation measures. The chapter concludes with an analysis of the RAMS criteria to complete the risk assessment.

To ensure the long-term development of the de-icing drone project, a sustainable development strategy must be considered after the design phase, with a primary focus on reducing environmental impact throughout the system's life cycle. Chapter 16 evaluates the environmental footprint of drone manufacturing, battery usage, chemical de-icing agents, and ground station logistics. It concludes with identified limitations and forward-looking recommendations aimed at guiding future improvements in both technology and operations.

Implementation

In order to clarify the steps required to bring the drone system into service, this chapter provides a structured overview of the necessary development phases. A development logic diagram illustrates the sequence and interdependence of key activities prior to deployment, including detailed design, prototype manufacturing and testing, and certification requests. A Gantt chart then allocates time frames to each task, supporting clear planning and traceability throughout the project.

Contents

Executive overview i

Nomenclature 1

I Vol. 1 | Context, Project justification and Problem statement 4

1 Introduction 5

2 Fundamentals of de-icing 6
- 2.1 Different forms of ice and their formation processes 6
- 2.2 Comparing de-icing methods . 7
- 2.3 Chemical de-icing mechanism . 8

3 De-icing fluid 9
- 3.1 Eutectic system 9
- 3.2 Biodegradability 10
- 3.3 Logistical and financial feasibility 11
- 3.4 Limitations and recommendations 12

4 Market analysis 13
- 4.1 Financial outcome 13
- 4.2 Design philosophy 13
- 4.3 Design process overview 14
- 4.4 Case study: Stor-Rotliden . . . 15
- 4.5 Financial analysis 18

II Vol. 2 | Design & Engineering Development 28

5 Drone sizing 29
- 5.1 Engineering drone sizing . . . 29
- 5.2 Component selection and sizing 32

6 De-icing component design 38
- 6.1 All-in-one solutions 38
- 6.2 Assembled solutions 38
- 6.3 Thermal insulation 40

7 Structural characteristics 41
- 7.1 Configuration design 41
- 7.2 Drone structure and material . 43
- 7.3 Drone dimensions 44
- 7.4 Production plan 48

8 Aeroacoustic characteristics 50
- 8.1 Conventional industrial simulation method (CFD) . . . 50
- 8.2 Xrotor 51
- 8.3 Far-field theory 51
- 8.4 Xrotor validation 52
- 8.5 Noise correction for co-axial layout 55
- 8.6 Noise prediction for the actual drone design 56
- 8.7 Xrotor sensitivity analysis . . . 57
- 8.8 Limitations and recommendations 58

9 Configuration 59
- 9.1 Internal and external layout . . 59
- 9.2 Centre of gravity of drone . . . 59
- 9.3 Thermal 60

III Vol. 3 | System Integration 61

10 Stability & control characteristics 62
- 10.1 Simulation 62
- 10.2 Stability 65
- 10.3 Control 67
- 10.4 Limitation and recommendations 71

11 Computer vision module 72
- 11.1 Computer vision objective . . . 72
- 11.2 Data strategy 72
- 11.3 EFInet-2D model architecture . 73
- 11.4 Evaluation metrics 74
- 11.5 3D Integration 75
- 11.6 Hardware selection 76
- 11.7 Limitations and recommendations 77

12 Software and hardware integration 78
12.1 Hardware integration 78
12.2 Software integration 78
12.3 Electrical block diagram 80
12.4 Data handling and communications 80

13 Operations and logistics 82
13.1 Mission operation 82
13.2 Logistics 84
13.3 Digital twin strategy 90
13.4 Functional overview of drone system 91

IV Vol. 4 | Performance, Testing & Verification 95

14 Verification & validation 96
14.1 Verification 96
14.2 Validation 98
14.3 Testing campaign 100

15 Risk assessment 102
15.1 Risk assessment criteria definition 102
15.2 Subsystem and operational risks assessment 103

16 Sustainable development strategy 112
16.1 Life cycle assessment 112
16.2 Limitations and recommendations 115

V Vol.5 | Implementation Logistics 116

17 Project development strategy 117

18 Conclusion 120

References 122

A Financial analyses 126
A.1 Financial analysis parameters . 127

B Drone Sizing 131
B.1 Thrust-to-weight ratio 131
B.2 Thrust filtering 131
B.3 Databases 131

C Verification & Validation Strategies 134

D Requirements 138

Nomenclature

Likun

Abbreviation

Abbreviation	Definition
UAV	Unmanned Aerial Vehicle
RGB	Red Green Blue (Camera)
LCA	Life Cycle Assessment
IMU	Inertial Measurement Unit
GNSS	Global Navigation Satellite System
RTK	Real-Time Kinematic
DOF	Degrees of Freedom
ToF	Time of Flight
LFP	Lithium Iron Phosphate
VTOL	Vertical Take-Off and Landing
NLR	Netherlands aerospace centre
CFD	Computational Fluid Dynamics
FEM	Finite Element Modelling
V&V	Verification and validation
EASA	European Union Aviation Safety Agency
UV	Ultraviolet
IR	Infrared
ROI	Return-on-investment
CAD	Computer aided design
LiDAR	Light Detection and Ranging
DC	Direct Current
SLAM	Visual Simultaneous Localisation and Mapping
UWB	Ultra-wide Bandwidth
VIO	Visual Inertial Odometry
MTOW	Maximum Take-Off Weight
GFRP	Glass Fibre Reinforced Epoxy Polymer
FOV	Field of View
IEA	International Energy Agency
DSE	Design Synthesis Exercise
BOD_5	Biochemical Oxygen Demand over 5 days
COD	Chemical Oxygen Demand
FANET	Flying Ad-hoc Network
RAMS	Reliability, Availability, Maintainability, and Safety
TRL	Technical Readiness Level
TEU	Twenty-foot Equivalent Unit
DoD	Depth-of-Discharge
IBC	Intermediate Bulk Container
COGS	Cost of Goods Sold
SG&A	Sales, General & Administrative
SBUS	Serial Bus protocol
CUDA	Compute Unified Device Architecture
LQG	Linear-Quadratic-Gaussian
LQR	Linear Quadratic Qegulator
RTL	Return To Launch
NVMe	Non-Volatile Memory Express
eMMC	embedded MultiMediaCard

Abbreviation	Definition
LTI	Linear Time-Invariant
IP67	Ingress Protection 67 rating
GDPR	General Data Protection Regulation
RoHS	Restriction of Hazardous Substances
SDS	Safety Data Sheet
H/W	Hardware
S/W	Software

Symbol

Symbol	Definition	Unit
ω	Icing-induced power loss fraction	-
P_{lost}	Power loss to icing	W
$P_{generated,icing}$	Actual power generated with icing	W
Δ	Change in margin	-
r_t	Thrust-to-weight ratio	-
$P_{\pi_{avg}}$	Power required at a data point	W
P_π	Listed power	W
τ_π	Torque	Nm
ω_π	Angular velocity	rads^{-1}
$V_{cell,full}$	Voltage for a full charge cell	V
n_{cell}	Number of cells in series	-
P_{pack}	Motor-sizing output	-
n	Peulert constant	-
k_1	Sag slope	-
C_{raw}	Initial battery object	mAh
V	Pack voltage	V
C	Actual battery capacity	mAh
C_0	Initial battery capacity	mAh
m_{batt}	Battery mass	kg
t_{target}	Target endurance	min
$m_{structure}$	Structure mass	kg
m_{total}	Total system mass	kg
F_{impact}	Impact force	N
v	Flight speed	ms^{-1}
h	Flight altitude	m

Symbol	Definition	Unit
Δt	Contact time	s
σ_1	Longitudinal stress	Pa
σ_2	Transverse stress	Pa
τ_{12}	In-plane shear stress	Pa
X	Longitudinal tensile	Pa
Y	Transverse tensile	Pa
S	In-plane shear strength	Pa
r_o	Rod outer radius	mm
r_i	Rod inner radius	mm
d_o	Rod outer diameter	mm
d_i	Rod inner diameter	mm
F_{shear}	Shear force	N
g	Gravitational acceleration	ms^{-2}
τ_{yield}	Yield shear stress	Pa
$\tau_{failure}$	Failure shear stress	Pa
A_{yield}	Required area against yield stress	mm^2
$A_{ultimate}$	Required area against ultimate stress	mm^2
p	rms sound pressure level	Pa
m	order of the harmonic	-
S	distance from propeller hub to observer	m
R	Propeller radius	m
A	Propeller disc area	m^2
P_h	Absorbed power	hp
T	Thrust	N
B	Blade count	-
M_t	Tip Mach number	-
J_{mB}	Bessel function of order mB	-
θ	Angle between propeller axis and observer	°
L	Total lift	N
ρ	Air density	kgm^{-3}
C_l	Lift coefficient	-
$L_{A_{eq}}$	Equivalent noise level	Pa
D	Propeller separation distance	m
C	Correction factor	-
λ	Eigenvalue	-
P	Period	s
$T_{\frac{1}{2}}$	Time required for twice or half amplitude	s
ζ	Damping ratio	-
f_n	Natural frequency	Hz
μ_i	Control variable	-
$A_{components}$	Components land area	m^2
A_{site}	Available site are under wind turbine	m^2
P	Likelihood of the risk	%
C	Consequence classes	-

Part I:

Vol. 1 | Context, Project justification and Problem statement

1

Introduction

Patryk

As the world searches for sustainable alternatives to fossil fuel, wind energy generation is growing at a significant rate of approximately 8% yearly[1]. A quarter of the world's wind turbines are deployed in cold climates, where ice accumulation threatens both performance and safety (Stoyanov et al., 2021). Ice accretion particularly degrades aerodynamic performance, by reducing power efficiency and increasing maintenance demands (Gao & Hu, 2021). Traditional manual methods of wind turbine de-icing, such as with chemical sprays, turbine or mechanical removal by scraping, are labour-intensive and inefficient. Consequently, many operators allow ice to melt naturally, resulting in significant revenue losses. This situation presents a clear business opportunity for providers of efficient de-icing solutions. This project aims to design an autonomous drone swarm for wind turbine de-icing.

The report provides a thorough justification of mission objectives and describes how those objectives are met. The first step in defining its scope is to state the mission need and project objective clearly. These are as follows.

> **Mission need statement**
> *To enhance the operational efficiency and safety of ice detection and removal on wind turbines, thereby contributing to sustainable energy production and reducing maintenance costs.*
> **Project objective statement**
> *To design an unmanned aerial vehicle (UAV) that can detect ice build-up with computer vision and remove it from wind turbine blades in a safer, more sustainable, and lower-cost manner than commercially available solutions, by 10 students in 10 weeks.*

To fully justify the design, the report is structured into five volumes. Volume I presents the context and justification for the project, leading to the formulation of a problem statement. Volume II tackles the sizing of the drone by delving deep into the structural configuration and noise analysis. With the configuration selected, the design moves into integration with control, computer vision and hardware systems in the third volume. In the fourth volume, the performance of the drone is assessed and verified, including assessments of risk, safety and sustainability. The Final (fifth) volume focuses on the implementation of the mission design to the planned operation.

[1] https://www.statista.com/outlook/io/energy/renewable-energy/wind-energy/worldwide

2

Fundamentals of de-icing

Gavin

This chapter discusses ice formation and de-icing principles as a crucial first step toward understanding the problem. Section 2.1 covers ice formation processes, ice types, and their detailed properties. Section 2.2 discusses tools and strategies for de-icing. The final section, Section 2.3, explains the chemical de-icing mechanism.

2.1. Different forms of ice and their formation processes *Gavin, Mike*

Meteorological definitions in this chapter follow those from *International Cloud Atlas Volume I: Manual on the Observation of Clouds and other Meteors* (1975). Four major types of ice formation are distinguished: (1) white dew, (2) hoar frost, (3) rime, and (4) glaze. Each type is described in the following subsections. Subtypes of hoar frost and rime are also included in the comparison. An overview table is available in *International Cloud Atlas Volume I: Manual on the Observation of Clouds and other Meteors* (1975).

White dew

When water vapour condenses on a cold surface and subsequently freezes at rest, it forms pseudo-spherical ice formations. Given that water droplets on wind turbine blades are rarely at rest, both due to the rotation of the blades as well as the wind, white dew is not a significant source of disruption.

Hoar frost

Hoar frost forms from the direct de-sublimation of water vapour in the surrounding air on a cold surface. It typically occurs nocturnally with clear skies, in calm air in the case of hoar frost proper or when relatively warm and humid air hits a sufficiently cold surface in the case of advection hoar frost. Hoar frost formation requires calm airspeeds, making the formation unlikely when the turbine is operational.

Rime

In low airspeeds, low humidity, and in temperatures down to -40 °C, rime forms from the freezing of supercooled fog or cloud droplets. It forms relatively thin and smooth layers. Rime is further subdivided into three subtypes: (1) soft rime, (2) hard rime, and (3) clear ice.
Soft rime - Under calm or low-wind conditions and temperatures below -8 °C, a needle-like ice formation might present itself in the form of soft rime. As the name suggests, it does not adhere to surfaces too well and can typically be dislodged with minimal effort.
Hard rime - In temperatures between -2 °C and -10 °C and under high-wind conditions, a granular rime forms from the rapid freezing of fast-moving supercooled water droplets, leaving pockets of air between the ice crystals. This makes for quite adhesive, thick white layers of ice crystals in the direction of the wind. Removal typically requires mechanical scraping.
Clear ice - In case the freezing is too slow to form hard rime (see above), it forms clear ice. Here, the water fills air gaps, leading to a mostly transparent and highly adhesive layer of ice, which is smoother than other forms of ice. *International Cloud Atlas Volume I: Manual on the Observation*

of Clouds and other Meteors (1975) states that it can only be removed by breaking or melting.

Glaze

Glaze is caused by the freezing of supercooled water droplets from rain or drizzle. It forms smooth, homogeneous and mostly transparent layers, closely resembling *clear ice*, though forming through a different process.

2.1.1. Ice formation on wind turbines: types

Yirtici et al. (2019) performed a study on ice formation on wind turbines in icy conditions. They found that the type of ice formation primarily depends on the airspeed and weather conditions. Due to the rotation of the blade, local relative airspeeds further away from the nacelle are higher, leading to the formation of rime there. Hence, higher de-icing intensity would be needed closer to the tips of wind turbine blades. However, this must be balanced against maintaining the structural integrity of the blade due to high moments caused by forces far away from the clamping. For example, it might not be an option to perch on the tips, depending on the weight of the drone.

Closer to the axis of rotation, glaze ice formation is more probable, they assert. As the nacelle is where the joints and clamping of the blades and other structural elements of the wind turbine are located, inducing vibrations there would pose risks to the structure, due to the greater forces involved. Despite this, glaze ice at the nacelle is not a big threat to the aerodynamic efficiency of the wind turbine, and is not a critical region to thoroughly de-ice. If needed, a chemical agent can be used to target these hard to access places.

2.1.2. Ice formation on wind turbines: process

Understanding the timeline of ice formation may be even more critical than identifying its type. Lehtomäki and Task (2016) define several phases of an icing event: the incubation phase, the accretion phase, and the persistence/ablation phase. The names of these phases are self-explanatory; they are graphically shown in Figure 2.1. Lehtomäki and Task (2016) also distinguished three types of icings: meteorogical, instrumental, and rotor icing. Meteorogical icing is defined as "the period during which the meteorological conditions (temperature, wind speed, liquid water content, droplet distribution) allow ice accretion". Instrumental icing is defined as "the period, during which the ice is present/visible at a structure and/or a meteorological instrument". Finally, the most relevant type of rotor icing is defined as "the period during which ice is present at the rotor blade of a wind turbine". Lehtomäki and Task (2016) go on to explain that due to the "dimension, shape, flow velocity and vibrations" rotor icing is not equivalent to instrumental icing, hence the distinction in Figure 2.1.

The question then arises: "When should wind turbine de-icing be performed?". Assuming that the accretion phase is relatively short compared to the others (see Subsection 4.5.5), the most obvious (and correct answer) is that wind turbine icing should be performed as soon as possible after the accretion phase is terminated, i.e. when the meteorological icing phase is finished. This is because it would be unwise to de-ice a wind turbine while the ice is still accumulating on it. Optimally, the lengths of these phases would be known. However, this information is not available publicly and it can only be assumed that the accretion period is relatively short.

2.2. Comparing de-icing methods *Maxim, Michal*

This section aims to cover various de-icing methods specificity tailored to wind turbines. These de-icing methods can be subdivided into two separate groups, passive or active. Passive methods rely solely on the physical properties of the wind turbine and do not require any external energy. Due to the scope of the mission passive methods will not meet the required criteria and the

different active methods will be explored (Quayson-Sackey et al., 2025). The main options of de-icing methods are: **Chemical spraying** (Li et al., 2022), **Thermal active heating** (Quayson-Sackey et al., 2025), **Ultrasonic vibration induction (experimental)** (Habibi et al., 2015).

Quayson-Sackey et al. (2025) provides a thorough investigation of existing de-icing methods. Among the options, only the chemical approach has been fully validated in field operations (Fraunhofer IFAM, 2023; Wisson Robotics, 2025). Other methods have been integrated into wind turbines, but adapting them for external applications would require new innovations and carry a higher risk of project failure. The primary drawback of the chemical option is its large consumption of de-icing agents, which raises sustainability and cost concerns. Nevertheless, it remains the only viable choice. Moreover, technologies such as ultrasonic vibration hold a low TRL of 2–4, whereas chemical sprays have achieved TRL 8-9[1], making the chemical method significantly more reliable.

2.3. Chemical de-icing mechanism *Gavin*

The following details are based on the "SAE AMS 1424/1A-2023: Deicing/Anti-Icing Fluid, Aircraft SAE Type I Glycol (Conventional and Nonconventional Based)" (2023) standard to use type 1 fluid de-icers, which includes one of our de-icers based on propylene glycol and is applicable to this project. The mechanisms by which the de-icer works are: Freeze point depression, Heat transfer, Kinetic energy.

The main mechanism of chemical de-icing relies on freeze point depression. By mixing de-icer as solute and treating ice as solvent produces a solution with a much lower freeze point, causing the ice to melt. The secondary mechanism depends on heat. The de-icing liquid must be heated to 60-80°C, with the added thermal energy enhancing the melting process. Finally, high-pressure spraying delivers kinetic energy to fracture clear or glaze ice. Cracks propagate until ice sections detach from the blade surface. This method also proves the fastest and most effective for removing large volumes of rime ice. Rime ice formed at high rotor speeds creates large moment arms and readily breaks off under the force of the spray.

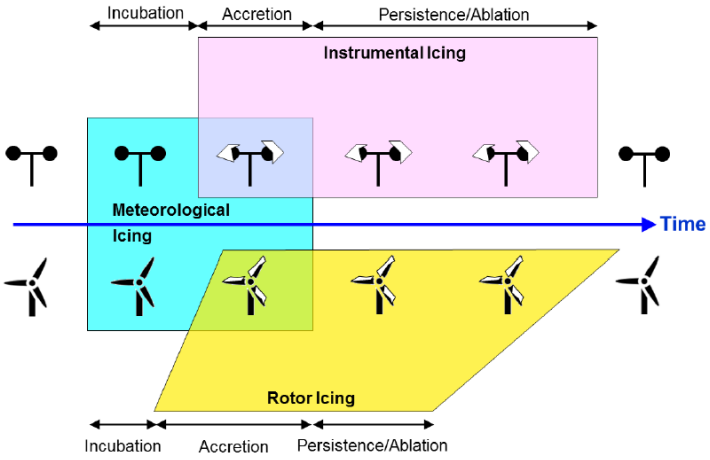

Figure 2.1: *Process of wind turbine showing Instrumental Icing, Rotor Icing, Incubation, Accretion, Persistence, and Ablation (Lehtomäki & Task, 2016)*

[1]https://www.nasa.gov/directorates/somd/space-communications-navigation-program/technology-readiness-levels/

3

De-icing fluid

Gavin

In this chapter the final de-icing fluid is selected. As seen in Section 2.2, the de-icing chemicals have been narrowed down based on these requirements:

- USER-M-SUST-2.1: Biodegradable chemicals only
- ENV-M-SUST-2.2: No substances in EU REACH Annex XVII
- GOV-M-LEGL-3.3: SDS rating ≤ 1, non-toxic and non-flammable
- GOV-M-LEGL-3.3: SDS rating ≤ 1, non-toxic and non-flammable
- GOV-M-LEGL-3.4: Double-walled chemical storage
- USER-S-PAYL-5.2: Maintain tank at ≥60°C throughout mission

These remaining options are:

- Propylene glycol
- Ethanol
- Potassium acetate-water solution
- Potassium formate-water solution

In the remainder of this chapter, various details of the de-icing chemicals are investigated and a chemical is chosen.

3.1. Eutectic system

Gavin

This section provides background on de-icing fluids and explains why each solution compared in this chapter is diluted with de-ionised water.

A eutectic system is a solution of two chemicals, where the melting point is lower than each component on its own. Two chemicals that do not react and form new compounds will inhibit each other's crystallisation. Thus, a mixture will always have lower freezing points than each individual component alone. The eutectic point is the lowest possible point in the ratio. For the options in this chapter, the following points in Table 3.1 are the eutectic points when diluting with water, and the rest of chapter will assume the solutions are diluted in their eutectic ratio to ensure maximum performance. Water is selected as the diluent due to its low cost, effectiveness, and extensive study.

Table 3.1: *Some chemical properties of de-icers*

	Dilution ratio at eutectic point(dilutant: water)	Freezing point at eutectic point	BOD_5(g/g) [1]	COD(g/g)	BOD_5/COD
Potassium Acetate	49%:51% [2]	-60 °C	0.82	1.01	0.81
Potassium Formate	52%:48% [3]	-60°C	0.02	0.1 [4]	0.2
Propylene Glycol	60%:40% [5]	-60°C	1.09	1.55	0.7
Ethanol	94%:6% [6]	-124.3°C	NA(2.09)	2.09	NA(1)

As an example, the freezing point of propylene glycol is -55°C, and water has a freeze point of 0°C. When propylene glycol is diluted in water at the eutectic point, the resultant solution will have a freeze point of -60°C.

3.2. Biodegradability *Gavin*

This section provides information on the metrics used to evaluate biodegradability. All candidates selected in the previous report are fully biodegradable, however, their degradation performance varies. A brief overview of the metrics for assessing environmental impact through biodegradation follows.

3.2.1. Biochemical oxygen demand over 5 days(BOD_5)

Biochemical oxygen demand is the amount of dissolved oxygen the biodegradable chemicals consume during a breakdown in water in 5 days. In general, a lower BOD is preferred. However, if it is too low compared to chemical oxygen demand, it might be problematic as shown in the following subsection about ratio.

3.2.2. Chemical oxygen demand (COD)

Chemical oxygen demand is the total oxygen required to chemically degrade the solution in water. The lower is better. Less oxygen demand during breakdown reduces impact on the wildlife during breakdown.

3.2.3. BOD_5/COD ratio

The ratio of biochemical oxygen demand to chemical oxygen demand indicates the fraction of biodegradable compounds. Higher ratios are preferable. According to OECD 301 A–F testing standards, a BOD/COD ratio above 0.6 is classified as readily biodegradable.

If the BOD value is very low but the COD value is high, this means the majority of materials is broken down into non-organic materials via non-biochemical processes. This also means the material is no longer readily biodegradable if this ratio is below 0.6.

Table 3.1 summarizes the properties. BOD data for ethanol are often omitted due to its simple structure and complete biodegradability. This is due to the fact that ethanol is not a compound but an organic base material and bod would not be applicable. For simplicity, a BOD/COD ratio

[1] https://www.researchgate.net/figure/COD-and-traditional-BOD-5-for-selected-aircraft-and-airfield-deicer-and-anti-icer_tbl4_257673376
[2] https://www.fhwa.dot.gov/publications/research/safety/95202/004.cfm
[3] https://aerospace.basf.com/potassium-formate-for-runway-deicing.html
[4] https://aerospace.basf.com/potassium-formate-for-runway-deicing.html
[5] https://www.sciencedirect.com/science/article/pii/S235243162100033X
[6] https://commons.wikimedia.org/w/index.php?curid=10159735

of 1 is assumed to simplify the calculations, as technically, it is fully organic, fully breaks down to organic materials and is totally biodegradable. Another detail is that although potassium formate is not technically biodegradable according to the ratio, it has a very small COD in total and has minimal impact on the environment compared to the other de-icers.

From the table we can see that ethanol out performs all other de-icers in freezing point, but the eutectic point concentration is very high compared to the other chemicals, this will have an impact on logistics and financials. The other chemicals perform similarly with regards to de-icing, with all being biodegradable and or have low environmental impact.

3.3. Logistical and financial feasibility *Gavin*

In previous market analysis a major cost identified is the chemical de-icer, as such a thorough research is needed.

In this chapter, chemicals are evaluated from both logistical and financial perspectives to examine their feasibility for implementation. L Logistical feasibility examines the shipment of raw materials to the deployment site, last-leg transport and the deployment in a drone. Financial feasibility looks into the price for bulk purchase and compared against data from the previous market analysis.

3.3.1. De-ionised water

Minerals can cause scaling and residue buildup on wind turbine blades, as well as within the drone's tanks and plumbing systems. To prevent this, demineralised water either de-ionised or distilled is preferred as the base for the de-icing solution. By sourcing this water locally, transport costs are minimised, and on-site mixing becomes a practical and cost effective solution.

As an example for research the Stor-Rotliden site is used, when buying distilled water in Sweden, which is known as batterivatten in Sweden, this costs 3690 Swedish kroner[7] and is purchasable off the shelf. This will be included in the total cost of solution preparation.

3.3.2. Logistical feasibility

For logistics, the primary shipping method is sea freight in standardised twenty-foot equivalent unit (TEU) containers. With in this the most common package method is barrel drum or a standardised 1000 L intermediate bulk container(IBC). For easy calculation with metric units the assumption is that all logistics will be in 1000 L IBC, of which 20 fit into 1 TEU container. After shipping the containers fit on trucks to be delivered to warehouses. By mixing de-ionised water in the tanker vehicle to the eutectic point the solution is ready to be used, in the end 20kg or 20L is added to drones and deployed.

3.3.3. Financial feasibility

For reference, the break even point found in previous market research for chemical price is slightly above €1 per litre. Moreover the preference should be for the project to be profitable with a margin in order to be sustainable to de-ice in more situations. Hence the profitability should be a driving factor in choosing the chemical.

Costs of chemical are bought in kilograms but the final unit will be litres since the spraying performance hinges on litres. The final price includes a shipping price calculated from an assumption that every ISO/TEU container costs 3000 to 5000 dollars to ship, with the conservative estimation that it costs 5000[8]. Note that the shipping costs are for the concentrated liquid instead of solids, both for ease of comparison and to minimize equipment requirements

[7] https://kemexperten.se/produkter/batterivatten-1000-liter
[8] https://www.freightos.com/freight-resources/container-shipping-cost-calculator-free-tool/

Table 3.2: *Financial properties of chemical de-icers*

	Import concentration	Target concentration	Density (kg/L)	Price ($/T)	Logistic costs ($/T)	Total cost per L (€/L)
Potassium Acetate	50%	50%	1.57	800 [9]	159.2	1.225
Potassium Formate	75%	52%	1.339	346.7 [10]	110.4	0.637
Propylene Glycol	99.5%	60%	1.0228	300 [11]	150	0.52
Ethanol	96%	94%	0.847	1548.3 [12]	283	1.385

to mix the final solution.

3.3.4. Results

From the calculations the potassium formate and potassium acetate face a limitation during deployment. By being high in density, the weight limit is reached far before volume limit. However the total area covered depends on the volume of de-icing liquid sprayed. This puts both potassium salt solutions in disadvantage and requires more drone deployments per turbine.

On the financial side both diluted potassium formate and propylene glycol have significantly better economics compared to potassium acetate and ethanol. This combined with the logistical disadvantage of the potassium salts means that propylene glycol emerges as the most suitable option. Both potassium acetate and ethanol have a total cost per litre too high, close to the break even point, meaning that the mission will be minimally profitable. This results in the choice of propylene glycol as choice of de-icing chemical.

3.4. Limitations and recommendations *Gavin*

The choice of the de-icing agents is limited by the fact that almost all chemicals are still polluting to some extent. Even the least polluting choices, such as ones mentioned in this chapter, are still disruptive in large amounts in aquatic conditions, making off-shore wind farms de-icing difficult without new scientific breakthrough in de-icing fluid.

The recommendation is to research into alternative de-icing mechanisms. Due to technical readiness level (TRL) limitations and development budget limitations this project cannot risk to initiate development of vibration- or ultrasonic-based de-icing systems from Xu et al. (2025) or Habibi et al. (2015). Both methods are only tested on a small scale in lab conditions and have a low TRL and are not yet viable for deployment. If future de-icing can be made without using de-icing chemicals this would greatly improve the sustainability aspect of the project.

[9] https://www.alibaba.com/product-detail/Liquid-50-Ice-Melt-Potassium-Acetate_60771825306.html

[10] diluted value of https://www.alibaba.com/product-detail/Best-Price-Liquid-Potassium-Formate-75_1600220021352.html

[11] diluted 60% value of https://www.alibaba.com/product-detail/CAS-NO-57-55-6-Propylene_1600278567149.html?s=p

[12] https://www.alibaba.com/product-detail/Food-Grade-Ethanol-96-Wholesale-Anhydrous_1601428882399.html

4

Market analysis

Michal

To guide the design process with real-world values, this chapter defines the practical and economic context of the mission in the form of a case study and financial analysis, before diving into the engineering sizing of the drone. The primary concern in this chapter is that the drone is both technically and financially viable. First off, Section 4.4 presents the Stor-Rotliden wind farm as the background of this study. After this, the financial impact of wind turbine icing is assessed in Section 4.5. This information is used to set a payload and flight time requirement, factors that drive the engineering sizing (see Section 5.1) in the next chapter.

4.1. Financial outcome

Michal

Damodaran (2025), from NYU Stern[1], observes that the average net profit margin of 67 companies in the aerospace and defence sector is 4.37%. The gross profit for the same companies sits at 17.05%. The difference between gross and net profit is that net profit includes operating expenses (marketing, R&D, rent, salaries not in COGS[2]), depreciation & amortization, interest expenses, and taxes. The market analysis that follows, includes most of these factors to some degree, except for taxes and interest expenses. Observing Table 4.1, a profit margin of 8.6% is therefore very much in-line with the estimates of Damodaran (2025). Such a financial outcome hints at a challenging yet potentially lucrative opportunity, especially for a new venture.

Table 4.1: *Key financial outputs for the wind-farm de-icing scenario.*

Parameter	Value	Unit
Return on investment (wind farm)	33	%
Additional revenue (wind farm)	383 075	€ / yr
% of additional revenue (wind farm)	3.4	%
Profit from de-icing (operator)	133 373	€ / yr
Profit margin (operator)	8.6	%

4.2. Design philosophy

Michal

*"Design thinking is a human-centered approach to innovation that draws from the designer's toolkit to integrate the **needs of people**, the **possibilities of technology**, and the requirements for **business success**."* [3] *- Tim Brown, Executive Chair of IDEO*

Brown's quote is an excellent way to begin thinking about the design process of a wind turbine de-icing drone. It combines all the elements of the sizing process presented in this work into a

[1] https://www.stern.nyu.edu/

[2] https://www.investopedia.com/terms/c/cogs.asp

[3] https://designthinking.ideo.com/

coherent design philosophy. Brown mentions the "needs of people" which will be discussed in Section 4.4, the "requirements for business success", which is explored in Section 4.5, and finally, the "possibilities of technology" which is explored in Section 5.1. These three sections provide all the necessary information to design an impactful, technically feasible, and commercially viable solution.

The flow between all three parts of what Brown calls "the designer's toolkit" are shown in Figure 4.1. Firstly, the case study (in gray) feeds the first pass through the financial analysis. Next, following the yellow numbers, some parameters are passed to the engineering sizing process (which is in itself highly iterative). After that, a final engineering design is agreed upon. Finally, following the arrows, the final design is fed back into the financial analysis to update the model from any missing parts and verify the financial viability of the project. As will be mentioned in the conclusion, this loop is highly adapted for iteration, and this "updated" financial model could serve as a basis for a new engineering analysis. Nonetheless, this is left as a possibility to explore in further work.

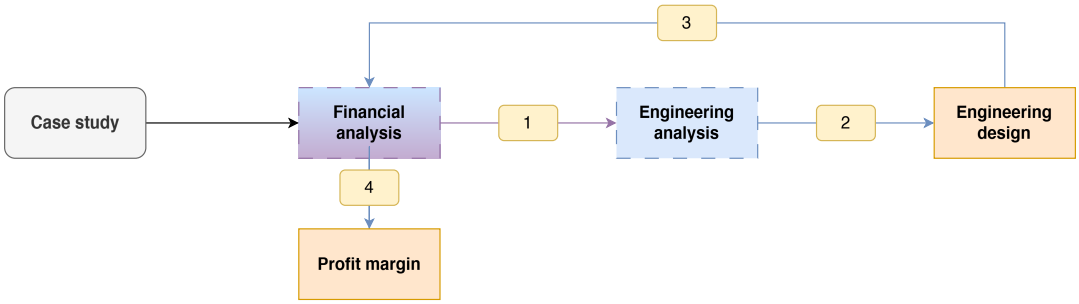

Figure 4.1: *Simplified overview of the drone design process, including financial analysis and engineering sizing. The financial process optimized parameters to maximize profit margin, while the engineering analysis minimized the power required to hover.*

4.3. Design process overview *Michal*

To design a UAV that is optimized for a commercial task, financial and engineering principles have to be used in tandem. It is paramount to give equal importance to both the financial and the engineering side of the design. Figure 4.2 shows how the financial analysis and the engineering sizing come together to create a drone design which excels in the task it was designed for while being commercially viable. This diagram is simplified and only includes the very central parameters while abstracting the iteration steps to simple loops (see 1 and 3). The design process is as follows.

- Using the financial model based on the case study parameters, find an optimal set of parameters that result in the highest profit margin.
  - 1. Set the spraying rate (L/m) and payload (kg) to optimize the profit margin using the concept of diminishing returns (see Subsection 4.5.3).
  - 2. Determine the mission flight profile based on parameters such as range, velocity, spraying time, detection time, charging time, and others.
  - Determine the required flight autonomy.
- With the sizing model populated with propeller and motor databases, find the drone configuration that, with the least amount of propellers, can sustain a UAV with a given payload for a given flight time. The design is iterated to minimize the power required to hover.

  - 3. Size the drone based on the mission flight time for a given payload weight. Iterate until the final design weight changes less than 1%.
  - 4. Confirm a final design by selecting any remaining elements with commercial solutions (specifically the batteries)

- Review the financial outcome with the final, more detailed drone design.
  - 5. Isolate the battery characteristics and explore the pricing of the selected batteries (they are a major cost driver). At the same time, explore options for the ground station design now that the number (financial analysis) and size/geometry (engineering sizing) are known. Produce preliminary cost values for the ground station.
  - 6. Update the financial analysis with the more detailed costs from 5 and determine a final outcome. Note: the original estimate and final estimate differed by less than 0.5%.

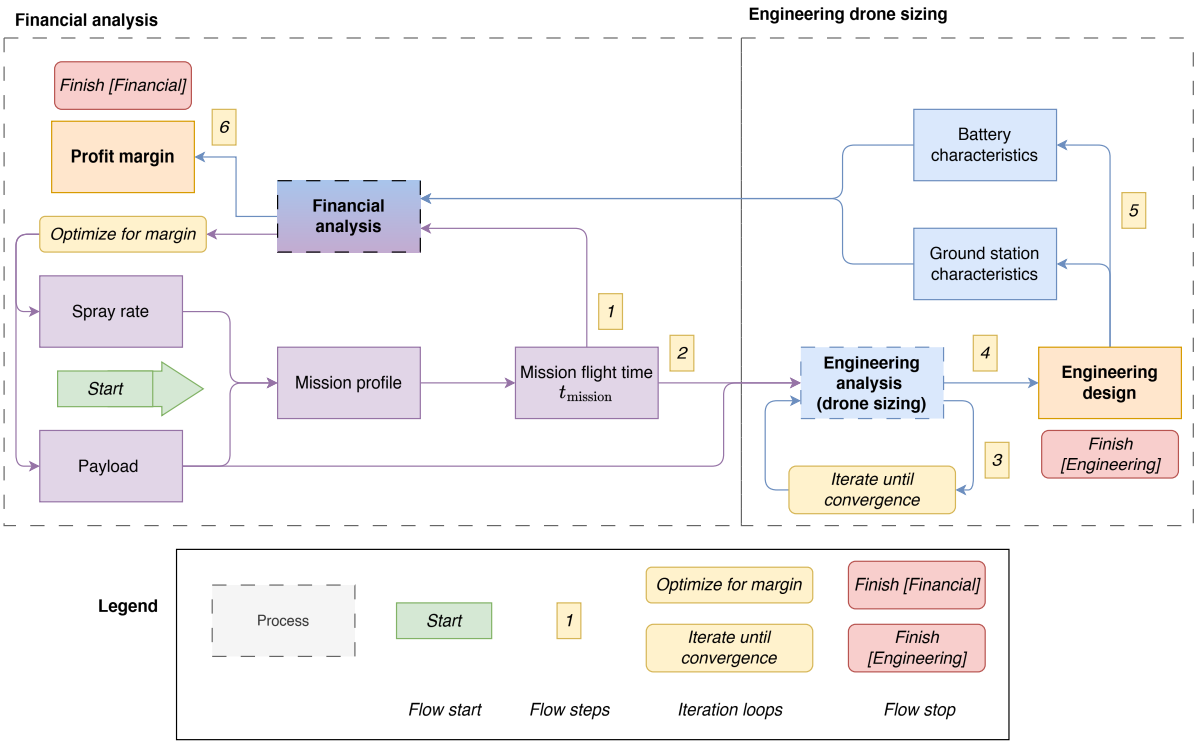

Figure 4.2: *Overview of the drone design process, including financial analysis and engineering sizing.*

4.4. Case study: Stor-Rotliden *Michal*

To anchor the design of a de-icing UAV, one wind farm is selected as the beachhead market; its characteristics are used to ground the design process in real-life data. Firstly, Subsection 4.4.1 highlights the most pertinent characteristics of the selected wind turbine farm: Stor-Rotliden in Sweden. Secondly, Subsection 4.4.2 discusses the current wind turbine icing mitigation strategies that are in place at Stor-Rotliden. Finally, Subsection 4.4.3 explores the power generation losses that Stor-Rotliden experiences.

Initial analysis considered off shore wind turbine farms as well as onshore. However, due to lower icing, more complex logistics, less publicly available data, and the need for a single case study (such as to have a single solid reference), offshore wind farms were eventually excluded from consideration. Nevertheless, they remain a target area in the future.

4.4.1. Wind farm overview

This section will go over the main characteristics of Stor-Rotliden. Vattenfall's Stor-Rotliden, commissioned in 2011, is one of the northernmost wind turbine farms in the world. Located in Sweden, it has been selected for the case study for several reasons.

- It is located just below the Arctic Circle and experiences severe and prolonged icing episodes, resulting in a significant power loss (Vattenfall et al., 2016).
- It is fully owned and operated by Vattenfall. Considering the company's commitment to innovation and sustainability [4], the chances of support and collaboration are increased.
- The scale of the wind turbine, consisting of 40 individual Vestas V90 1.8- 2.0MW turbines (The Wind Power, 2025) is manageable for pilot logistics but large enough for a scalable effort.
- There is a large amount of publicly available data about the wind farm's technical parameters and environmental conditions. It is cited throughout this section.
- The currently used wind turbines do not feature any blade heating or active de-icing. They are simply turned off during icing events (Vattenfall et al., 2016).

Some characteristics of the wind turbine farm, which will be used throughout the report, are presented in Table 4.2.

Table 4.2: *Stor-Rotliden Wind Farm Overview, (Vattenfall, 2011), (The Wind Power, 2025), (Kgi-Admin, 2022)*

Attribute	Details
Name	Stor-Rotliden
Location	Åsele, Sweden
Commissioned	2011
Operator	Vattenfall
Total Capacity	78 MW
Number of Turbines	40
Turbine Models	Vestas V90*
Turbine Capacity	1.8–2.0 MW
Annual Production	200 GW

**11x Vestas V90-1.8 MW (IEC IIA), 29x Vestas V90-2.0 MW (IEC IIIA) (The Wind Power, 2025), to make the analysis slightly more general, all wind turbines are assumed to be 2.0 MW. The effect on the final result is minimal.*

The blade area estimate is based on the reference wind turbines by Rinker and Dykes (2018). These reference turbines include a reference turbine blade, with a span-dependent chord, for which a graph is given. Analysis of this graph leads to the approximation of three linear regions. Integration gives the estimates for the wetted blade area as shown in Table 4.3.

4.4.2. Current mitigation strategies

While both passive and active de-icing solutions are available in early and commercial stages (see Section 2.2), none are implemented at Stor-Rotliden. This might partially be due to commercial solutions being unavailable, impractical, or economically unsustainable during the wind farm commissioning (2011). Whatever the reason, the current strategy for dealing with wind turbine icing is waiting until the ice melts (Vattenfall et al., 2016). No effort is made to de-ice the wind turbines.

[4] https://group.vattenfall.com/our-operations/innovation

Table 4.3: *Blade wetted area estimates based on the reference blade as defined in (Rinker & Dykes, 2018, p. 5)*

	Vestas V90-2.0 MW *Corresponding blade*
Radius (m)	45
Single-side area (m^2)	107
Two-side area (m^2)	215
Total turbine area (m^2)	644

This does not mean that icing is not a problem; it very much is. According to Clausen et al. (2014), there are 9 annual instrumental icing events and thus rotor icing events. This usually means at most 9 rotor icing events. For definitions of wind turbine icing phases, see Subsection 2.1.2. The next section will explore what this translates to in a financial sense.

4.4.3. Current power generation losses

The yearly revenue loss is equated to the wholesale value of the electricity in the country of generation from December to February 2024 and 2025. Yearly electricity prices in Europe and in Sweden can be seen in Figure 4.3. Other factors, such as government subsidies, are outside the scope of this report.

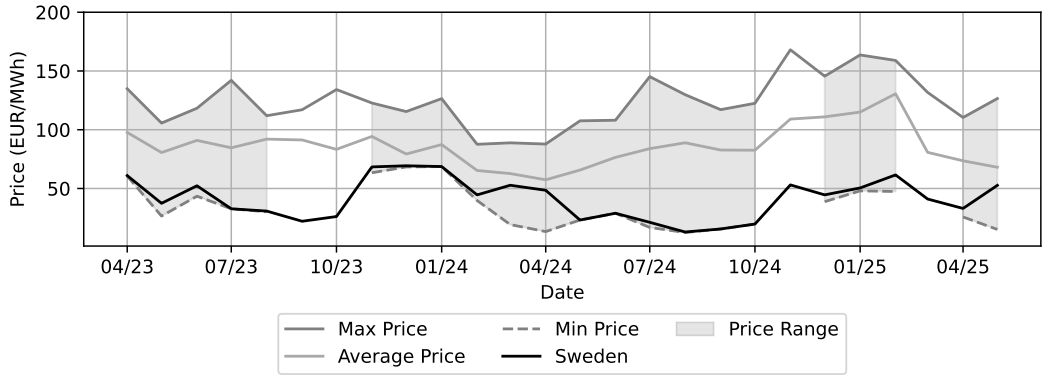

Figure 4.3: *Monthly wholesale electricity prices (EUR/MWh) in Europe and Sweden. Minumum prices below 5 EUR/MWh are excluded from the graph (resulting in blank areas) but remain present in the analysis.*

To estimate this value, each wind turbine location is classified according to the IEA Ice Class index (Cattin, 2016) using Figure 4.4, which classifies geographical zones based on their susceptibility to icing-induced power generation losses. Each IEA Ice Class is associated with a certain power generation loss. Stor-Rotliden being located in a number III Ice Class location (Vattenfall et al., 2016; VTT Technical Research Centre of Finland, 2015), the power generation loss is 5-12% per year (IEA Wind TCP, 2018). Next, this percentage is multiplied by the expected full power generation capacity of the wind farm according to Equation 4.1. In this equation, P_{lost} is the power lost to icing, $P_{\text{generated, icing}}$ is the actual generated power (taking into account icing losses), ω is the icing-induced power loss fraction (5-12% as mentioned above), and $P_{\text{generated, no icing}}$ is the theoretical total power generated if all icing losses are recuperated. This is then multiplied by the wholesale price of electricity to obtain a final monetary value. Note: The term "power" in this section technically refers to an energy (MWh).

$$P_{\text{lost}} = \omega \cdot P_{\text{generated, no icing}} = \omega \cdot \frac{P_{\text{generated, icing}}}{1-\omega} \tag{4.1}$$

The results of this analysis are shown in Table 4.4. This indicated that the financial impact of

Figure 4.4: *IEA Ice Class map showing Ice Classes I-III. Green → I, Yellow → II, Red → III. Stor-Rotliden is located in an Ice Class III region. (VTT Technical Research Centre of Finland, 2015)*

wind turbine icing on Stor-Rotliden is significant, which in turn supports the thesis that the market is ready to accept a novel de-icing platform. It is nonetheless necessary to verify that there is a financial opportunity in this endeavour, which is explored in the following section.

Table 4.4: *Ice-class parameters and associated yearly losses. (Vattenfall et al., 2016; Vattenfall, 2011; VTT Technical Research Centre of Finland, 2015; IEA Wind TCP, 2018)*

Parameter	Value		Unit
	Maximum	Minimum	
IEA Ice Class	III		–
Yearly revenue	11 322 000		€
MWh price	56.61		€ / MWh
Yearly production	200 000		MWh / yr
Yearly loss	5	12	%
Energy loss	10 526	27 273	€
Missed revenue	595 895	1 543 909	€

4.5. Financial analysis *Michal*

Having seen that there is a significant loss of power generation at Stor-Rotliden, the actual financial viability has to be explored. This is because if the cost to de-ice is higher than the lost revenue, the project can not turn a profit, no matter how large the revenue loss due to icing is. This section deals with this topic. Firstly, Subsection 4.5.1 discussed the various model inputs and their sources. Secondly, Subsection 4.5.2 deals with the calculation process the financial model uses. Next, Subsection 4.5.3 deals with the output of the model and the optimization of output parameters. Finally, the model constraints and assumptions are explained in Subsection 4.5.4 and Subsection 4.5.5, respectively. Finally, after a small note on model iteration, a sensitivity analysis can be found in Subsection 4.5.6. Subsection 4.5.8 provides a conclusion and proposes further work.

4.5.1. Inputs (Cost breakdown)

Various parameters are entered in the financial model. Table 4.5 structures all the inputs in six categories alongside their value, unit, and source. The following is a brief overview of input parameters that have not been mentioned until now.

- 1. Wind farm overview
  - 1.1 - 1.7: Are directly based on information regarding the case study location, Stor-

Rotliden, in Sweden.

- 3. Drone operational properties
  - 3.1: The number of de-icing operations per year is based on the occurrence of 9 instrumental icing events (see Subsection 2.1.2) from November 2012 to April 2013 Clausen et al., 2014. The number is rounded to 10 to err on the conservative side.
  - 3.4: The required vertical distance is based on the maximum height of Vestas V90 1.8-2.0MW turbine blade Vestas, 2011. A sensitivity analysis can be found in Subsection A.0.1.
  - 3.6: The horizontal travel distance (one way) is set to be roughly the distance between three wind turbines. This is done such that the drone is able to reach multiple wind turbines and can be adapted to other wind farm designs. A sensitivity analysis can be found in Subsection A.0.1.
  - 3.10: The detection time is approximated to be half of the spraying time. This is an initial estimate that has proven to be adequate in the operational sequence (see Section 13.2) and has therefore been kept.
  - 3.14: The time to refuel is to be as small as possible to maximize the fraction of time spent spraying. The minimum time that appears feasible is 60 seconds. This is based on an estimated required time to change all three batteries and is also limited by realistic flow rates to refuel the drone (see Section 13.2).
  - 3.15: A safety margin of 10% is set to account for uncertainties in the operation of the drone.
- 4. Drone costs
  - 4.1: The drone price of €50 000 (over five years) is based on the DJI Flycart 30 [5] that has specs that are similar to the ones expected of the final design. For example, it has a maximum take-off weight of 95kg, can fly for 18 minutes loaded with a 30kg payload, and is operational down to -20$°C$. The price of such a drone starts at roughly €20 000 [6]. Considering additional costs such as software, transport equipment, GNSS RTK Tower[7] (cost being split between all 8 drones), and controllers, it can be estimated that the price of such a system climbs to €40 000 (a 2x increase). Considering that maintenance in the harsh Swedish winters will be substantial, 50% of the initial price of €20 000 can be added. This results in €50 000 over five years, or €10 000 per year (per drone).
  - 4.2: The useful lifetime of a drone is taken to be five years. This a standard value used in financial accounting [8] [9].
  - 4.5: Corresponds to the required number of 44,000mAh batteries. This number is a result of the engineering sizing in Section 5.1.
  - 4.6: This number corresponds to the required number of sets of three batteries required for the drones to always have a charged set of batteries ready for flight. This is based on the following calculation. Each drone needs three 44,000mAh

[5] https://www.dji.com/ch/flycart-30

[6] https://www.floridadronesupply.com/products/dji-flycart-30-delivery-drone

[7] https://positioningsolutions.com/products/trimble-r750-gps-gnss-base-station-450-mhz-uhf

[8] https://www.irs.gov/publications/p946 under "Any qualified technological equipment"

[9] https://ofm.wa.gov/sites/default/files/public/legacy/policy/30.50.pdf under "Unmanned Aerial Vehicles (UAV), Drones"

batteries to fly. By observing similar batteries, such as the ones used in the DJI Flycart 30 mentioned previously [10], the charging power of the batteries can be taken as approximately 5700W. For a first order estimate, it can then be assumed that a 44,000mAh, 51.8V battery takes 24 minutes ($(44\text{Ah} \cdot 51.8\text{V})/5700\text{W} \cdot 60\text{min} = 24\text{min}$). Considering that the mission time of a drone is 13.6 minutes (see parameter 3.18 in Section A.1), each drone will fly two times before the first set is fully charged. Each drone, therefore, needs three sets of three batteries.

  - 4.7: Is the cost of a 44,000mAh, 14S battery from Foxtech [11] (see Section 5.1).

- 6. De-icing fluid cost
  - 6.1: The type of fluid has been selected to be a 60% solution of Propylene Glycol and distilled water in Chapter 3.
  - 6.2: The required amount of de-icing fluid is set to be 1 L/m^2 based on work by the U.S. Department of Transportation and Federal Aviation Administration (2023).
  - 6.3: The cost of the de-icing fluid is computed in Chapter 3.
- 7. Ground station and SG&A cost
  - 7.1: Similar to 4.2, the standard value for the lifetime of a trucks, and generators is five years [12] [13].
  - 7.2: The required generator size is computed by multiplying the charging power (5700W, mentioned in 4.6) by the number of batteries charging at any given time. Since two sets of three batteries are charging for each of the 8 drones (the number of drone is based on an optimal number that maximizes margin and operational ease) that brings the total to roughly 274kW. As a first order estimate, the batteries can be charged for up to two times the length of the mission flight time of 13.6 minutes. Leaving 30 seconds to physically change the battery, the maximum charging time of a battery is 26 minutes. This reduces the required power draw to 5260W, bringing the total power required to just over 250kW. As a first order estimate, a standard 250kW diesel generator costs around €50 000. [14].
  - 7.3: Is the price of diesel in Sweden.
  - 7.4: Represents fuel consumption of a D250 GC Caterpillar diesel generator (Caterpillar Inc., 2025).
  - 7.6 - 7.7: Is the price of trailer truck and tank truck necessary for the ground station (see Section 13.2).
  - 7.9: Is the ratio between the SG&A (Sales, General, and Administrative) costs and the revenue [15]. It is used to account for expenses such as administrative, sales, marketing, compliance, insurance, and logistics costs.
- 8. Financial outcome
  - 8.1: The return on the investment for the wind turbine company has to balance competitive pricing such that both the wind turbine operator and the drone operator

[10] https://www.dji.com/ch/flycart-30/specs
[11] https://store.foxtech.com/diamond-hvt-12s-66000/
[12] https://ofm.wa.gov/sites/default/files/public/legacy/policy/30.50.pdf
[13] https://www.irs.gov/publications/p946
[14] https://www.machinerytrader.com/listing/auction-results/245254465/caterpillar-d250gc-stationary-generators-powersystems
[15] https://finlistics.com/metric-of-the-month-selling-general-and-administrative-sg-a-as-a-percentage-of-revenue/

are incentivized to pursue this project. Benchmark Internal Rate of Return ranges hover around 8-15%, realizing the inherent risk associated with a new project such as this one, the Return on Investment for the wind turbine company is set to 33%.

4.5.2. Process

The financial model that is modelled here is a fixed-return gain-sharing model where the ROI for the wind turbine operator is fixed at 33% and any remaining profit is left for the operator of the de-icing operator. This kind of business model is relatively low risk with predictable returns for the wind turbine operator, which makes it quite attractive. The idea of the business model is as follows: by de-icing wind turbines (up to 10 times per year), the wind turbine operator unlocks an additional €1 500 000 in revenue, the wind turbine operator keeps €380 000 and the remaining €1 120 000 is used for the cost of the wind turbine de-icing and profit of the drone operator. This can be explained by the following formula:

```
Recuperated revenue (2.2)
- Cost of drone (4.4)
- Cost of batteries (4.8)
- Cost of de-icing downtime (5.6)
- Cost of de-icing fluid (6.5)
- Cost of ground station and SG&A (7.11)
- Profit for wind farm (8.2)
= Profit for drone operator (8.4)
```

However, this is only the final calculation line, and the model itself is complex, interconnected, and requires iteration. A simplified version of this process is shown in Figure 4.5.

The model starts with the input of parameters from the case study (Stor-Rotliden) into `1. Wind-farm overview`. This is where the yearly revenue is computed. Next, the revenue losses due to wind turbine icing are computed in `2. Baseline icing losses`. Simultaneously, operational requirements such as the required vertical and horizontal distances the drones have to cover are input into `3. Drone operational properties`. This is where the spray rate, payload, horizontal, and vertical velocities are optimized. This section also outputs the mission time and flight time. Next, the de-icing downtime costs are computed in `5. De-icing downtime cost`. The premise behind this section is that the eight drones de-ice the wind turbine one after another. Therefore, the first wind turbine is off for roughly 1 hour while the last one is down for roughly 38 hours. For this sequence, the total number is computed as the sum of an arithmetic series. This number of hours is translated as missed revenue (it is expected that this fraction of production cannot thus be recuperated). From `3`, the path leads to `4. Drone costs` which takes as input parameters relating to the price of the drone, the price of batteries, along with the required number of batteries, the latter of which flows from the engineering analysis in Section 5.1. This is where the number of drones is optimized for. At the same time, `3` leads to `6. De-icing fluid cost` where based on an input that contains information about the required number of liters per square meter of de-icing fluid, along with the cost of the fluid; the total cost of the fluid is computed. The last cost component is `7. Ground station and SG&A cost` which flows from information about the ground station (which depends on Section 5.1 and Section 13.2) as well as a set SG&A/Revenue ratio.

Finally, combining the cost components `2,4,5,6,7` with the recuperated revenue `2.2` and the set ROI for the wind turbine company `8.1` results in the profit margin for the drone operator.

Again, this process is not linear or as straightforward as it may seem. The following section deals with optimizing the output to maximize the profit margin.

Table 4.5: *List of input parameters for wind farm de-icing cost-benefit analysis.*

#	Parameter	Value	Unit	Source
1. Wind-farm overview				
1.1	MWh price [!]	56.61	€ / MWh	(Ember, 2025)
1.2	Yearly production	200 000	MWh / yr	(Vattenfall, 2011)
1.3	Yearly loss	12	%	(VTT Technical Research Centre of Finland, 2015; IEA Wind TCP, 2018)
1.5	Turbine power	2	MW	(The Wind Power, 2025)
1.6	Turbine number	40	–	(Vattenfall, 2011)
1.7	Turbine area [!]	644	m^2	Subsection 4.5.1
3. Drone operational properties				
3.1	Number of de-icings [!]	10	/ yr	(Clausen et al., 2014)
3.4	Travel distance (vertical)	169	m	(Vestas, 2011)
3.6	Travel distance (horizontal)	1 000	m	Subsection 4.5.1
3.10	Detection time	126	s	Subsection 4.5.1
3.14	Time to refuel	60	s	Subsection 4.5.1
3.15	Operational safety margin	10	%	Subsection 4.5.1
4. Drone costs				
4.1	Drone price (total) [!]	50 000	€	Subsection 4.5.1
4.2	Operational lifetime	5	years	Subsection 4.5.1
4.5	Number of batteries (/drone)	3	–	Subsection 4.5.1
4.6	Number of battery sets (/drone)	3	–	Subsection 4.5.1
4.7	Battery cost (/battery) [!]	2 000	€	Foxtech Diamond [16]
6. De-icing fluid cost				
6.1	Fluid type	Propylene Glycol	–	Chapter 3
6.2	De-icing fluid use [!]	1	L / m^2	(U.S. Department of Transportation & Federal Aviation Administration, 2023)
6.3	Fluid cost [!]	0.52	€ / L	Subsection 3.3.3
7. Ground station and SG&A cost				
7.1	Operational lifetime (ground)	5	years	Subsection 4.5.1
7.2	Diesel generator cost	50 000	€	CAT D250 GC [17]
7.3	Diesel fuel cost (/L)	1.49	€ / L	Cargopedia [18]
7.4	Diesel consumption	73.3	L / h	(Caterpillar Inc., 2025)
7.6	Trailer cost	50 000	€	Norstar Company [19]
7.7	Tank truck	50 000	€	Sinotruck HOWO [20]
7.8	Number of tank trucks	2	–	Section 13.2
7.9	SG&A / Revenue [!]	20	%	Finlistics [21]
8. Financial outcome				
8.1	Wind farm return on investment [!]	33	%	Subsection 4.5.1

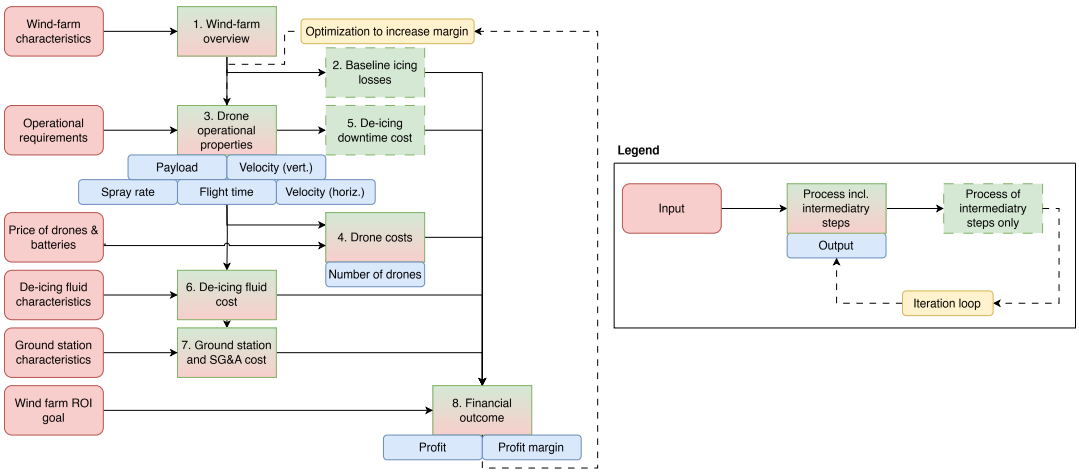

Figure 4.5: *Simplified process flow diagram of the financial analysis of a drone-based wind turbine de-icing solution.*

4.5.3. Outputs

The reason to make a financial model is usually to determine, given a set of parameters, the profitability of a business operation. In this case, some of the "inputs" are themselves "outputs" of the operation, the goal being to find what value they should take on to result in the maximum profitability of a process. All of these parameters are exposed in Table 4.6. Parameters that have "Optimization" as a source are parameters that can freely be varied (example: spray rate); others are directly determined from other parameters and cannot be varied directly (example: flight time).

The question is now to optimize the parameters that can be input arbitrarily. To do this, the definition of optimum has to be laid out. Before doing this, it is necessary to realize that in any engineering product, there is always an inherent trade-off between performance and complexity, and cost. In general, the higher performing a product is (no matter the metric), the more expensive it is. This leads directly to the concept of diminishing returns, which is "the decrease in marginal (incremental) output of a production process as the amount of a single factor of production is incrementally increased" [22]. This effect is seen across all parameters that are optimized; the incremental increase in one unit (say 1 L/min for the spray rate) will increase the profit margin less and less each time. One way to optimize the value of the input in this case is to aim for a given slope (change in output for one unit change in input), say 5%.

Figure 4.6 is used to optimize several output parameters. Each subplot, **(a)** to **(e)**, is composed of two parts. The upper part shows the relation between the independent parameter and the profit margin. The other, below it, shows the change of profit margin that results from an increase of one unit of the independent parameter. For example, in Figure 4.6a, the lower plot shows that the change of profit margin that results from the increase of vertical velocity from 2 to 3 L/min is 1.8%. All plots also include a visual profitability threshold and a threshold for the change (Δ) in margin. Now, all the output parameters can be optimized.

- **The vertical speed** is selected to be 3 m/s. Note, in Figure 4.6 (a), that the potential increase to 4 m/s would increase the margin by less than 1% (0.9%), it is judged to be not productive enough. Observing that the DJI Flycart 30 has a maximum vertical speed of 5 m/s [23], this value seems reasonable and attainable.
- **The horizontal speed** is selected to be 7.5 m/s (USER-S-PROP-1.2). As before, note, in Figure 4.6 (b), that the potential increase to 4 m/s would increase the margin by less than

[22] https://en.wikipedia.org/wiki/Diminishing_returns
[23] https://www.dji.com/ch/flycart-30/specs

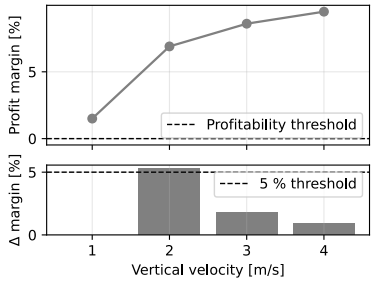

(a) *Impact of vertical climb/descent speed on profit margin.*

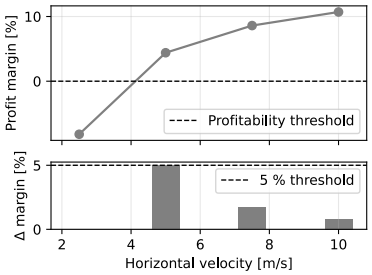

(b) *Impact of horizontal cruise speed on profit margin.*

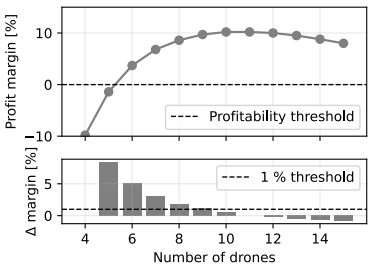

(c) *Impact of fleet size on overall profit margin.*

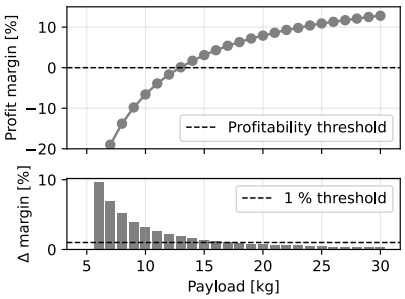

(d) *Impact of payload mass on profit margin.*

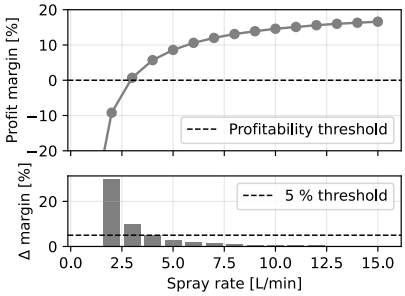

(e) *Impact of spraying rate on profit margin.*

Figure 4.6: *Optimization of key operational parameters for the de-icing drone concept. Each subplot shows how varying a single parameter affects the projected profit margin, with all other inputs held at their baseline values.*

1% (0.8%), it is judged to be not productive enough. Observing that the DJI Flycart 30 has a maximum horizontal speed of 20 m/s [24], this value seems reasonable and attainable.

- **The number of drones** is the only parameter that shows a global optimum of 11 drones. However, observing Figure 4.6 (b), starting from 8 drones, the incremental addition of 1 drone yields less than 1% increase in margin. Furthermore, an even number makes operations and storage slightly easier. For this reason, the optimal number of drones is set to be 8.

  Note: this number is an optimal value for Stor-Rotliden. As this project expands, the same process is used to determine the optimal number of drones for any wind turbine farm.

- **The payload mass** shows that any payload increase (of 1 kg) above 17 kg increase the margin by less than 1%. Nevertheless, to aim for a reasonable profit margin, the design payload is set to be 21 kg. This results in a profit margin of 8 %, a reasonable value based on Damodaran (2025).

- **The spraying rate** is set to be 5 L/min (USER-S-PAYL-3.1). Although the increase from 4 to 5 L/min is arguably unproductive considering that the profit margin increase is smaller than 5%, it appears quite productive when it is observed that the margin at 4 L/min is barely more than 5%. Furthermore, 5 L/min appears to be an easily attainable goal considering existing spraying payloads [25]. The range of 4-16 L/min is a realistic range[26],[27].

[24] https://www.dji.com/ch/flycart-30/specs
[25] https://www.drone-payload.com/product/dji-flycart-fc30-drone-high-pressure-spray-cleaning-system/
[26] https://www.dji.com/ch/t30/specs
[27] https://ag.dji.com/t50/specs

Table 4.6: *List of output parameters from the wind farm de-icing cost-benefit model.*

#	Parameter	Value	Unit	Source
3. Drone operational properties				
3.2	Spraying rate	5	L / min	Optimization
3.3	Payload	21	kg	Optimization
3.5	Velocity (vertical)	3	m/s	Optimization
3.7	Velocity (horizontal)	7.5	m/s	Optimization
3.19	Flight time	12.6	min	`SUM(3.8;3.14)-3.14/60`
4. Drone costs				
4.3	Number of drones	8	–	Optimization
8. Financial outcome (De-icing operator)				
8.4	Profit from de-icing	133 373	€	`2.2-4.4-4.8-5.6-6.5-7.11-8.2`
8.5	Profit margin	8.6	%	`8.4/(2.2-5.6-8.2)`

4.5.4. Constraints

In the financial model, there are not any hard "constraints" as can be imagined would be present in a technical design. All engineering constraints are enforced in the engineering design section. The financial constraints are:

- The net profit margin for the operator should be above 5%. This is based on the average net profit in the aerospace and defence industry given by Damodaran (2025).
- The return on investment for the wind turbine operator should be above 12%. This is a commonly used hurdle rate [28] for various projects and is sufficient as an early estimate.

4.5.5. Assumptions and limitations

Needless to say, this financial model hinges on a number of assumptions. In this context, the word "assumptions" refers specifically to high-level assumptions about how the financial model behaves. It does not refer to values that contain uncertainties. Thus, the assumptions (as previously defined) are:

1. The model assumes that the icing results in the highest possible level of revenue loss, i.e. 12%. As a reminder, the possible loss at a IEC Class III site is 5-12% (Cattin, 2016).

   Effect Observing Table A.10, it can be seen that the project produces a loss if the annual power loss dips below 11%. This shows that the 12% is thus vital for the projects survival. However, since the aim of the project is to provide de-icings, it logically only makes sense to pursue if that produces a significant loss.

2. The model assumes that 10 de-icing operations per year `[3.1]` are enough to recuperate all 12% of the lost revenue (some revenue is lost again due to the de-icing time `[5.6]`).

   Effect Observing Table A.3 shows that the operation is only profitable if the 12% can be recuperated in under 12 de-icing operations. Considering that there are 9 icing events, (Clausen et al., 2014) it is reasonable to expect the recuperation of the majority of the lost revenue.

3. The model does not account for an increase in the price of a drone due to a higher payload `[3.3]` or spraying rate `[3.2]`.

   Effect This assumption is most likely the least consequent of the list. The way this effect was treated was through the concept of diminishing returns (Subsection 4.5.3). In any case, the payload and spray rate ranges are reasonable and in the range of existing

[28] https://www.investopedia.com/terms/h/hurdlerate.asp

systems.

4. It is assumed that the period of ice accretion is relatively short compared to the period of icing (see Subsection 2.1.2). Only in this way, the 10 de-icing operations can reasonably be expected to be enough. Otherwise, ice would cover the wind turbine again after it has been de-iced.

   Effect This assumption is quite central to the financial analysis of the model. It is difficult to quantify how much this affects the results of the financial analysis. Nevertheless, it directly correlated with the number of wind turbine de-icing operations (see Table A.3).

5. Inline with the assumption above, another assumption that is made is that instrumental icing events correspond to rotor icing events such that the number of 9 instrumental icing events per year can be equated to 9 rotor icing events per year.

   Effect This assumption seems reasonable at an early stage based on IEA Wind TCP (2018). Nonetheless, refinement is necessary in later stages.

Overall, several assumptions that shape the way the model behaves have been presented, and their effects have at least been discussed qualitatively, if possible. It is clear that the model is sensitive to some input data. For this reason, an in-depth sensitivity analysis is presented in the following section.

4.5.6. Sensitivity analyses

Several sensitivity analyses are performed to reduce the effect of uncertainties in the financial model. These analyses, exposed in Subsection A.0.1, explore the impact of various parameters on the profit margin. The parameters that are selected for the sensitivity analysis are:

- Parameters that have a higher degree of uncertainty compared to the average expected uncertainty.
- Parameters that are central to the model and can reasonably be expected to drive the profit/loss of the operation.

Table 4.7 shows the ranges of various parameters that were analysed alongside the effect on the profit margin. It can be seen that changes that might appear slight at first can have a significant impact on the profit margin. Nonetheless, the project remain profitable along a relatively large range of input parameters.

Firstly, this means that if further research shows a deviation in one of the input parameters, the project remains viable. Secondly, this shows that the project is financially viable in a variety of environments and thus paves the way for expansion at new wind farm locations. Therefore, most parameters are allowed to change, at least slightly, to accommodate for a design that may be iterated and changed. The next section discusses in what circumstances this will be useful.

Please note: all sensitivity analyses are conducted "all else being equal". This means that no other parameters are adjusted to optimize for the profit margin during each sensitivity analysis.

4.5.7. Iteration based on the drone sizing

As mentioned above, certain input parameters in the financial analysis are subject to change based on the engineering drone sizing. For example, the battery price is a direct result of sizing the drone. In this sizing process, some parameters from the engineering design (namely the battery price and costs related to the ground station) go back to the financial analysis to update the final profit margin (see Figure 4.2). This information does not result in a new iteration of the engineering sizing because the design remains financially viable. However, this loop could easily be envisioned in the future: if the engineering analysis shows that the drone is capable

Table 4.7: *Input spans and resulting extremes of operator profit margin for each one-way sensitivity parameter (ordered: low-input → high-input).*

Parameter	Input range	Profit-margin range
MWh price	30 – 120 €/MWh	–16.6 % → 23.7 %
Turbine area	300 – 1200 m^2	27.0 % → –21.1 %
Number of de-icings	3 – 12 (–)	32.7 % → 1.8 %
Total drone price	€25 000 – €125 000	11.2 % → 0.9 %
Battery cost (/battery)	€1 000 – €4 000	13.3 % → –0.7 %
De-icing fluid use	0.5 – 2 L m^{-2}	13.0 % → 0.0 %
Fluid cost	€0.2 – €1.1 L^{-1}	14.0 % → –1.0 %
SG&A / Revenue	10 – 40 %	13.3 % → –0.6 %
Wind-farm ROI	10 – 40 %	21.2 % → 5.6 %

of a higher performance (or that the requirements exceed its capacity), the financial model can adjusted and the process repeats itself.

4.5.8. Discussion & further work

To conclude, this section determined that a drone-based wind turbine de-icing solution is a financially viable business opportunity. After discussing the inputs of the financial model, the discussion turned to the process that the model follows. Next, the optimization of the outputs is expanded on. Following this, the financial constraints of the model are discussed. Assumptions that drive the model, along with the expected effects, are discussed next. Finally, a variety of sensitivity analyses reinforces the confidence in the financial model. Iteration is, of course, a part of the general sizing process and is touched on as a final part. Furthermore, as all input parameters, especially those that relate to the wind farm, are easily updated, this method is easily adapted to a new customer's needs. Overall, this model is highly flexible and thus streamlines commercial expansion.

The financial model indicates that the following parameters result in an optimal profit margin: 8 drones, 21 L payload (USER-S-3.2), 5 L/min, 3 m/s vertical flight velocity, 7.5 m/s horizontal flight velocity, and flight time of 12.6 min (USER-S-POW-5.1). The resultant profit margin for the drone operator is 8.6% (excluding interest payments and taxes) or slightly over 130,000 €.

The following further work is proposed to improve the model:

- Conduct further research on the weather conditions at Stor-Rotliden, specifically on the topics of resultant power loss percentage, rotor icing length, ratio between accretion and persistence.
- Include a performance/price relation with the optimized parameters.
- Expand on the secondary financial parameters (SGA, taxes, interests, liquidity) and conduct a Discounted Cash Flow analysis. In addition, the elaboration of a broader business plan for the company (including prospective clients and market capture projections) is needed.

Parameters passed to the engineering sizing Only two parameters are passed directly to the engineering sizing: the payload weight and the mission flight time. It is crucial to understand that these parameters result from a complex iteration and optimization process. They are influenced by all other inputs and should not be seen as independent parameters.

4.5.9. Summary of appendix

The appendix contains all sensitivity analysis that were performed (Table A.4) and a complete list of parameters (Table A.13).

Part II:

Vol. 2 | Design & Engineering Development

5

Drone sizing

Leonardo, Michal, Edlyn

To create an efficient and innovative design, the technical aspects have to be considered carefully. In this chapter, the engineering sizing of the drone is presented. Firstly, Section 5.1 presents the final design and the sizing loop. Afterwards, Section 5.2 expands on the specific methodology to select motors and propellers. It also discusses assumptions and proposes further work.

Unlike for fixed-wing aircraft, for which early sizing models are plentiful and accurate (Torenbeek, 1982; Raymer, 2018; Roskam, 1989), there exist only sparse and incomplete sizing methodologies for multicopter drones (Delbecq et al., 2020; Budinger et al., 2020; Biczyski et al., 2020; Gatti, 2017). The following sections will expand on the work done by Biczyski et al. (2020) by creating a full iterative loop including new statistical data (similarly to Gatti (2017)). This method is particularly adapted for heavy lifting drones, which are excluded from considerations in a number of papers (Gatti (2017) focuses on drones under 20 kg).

5.1. Engineering drone sizing

Leonardo, Michal, Edlyn

This section discusses the final design in Subsection 5.1.1 after which, the sizing process is explained in Subsection 5.1.3. The sizing process is highly iterative and expands on the work of Biczyski et al. (n.d.) and improves it with new statistical relations to fit high-lift drone design.

5.1.1. Final drone design

The sizing process establishes a configuration that fulfils all relevant top-level requirements: payload power < 700 W (SER-S-POW-1.1), comms/control power < 50 W (USER-S-POW-2.1), endurance ≥ 10 min (USER-S-POW-5.1) with 80 % recharge in ≤ 30 min (USER-S-POW-3.1), operation in winds up to 12 m s $^{-1}$ (USER-S-POW-5.2), battery life ≥ 1000 cycles (ENV-M-SUST-2.4), sea-level thrust ≥ 1500 N (USER-S-PROP-1.2) and cruise speed ≥ 5 m s $^{-1}$ (USER-S-PROP-3.1).

5.1.2. Design goals

There are three design goals in this process, together creating a coherent set of design principles. These goals are:

- Minimize number of rotors: fewer rotors reduce risk of mechanical or control system failure as well as simplifying maintenance.
- Minimize the power needed to hover. This is used to size the propeller and the motor.
- Allow the drone to achieve a minimum thrust to weight ratio of 2.2 (Appendix B). This can also be interpreted as a constraint but is mentioned here due to its importance in the drone sizing process.

Table 5.1: *Mass breakdown, battery configuration, propulsion details and power requirements for the UAV. Values are based on the output of the iterative sizing loop.*

Mass overview	
Take-off mass	99.2 kg
Payload mass	27.0 kg
Battery mass	32.5 kg
Empty weight	39.7 kg
Empty-weight breakdown	
Avionics	1.0 kg
Propellers (total)	1.9 kg
Motors (total)	0.2 kg
ESCs (total)	1.0 kg
Primary structure	35.6 kg
Battery	
Capacity	132,000 mAh
Configuration	14S
Propulsion	
Propeller model	22x10E
Propeller diameter	0.56 m
Motor model	T-Motor F20 II 2800
Number of rotors	14
Power requirements	
Total energy required	4 415 Wh
Total power required	22 074 W
Motor power (total)	14 282 W
Manoeuvre margin (total)	7 141 W
Payload + avionics	650 W

5.1.2.1. Inputs

There are only three parameters that act as inputs to the drone sizing loops (excluding the databases for the propeller and motors). They are shown in purple in Figure 5.1. These parameters are:

- Payload mass: 27kg. This includes a 21kg (L) of de-icing liquid coming from the Section 4.5 and a 6kg pump and spraying system from Chapter 3.
- Total flight time: 12.6 mins from Section 4.5.
- Thrust-to-weight ratio: 2.2 from Appendix B.

5.1.3. Sizing loop

The component selection and sizing method developed for this project significantly extends a current method proposed by Biczyski et al. (n.d.). The original method provided a straightforward, single-pass algorithm for selecting a propeller, motor and battery based on given mission criteria, mainly required thrust and endurance. This work closes this loop to provide a more robust, iterative process, enhancing accuracy and reliability. This section corresponds to the third iteration in Figure 4.2.

The first step in the sizing loop in accordance with Figure 5.1 is making a first estimate of the empty weight, W_{TO}, via :

$$W_{TO} = \frac{W_{PL} + W_b}{1 - \frac{W_0}{W_{TO}}} \tag{5.1}$$

Where W_{PL} and W_b are payload and battery weight, respectively. The payload is calculated in the previous section, and the battery weight is an initial guess to be iterated on in the loop. The

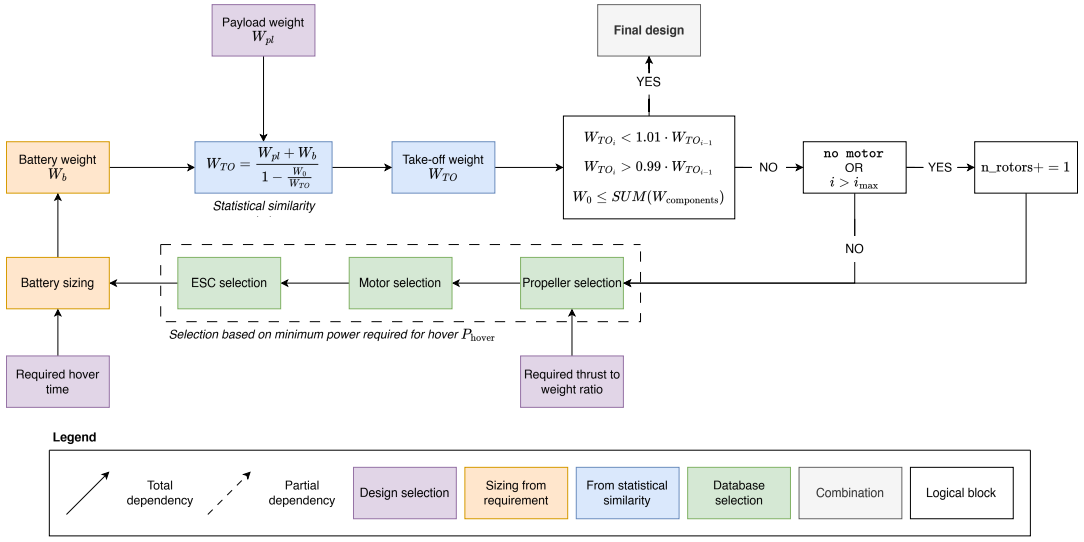

Figure 5.1: *Iteration loop for the drone design, showing how the design is based on selected components, statistical similarity, and database selection.*

empty weight to take-off weight ratio $\frac{W_0}{W_{TO}}$ is computed when looking at 9 other drones with similar payload weights (DJI FlyCart 30[1], DJI Agras T30[2], DJI Agras T25[3], XAG V40[4], Harris H6 HL[5], DJI Agras T40[6], DJI Agras T50[7], XAG P100 (2022)[8], Freefly Alta X[9], XAG V50[10]). The average is found to be 0.4. This value is used to make the first input of the take-off weight.

The take-off weight as illustrated in Figure 5.2 is made up of Payload weight, Battery weight and Empty weight. A key constraint in the sizing loop is the fact that regardless of the configuration that is compiled, if the empty weight exceeds the combined weight of its components i.e. motor weight, fuselage, esc weight, propeller weight and avionics weight it discards the configuration and repeats the sizing loop.

This iterative approach addresses a critical gap in existing methods, which typically rely on open-loop calculations, potentially leading to suboptimal selections, as they neglect the interdependence of components. By repeatedly recalculating total mass after each selection process and resizing the components accordingly, this method ensures a fully converged design, indicated by a 1% tolerance margin of total mass at the end.

5.1.3.1. Constraints

There are certain constraints on the general drone design. These requirements ensure that the drone fulfills the mission it was designed for within a certain envelope.

- Total energy used needs to remain below 5kWh (`USER-M-SUST-2.2`).
- The total mass of the drone needs to remain below 100 kg (`USER-S-STR-3.1`).

[1] https://dl.djicdn.com/downloads/DJI_FlyCart_30/202406UM/DJI_FlyCart_30_User_Manual_v1.1.pdf
[2] https://www.dji.com/t30/specs
[3] https://grainsco.com/wp-content/uploads/2024/06/DJI_T25_Technical-Brochure.pdf
[4] https://static.xag.cn/img/service/%283WWDZ-15.2A%29%20V40%20User%20Manual-V1.2%20EN202207041759.pdf
[5] https://harrisaerial.com/wp-content/uploads/2023/08/H6-HL-DataSheet.pdf
[6] https://www.frostserv.com/live/wp-content/uploads/2024/04/DJI-T40-Spec-Sheet.pdf
[7] https://grainsco.com/wp-content/uploads/2024/06/DJI_T50_Technical-Brochure.pdf
[8] https://www.airbornesolutions.co.nz/wp-content/uploads/2023/07/XAG-P100-Operating-Handbook.pdf
[9] https://freefly-prod.s3.amazonaws.com/support/alta-x-brochure.pdf
[10] https://www.xa.com/en/v50/v50spec

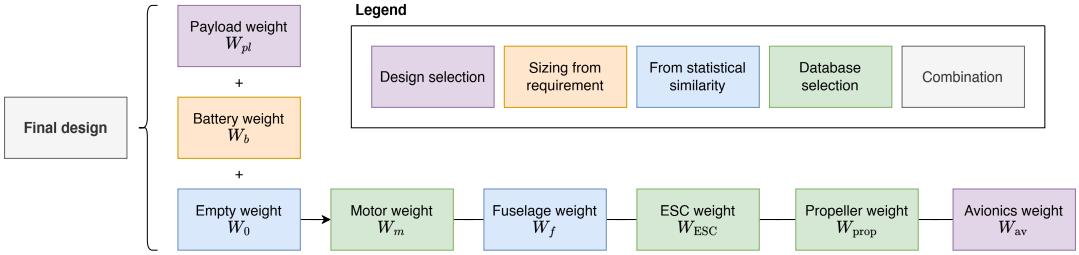

Figure 5.2: *Mass breakdown of the final design showing the source of each component through the color of the block.*

- endurance ≥ 10 min (`USER-S-POW-5.1`)
- payload power < 700 W (SER-S-POW-1.1)
- comms/control power < 50 W (USER-S-POW-2.1)

5.2. Component selection and sizing *Edlyn, Leonardo, Michal*

This section details the logical flow from thrust-to-weight ratio chosen to the selection of real-world subsystems: propellers, motors and ESCs based on minimum hover performance, and battery sizing derived from flight time requirements. (Figure 5.1)

5.2.1. Propeller selection

1. **Initial filter** The following are the constraints first applied to filter through the propellers database
   (a) Diameter <0.6m - This upper limit allows for an overall design which does not introduce a structural challenge Carhart et al. (2020)
   (b) Mass < 0.35kg
   (c) Thrust per rotor: this value will depend on the number of rotors used. The code runs through all even number of rotors 6-16 Appendix B
2. **Thrust filtering** The static information for all of the propellers are fetched. These values include the thrust, RPM, torque and electrical power across different throttle setting. Propellers whose thrust maxes out below reaching the Wide Open Throttle (WOT) thrust are discarded Appendix B.
3. **Interpolation** The test bench values of power P, torque τ and RPM ω are linearly interpolated to find their values at Hover and WOT thrust setting.
4. **Selection objective** The average shaft power is calculated using:

$$P_{avg} = \frac{1}{2}(P + \tau\omega) \tag{5.2}$$

   where the code runs all of the remaining propellers based on their average power at hover. After which the propeller with the lowest P_avg at hover is chosen, thus minimising energy drawn at the missions most critical operating mode (hover).

5.2.2. Motor Selection

1. **Initial filter** The initial filtering consists of the following constraints:
   (a) Mass > 0.35 kg to avoid outliers
   (b) No performance data available at all

2. **Motor reference point** For all the motors the code chooses the row which is measured closest to the voltage input for the design from the battery. From the row a "no-load" current I_0 is utilized to estimate the motor's internal (iron) loss:

$$P_{Fe} = V I_0 \tag{5.3}$$

3. **Operating currents** Considering the shaft-power from the propeller hover ($P_{shaft,h}$), the code solves the electrical balance

$$R I^2 - V I + (P_{Fe} + P_{avg}) = 0,$$

where $R = 2R_m$ which is the winding resistance.

P_h The smaller positive root yields the operating current I_{hover}. This current for each drone is used to calculate their respective electrical power for hover

$$P_{el,h} = V I_{hover} - P_E \tag{5.4}$$

4. **Motor selection** Similar to the propeller, the final motor is found by selecting the lowest electrical power in hover.

The motor selection represents the optimum choice based on the minimum electrical power consumption for hover. This method accurately sizes for the mission-specific operational priority

5.2.3. Battery Sizing

The first inputs of the battery sizing are derived from an initial market analysis taking into account drones with similar weight and applications(USER-S-STR-5.1):

- Battery configuration 14S, 51.8V nominal voltage. Based on DJI agras T30 [11], and DJI Flycart 30 [12].
- Battery energy is computed with a 3.7V nominal voltage.
- Batteries are assumed to have a max voltage of 4.2V and a cut-off voltage of 3.7V (which happens at 20% capacity).

Therefore key parameters are summarized as follows:

Table 5.2: *Parameters used in the battery model (Biczyski et al., n.d.)*

Symbol	Value / expression	Source in code
$V_{\text{cell,full}}$	$4.2V$	`voltage` (per–cell full charge)
n_{cells}	14	`ncells` (series count)
P_{pack}	$p_{\text{req}}\, n_{\text{rotors}}$	motor-sizing output
DoD	0.80	hard–coded (depth of discharge)
n (Peukert)	1.3	`n_peukert`
k_1 (sag slope)	$\dfrac{4.2-3.7}{\text{DoD}\, C_0\, n_{\text{cells}}}$	eq. in code
Energy density Evro et al., 2024	$205\,\text{mAh}\,\text{g}^{-1}$ @ 3.7 V	constant

Computation

[11] https://www.dji.com/uk/t30/specs
[12] https://www.dji.com/uk/flycart-30/specs

1. **Initial guess.** Create a `Battery` object with $C_{raw} = 10\,000 mAh$.
2. **Minute-step discharge simulation** (`discharge_time`):
   2.1. Update pack voltage $V = V_0 - k_1 (C_0 - C)$.
   2.2. Compute current $I = P_{\text{pack}} / V$.
   2.3. Apply Peukert's law to remaining capacity
   $$C \leftarrow (\tfrac{I}{I_0})^{1-n} C_0 - \sum \text{discharged}.$$
   2.4. Repeat until $V < 3.7 V\,cell \cdot n_{\text{cells}}$ (at which point the battery is assumed to have reached 20% capacity (Biczyski et al., n.d.)) or $C < 0.2\,C_0$.
3. **Capacity root–solve** (`required_capacity`): Embed the simulation in a Brent root–finder so that endurance = t_{target} (12.6 minutes based on Table 4.1).

   The drawn power is assumed to be the power required for hover. In addition, a margin of 50% is added to account for movement. To that, 650W of power is added as an early estimated for all components excluding the motors.
4. **Finalize pack** (`set_capacity`):
   $$m_{\text{batt}} = n_{\text{cells}} \frac{C_{\text{raw}}}{1000} \frac{3.7}{205} \quad \text{[kg]},$$
   $$C_{\text{min}} = \frac{I_{\text{ESC}}\, n_{\text{rotors}}}{C_{\text{raw}}/1000} \quad \text{(continuous C-rating)}.$$
5. **Return** a `pandas.Series` containing `batt_capacity` (mAh), `batt_weight` (kg), and required `c-rate`.

Outcome: Each outer sizing iteration therefore receives the lightest Li-ion pack which

- provides the total hover power,
- sustains the mission endurance, and
- satisfies the ESC current demand of all rotors.

5.2.3.1. Outputs

- Number of rotors: 14
- Selected propeller: 22x10E
- Selected motor: T-Motor F20II 2800
- Battery Capacity: 128747.7mAh

5.2.4. Resource allocation and budget breakdown

As the final design comes together, it is necessary to verify that the budget allocation is respected. As a reminder, the maximum mass of the system is 99.2 kg, the maximum power requirement is 650 W as per SER-S-POW-1.1(on average, excluding the motor power), and the price is below 30,000€. These requirements are based on the inputs to the financial and engineering analyses with which the final design has to comply. Observing Table 5.5, it can be seen that the design complies with the required budgets.

Battery selection The sizing suggests that a minimal battery capacity should be 128,000mAh. A search is conducted, focusing on NMC Li-ion batteries. NMC batteries were shortlisted as early

favorites due to their energy density and cold-weather performance. Batteries from Maxamps [13] appear to be the highest quality candidates. However, since the batteries are the main cost drivers in the financial sizing Subsection 4.5.1, less expensive options are prioritized. Finally, batteries from Foxtech [14] are selected because they provide an excellent performance, especially at very low temperatures, for a reasonable price. Three 44,000mAh batteries are selected and result in a final capacity of 132,000mAh.

Thermal control strategy To maintain the internal components at a reasonable operating temperature a STEGO 250W heater is installed. It can heat 1 cubic meter by 20°C in under 5 minutes. As an early estimate, this is quite sufficient.

5.2.5. Sensitivity analysis

Several sensitivity analyses are performed to reduce the effect of uncertainties in the financial model. Since there are only two direct input parameters to the sizing process, payload mass and flight time. Table 5.3 shows that a flight time of 16 minutes or above is too high (the required battery capacity is either too high or no configuration is found at all). Table 5.4 shows that a payload much above the current mass (27 kg) makes the design unfeasible. Overall, the sensitivity analyses show that the drone is pushing the limits of flight time and payload mass. This is a positive outcome showing that the design is optimized for its intended purpose.

Table 5.3: *Sensitivity analysis of the engineering drone sizing to flight time (for a constant payload). All other parameters are sized and optimized according to Section 5.1. N/A means no suitable configuration was found.*

$m_{\text{structure}}$	Payload Mass [kg]	Flight Time [min]	# Rotors	Battery Capacity [mAh]	Battery Weight [kg]
30.7	27	10	12	97180	24.6
35.2	27	12	14	126107	31.9
43.1	27	14	16	176307	44.6
N/A	27	16	N/A	N/A	N/A

Table 5.4: *Sensitivity analysis of the engineering drone sizing to payload mass (for a constant flight time). All other parameters are sized and optimized according to Section 5.1. N/A means no suitable configuration was found.*

m_{total} [kg]	$m_{\text{structure}}$ [kg]	Payload Mass [kg]	Flight Time [min]	# Rotors	Battery Capacity [mAh]
80.3	28.5	20	13.5	12	111497
114.2	39.8	25	13.5	14	172284
N/A	N/A	30	13.5	N/A	N/A

5.2.6. Assumptions and limitations

The sizing loop developed relies on a list of assumptions:

- The battery sizing uses a fixed Peukert exponent of 1.3.

  Effect The value between 1-1.5 is commonly used for lithium-ion batteries, which approximates the internal resistance effects (Galushkin et al., 2020).

- The battery voltage is assumed to follow a linear decline.

[13] https://maxamps.com/collections/14s-lipo-battery-51-8v
[14] https://store.foxtech.com/diamond-hvt-12s-66000/

Effect This assumption is reasonable and has been validated externally by Traub (2013).

- Hover as the critical condition: Both the propeller and motor selection are based on minimizing the power consumption as according to the hover requirement.
- The power required for movement is assumed to be 50% of the power required to hover.

  Effect This assumption is crucial, and verifying it with tests and further research is a necessity to ensure a reliable drone design.
- One important limitation of this method is that it can only pick motors and propellers that are available in the database.

  Effect The advantage of this is that there is immediate commercial selection. The disadvantage is that if an optimal motor exists but is not in the database, it will not be selected.

5.2.7. Discussion and further work

To conclude, the sizing model provides a novel and iterative solution to the sizing of a high-lift drone. The process is based on a combination of sizing types including statistical relations and database selection (following Figure 5.1). The authors suggest the following future work to be completed under Chapter 17:

- Expansion of the motor and propeller databases with more relevant data for high-lift drones.
- The battery model can be improved by using a non-linear voltage sag slope.
- The effect of co-axial rotors (on required power) should be included directly in the sizing loop.

Table 5.5: *Consolidated, categorised bill of materials for the drone de-icing system. Blank entries ('–') indicate data not supplied. Asterisks (*) mark items excluded from total cost.*

Item	Units	Price [€]	Mass [kg]	Power [W]	Size [mm]	Source
Frame and structural components						
Carbon fibre rod	8.5	75	0.268	–	32 ext. ∅–28 int. ∅ × 1000	ClipCarbono
Aluminium spacer	1	20.67	–	–	4 × 10	MISUMI
Steel 8.8 M4 bolt	30	1.59	0.042	–	4 × 10	MISUMI
Pipe union connection	5	46	0.200	–	100 × 35	RJX Hobby
Power system						
Semi-solid Li-ion battery	1	6 000.00	30.000	–	250 × 165 × 126	Foxtech
High-pressure pump	1	52.00	4.300	2000*	320 × 190 × 190	AliExpress
STEGO Heater	1	1.00	1.1	250	182 × 100 × 85	STEGO
Control & Processing						
NVIDIA Jetson module	1	595.00	0.300	25	69.6 × 45	Amazon
IMU 9-DOF	1	15.00	0.009	<5	85 × 10 × 140	Distrelec
RTK-GNSS antenna	1	60.00	0.173	<1	82 × 60 × 22.5	DigiKey
RTK-GNSS base station	1	13 702.00*		–	–	Positioning Solutions
RTK-GNSS receiver	1	120.00	–	<1	17 × 22 × 2.4	Mouser
Sensors						
RGB camera	1	233.00	0.095	5	55 × 55 × 70	(A8-mini manual)
Tank-fluid meter	1	14.00	0.100	<1	(embedded)	DroneRoboticsTec
ToF sensor VL53L1X	20	6.50	<0.1	<1	4.4 × 2.5 × 1.56	TinyTronics
Hall-effect flow sensor	1	11.40	0.100	<1	58 × 33 × 38	AliExpress
Box (electronics)	1	9.53	0.582	–	255 × 200 × 80	Elektroshop
Spraying system						
Agras sprayer tank	1	65.00	21.000	–	610 × 420 × 210	Alibaba
Flat-fan nozzle	1	2.67	0.050	–	(embedded)	AliExpress
Stainless-steel tube	1	2.57	1.000	–	2500 L; ∅14 / 10	AliExpress
Propulsion						
Propeller 22×10 E	14	490.00	1.876	–	∅560	Aerobertics
T-Motor F20 II 2800 kV	14	224.00	0.224	–	–	Racer LT
Accessories						
Light (LED)	1	30.00	0.081	2	68 × 50 × 49.5	(datasheet)
Totals →	**65**	**8147.34**	**61.19**	**432**	–	–

6

De-icing component design

Gavin

In this chapter, the detailed design of the chemical spraying mechanism is investigated and discussed. A chemical de-icing system consists of a spray nozzle, connectors, a tank, and a pressurisation mechanism. Pressurisation can be achieved using a pump or a centrifugal nozzle. The following sections outline the key design decisions and how they were reached.

6.1. All-in-one solutions

Gavin

The simplest off-the-shelf setup includes commercial de-icing payload modules for heavy-lift drones. These solutions meet all the requirements and have some additional functionality and sensors. However, these solutions are beyond the budget, since they cost approximately €10k-12k. Therefore they are not possible to be deployed in the design. However, they are still interesting to analyse to see what the setup capabilities are.

One of the commercially available options contains a remote controllable nozzle pivoting around the end of the boom[1]. Mounting this system does mean that control needs to be updated due to the changeable direction. This will induce significant torque, which the drone must actively counter to maintain precision. In previous research by (Villeneuve et al., 2022), a solution is to adapt the control system to work with predicting and stabilising. Therefore, adding this controllable nozzle will increase complexity.

Another commercial, all in one solution [2] has a system where the entire arm is moved to aim the spray. During operation this provides more stability as there is no moment. However, the movement is limited to one axis (vertical) and the rest relies on the drone attitude control. Another interesting aspect of this design is that the tank fills a near spherical space at the centre of the boom hinge, with counter weight in the form of other components on the opposite side of the boom to facilitate the ease of rotation. This ensures that the change in centre of gravity is minimised during deployment as the tank empties up.

6.2. Assembled solutions

Gavin

Since all-in-one solutions are too expensive, a custom spray system was designed using primarily off-the-shelf components. The payload is to be designed with as many commercial off the shelf components as possible to simplify production and development.

6.2.1. Nozzle choice

After performing research it became clear that the first major design decision is to choose the nozzle and related spray pattern. Research of current working options are from drone deployment of liquids in other closely related fields. The following options for the nozzle are considered:

[1] https://www.foxtechfpv.com/aeroclean-a30-aerial-high-pressure-cleaning-system-for-dji-drones.html

[2] https://www.foxtechfpv.com/aeroclean-a2-precision-aerial-spraying-cleaning-system-for-dji-drones.html

6.2.1.1. Robotic swivel nozzle

First, swivel nozzles are used in a very similar de-icing drone used for aircraft's as described by Villeneuve et al. (2022). This nozzle configuration uses a single focused jet delivered through a remotely controlled swivel nozzle originally designed for firefighting. The advantages of this setup are the relatively low amount of movement the drone has to do as the nozzle swivels for targeting de-icing fluid, and the possibility to turn the swivel to aim at hard to reach places. The disadvantages of this option are the price as the TFT nozzle being used would consume a large portion of the budget (€1k+), complex controls needed to counter movements during fluid deployment due to reaction forces and moments, and lastly the spray pattern of the jet spray is relatively low in area coverage.

6.2.1.2. Centrifugal nozzle

The second option is a centrifugal nozzle[3] used by agricultural industry for pesticide spraying, on the DJI drone Agras T25/T30. This is a relevant deployment method since the high pressure, high deployment rate of pesticide with a thin spread over a large area are beneficial to a de-icing operation as well. An upside is the lack of a pressurisation pump in this setup as the pressure comes from the spinning disk in the centrifugal nozzle. By the disk striking the high pressure liquid into the shroud, the liquid is atomised into an aerosol and sprayed out. The mist can be electrostatically charged to ensure even distribution across the surface. With a wide cone spraying plus an angled mounting point this can cover many angles and cover the hard to reach places. The major downside of centrifugal nozzle is low range since the misting of fluid makes it slow and very easily affected by the rotor downwash and gusts of wind. This is not an issue in agriculture, where spraying is downward and rotor downwash aids distribution. This is, however, not possible for de-icing the wind turbine. Given the wind gusts requirement of 12 meters per second, it means that this nozzle is unsuitable for the mission profiles and thus fails as an option.

6.2.1.3. Flat fan nozzles

The third option is a nozzle choice from pressure washing industry, where there are drones using flat fan nozzle pressure washing windows and building exteriors. This maintains a high pressure spray without atomising the spray at the nozzle, and kinetic energy can be used to strike the ice. This nozzle forms a vertical line, covering more area than a solid jet but less than a centrifugal nozzle. This setup covers only a wider vertical angle, the horizontal angle relies on the attitude control from the drone. This trade-off is acceptable. Since it meets all other requirements, the flat fan nozzle is selected.[4]

6.2.2. Pressurisation system choice

Furthermore, the pressurisation system must be chosen. According to the aircraft de-icing fluid application guideline (Struk, 2017), application of type 1 aircraft de-icing fluid needs to be pressurised.

For this the choice comes from pressure washers, the high pressure washer pump pressurises the fluid to 6MPa [5], similar to one of the all in one solutions. This ensures deployment distance and increases de-icing efficiency. It also satisfies the requirement of 5 litre per minute in the flow rate. The pump exceeds the required specifications, delivering up to 7 L/min at 6 MPa. Additionally the size and weight fit the drone payload easily.

[3] https://www.aliexpress.com/item/1005008552457242.html
[4] https://www.aliexpress.com/item/1005005978878884.html
[5] https://www.aliexpress.com/item/1005009041008665.html

6.2.3. Reservoir choice
For the 20 litre tank this can be easy acquired from existing manufacturers. These commercially available tanks support rapid refilling and come with integrated anti-sloshing baffles[6].

6.2.4. Sensor choice
For decision making in control it is essential to know what the status is of the current payload. Multiple sensors are integrated to support autonomous decision-making.

First a tank fluid meter is needed. For the chosen tank there is already a commercial off the shelf solution specifically tailored to the tank, and as such this should be the choice for the tank fluid meter[7].

Secondly, a flow meter[8] is also bought commercially off the shelf. This is to be added in the pipe section that runs through the sensor box. The flow meter, installed in the pipe segment within the sensor housing, must be calibrated for the specific properties of the de-icing solution.

6.2.5. Connectors material choice
For linking every component up, pipes are used. Pipe materials must be selected carefully due to the corrosive nature of some de-icing solutions. The biggest limitation is the possibility to deploy diluted potassium formate solution means certain metals are out of the question due to the corrosive nature of the de-icing solution. In order to accommodate this de-icer the decision is to use only stainless steel and rubber hoses to transport. The non-pressurised connectors, which run from the tank to the pump, is constructed with rubber, whereas the boom is equipped with a long stainless steel pipe. The stainless steel choice makes sure that the system is able to handle the pressure, corrosion, and supporting the structure of the boom.

6.3. Thermal insulation *Gavin*

As the fluid is heated to 80°C, in order to deploy the fluid between 60-80°C, the temperature must be maintained for 10-20 minutes to account for flight time and refuel time. For this, an insulating layer is applied to the outside of the fluid tank. The insulation is an off-the-shelf foam wrap with an external foil layer.

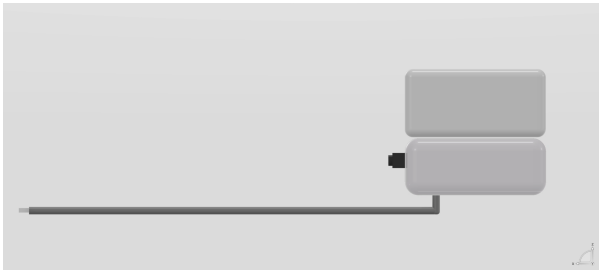

Figure 6.1: *Payload section layout*

[6]https://www.alibaba.com/product-detail/20-L-16-L-18-L_1600260739620.html
[7]https://droneroboticstec.com/products/dji-agras-t16-liquid-level-meter-module
[8]https://www.aliexpress.com/item/1005004625941774.html

7

Structural characteristics

Hew

Following the work done on the payload module, the focus now shifts towards designing the chassis of the de-icing drone. The chassis serves as the primary structural framework, integrating payload support, propulsion system, and stability under operational conditions. First, Section 7.1 shows the configuration design of the drone, followed by Section 7.2 which elaborates on the structure of the drone and chosen material, Section 7.3 which shows the structural sizing of the drone, and finalised by which lays out the production plan.

7.1. Configuration design

Hew

First, an optimal drone configuration must be selected based on mission constraints defined by the payload operation. From Chapter 5, 7 coaxial rotors are required. Following this, a design option tree is developed to shortlist feasible options. Each design was assessed based on key performance factors, including structural balance, flight dynamics, spray path clearance, and mechanical integrity of joints. Figure 7.1 shows the design option tree.

As the de-icing procedure will be carried out by spraying, a primary factor of consideration when choosing a drone configuration will be the attachment of the spraying module to ensure that there is no obstruction in the spray path. Thus, the triangle drone, 7-arm drone and forked arm configurations are rejected. This is because based on the way the drone configuration is designed in these options, the manner in which the spraying module is attached will restrict the spray path of which the spraying nozzle is able to perform de-icing, which is problematic when there are small corners or gaps where ice is formed. In addition to that, the 7-arm configuration has an unbalanced centre of gravity based on the payload placement which makes the control system tuning a longer process and thus not ideal. Furthermore, the forked arm configuration will have weaker joints where the arms branch out which then requires additional structural support.

The T-shape drone is selected as a plausible drone configuration mainly due to the possibility of foldable arms of the drone and thus can be disassembled and assembled easily, further

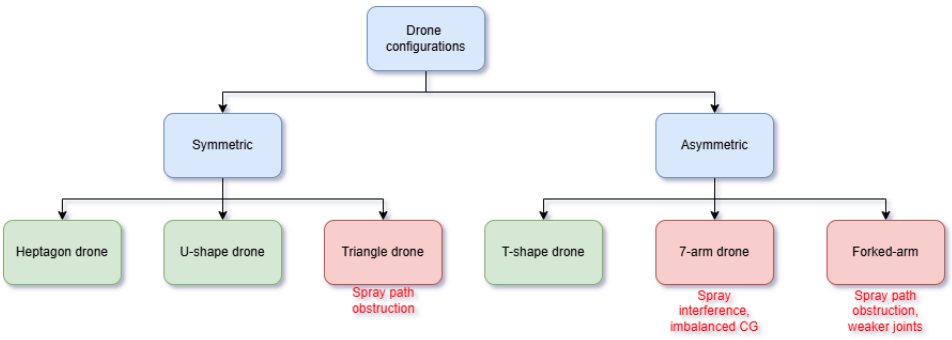

Figure 7.1: *Design option tree for drone configuration*

facilitating transportation. The symmetric heptagon drone configuration is chosen due to its favourable stability in flight conditions, and the U-shaped drone configuration is selected because it is easier to store and manufacture. Hence, these three options are shortlisted.

Trade-off point system

A trade-off is conducted to select the most suitable option. For this, an assessment point system is constructed on a scale from 0 to 3 as follows:

- **3 green [g]** - Excellent (exceeds requirements)
- **2 blue [b]** - Good (meets requirements)
- **1 yellow [y]** - Correctable deficiencies
- **0 red [r]** - Unacceptable performance

As 0 (red) indicates unacceptable performance, this option is considered to fail the trade-off and will not remain an option moving forward. The weighted score, or trade-off points, of each option will be normalized into a percentage, as per the following equation:

$$\text{trade-off points} = \frac{\Sigma_i^{\#\text{ of criteria}} (\text{criteria score})_i \cdot (\text{criteria weight})_i}{\Sigma_i^{\#\text{ of criteria}} 3 \cdot (\text{criteria weight})_i} \cdot 100\% \tag{7.1}$$

7.1.1. Configuration trade criteria

A multi-criteria decision-making method was used to evaluate various drone configurations for their suitability in carrying out effective aerial de-icing operations. Each configuration was scored against five core criteria, each with an assigned weight reflecting its relative importance to mission success, system integration, and environmental performance. The selected weights were based on technical priorities, operational context, and design requirements.

Spray accommodation

De-icing performance is fundamentally dependent on the drone's ability to deliver de-icing agents precisely, uniformly, and effectively over a wide area. This criterion evaluates how well a given configuration accommodates spray systems in terms of bar placement, propeller obstruction, spray angle coverage, and nozzle clearance. Spray effectiveness is mission-critical as poor integration leads directly to mission failure. As such, this criterion is given the highest weight of 5, as it directly impacts the success and safety of ice removal operations, aligning with primary functional objectives.

Ease of storage

Deployability affects how quickly and safely the drone can be transported, stored, and set up in field conditions. This is especially relevant in icy environments where time and mobility are constrained. Configurations that are foldable, compact, or modular offer superior portability. However, because this factor affects pre- and post-flight phases rather than in-mission performance, it is assigned a moderate weight of 3. It supports operational efficiency but is not as critical as flight or spray performance.

Controllability

This criterion measures the ease of in-flight handling of the drone configuration, particularly under dynamic or turbulent conditions. It considers factors such as symmetry, yaw and pitch stability, and ease of tuning flight controllers. A configuration with poor controllability increases pilot workload, risk of mission deviation, or in extreme cases, system loss. Given its importance for stability and safety during flight, a weight of 4 is assigned to controllability.

Table 7.1: *Drone structure trade-off table*

Criterion (Weight)	T-shape	Heptagon	U-shape drone
Spray accommodation (5)	Wide spray bar, little prop obstruction [3]	Central payload bay, limited upward rotation [2]	Open front, max spray path, props clear [3]
Ease of storage (3)	Foldable and easy to store [3]	Unfoldable, payload mount occupies space [1]	Compact compared to heptagon, moderate to store [2]
Controllability (4)	Asymmetric, needs careful tuning for stability [1]	Most stable and predictable for control [3]	More symmetric than T-shape configuration [2]
Accessibility and reach (4)	Good wide/sweep reach, moderate DOF [2]	Good for all angles, limited on wide targets [1]	Outstanding forward reach and high DOF [3]
Payload capacity and endurance (5)	Asymmetry limits endurance; needs energy compensation [1]	Great payload capacity and endurance [3]	Aerodynamic shape, asymmetry limits endurance [2]

Accessibility and reach
Effective de-icing requires drones to not only fly over surfaces but to be able to reach specific angles and under-structures, especially around rotor blades. This criterion assesses the drone's spatial freedom, directional spray range, and ability to position close to difficult-to-reach surfaces. Since this directly impacts spray delivery precision and mission efficacy, a high weight of 4 is assigned. While not as universal as spray accommodation itself, accessibility is a decisive factor in covering full aircraft geometries.

Payload capacity and endurance
The drone must carry both the de-icing fluid and power system for sufficient mission time and coverage. This criterion evaluates how much payload the configuration can handle relative to energy consumption, as well as aerodynamics and efficiency of the layout. Since endurance and capacity determine length and distance of the drone operation in a mission-critical role, this criterion receives the maximum weight of 5. Like spray accommodation, failure in this area can compromise operational reach or coverage entirely.

7.1.2. Configuration trade-off summary

Table 7.1 shows the trade-off table of the drone structure. As seen in the table above, the U-shaped drone is the best option based on the trade-off criteria. The main advantage of this configuration compared to others is that it allows for an unobstructed spray path of the spray nozzle without the obstruction of any of the propellers due to its location in front of the drone. By implementing foldable joint arms, the drone can also be easily transported during operations. This configuration also inherits stability benefits from it's symmetry, thus making it more controllable than the T-shape drone.

7.2. Drone structure and material *Hew*

With the configuration selected, a detailed design process of the drone is then performed. Firstly,

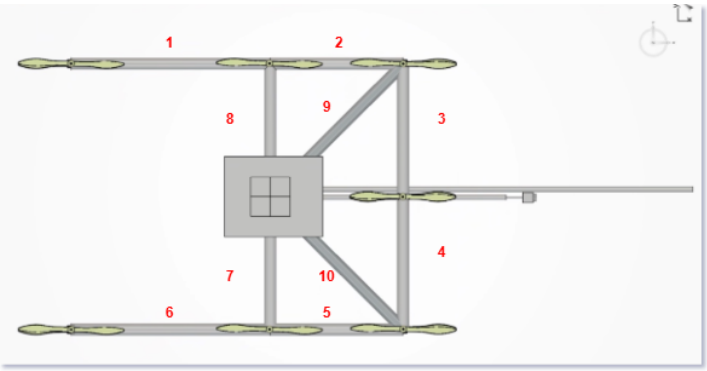

Figure 7.2: *Top view of de-icing drone*

based on the materials trade-off done in the midterm report, carbon fibre is to be utilised for the chassis of the drone. The drone structure requires a carbon fibre that offers an excellent balance of high tensile strength and intermediate modulus which provides both durability and stiffness without introducing excessive brittleness. Based on weight considerations and the drone's structural mass budget allocation in the previous sections, a material with high specific strength while keeping the structure lightweight and within budget is optimal. Manufacturability is also an important factor to consider as the entire drone chassis will be made solely from carbon fibre.

Based on these criteria, certain options were shortlisted: HexTow® IM5, Toray T800, Toray T1000, and Mitsubishi MR70. While all options are viable, the IM5 provides a balanced intermediate modulus (275 GPa) and a high tensile strength (5.5 GPa) at a relatively lower density, which allows for a lighter structure. Furthermore, Hexcel's HexTow® carbon fibre has a proven track record and is widely used in the aerospace industry in aircraft such as the Airbus A350 XWB and A380, making it a good choice for the drone chassis.

7.3. Drone dimensions *Hew*

To ensure the structural integrity and reliability of the drone during operation, careful consideration is given to the design and sizing of all joints. A conservative approach is adopted and based on the constraints and requirements previously established, where each of the component of the drone structure is sized accordingly to ensure structural integrity.

Drone structure dimensions

In order to properly size the drone based on the requirements set in the previous chapters, assumptions are made to better facilitate preliminary sizing. First, the centre of gravity is assumed to be at the location of the payload module as the majority of the drone's weight is concentrated in the module. Additionally, the centre of gravity of the drone is assumed to be in line with the neutral axis as this assists the simplification of the sizing process based on the moments generated by each rotor. The last assumption is that the thrust generated by each motor is the same in hover conditions.

With these assumptions established, the location of the rotors can then be expressed as a ratio of the total length based on the number of rotors on the respective axes. Another constraint included is the 15 cm clearance between each propeller. Therefore, the drone is sized according to these parameters and the top view of the drone can be seen in Figure 7.2 below along with its dimensions which will be listed in a summary table at the end of the chapter.

The cross sectional area of the carbon fibre rods used in the drone chassis' production can

be sized first by setting maximum bending stress on the drone structure as the yield strength of carbon fibre, which is the bending stress at rod member 9 and 10 in Figure 7.2 using the equation below:

$$\sigma = \frac{My}{I} = 5171 \times 10^6 Pa$$

Then, by setting the inner diameter of the rod as a ratio of the outer diameter and applying a safety factor of 8 in the calculation followed by the thrust-to-weight ratio of 2.2, the dimensions of the carbon fibre rod to be used in the chassis can be calculated and presented in Table 7.2 below:

Table 7.2: *Landing Gear Rod Specifications*

Outer Diameter (mm)	Inner Diameter (mm)	Wall Thickness (mm)	Density (kg/m^3)
32	28	2	1780

Landing gear dimensions

To facilitate the deployment and return of the drone to and from ground station, a landing gear is designed for the drone. Using the same material selected for the chassis of the de-icing drone, the landing gear is sized accordingly. The height of the landing gear is set to 40 centimetres to allow for clearance for the payload module. First, the impact force of the drone's ground landing is calculated using Equation 7.2 below, where Δt is assumed to be 0.5 seconds as a preliminary value:

$$F_{\text{impact}} = \frac{mv}{\Delta t} = \frac{m\sqrt{2gh}}{\Delta t} = 5602.86N \tag{7.2}$$

This then sums up to around $1400N$ of impact force per leg as a 4 leg configuration is used. Then, by setting the ratio of the of the outer diameter to the inner diameter, the safety factor as 10, and using the the tensile strength value of the chosen carbon fibre, the carbon rods in the landing gear can be sized as shown below:

$$\sigma = \frac{F}{A}, SF = 10, D_i = \frac{14}{15} D_o$$

$$\sigma = \frac{1400.7 \times 10}{\frac{\pi}{2}(r_o^2 - r_i^2)} = 5171 \times 10^6$$

$$d_o = 10.851\text{mm}, d_i = 10.12\text{mm}$$

For ease of manufacturing, the dimensions of the rod are set in Table 7.3 below along with the weight estimation. As a verification procedure, the landing gear is also evaluated based on the Tsai-Hill criterion to determine if it will fail under the given landing impact force.

Table 7.3: *Landing Gear Rod Specifications*

Outer Diameter (mm)	Inner Diameter (mm)	Wall Thickness (mm)	Weight (kg)
14	10	2	0.215

$$\left(\frac{\sigma_1}{X}\right)^2 - \left(\frac{\sigma_1 \cdot \sigma_2}{X^2}\right) + \left(\frac{\sigma_2}{Y}\right)^2 + \left(\frac{\tau_{12}}{S}\right)^2 \leq 1$$

Where:

- σ_1: Longitudinal stress (along fibre direction)
- σ_2: Transverse stress (perpendicular to fibre)
- τ_{12}: In-plane shear stress
- X: Longitudinal tensile/compressive strength
- Y: Transverse tensile/compressive strength
- S: In-plane shear strength

$$\sigma_1 = 21.5\,\text{MPa}, X = 5171\,\text{MPa}$$

$$\left(\frac{\sigma_1}{X}\right)^2 = \left(\frac{9.3}{5171}\right)^2 = (0.004158)^2 = 3.227 \times 10^{-6}$$

$$\text{Tsai-Hill Index} = 3.227 \times 10^{-6} \ll 1 \Rightarrow \text{Safe under given loading conditions}$$

Bolt and joint sizing

As stated earlier in this chapter, the drone structure is designed to be foldable to further facilitate the operations logistically. Therefore, each of the carbon rods will be joined together by using a pipe union connection horizontal folding arm tube joint which has an outer diameter of 35mm. The cavity in the joint will be filled by inserting an aluminium sheet with a 3mm thickness. This joint will be secured by using a steel bolt sized through considerations of critical loading case through the hinge to withstand shear. The primary bolt will be carrying the shear induced by the thrust of the rotor and the weight of the payload. Thus, to keep the size of the bolts consistent throughout the drone, the bolt sizing will be done based on the the longest of the three arms connecting the payload module to the chassis, which will the arms connecting the two middle rotors to the payload module namely members 9 and 10. This is followed by a calculation of the shear force that the bolt has to endure with a safety factor of 8 which is shown below:

$$F_{shear} = \frac{99.2 \times 9.81}{4} \times 8 = 1.946\text{kN}$$

A higher safety factor than usual is used as this is a crucial joint in the structure and failure of the bolts would mean the disconnection of the payload module from the main structure of the drone and thus resulting in mission failure. Based on the value calculated above, we can use the von Mises criterion and determine the failure shear stress for the bolt:

$$\tau_{yield} = 0.6 \times 0.8 \times 800\text{MPa} = 370\text{MPa}$$

$$\tau_{failure} = 0.6 \times 800\text{MPa} = 480\text{MPa}$$

Then, the required area for the Steel 8.8 bolt can be calculated as follows:

$$A_{\text{yield}} = \frac{F}{\tau_{\text{yield}}} = \frac{1946}{369.6 \times 10^6} \approx 5.68 \times 10^{-6}\,\text{m}^2 = 5.265\,\text{mm}^2$$

$$A_{\text{ultimate}} = \frac{F}{\tau_{\text{ultimate}}} = \frac{1946}{480 \times 10^6} \approx 4.38 \times 10^{-6}\,\text{m}^2 = 4.054\,\text{mm}^2$$

Based on these values, it can be seen that the minimum bolt size that can meet both criteria is the Grade 8.8 steel M4 bolt. If one joint experiences a maximum shear load F_{max}, and each bolt can withstand F_{bolt}, then:

$$n \geq \frac{F_{\max} \cdot SF}{F_{\text{bolt}}}$$

Assuming a maximum shear of $F_{\max} = 2102\,\text{N}$ from moment-induced loading (as previously discussed):

$$n \geq \frac{1946 \cdot 2}{4214} = \frac{3892}{4214} \approx 1.0$$

Table 7.4 shows the specifications of the material and the dimensions of the bolt that will be used to join the carbon rod and the payload module. Two bolts are to be used per joint to provide resistance to both shear and bending moments as well as ensure redundancy in case of fatigue or vibration loosening.

Table 7.4: *Shear capacity of an M4 bolt made of steel grade 8.8.*

Property	**Value**
Material	Steel Grade 8.8
Ultimate Tensile Strength (σ_u)	800 MPa
Allowable Shear Stress (τ_{allow})	480 MPa
Threaded Area (A)	8.78 mm^2
Shear Capacity ($F_{\text{shear}} = \tau \cdot A$)	4214 N

Displacement analysis *Hew*

In this section, the displacement of the structure away from the neutral axis will be evaluated to ensure that the structure can in fact withstand the payload loading on the structure. The deflection is given by Equation 7.3 below:

$$\delta = \frac{FL^3}{3EI} \tag{7.3}$$

For a hollow circular cross-section (typical of carbon fibre tubes), the second moment of area I is given by:

$$I = \frac{\pi}{64}\left(D^4 - d^4\right) \tag{7.4}$$

By setting the value of D to be constant and substituting the appropriate values for F, L, E, D, the value of d can be found and with it, the required thickness of the carbon fibre rod can be computed. The criteria for the arm displacement, δ is such that the displacement does not exceed $1/200$ of the value of the span of the rod. Thus, the arms that are connecting to the payload from the top left and bottom left rotor based on Figure 7.2 can be sized as follows:

$$\delta = \frac{(99.2/4)(9.80665)L^3}{3(279 \times 10^9)\frac{\pi}{64}(0.032^2 - d^2)}, \text{where} L = 1m, \frac{L}{200} = 5mm$$

$$d = 19.18mm \approx 20mm, t = 6mm$$

Similarly, the arms connecting the top middle and bottom middle rotor to the payload can be sized as shown below:

$$\delta = \frac{(99.2/4)(9.80665)L^3}{3(279\times10^9)\frac{\pi}{64}(0.032^2-d^2)}, \text{where} L = 0.71m, \frac{L}{200} = 3.55mm$$

$$d \approx 26mm, t = 3mm$$

With this procedure the deflection of the chassis of the drone is kept to a minimum to prevent permanent deformation and fatigue as well as optimise for the weight of the structure. *Hew*

Table 7.5: *Carbon fibre rod member properties for drone structure*

Rod Member	Length (m)	Outer Diameter (m)	Inner Diameter (m)	Thickness (mm)	Mass (kg)
1	1.065	0.032	0.016	2	1.143
2	0.71	0.032	0.016	2	0.762
3	0.71	0.032	0.016	2	0.762
4	0.71	0.032	0.016	2	0.762
5	0.71	0.032	0.016	2	0.762
6	1.065	0.032	0.016	2	1.143
7	0.71	0.032	0.026	3	0.345
8	0.71	0.032	0.026	3	0.345
9	1.0	0.032	0.020	6	0.872
10	1.0	0.032	0.020	6	0.872
Landing Gears	0.400	0.014	0.010	2	0.215
Total					**7.983**

7.4. Production plan *Hew, Gavin*

This section outlines the production strategy for the drone, including sourcing, manufacturing, assembly, quality assurance, and logistics. The process has been designed with an emphasis on efficiency, reliability, and suitability for a start-up context with limited in-house manufacturing capabilities.

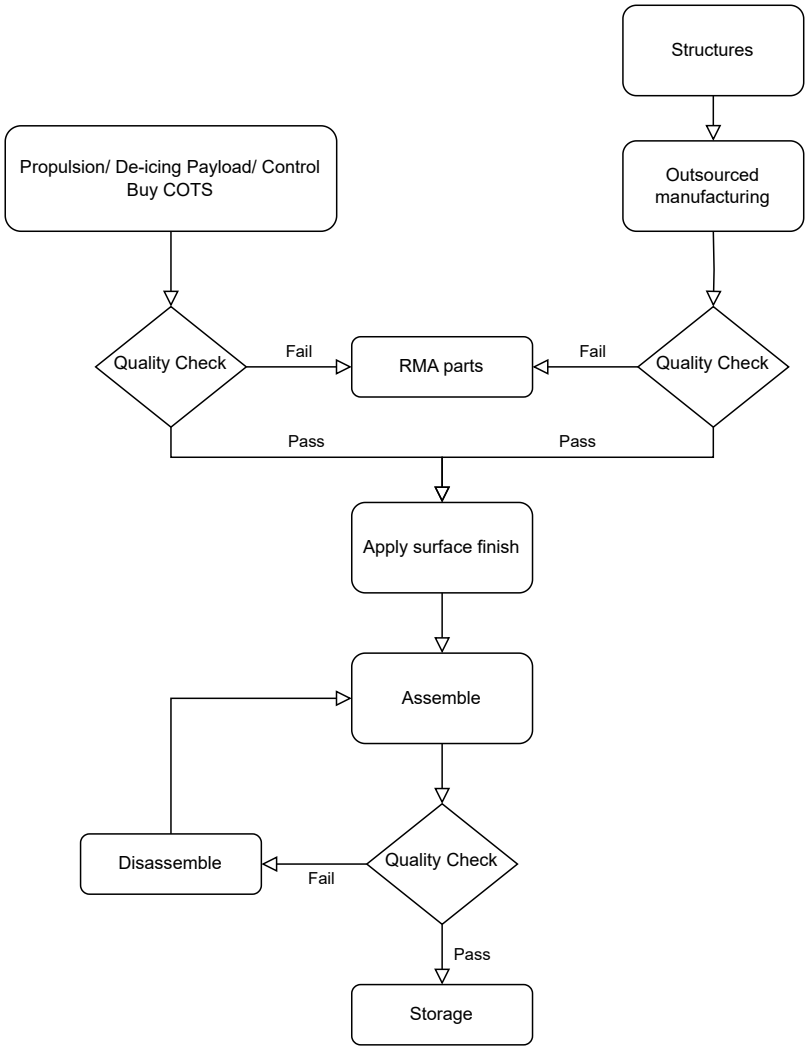

Figure 7.3: *Production Plan*

This plan is a quick overview of the production of the drone. De-icing payload, control and stability sensors, motors and batteries for propulsion are all obtainable off the shelf. The frame and any structural element enclosing the parts are outsourced for manufacturing due to this being from a start-up with no production abilities and the time to market is to be relatively short.

On the assembly procedure the parts are checked for quality before assembly. Any failure during quality check is returned to the previous step, parts are returned to manufacturer. Surface finish is applied in this phase to protect some parts exposed to the elements. After the surface finish, parts are assembled into drones. At the last stage the quality check is performed for the whole system. Any failed system is disassembled and the parts returned to the assembly stage to re-assemble. When a system passes all the checks it is put into storage ready for use or shipping.

8

Aeroacoustic characteristics

Likun

In the requirement list given in the Appendix D, a requirement for noise level is strictly limited, namely: `USER-M-SUST-2.3` - *The system shall have noise emissions below 85 dB at 10 meters*. A series of studies has been made to evaluate the acoustic parameters for the final design of the drone configuration.

Based on the literature study, for aeroacoustic analysis, the noise sources can be categorized into two aspects, aerodynamics and acoustics as described by Haddaoui (2019). The aerodynamics noise mainly originates from the unsteady motion of the fluid or solid body in a free stream, while the acoustics noise is generated from the vibration of the motor or the propeller during the operation. With this information, 3 possible aeroacoustic analysis approaches have been considered as shown in Table 8.1 with CFD being explained in Section 8.1, Xrotor method explored in Section 8.2 and far-field theory in Section 8.3. After choice of Xrotor as the primary method it is validated in Section 8.2, noise correction for a co-axial design is given in Section 8.5 and noise is predicted for the actual design in Section 8.6. Then the calculation has a sensitivity analysis conducted in Section 8.7, with recommendations and limitations considered in Section 8.8.

Table 8.1: *Comparison of Noise Estimation Methods*

Method	Setup Complexity	Accuracy	Computation Cost / TRL
CFD	Needs CAD and tuning	High (realistic)	High / Widely used
Xrotor	Basic geometry input	Moderate (1 rotor)	Low / Common in design
Far-field theory	Few parameters	Rough estimate (1 rotor)	Very low / Legacy-based

8.1. Conventional industrial simulation method (CFD)

Likun

CFD is widely considered as the highest-fidelity approach for simulating fluid dynamic problems, apart from physical experiments (Afari, 2019). Two CFD tools frequently employed in aeroacoustic studies are OpenFOAM and ANSYS, whose workflows are broadly similar. First, the entire drone geometry needs to be created in CAD. Next, a surrounding fluid domain is defined and meshed. Then, appropriate boundary conditions and models for the solver settings are applied. Finally, the solver produces datasets requiring post processing, such as placing monitoring points and visualizing pressure fields or acoustic sources. However, this description represents only a preliminary sequence, the actual application process for these tools is significantly more complex.

CFD would yield the most accurate aeroacoustic predictions for this project, since it will take into account the interference from the airframe and payload during operation. However, it demands an in depth understanding of simulation theory, turbulence modelling, mesh generation, and numerical stability. Given the current knowledge and available expertise, CFD is beyond the scope of the project and therefore, it will be excluded from current analysis.

8.2. Xrotor

Likun

Xrotor is an interactive program for the design and analysis of ducted and free-tip propellers and windmills (Mark Drela, 2011). It includes functionality for designing minimum induced loss rotors, aerodynamic loading analysis, noise footprint prediction, aerodynamic performance analysis and more. For noise analysis, the main theory is based on far-field analysis (Haddaoui, 2019). It is one of the most commonly used aerodynamic performance analysis tools at Flight Performance and Propulsion department of TU Delft (Haddaoui, 2019).

One limitation of this approach is that Xrotor can only model an isolated propeller and rotor hub for a fixed-wing aircraft. This reduces its accuracy for multicopter noise predictions, as the rotor orientation in fixed-wing aircraft and multicopters is fundamentally different. It is assumed that this limitation has a negligible effect on the final outcomes. Nevertheless, the total noise level for a multicopter design can still be approximated by assuming identical rotors and summing the sound pressure levels to obtain an integrated noise level. The detailed analysis steps will be discussed in Section 8.6

To generate a preliminary noise footprint prediction map, the program requires basic input parameters listed in Table 8.2.

Table 8.2: *Model Input Parameters*

Input	Element	Unit
Rotor geometry	Number of blades	–
Rotor geometry	Propeller tip radius	m
Rotor geometry	Rotor hub radius	m
Rotor parameter	Air speed	m/s
Rotor parameter	Advance ratio / RPM	–/-
Rotor parameter	Thrust / Power	N/W
Rotor parameter	Lift coefficient	–
Operating condition	Flight altitude above ground	m
Operating condition	Climb angle	degree
Plot setup	Contour grid size	m

Using these inputs, the program generates a contour map showing decibel magnitudes across the defined grid, as illustrated in Figure 8.2. Due to its moderate accuracy, simplified setup, and clear visualization on final outcome features, Xrotor will be selected for the further analysis.

8.3. Far-field theory

Likun

In 1948, L.Gutin from NACA has conducted theoretical works and developed a formula that can be used to roughly estimate the sound pressure at the far-field (Gutin, 1948), which is generally considered as 10 times the radius of the propeller away from the observation point (Haddaoui, 2019). Further detailed explanation for the formula was discussed by Afari (2019). Formula produced by Afari is given in Equation 8.1

$$p_m = \frac{169.3mVRM_t}{SA}\left(\frac{0.76P_h}{{M_t}^2} - Tcos\theta\right)J_{mB}(x) \tag{8.1}$$

where p is the RMS sound pressure level, where RMS stands for Root Mean Squared, m is the Order of the harmonic, S is the Distance from propeller hub to observer, V is the Air speed, R is the Propeller radius, A is the Propeller disc area, P_h is the Absorbed power, T is the Thrust, B is the Blade count, M_t is the Tip Mach number, J_{mB} is the Bessel function of order mB and θ is the Angle between propeller axis and observer.

The outcome of this formula provides a rough estimate of the sound pressure level at a given distance from an isolated propeller. However, as noted by Afari, the formula offers poor noise prediction accuracy, particularly when the tip Mach number falls within the range of 0.3 to 0.5. This limitation is especially relevant for drone propeller applications and should be carefully considered. Due to the method's limited visualization capability in the final noise assessment, poor prediction accuracy, and operational constraints, it is excluded for the final analysis.

8.4. Xrotor validation *Likun*

During the literature review, several master's theses from TU Delft have validated and demonstrated that Xrotor is a reliable open source program. Its accuracy has been confirmed by comparison with complex experimental data (Haddaoui, 2019) as well as with other similar tools (Klein, 2017). It has been shown that Xrotor outperforms other methods in terms of accuracy. However, it is important to note that during the validation process (N.S.L.Elbers, 2021), an auxiliary tool, Xfoil was also used to compensate for Xrotor's weak point of generating propeller geometry.

As a result, this report considers an additional preliminary validation strategy by comparing the results from a lower-fidelity method of far-field theory with the output of Xrotor.

The general idea for validation is to compare the noise footprint module from Xrotor with the calculation results from the analytical formula. To ensure consistency, the analysis must be performed on the same target propeller. Therefore, additional research was conducted to select a well defined propeller geometry. The NS 26*8.5 propeller designed by T-Motor (T-MOTOR, n.d.) is chosen as the subject of analysis, as shown below in Figure 8.1.

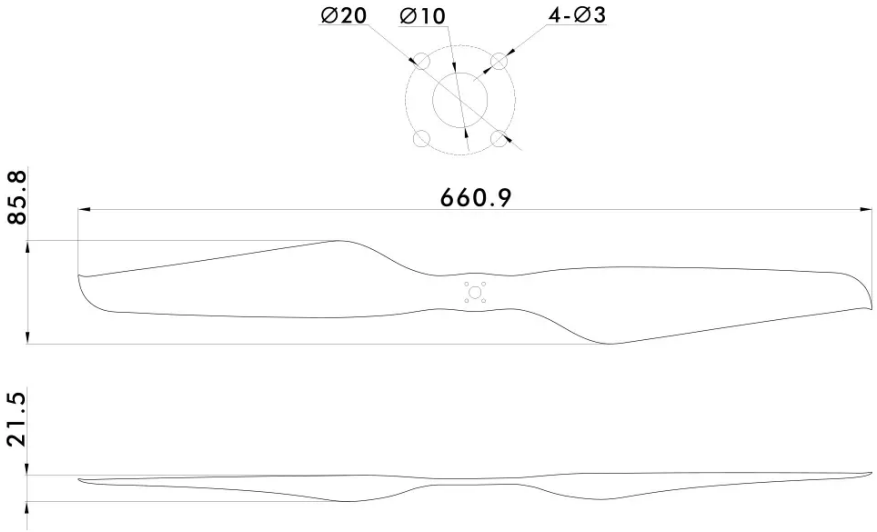

Figure 8.1: *NS 26*8.5 propeller technical drawing*

To gather all necessary inputs as shown in Table 8.2, a motor must also be considered. For this purpose, another component from T-Motor U11-II KV120 is selected (T-MOTOR, n.d.). According to the manufacturer's website, a series of test data is available for this motor when paired with the NS 26×8.5 propeller. This significantly reduces the effort required for determining input parameters.

Furthermore, to achieve the most accurate noise prediction using far-field theory, a 40% throttle condition is selected. This choice ensures that the tip Mach number remains below 0.3, as

required for the theory's validity. The tip Mach number in this case is calculated using Equation 4.7 from paper by Haddaoui (2019).

Table 8.3 summarizes the final set of input parameters required for the Xrotor simulation.

Table 8.3: *NS 26*8.5 propeller model Input Parameters*

Element	Magnitude	Unit
Number of blades	2	–
Propeller tip radius	0.33	m
Rotor hub radius	0.01	m
Air speed	10	m/s
RPM	1978	–
Thrust	23.12	N
Lift coefficient	1.1	–
Flight altitude above ground	5	m
Climb angle	0	degree
Contour grid size	(-10, 10) × (-10, 10)	m

Among these elements, the air speed is estimated based on the tip velocity of the propeller. This is calculated by multiplying the angular velocity by the propeller radius, resulting in an approximate value of 10 m/s. This velocity will also be used in the far-field theory analysis. Once the air speed is determined, the lift coefficient can be calculated using the lift equation (assuming ISA sea-level conditions) given in Equation 8.2.

$$T = L = \frac{1}{2}\rho V^2 S C_l \tag{8.2}$$

The T here represents the thrust generated by the propeller, which is assumed to be equal to the lift L, since only an isolated propeller is considered in this analysis. Additionally, because the focus is on a specific monitoring point, the climb angle is set to zero. This simplification helps make the resulting noise contour map easier to interpret and compare.

Figure 8.2 presents the output from Xrotor, showing the ground noise footprint map when the NS 26×8.5 propeller operates at an altitude of 5m. In the map, the aircraft icon represents the propeller's position, which also located as the origin of the coordinate system. The red cross indicates the monitoring point, which is strategically selected so that the three vertices form a right triangle. This configuration places the angle between the observer's line of sight and the propeller axis at approximately 30°, simplifying the calculations required for far-field theory.

Moreover, this setup allows for a sanity check of the requirement, as the distance between the propeller and the observer is exactly 10m. According to the map, the noise level at this monitoring point is approximately 48 dB, which will be recorded for the following comparison.

Subsequently, the calculation from Far-field theory was conducted. First, it is necessary to determine the magnitude of each term. While most values—such as propeller radius, disc area, thrust, and blade count can be observed or calculated from the experimental data available on the manufacturer's website, some terms require additional literature research to complete the calculations.

First the absorbed power is determined by calculating the torque generated by the propeller at 40% throttle. Then, Equation 2.8 and Equation 2.14 from paper by Haddaoui (2019) are applied. Once the result is obtained, a unit conversion is required to convert watts to horsepower.

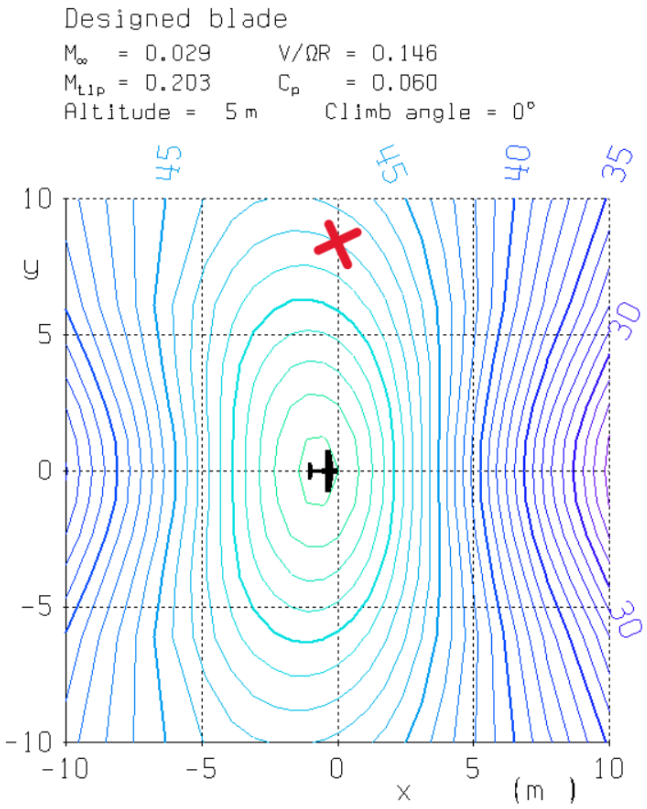

Figure 8.2: *Isolated NS 26*8.5 propeller noise footprint map at 5 m above ground level (10 m from observer)*

Next, the tip Mach number is calculated using Equation 4.7 as described in Haddaoui (2019) thesis.

To compute the result from the Bessel function, both the type and order of the function must be determined. In acoustic analysis, the Bessel function of the first kind is typically used. The order is calculated by the product m·B, where m is taken to be 1 which is the first harmonic to simplify the calculation. With the given propeller geometry, this results in a second-order Bessel function of the first kind. The full expression is given in Equation 8.3.

$$J_2(x) = \left(\frac{3}{x^2} - 1\right)\frac{\sin(x)}{x} - \frac{3\cos(x)}{x^2} \tag{8.3}$$

To evaluate this function, the argument x must first be calculated, as explained on page 27 of Haddaoui (2019) thesis. With these considerations, the final input parameters and outcome based on the theory are summarized in Table 8.4, where the selections for S and θ were previously defined.

Table 8.4: *Far-field theory inputs and outcome*

Element	Magnitude	Unit
B	2	–
S	10	m
R	0.33	m
A	0.729	m^2
T	23.12	N
P_h	0.197	hp
$J_2(x)$	0.000273	–
M_t	0.064	–
m	1	–
θ	30	degree
p_m	46.9	dB

Finally, by comparing the results, it is observed that the difference between the two methods is only about 2.3%, which validates that Xrotor provides a reliable prediction of the noise footprint and can be confidently used in the final analysis.

8.5. Noise correction for co-axial layout *Likun*

As noted, Xrotor provides noise predictions only for isolated propellers, such that it does not account for the interference effects present in a co-axial layout, which can vary with both RPM and rotor separation distance. To address this, the literature research has been conducted comparing noise levels between co-axial and isolated rotors and derived a simple correction factor that scales isolated propeller predictions to approximate co-axial noise levels.

Russo et al. (2023) conducted a series of experiments under two configurations. One included an isolated propeller to establish a baseline reference, and another two identical propellers rotating in opposite directions in a co-axial arrangement. Results showed in Figure 19 from the report by Russo et al. (2023) indicate that above 1500 RPM, rotor separation has a negligible effect on overall noise and this phenomenon becomes more obvious when it achieves 2800. However, when the RPM is in the range from 1260 to 1500, separation between the propellers has significant impact on the noise level that the separation must be treated as an independent variable. Cases below 1260 RPM are excluded from the following analysis, since industrial use drones rarely operate at such speeds according to the motor operation database.Therefore, two scenarios need to be separately analysed.

First, when the RPM is larger than 1500, using the data from Figure 16 of Russo et al. (2023) report, four noise-level measurements are recorded for the isolated rotor at 1620, 1740, 1860, and 2820 RPM. Then, from Russo et al. (2023) co-axial configuration data at the same RPMs, four discrete correction factors were calculated by dividing the co-axial noise levels by the corresponding isolated rotor noise levels. Finally, the statistical analysis was applied to obtain the overall mean correction factor and its standard deviation, as summarized in Table 8.5.

Table 8.5: *Comparison of noise levels between isolated and co-axial propellers from 1500 to 2800 RPM*

RPM	$L_{A_{eq}}$ (Isolated) [dB]	$L_{A_{eq}}$ (Co-axial) [dB]	Correction factor
1620	53.0	59.0	1.1132
1740	53.5	59.5	1.1121
1860	54.0	60.0	1.1111
2820	63.0	68.0	1.0794
Overall correction factor (mean ± SD)			1.10396 ± 0.01642

Next, when the propeller operates within the RPM range of 1260 to 1500, the separation between the two propellers in a co-axial layout is treated as the independent variable. A data collection method similar to the previous case is applied, but focused specifically on this RPM range. For analysis, three data points at 1260 RPM are recorded, as shown in Table 8.6.

Table 8.6: *Comparison of noise levels between isolated and co-axial propellers at 1260 RPM*

Separation (D)	L_A (Isolated) [dB]	L_A (Co-axial) [dB]	Correction Factor (C)
0.65	54.5	68	1.2477
1.00	54.5	61	1.1193
1.50	54.5	63	1.1560

The separation is expressed in terms of the propeller diameter. In this case, the correction factor is considered the dependent variable, while separation is the independent variable. Based on the observed trend from these three data points, a quadratic relationship is suggested. To determine a fitting function, a simple Python script using NumPy's polyfit command is applied with a second order polynomial fit. The resulting function is:

$$C = 0.5311D^2 - 1.2477D + 1.8366$$

8.6. Noise prediction for the actual drone design *Likun*

As illustrated in Subsection 5.2.1, the final geometry of the propeller has been obtained through the iterative process. A series of similar calculations as previously described in Section 8.4 were conducted. Based on this, the input parameters for Xrotor were derived and are listed in Table 8.7.

Table 8.7: *Actual design model Input Parameters*

Element	Magnitude	Unit
Number of blades	2	–
Propeller tip radius	0.28	m
Rotor hub radius	0.0175	m
Air speed	7.5	m/s
RPM	5103	–
Thrust	69.19	N
Lift coefficient	0.809	–
Flight altitude above ground	5	m
Climb angle	0	degree
Contour grid size	(-20, 20) × (-10, 10)	m

Using these inputs, the final output of the model is presented as a ground noise footprint map, as shown in Figure 8.3. To simplify comparison with regulatory requirements, the flying altitude is set at 5 meters above ground level. The monitor point is indicated by a red cross, placed at coordinates x = 0, y = 8.7, corresponding to a 10 meter straight line distance from the noise source. This choice follows the same reasoning discussed in Section 8.4. From the contour map, the noise level at this point can be read as approximately 63 dB.

It should be noted that this footprint map evaluates only the isolated propeller configuration. For a co-axial layout, a correction factor must be applied, as described in Section 8.5. Given that the RPM exceeds 2800, the corrected noise level can be estimated by multiplying the simulated result by the correction factor. To consider the worst case scenario, the correction factor used

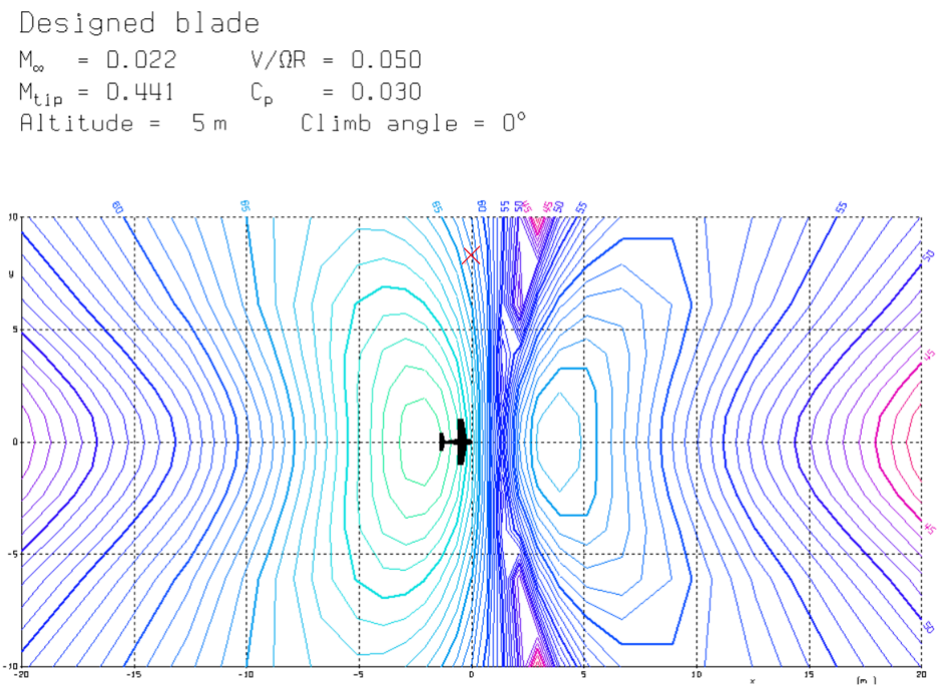

Figure 8.3: *Ground noise footprint map generated by the actual isolated propeller design operating at 5 m above ground level (10 m from observer)*

here is the mean plus one standard deviation. This yields a final noise level of approximately 70.6 dB for the isolated co-axial propeller.

At this stage, the noise generated by a single co-axial rotor is estimated. To evaluate the full design, further calculations are performed under the assumption that seven co-axial rotors operate simultaneously. Four simplifying assumptions are made:

- All seven rotors emit the same noise level
- Interference and resonance effects with the airframe and motors are neglected
- The rotors are assumed to be located at the same point, which make the use of the multiple source noise summation formula become reasonable
- Standard atmospheric sea-level condition

The multiple source noise summation equation is shown as following:

$$L_\Sigma = 10log_{10}(10^{\frac{L_1}{10}} + 10^{\frac{L_2}{10}} + \cdots + 10^{\frac{L_n}{10}})$$

Where L represents the noise level in dB for each source, n is the number of sources, and $L_\Sigma$is the combined noise level. Applying this formula with seven identical sources that each emits at 70.6 dB, the total observed noise level at 10 meters is calculated to be approximately 79 dB. Compared to the requirement `USER-M-SUST-2.3`, this result proves that the design is feasible from aeroacoustic perspective.

8.7. Xrotor sensitivity analysis *Likun*

Once the results have been obtained, an essential next step is sensitivity analysis, which assesses whether small changes in the inputs lead to significant deviations in the outputs. In this section,a sensitivity analysis of the noise-prediction model is performed by perturbing each

input parameter by ±10% of its nominal value and recording the resulting noise level at the same observation point. Note that the number of blades is held constant, because it must remain an integer, a ±10% change, such as 2.2 blades is not meaningful and adding or subtracting a full blade would fall outside the scope of a small perturbation analysis. The results are summarized in Table 8.8.

Table 8.8: *Xrotor sensitivity analysis results (based on actual isolated propeller design data)*

Input Parameter	Change	Magnitude	Result [dB]	Difference [%]
Propeller tip radius	+10%	0.308	63	0.00
Propeller tip radius	–10%	0.252	68	7.94
Rotor hub radius	+10%	0.01925	63	0.00
Rotor hub radius	–10%	0.01575	62	1.59
Air speed	+10%	8.25	64	1.59
Air speed	–10%	6.75	62	1.59
RPM	+10%	5613.3	64	1.59
RPM	–10%	4592.7	62	1.59
Thrust	+10%	76.11	64	1.59
Thrust	–10%	62.27	62	1.59
Lift coefficient	+10%	0.890	63	0.00
Lift coefficient	–10%	0.728	63	0.00

From the results, the largest deviation occurs when the propeller tip radius is reduced by 10%, producing a 7.94% change in noise level which is still smaller than the 10% input perturbation. All other parameters demonstrate negligible impact. Therefore, it can be concluded that small variations in input parameters have minimal effect on the noise predictions from the Xrotor model.

8.8. Limitations and recommendations *Likun*

At this phase, due to the authors' current knowledge and available skills, the acoustic analysis still has some obvious limitations, because the present noise prediction relies on Xrotor's isolated propeller model and far-field analytical validations.

Xrotor cannot account for airframe interference, turbulent wakes, or mechanism noise from multirotors. Secondly, the co-axial noise correction factor has been analysed from a narrow RPM range and limited separation ratios, which is still lacking accuracy for other operating conditions. Finally, no empirical flight measurements have been performed to account for the ground and wind turbine reflections or environmental absorption.

To address these gaps, the following improvements are recommended. Introducing CFD simulation of seven co-axial rotor pairs with more precise acoustic analogies and validating it against Xrotor results under hover, climb, and cruise conditions with full design configurations. Alternatively, practical experiments could be introduced, such as deploying microphone arrays and acoustic sensors to measure the noise footprint at the required distance under expected operating environments, which would lead to the most accurate noise predictions.

9

Configuration

This chapter shows the layout for both external and internal configurations of the drone. The layouts are shown in Section 9.1. The center of gravity is presented in Section 9.2, followed by thermal considerations in Section 9.3.

9.1. Internal and external layout *Gavin*

The external layout of the drone is given in Figure 9.1. The frame is made of carbon fibre tubes and houses 14 propellers in 7 pairs of co-axial propellers. There are 3 pairs in the front, 2 in the middle and 2 in the back. In the middle, 4 tubes connect to the centre section, which has 2 enclosures housing the payload and sensors. The lower enclosure includes the tank. The upper enclosure includes all the other internal parts, including batteries, pump, sensors, plumbing and control computer.

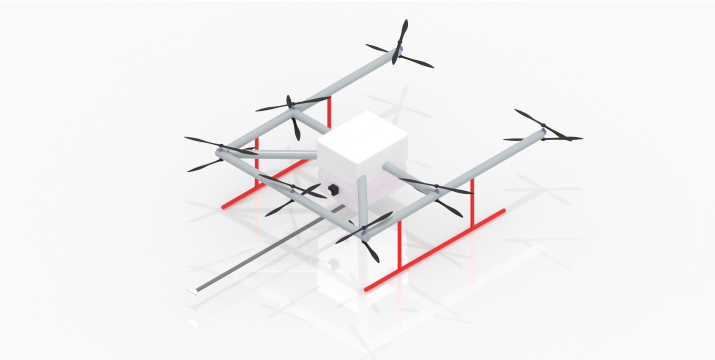

Figure 9.1: *Isometric view of the drone*

The internal layout (given in Figure 9.2) focuses on a balance of the centre of gravity position and connectivity with the sensors. All sensors are routed on the right to connect to the computer. The pipe has to pass through slightly off to the left due to the pump inlet and outlet position. At the end of the enclosure, the fluid passes through the flow meter, which is connected to the computer. All batteries are as close to the middle as possible for centre of gravity purposes.

With this layout, the centre of gravity lies 11 mm off to the right side of the drone and 5.5 mm off to the rear with respect to the centre of the drone. This off-axis to the right is due to the asymmetric layout of the pump with the outlet and pipe, forcing the batteries to be slightly offset to the right. This is shown in Figure 9.2

9.2. Centre of gravity of drone *Gavin*

The centre of gravity of the full drone with a full tank is 6.5 mm to the right of the drone, 3.3 mm to the rear, and 54 mm above the centre point of the drone. With an empty tank, the

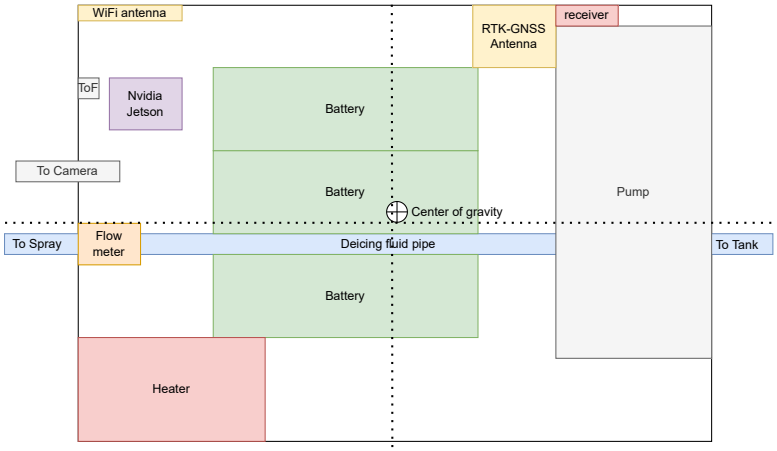

Figure 9.2: *Internal layout*

centre of gravity shifts to 9.7 mm to the right, 4.9 mm to the rear, 135.7 mm above the centre point. The shift in centre of gravity is shown in Figure 9.3

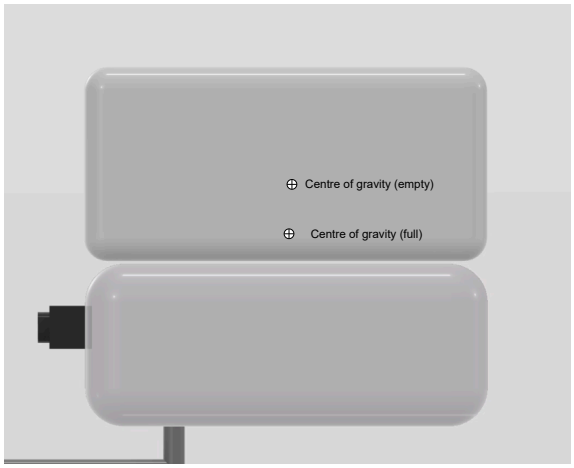

Figure 9.3: *Centre of gravity shift between the full and empty tank configurations*

9.3. Thermal *Gavin*

The strictest temperature requirement comes from the NVIDIA Jetson computer. Temperature tolerance is from -20°C to 80°C, so this module is the limiting factor on the system.

To passively deal with thermal issues, the enclosure is wrapped on the outside with the same foil as the tank. This prevents the enclosure from losing temperature even when the active heating is no longer in operation, and gives enough time to move the drone back to the ground station within the mission time after spraying.

To actively increase the temperature, the system must use some sort of heat source and a way to distribute the heat. For this, there is a heater that blows air into the enclosure.

Part III:

Vol. 3 | System Integration

10

Stability & control characteristics

Mike, Patryk

Given the narrow operational room for error in servicing wind turbines, the drone control system must ensure stability and control. To make sure that this is the case, an analysis of system dynamics was done, which led to the model described in Section 10.1. Section 10.2 highlights theoretical control architecture in the absence of disturbances. Section 10.3 elaborates on practical control architectures, accounting for sensor inaccuracies, time delays, and sensor fusion.

10.1. Simulation

Mike

To simulate the dynamics of the drone, a state-space model can be constructed, which is in the form of $\dot{\boldsymbol{X}} = A\boldsymbol{X} + B\boldsymbol{U}$ and $\boldsymbol{y} = C\boldsymbol{X} + D\boldsymbol{U}$, where $\boldsymbol{X}$ is a vector containing the state variables, $\boldsymbol{U}$ is a vector containing the inputs, and A, B, C, and D are matrices that describe the interrelationship between the state and input variables. Constructing a state-space model is the process of choosing state variables and determining the transformations required. Here, the relevant state variables are those related to location, velocity, orientation, and rotation, leading to

$$\boldsymbol{X} = \begin{bmatrix} x & y & z & \dot{x} & \dot{y} & \dot{z} & \phi & \theta & \psi & \dot{\phi} & \dot{\theta} & \dot{\psi} \end{bmatrix}^T. \tag{10.1}$$

For the system to be full-rank, four vector equations relating the state variables are required. Here, selected were the derivative relationships for location and orientation, Newtonian mechanics, and Euler's law of rotation:

$$\begin{cases} \dot{\boldsymbol{x}}|_g = \frac{d}{dt}\boldsymbol{x}|_g \\ \boldsymbol{\omega}|_b = \frac{d}{dt}\boldsymbol{\theta}|_g \\ \boldsymbol{F}|_g = m\ddot{\boldsymbol{x}}|_g \\ \boldsymbol{M}|_b = I_b\dot{\boldsymbol{\omega}}|_b + \boldsymbol{\omega}|_b \times (I_b\boldsymbol{\omega}|_b) \end{cases}, \tag{10.2}$$

where $\boldsymbol{x} = \begin{bmatrix} x & y & z \end{bmatrix}^T$, $\boldsymbol{\theta} = \begin{bmatrix} \phi & \theta & \psi \end{bmatrix}^T$, m is the instantaneous vehicle mass, I is the instantaneous vehicle inertia tensor in the body axis frame, F is the force on the vehicle caused by its motor thrust, and M is the torque caused by differential motor thrust. To use this, $\boldsymbol{F}$ and $\boldsymbol{M}$ have to be further specified.

Starting with $\boldsymbol{F}$, it is first important to note that x, y, and z are defined in the global frame (denoted $\square|_g$). The motors, however, are mounted in the *vehicle-normal* direction, more easily defined in the body frame (denoted $\square|_b$). Therefore, $\boldsymbol{F}|_g = \mathbb{T}_{gb}\boldsymbol{T}|_b + mg\hat{\boldsymbol{z}}_g$, where

$\mathbb{T}_{gb} = \mathbb{T}_x(\phi)\,\mathbb{T}_y(\theta)\,\mathbb{T}_z(\psi)$, which can be expanded and simplified as

$$\mathbb{T}_{bg} = \mathbb{T}_{\boldsymbol{i}}(\phi)\,\mathbb{T}_{\boldsymbol{j}}(\theta)\,\mathbb{T}_{\boldsymbol{k}}(\psi) = \begin{bmatrix} c_\psi c_\theta & -s_\psi c_\theta & s_\theta \\ s_\phi s_\theta c_\psi + s_\psi c_\phi & -s_\phi s_\psi s_\theta + c_\phi c_\psi & -s_\phi c_\theta \\ s_\phi s_\psi - s_\theta c_\phi c_\psi & s_\phi c_\psi + s_\psi s_\theta c_\phi & c_\phi c_\theta \end{bmatrix} \tag{10.3}$$

$$\approx \begin{bmatrix} 1 & -\psi & \theta \\ \psi & 1 & -\phi \\ -\theta & \phi & 1 \end{bmatrix} \triangleq \hat{\mathbb{T}}_{bg}, \tag{10.4}$$

where $s_\square$ and $c_\square$ are shorthand for the sine and cosine function respectively, and $\hat{\mathbb{T}}_{bg}$ represents the linearised rotation matrix for small angles of ϕ, θ, and ψ, and after neglecting higher-order terms.

Then, $\boldsymbol{T}|_b = -\hat{\boldsymbol{z}}_b \sum_{n=1}^{N} T_n$, where $T_1, \ldots, T_N$ are the motor thrusts of all N motors. Note the minus sign, since the z-axis points down if the drone is upright.

Since $\boldsymbol{M}|_b$ is defined in the body frame, this yields $\boldsymbol{M}|_b = -\sum_{n=1}^{N}\left((\boldsymbol{r_n} \times \hat{\boldsymbol{z}}_b T_n) + \boldsymbol{\mu}_n\right)$ for N motors placed at $\boldsymbol{r}_1, \ldots, \boldsymbol{r}_N$, causing aerodynamic yawing moments $\boldsymbol{\mu}_1, \ldots, \boldsymbol{\mu}_N$.

$$\boldsymbol{\omega}|_b = \mathbb{T}_{gb}\frac{d}{dt}\boldsymbol{\theta}|_b = \mathbb{T}_{bg}^{T}\frac{d}{dt}\boldsymbol{\theta}|_b \tag{10.5}$$

$$\approx \hat{\mathbb{T}}_{bg}^{T}\frac{d}{dt}\boldsymbol{\theta}|_b = \begin{bmatrix} 1 & \psi & -\theta \\ -\psi & 1 & \phi \\ \theta & -\phi & 1 \end{bmatrix}\frac{d}{dt}\boldsymbol{\theta}|_b = \begin{bmatrix} \dot{\phi} + \psi\dot{\theta} + \theta\dot{\psi} \\ -\psi\dot{\phi} + \dot{\theta} + \phi\dot{\psi} \\ \theta\dot{\phi} - \phi\dot{\theta} + \dot{\psi} \end{bmatrix} \tag{10.6}$$

$$\approx \begin{bmatrix} \dot{\phi} \\ \dot{\theta} \\ \dot{\psi} \end{bmatrix} = \frac{d}{dt}\boldsymbol{\theta}|_g. \tag{10.7}$$

In other words, in this small-angle approximated, linearised model, it can be assumed that rotation components in the b-frame equal those in the g-frame. Hence, dropping the $\square|_b$ and $\square|_g$ for brevity, the linearised model is based on

$$\begin{cases} \dot{\boldsymbol{x}} = \frac{d}{dt}\boldsymbol{x} \\ \ddot{\boldsymbol{x}} = -\frac{1}{m}\sum_{n=1}^{N} C_T \tau_n \hat{\boldsymbol{z}} + \hat{\mathbb{T}}_{bg} g\hat{\boldsymbol{z}} + \boldsymbol{F}_{disturb} \\ \boldsymbol{\omega} = \frac{d}{dt}\boldsymbol{\theta} \\ \dot{\boldsymbol{\omega}} = -I^{-1}\sum_{n=1}^{N}\left(\boldsymbol{r_n} \times C_T\tau_n\hat{\boldsymbol{z}} + \delta_n C_Q \tau_n \hat{\boldsymbol{z}} + \boldsymbol{M}_{disturb}\right) \end{cases}, \tag{10.8}$$

where C_T and C_Q are coefficients that relate motor input to thrust and yaw moment, $\boldsymbol{r_1}, \ldots, \boldsymbol{r_N}$ are the location vectors of the motors relative to the centre of gravity, $\delta_1, \ldots, \delta_N \in \{1, -1\}$ are the moment directions due to the alternating direction of rotation of the propellers, causing opposite moments.

System matrix

Since the components of $\boldsymbol{x}$, $\dot{\boldsymbol{x}}$, $\boldsymbol{\theta}$, and $\boldsymbol{\omega}$ are all state variables, the first and third row in Equation 10.8 can be incorporated as a linear transformation directly through A as

$$\frac{d}{dt}\begin{bmatrix} x \\ y \\ z \\ \dot{x} \\ \dot{y} \\ \dot{z} \end{bmatrix} = \underbrace{\begin{bmatrix} \cdots & 1 & \cdots \\ \cdots & \cdots & 1 \\ \cdots & \cdots & \cdots \\ \cdots & \cdots & \cdots \\ \cdots & \cdots & \cdots \\ \cdots & \cdots & \cdots \end{bmatrix}}_{A_{\boldsymbol{x}\to\boldsymbol{x}}} \begin{bmatrix} x \\ y \\ z \\ \dot{x} \\ \dot{y} \\ \dot{z} \end{bmatrix} \quad \text{and} \quad \frac{d}{dt}\begin{bmatrix} \phi \\ \theta \\ \psi \\ \dot{\phi} \\ \dot{\theta} \\ \dot{\psi} \end{bmatrix} = \underbrace{\begin{bmatrix} \cdots & 1 & \cdots \\ \cdots & \cdots & 1 \\ \cdots & \cdots & \cdots \\ \cdots & \cdots & \cdots \\ \cdots & \cdots & \cdots \\ \cdots & \cdots & \cdots \end{bmatrix}}_{A_{\boldsymbol{\theta}\to\boldsymbol{\theta}}} \begin{bmatrix} \phi \\ \theta \\ \psi \\ \dot{\phi} \\ \dot{\theta} \\ \dot{\psi} \end{bmatrix}, \tag{10.9}$$

where dots in the matrices represent zeros.

A priori, it can be inferred that the second row of Equation 10.8 depends on state variables only through the second term. This term can be expanded and rewritten as

$$\hat{\mathbb{I}}_{bg} g\hat{\boldsymbol{z}} = g \begin{bmatrix} 1 & -\psi & \theta \\ \psi & 1 & -\phi \\ -\theta & \phi & 1 \end{bmatrix} \hat{\boldsymbol{z}} = g \begin{bmatrix} \theta \\ -\phi \\ 1 \end{bmatrix} = \begin{bmatrix} \cdot & g & \cdot \\ -g & \cdot & \cdot \\ \cdot & \cdot & \cdot \end{bmatrix} \boldsymbol{\theta} + \begin{bmatrix} \cdot \\ \cdot \\ g \end{bmatrix}, \tag{10.10}$$

where the left term is a linear transformation of the orientation state variables, and the right-hand side can be added to the state-space model as a pseudo-input. Finally, the last row of Equation 10.8 depends solely on constants and the inputs τ_n, leading to

$$\frac{d}{dt}\begin{bmatrix} x \\ y \\ z \\ \dot{x} \\ \dot{y} \\ \dot{z} \end{bmatrix} = \underbrace{\begin{bmatrix} \cdot & \cdot & \cdot & \cdot & \cdot & \cdot \\ \cdot & \cdot & \cdot & \cdot & \cdot & \cdot \\ \cdot & \cdot & \cdot & \cdot & \cdot & \cdot \\ \cdot & g & \cdot & \cdot & \cdot & \cdot \\ -g & \cdot & \cdot & \cdot & \cdot & \cdot \\ \cdot & \cdot & \cdot & \cdot & \cdot & \cdot \end{bmatrix}}_{A_{\boldsymbol{\theta}\to\boldsymbol{x}}} \begin{bmatrix} \phi \\ \theta \\ \psi \\ \dot{\phi} \\ \dot{\theta} \\ \dot{\psi} \end{bmatrix} \quad \text{and} \quad \frac{d}{dt}\begin{bmatrix} \phi \\ \theta \\ \psi \\ \dot{\phi} \\ \dot{\theta} \\ \dot{\psi} \end{bmatrix} = \underbrace{\begin{bmatrix} \cdot & \cdot & \cdot & \cdot & \cdot & \cdot \\ \cdot & \cdot & \cdot & \cdot & \cdot & \cdot \\ \cdot & \cdot & \cdot & \cdot & \cdot & \cdot \\ \cdot & \cdot & \cdot & \cdot & \cdot & \cdot \\ \cdot & \cdot & \cdot & \cdot & \cdot & \cdot \\ \cdot & \cdot & \cdot & \cdot & \cdot & \cdot \end{bmatrix}}_{A_{\boldsymbol{x}\to A_{\boldsymbol{\theta}}}} \begin{bmatrix} x \\ y \\ z \\ \dot{x} \\ \dot{y} \\ \dot{z} \end{bmatrix}. \tag{10.11}$$

Then, combining Equation 10.9 and Equation 10.11 gives

$$A = \begin{bmatrix} A_{\boldsymbol{x}\to\boldsymbol{x}} & A_{\boldsymbol{\theta}\to\boldsymbol{x}} \\ A_{\boldsymbol{x}\to\boldsymbol{\theta}} & A_{\boldsymbol{\theta}\to\boldsymbol{\theta}} \end{bmatrix} = \begin{bmatrix} \cdot & \cdot & \cdot & 1 & \cdot & \cdot & \cdot & \cdot & \cdot & \cdot & \cdot & \cdot \\ \cdot & \cdot & \cdot & \cdot & 1 & \cdot & \cdot & \cdot & \cdot & \cdot & \cdot & \cdot \\ \cdot & \cdot & \cdot & \cdot & \cdot & 1 & \cdot & \cdot & \cdot & \cdot & \cdot & \cdot \\ \cdot & \cdot & \cdot & \cdot & \cdot & \cdot & \cdot & g & \cdot & \cdot & \cdot & \cdot \\ \cdot & \cdot & \cdot & \cdot & \cdot & \cdot & -g & \cdot & \cdot & \cdot & \cdot & \cdot \\ \cdot & \cdot & \cdot & \cdot & \cdot & \cdot & \cdot & \cdot & \cdot & 1 & \cdot & \cdot \\ \cdot & \cdot & \cdot & \cdot & \cdot & \cdot & \cdot & \cdot & \cdot & \cdot & 1 & \cdot \\ \cdot & \cdot & \cdot & \cdot & \cdot & \cdot & \cdot & \cdot & \cdot & \cdot & \cdot & 1 \\ \cdot & \cdot & \cdot & \cdot & \cdot & \cdot & \cdot & \cdot & \cdot & \cdot & \cdot & \cdot \\ \cdot & \cdot & \cdot & \cdot & \cdot & \cdot & \cdot & \cdot & \cdot & \cdot & \cdot & \cdot \\ \cdot & \cdot & \cdot & \cdot & \cdot & \cdot & \cdot & \cdot & \cdot & \cdot & \cdot & \cdot \end{bmatrix}. \tag{10.12}$$

Input matrix

Whereas the system matrix is always 12×12, the input matrix depends on the number of inputs, here dependent on the number of motors, N. Here, it was defined that

$$\boldsymbol{U} = \begin{bmatrix} \tau_1 & \cdots & \tau_N & F_x & F_y & F_z & M_x & M_y & M_z & g \end{bmatrix}^T, \tag{10.13}$$

leading to a B-transformation of $12 \times (N+7)$ of

$$B = \begin{bmatrix} B_{\dot{\boldsymbol{x}}} \\ B_{\ddot{\boldsymbol{x}}} \\ B_{\dot{\boldsymbol{\theta}}} \\ B_{\ddot{\boldsymbol{\theta}}} \end{bmatrix}, \tag{10.14}$$

where $B_{\square}$ reflects the Jacobian of the property with respect to the input variables.

Since the first and third row of Equation 10.8 are independent of input variables, the corresponding coefficients in the input matrix are zero. Therefore,

$$B_{\dot{\boldsymbol{x}}} = B_{\dot{\boldsymbol{\theta}}} = 0_{12,(N+7)}, \tag{10.15}$$

where $0_{n,m}$ represents an $n \times m$ matrix filled with zeros. Then, the $B_{\ddot{\boldsymbol{x}}}$-term can be evaluated using Newtonian mechanics and the second row of Equation 10.8, and implementing the pseudo-input for g to find

$$B_{\ddot{\boldsymbol{x}}} = \begin{bmatrix} \cdot & \cdots & \cdot & \frac{1}{m} & \cdot & \cdot & \cdots & \cdot \\ \cdot & \cdots & \cdot & \cdot & \frac{1}{m} & \cdot & \cdots & \cdot \\ -\frac{C_T}{m} & \cdots & -\frac{C_T}{m} & \cdot & \cdot & \frac{1}{m} & \cdots & 1 \end{bmatrix}. \tag{10.16}$$

Using the bottom row of Equation 10.8

$$B_{\ddot{\boldsymbol{\theta}}} = \begin{bmatrix} (I^{-1})_{xx}(\boldsymbol{r_1}\times C_T\hat{\boldsymbol{z}})\cdot\boldsymbol{i} & \cdots & (I^{-1})_{xx}(\boldsymbol{r_N}\times C_T\hat{\boldsymbol{z}})\cdot\boldsymbol{i} & \cdots & (I^{-1})_{xx} & \cdot & \cdot & \cdot \\ (I^{-1})_{yy}(\boldsymbol{r_1}\times C_T\hat{\boldsymbol{z}})\cdot\boldsymbol{j} & \cdots & (I^{-1})_{yy}(\boldsymbol{r_N}\times C_T\hat{\boldsymbol{z}})\cdot\boldsymbol{j} & \cdots & \cdot & (I^{-1})_{yy} & \cdot & \cdot \\ (I^{-1})_{zz}\delta_1 C_Q & \cdots & (I^{-1})_{zz}\delta_N C_Q & \cdots & \cdot & \cdot & (I^{-1})_{zz} & \cdot \end{bmatrix}. \tag{10.17}$$

Combining Equation 10.15, Equation 10.16, and Equation 10.17 gives

$$B = \begin{bmatrix} \cdot & \cdots & \cdot & \cdot & \cdot & \cdot & \cdot & \cdot & \cdot & \cdot \\ \cdot & \cdots & \cdot & \cdot & \cdot & \cdot & \cdot & \cdot & \cdot & \cdot \\ \cdot & \cdots & \cdot & \cdot & \cdot & \cdot & \cdot & \cdot & \cdot & \cdot \\ \cdot & \cdots & \cdot & \frac{1}{m} & \cdot & \cdot & \cdot & \cdot & \cdot & \cdot \\ \cdot & \cdots & \cdot & \cdot & \frac{1}{m} & \cdot & \cdot & \cdot & \cdot & \cdot \\ -\frac{C_T}{m} & \cdots & -\frac{C_T}{m} & \cdot & \cdot & \frac{1}{m} & \cdot & \cdot & \cdot & 1 \\ \cdot & \cdots & \cdot & \cdot & \cdot & \cdot & \cdot & \cdot & \cdot & \cdot \\ \cdot & \cdots & \cdot & \cdot & \cdot & \cdot & \cdot & \cdot & \cdot & \cdot \\ (I^{-1})_{xx}C_T(\boldsymbol{r_1}\times\hat{\boldsymbol{z}})\cdot\boldsymbol{i} & \cdots & (I^{-1})_{xx}C_T(\boldsymbol{r_N}\times\hat{\boldsymbol{z}})\cdot\boldsymbol{i} & \cdot & \cdot & \cdot & (I^{-1})_{xx} & \cdot & \cdot & \cdot \\ (I^{-1})_{yy}C_T(\boldsymbol{r_1}\times\hat{\boldsymbol{z}})\cdot\boldsymbol{j} & \cdots & (I^{-1})_{yy}C_T(\boldsymbol{r_N}\times\hat{\boldsymbol{z}})\cdot\boldsymbol{j} & \cdot & \cdot & \cdot & \cdot & (I^{-1})_{yy} & \cdot & \cdot \\ (I^{-1})_{zz}\delta_1 C_Q & \cdots & (I^{-1})_{zz}\delta_N C_Q & \cdot & \cdot & \cdot & \cdot & \cdot & (I^{-1})_{zz} & \cdot \end{bmatrix} \tag{10.18}$$

Output transformations

In this 6 degrees-of-freedom (DOF) simulation, mainly of interest are $\boldsymbol{x}$ and $\boldsymbol{\theta}$. This yields

$$C = \begin{bmatrix} 1 & \cdot & \cdot & \cdot & \cdot & \cdot & \cdot & \cdot & \cdot & \cdot \\ \cdot & 1 & \cdot & \cdot & \cdot & \cdot & \cdot & \cdot & \cdot & \cdot \\ \cdot & \cdot & 1 & \cdot & \cdot & \cdot & \cdot & \cdot & \cdot & \cdot \\ \cdot & \cdot & \cdot & \cdot & \cdot & \cdot & 1 & \cdot & \cdot & \cdot \\ \cdot & \cdot & \cdot & \cdot & \cdot & \cdot & \cdot & 1 & \cdot & \cdot \\ \cdot & \cdot & \cdot & \cdot & \cdot & \cdot & \cdot & \cdot & 1 & \cdot \end{bmatrix}. \tag{10.19}$$

Since all partial derivatives of the system variables with respect to the input variables are zero, $D = 0_{6,(N+7)}$. This concludes the linearised state-space model (USER-S-PROP-5.1).

Model assumptions and limitations

The primary limitation of the model is that it is linearised, and thus shows inaccurate physical behaviour for large Euler rotation angles (including ψ for yaw). Since the cross-product in Euler's rotational equation of motion was neglected, small angular rates are also a requirement for validity. The model assumes time-invariant inertia and mass.

10.2. Stability

Mike

For the preliminary stability assessment, a linear-quadratic regulator (LQR) was used to tune a linear (proportional) controller of the form

$$\boldsymbol{U} = -K\left(\boldsymbol{X} - \boldsymbol{X}_{ref}\right) + \boldsymbol{U}_{ref}, \tag{10.20}$$

which can also target non-zero target states, and which minimises a quadratic cost function based on state and input weight matrices Q and R, so that

$$\dot{\boldsymbol{X}} = A\boldsymbol{X} + B\boldsymbol{U} = A\boldsymbol{X} + B\left(-K\left(\boldsymbol{X} - \boldsymbol{X}_{ref}\right) + \boldsymbol{U}_{ref}\right) \tag{10.21}$$

$$= \underbrace{(A - BK)}_{A_{cl}}\boldsymbol{X} + BK\boldsymbol{X}_{ref} + B\boldsymbol{U}_{ref}. \tag{10.22}$$

Here, weight matrices were chosen as

$$Q = \begin{bmatrix} 10^3 & \cdot & \cdot & \cdot & \cdot & \cdot & \cdot & \cdot & \cdot & \cdot & \cdot & \cdot & \cdot & \cdot \\ \cdot & 10^3 & \cdot & \cdot & \cdot & \cdot & \cdot & \cdot & \cdot & \cdot & \cdot & \cdot & \cdot & \cdot \\ \cdot & \cdot & 3{\cdot}10^3 & \cdot & \cdot & \cdot & \cdot & \cdot & \cdot & \cdot & \cdot & \cdot & \cdot & \cdot \\ \cdot & \cdot & \cdot & 10^3 & \cdot & \cdot & \cdot & \cdot & \cdot & \cdot & \cdot & \cdot & \cdot & \cdot \\ \cdot & \cdot & \cdot & \cdot & 10^3 & \cdot & \cdot & \cdot & \cdot & \cdot & \cdot & \cdot & \cdot & \cdot \\ \cdot & \cdot & \cdot & \cdot & \cdot & 3{\cdot}10^3 & \cdot & \cdot & \cdot & \cdot & \cdot & \cdot & \cdot & \cdot \\ \cdot & \cdot & \cdot & \cdot & \cdot & \cdot & 2{\cdot}10^3 & \cdot & \cdot & \cdot & \cdot & \cdot & \cdot & \cdot \\ \cdot & \cdot & \cdot & \cdot & \cdot & \cdot & \cdot & 2{\cdot}10^3 & \cdot & \cdot & \cdot & \cdot & \cdot & \cdot \\ \cdot & \cdot & \cdot & \cdot & \cdot & \cdot & \cdot & \cdot & 5{\cdot}10^5 & \cdot & \cdot & \cdot & \cdot & \cdot \\ \cdot & \cdot & \cdot & \cdot & \cdot & \cdot & \cdot & \cdot & \cdot & 2{\cdot}10^3 & \cdot & \cdot & \cdot & \cdot \\ \cdot & \cdot & \cdot & \cdot & \cdot & \cdot & \cdot & \cdot & \cdot & \cdot & 2{\cdot}10^3 & \cdot & \cdot & \cdot \\ \cdot & \cdot & \cdot & \cdot & \cdot & \cdot & \cdot & \cdot & \cdot & \cdot & \cdot & 2{\cdot}10^3 & \cdot & \cdot \\ \cdot & \cdot & \cdot & \cdot & \cdot & \cdot & \cdot & \cdot & \cdot & \cdot & \cdot & \cdot & 2{\cdot}10^5 & \cdot \end{bmatrix}, \text{and} \tag{10.23}$$

$$R = 10^{-4}\mathbb{I}_N, \tag{10.24}$$

Table 10.1: *Drone eigenmodes for a full payload tank*

	First mode	Second mode	Third mode	Fourth mode		Fifth mode		Sixth mode	Seventh mode	Eighth mode	Ninth mode	Tenth mode
λ_i Re	−717.136	−29.978	−32.336	−1.859		−1.860		−1.634	−1.265	−1.000	−1.000	−1.000
Im	–	–	–	±1.866		±1.866		–	–	–	–	–
P (s)	∞	∞	∞	3.367		3.368		∞	∞	∞	∞	∞
$T_{1/2}$ (s)	0.001	0.023	0.021	0.373		0.373		0.424	0.548	0.693	0.693	0.693
ζ (-)	–	–	–	0.706		0.706		–	–	–	–	–
ω_n (rad s^{-1})	–	–	–	2.634		2.634		–	–	–	–	–
f_n (Hz)	–	–	–	0.419		0.419		–	–	–	–	–
$\boldsymbol{\mu}_i$	z	z	z	z	θ (°)	z	θ (°)	z	z	z	z	z
Δx	0.000	0.000	0.000	0.000	180.0	0.000	0.0	0.000	0.002	0.000	0.000	**1.000**
Δy	0.001	0.000	0.000	0.014	0.0	0.000	180.0	**0.230**	0.000	0.000	**1.000**	0.000
Δz	0.000	0.000	0.000	0.000	180.0	0.000	0.0	0.000	0.000	**1.000**	0.000	0.000
$\Delta \dot{x}$	**0.291**	0.000	0.000	**1.000**	0.0	0.000	170.3	**1.000**	0.000	0.000	0.002	0.000
$\Delta \dot{y}$	**0.291**	0.000	0.000	**1.000**	0.0	0.000	189.7	**1.000**	0.000	0.000	0.002	0.000
$\Delta \dot{z}$	0.000	**0.291**	0.000	0.000	286.1	0.000	303.9	0.000	0.000	0.002	0.000	0.000
$\Delta \phi$	0.000	**0.291**	0.000	0.000	73.9	0.000	56.1	0.000	0.000	0.002	0.000	0.000
$\Delta \theta$	0.000	0.000	**0.842**	0.000	180.0	**1.000**	180.0	0.000	0.000	0.000	0.000	0.000
$\Delta \psi$	0.000	0.000	**1.000**	0.000	180.0	**0.920**	180.0	0.000	0.000	0.000	0.000	0.000
$\Delta \dot{\phi}$	**1.000**	0.000	0.000	**0.922**	180.0	0.000	180.0	**0.496**	0.000	0.000	**0.072**	0.000
$\Delta \dot{\theta}$	0.000	**1.000**	0.000	0.000	0.0	0.000	180.0	0.000	0.000	**0.072**	0.000	0.000
$\Delta \dot{\psi}$	0.000	0.000	0.000	0.000	180.0	0.000	180.0	0.000	**1.000**	0.000	0.000	**0.707**

where $\mathbb{I}_N$ is the $N \times N$ identity matrix.

These weights have a large effect on the behaviour of the drone. Large values for R lead to slow responses to disturbances, but also small time-gradients in thrust. Q influences the relative importance of different state variables. There, location and orientation might be weighed more than for instance ϕ and θ, though ψ is high for pointing accuracy. The input weight matrix can be used to tweak how quickly and how intensely the system responds to disturbances. This changes the behaviour of the system, but (absolute) stability is largely unimpacted.

For co-axial behaviour, it can be asserted that $\delta_n = (-1)^n$ and that $\boldsymbol{r}_n = (\boldsymbol{r}_{arm})_{\lfloor \frac{n}{2} \rfloor}$ for $n \in \{1, \ldots, N\}$, where $(\boldsymbol{r}_{arm})_1, \ldots, (\boldsymbol{r}_{arm})_{\frac{N}{2}}$ contain the displacement vectors between the centre of gravity and the arms, where there are twice as many motors as arms, since the configuration is co-axial.

Stability with changing inertia

To assess whether the control system can be stable for the given drone configuration, the eigenvalue analysis was done for both the empty and full configuration. The results for that are shown in Table 10.1 and Table 10.2. It can be seen that both are stable.

Then, analysing stability becomes a matter of analysing the closed-loop system transformation A_{cl}. Since $\boldsymbol{X}$ contains 12 states, the characteristic polynomial of A_{cl} has exactly twelve solutions. These solutions may or may not have complex components. Control stability is reached if all eigenvalues have negative real components. From these eigenvalues, the resonant frequencies of the system can be determined alongside their eigenvector, showing the coupling between states, and phase difference for periodic states. Smaller $\mathrm{Re}(\lambda_i)$ leads to a faster decaying eigenmotion, also described by the half-decay time $T_{1/2}$, after which the modal amplitude has halved. Complex eigenvalues indicate oscillatory behaviour, leading to the notion of period P and natural frequency f_n.

Control assumptions and limitations

This control system limitation mainly stems from it neglect of the interpretation step. In reality it has to estimate the state variables before it can determine a control input. This is also present in the lack of delay between sensor measurements and actuator response, whereas delay is otherwise a major problem in control system design. Sensor measurements are also assumed to be noise free.

Additionally, the LQR assumes that actuators are infinitely accurate and deliver the desired torque/thrust instantly. It also does not consider the operating envelope of the actuators –

Table 10.2: *Drone eigenmodes for an empty payload tank*

	First mode	Second mode	Third mode	Fourth mode		Fifth mode		Sixth mode	Seventh mode	Eighth mode	Ninth mode	Tenth mode
λ_i Re	−988.132	−36.460	−36.479	−1.860		−1.860		−1.634	−1.265	−1.000	−1.000	−1.000
Im	–	–	–	±1.865		±1.865		–	–	–	–	–
P (s)	∞	∞	∞	3.369		3.369		∞	∞	∞	∞	∞
$T_{1/2}$ (s)	0.001	0.019	0.019	0.373		0.373		0.424	0.548	0.693	0.693	0.693
ζ (-)	–	–	–	0.706		0.706		–	–	–	–	–
ω_n (rad s^{-1})	–	–	–	2.634		2.634		–	–	–	–	–
f_n (Hz)	–	–	–	0.419		0.419		–	–	–	–	–
$\boldsymbol{\mu}_i$	z	z	z	z	θ (°)	z	θ (°)	z	z	z	z	z
Δx	0.000	0.000	0.000	0.000	180.0	0.000	180.0	0.000	0.001	0.000	0.000	**1.000**
Δy	0.000	0.000	0.000	0.010	180.0	0.000	0.0	**0.189**	0.000	0.000	**1.000**	0.000
Δz	0.000	0.000	0.000	0.000	180.0	0.000	180.0	0.000	0.000	**1.000**	0.000	0.000
$\Delta \dot{x}$	**0.291**	0.000	0.000	**1.000**	180.0	0.000	108.1	**1.000**	0.000	0.000	0.001	0.000
$\Delta \dot{y}$	**0.291**	0.000	0.000	**1.000**	180.0	0.000	251.9	**1.000**	0.000	0.000	0.001	0.000
$\Delta \dot{z}$	0.000	**0.291**	0.000	0.000	204.2	0.000	169.1	0.000	0.000	0.001	0.000	0.000
$\Delta \phi$	0.000	**0.291**	0.000	0.000	155.8	0.000	190.9	0.000	0.000	0.001	0.000	0.000
$\Delta \theta$	0.000	0.000	**0.842**	0.000	0.0	**1.000**	0.0	0.000	0.000	0.000	0.000	0.000
$\Delta \psi$	0.000	0.000	**1.000**	0.000	180.0	**0.920**	180.0	0.000	0.000	0.000	0.000	0.000
$\Delta \dot{\phi}$	**1.000**	0.000	0.000	**0.922**	0.0	0.000	180.0	**0.495**	0.000	0.000	**0.072**	0.000
$\Delta \dot{\theta}$	0.000	**1.000**	0.000	0.000	0.0	0.000	180.0	0.000	0.000	**0.072**	0.000	0.000
$\Delta \dot{\psi}$	0.000	0.000	0.000	0.000	180.0	0.000	0.0	0.000	**1.000**	0.000	0.000	**0.707**

thrust has to manually be clipped after the fact, which reduces the validity of the eigenvalue analysis.

Finally, an LQR is merely proportional control, and cannot, therefore, remove the steady-state offset that is present in the current model under external disturbance forces and torques due to the wind. Integral action could be added to the LQR by adding error states for the time-integral of position error – this is left as future work.

10.3. Control *Patryk*

The drone must be controllable towards the desired positions and hover there at a set attitude. For stability in all mission conditions a robust control system needs to be established that allows for autonomy and drone coordination.

As developed in detail in Chapter 13 the drones operate as a decentralized-communication swarm with a ground station. This requirement creates the need for the drones to be directed to a chosen position and persist in hover. In order to meet operational requirements two systems are developed for each drone: state measuring system and the controller.

The state measurements are made with the purpose of positioning the drone in 3D space. For tracking position of the drone two sensors were chosen: a 9-degree-of-freedom (DOF) inertial measurement unit (IMU) for angular velocity and a real-time kinematic-global navigation satellite system (RTK-GNSS) sensor for position and velocity measurements. These sensors are fused to ensure higher precision, further explained in Subsection 10.3.1. Increasing precision aims to meet `USER-S-ACC-2.1` and `USER-S-ACC-2.2`. The 9-DOF IMU is modelled to sample data at frequency of 100Hz and GNSS samples data at 10Hz.

The controller architecture needs to be determined based on the requirements on the system. The leading requirements for control are `USER-S-POW-5.20`, `USER-S-PROP-4.1`, and `USER-S-ACC-2.1`. These indicate that controller must withstand environmental disturbances and support future autonomous navigation.

Assuming steady-state operation (hover and cruise), a locally linearized model is valid (Heng et al., 2015). This motivates the selection of a Linear-Quadratic-Gaussian (LQG) controller, combining an LQR and a Kalman filter to ensure optimal control and state estimation under sensor noise. A large advantage of this is that the gain weighing matrices Q and R allow for prioritising chosen states. Hence, the controller is robust and optimal.

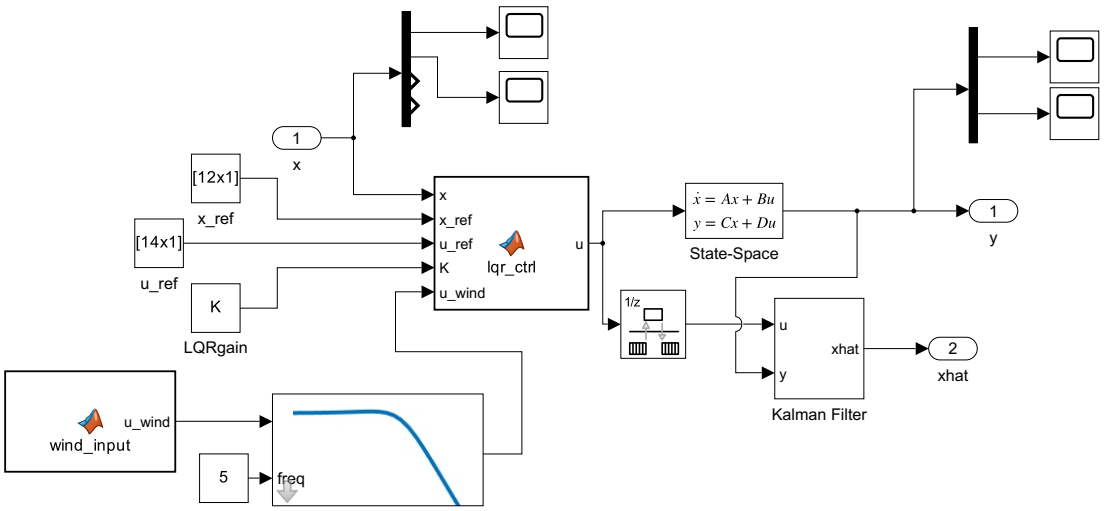

Figure 10.1: *Closed-loop system block diagram of the control loop.*

10.3.1. Control loop design

As previously stated, the two systems for measuring the states with sensor and controlling the drone are placed in a closed-loop system. The architecture can be observed in Figure 10.1, with the arrow going outside being the control output.

State measurement system design

This system must handle measurements collected by the IMU and GNSS and pass them after preprocessing into the controller. The way inputs to the controller are handled can be seen in Figure 10.2. In the purple boxes, the sensor inputs can be observed. As no real measurements are available in the simulated model, sensor outputs are simulated with added Gaussian white noise. The magnetometer is not modelled, with the assumption of automatic correcting.

All of the signals are first passed through a Butterworth filter of first order. As given by Pal (Pal, 2019), it is a low-pass filter that is frequently used to filter out electrical signal noise. For the cut-off frequency a value of 5 Hz is chosen everywhere. The equation describing the Butterworth filter is given in Equation 10.25 (Pal, 2019). The first filtering reduced signal noise.

$$G\omega = \frac{1}{\sqrt{1+\omega/\omega_c^{2n}}} \tag{10.25}$$

The IMU and GNSS are used together to provide more reliable positioning data. To handle the fusion between signals from the sensor a Kalman filter is employed. How a Kalman filter can be used for sensor fusion is extensively described by Jahja et al. (2019). As inputs, the linear accelerations from IMU are fed in, which are integrated with backwards Euler integration to match the derivative orders of the inputted GNSS positions and linear velocities. The weighing matrix Q is tuned to prioritise tuning of position and velocity, rather than acceleration, as it is not used as a state variable for control. For R matrix the GNSS positions x, y and z are given higher priority, as the sensor fusion with accelerometer requires double integration, which introduces possibly more error, than for velocity. The angular velocity and angle are not involved in sensor fusion.

All of the states are gathered together in one state vector, which is shown below.

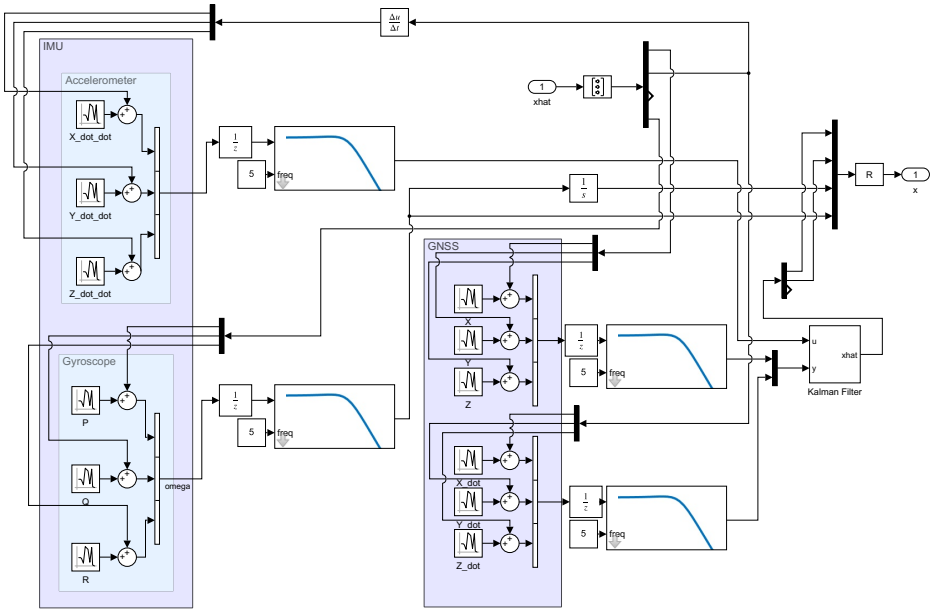

Figure 10.2: *State measuring system block diagram.*

$$\boldsymbol{x} = [x, y, z, v_x, v_y, v_z, \phi, \theta, \psi, \dot{\phi}, \dot{\theta}, \dot{\psi}]^T$$

Controller system design
The overall structure of the controller system (as seen in Figure 10.3) is that the reference values for input and state vectors are established. They are run into the LQR controller together with state vector from the previous system and artificial disturbance inputs, that are used to ensure robustness in the range of uncertainties defined by the mission profile. The input vector produced by the LQR controller is fed into both state-space model and the Kalman filter. The signal from state-space model is also fed into the Kalman filter and is output for providing processed position to the drone, outside this system. The Kalman filter using the input vector and the state-space output estimates the state variables, matching the sensors, of the control system. The weighing matrices are tuned in such a way that position is priorities over velocity as a filter input, while linear position and angular velocities are prioritised over linear velocity for the state variables.

As the linearized dynamics of the drone system are built into a state-space model in Section 10.2, the analysis of dynamics is omitted in this section in favour of explaining the LQR control. This controller provides state feedback gain, which optimizes on a quadratic costs function, which is a function of state variables and input (Gonçalves da Silva et al., 2019). The system is modelled as time continuous, therefore the optimisation cost function is as shown in Equation 10.26.

$$J(u) = \int_0^\infty (x^T Q x + u^T R u) d t \tag{10.26}$$

The state-feedback control is defined as shown in Equation 10.27.

$$u = -K \cdot (x - x_{ref}) + u_{ref} \tag{10.27}$$

To obtain the gain matrix K for the controller it has to be set to:

$$K = R^{-1} B^T S$$

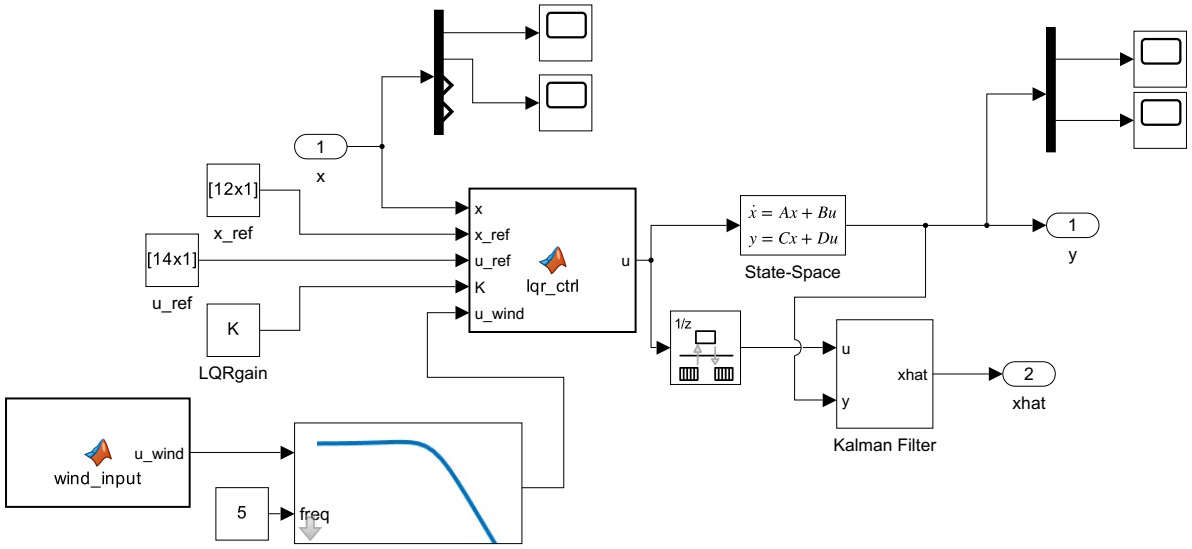

Figure 10.3: *Controller system block diagram.*

The matrix S is the solution to algebraic Ricatti Equation, which is given in Equation 10.28.

$$A^T S + SA - SBR^{-1}B^T S + Q = \mathbf{0} \tag{10.28}$$

In the state-space model block seen in Figure 10.3, the closed loop feedback around the LQR controller is defined by specifying the A matrix with a closed loop A_{cl} as shown in Equation 10.29.

$$A_{cl} = A - B[1:12, 1:8] \cdot K \tag{10.29}$$

10.3.2. Controller disturbance rejection

The purpose of LQG controller is to reject disturbance inputs and correct for error between the measurement and the simulated states. The disturbance here can mostly be attributed to sensor noise. The controller shown in Figure 10.3 also models disturbance inputs of wind perturbations. The wind is modelled as input of Perlin noise, that is low-pass filtered. The ability of the controller to reject disturbances was inspected on controller input (x signal in Figure 10.3) and controller output (y signal in Figure 10.3). The x position and yaw angle are taken for comparison in Figure 10.4 at rise to a flight level and continued hover. The x position shown in Figure 10.4a measurement can be seen to possess a significant amount of noise within ±1 meter. The noise comes mainly from the less accurate GNSS measurement, from which can be seen that the low frequency noise has higher amplitudes. The controller handles the disturbances by rejecting large spikes due to LQR and smoothing out the noise curve with the Kalman filter. The position is stable within ±0.1 error bounds. However the signal is slightly shifted upwards. In Figure 10.4b the yaw can be seen to be really noisy with the amplitudes of low frequency noise being very varied. This is due to the fact that the angular position is estimated using integration of angular velocities measured by the gyroscope. The controller handles the disturbances both in low and high frequency noise very well, by almost completely correcting for them. The remaining noise is irrelevant to stability during drone operation.

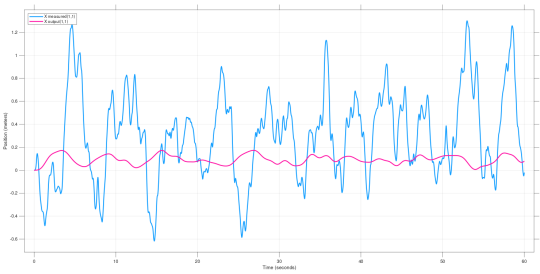

(a) *Comparison between measured state and controlled state x-position.*

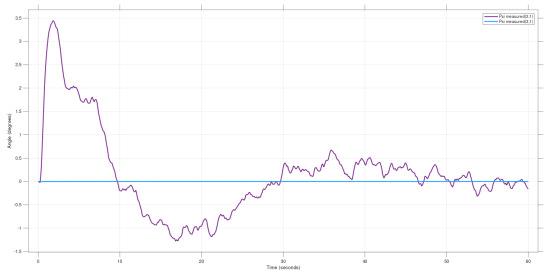

(b) *Comparison between measured state and controlled state yaw-position.*

Figure 10.4: *Comparison between measured and controlled states for (a) x-position and (b) yaw-position.*

10.4. Limitation and recommendations *Patryk*

The approach taken for design of the control system creates several limitations to the applicability of the design stemming from assumptions taken during modelling. Future work would involve steps to improve the system's accuracy and performance.

One limitation that is created in the process of modelling the aircraft dynamics is that the cases considered are limited to trim conditions. A linearized model of drone dynamics is only viable for conditions of low angle deflections, which approximates only hover conditions and level steady flight (Heng et al., 2015). To more comprehensively model the dynamics of the drone when manoeuvring, a non-linear model of the drone needs to be established. A more complex controller can be used, such as adaptive control, to provide greater autonomy of flight as explored by Dydek (2010).

The main limitation of a LQR controller is that it only can operate on linearized models, rather than non-linear models. Therefore it is only accurate near the operation point of hover, where linearization assumptions apply. The Kalman filter also has to assume a linear model, as the one employed in the controller is not extended. The presence of the filter also requires more complex tuning to achieve numerical stability and good knowledge of the noise model.

For further exploration of autonomous control, multiple neural network based controllers can be employed. Examples of such controllers can be model predictive control used for trajectory planning of the drone. Further mission planning can be expanded with integrating control with reinforcement learning algorithms for path planning or optimum search algorithms. Both of these activities need to be performed in order to meet the requirement `USER-S-ACC-2.1`.

11

Computer vision module

Edlyn

The computer vision (CV) module is a pipeline from image capture, processing, ice localisation to ice mapping. Due to restrictions on proprietary datasets and the lack of permission to use pre-existing models, a bespoke architecture and dataset must be developed. This chapter details the objectives of the computer vision in Section 11.1, data strategy in Section 11.2, model architecture in Section 11.3, evaluation framework in Section 11.4, and integration in operations in Section 11.5. Moving on, the hardware is selected Section 11.6 and the chapter ends with limitations and recommendations in Section 11.7.

11.1. Computer vision objective

Edlyn

The CV module is the perception backbone of the de-icing drone mission. It enables autonomous, reliable, and accurate detection of ice accumulation on wind turbines, ensuring that the de-icing agent is only employed on iced parts of the blade. This optimises energy use, chemical consumption, and overall mission time. As such, it is synonymous with the key requirement `USER-S-PAYL-3.1`, mandating a 95% accuracy of ice detection. Notably, this system does not attempt to classify the type of ice, as the dominant form in our operating region is rime ice (see Chapter 2), and chemical de-icing efficacy is not significantly impacted by ice subtype.

In a broad context, the CV module will first localise ice in the 2D frame of an RGB image, and then translate this to 3D coordinates relative to the hub of the wind turbine. To accomplish this, an artificial intelligence (AI) model will be trained for the first task. In this work, a novel convolutional neural network, Eyes for Ice Network (EFInet-2D), is developed for segmentation. The latter task for 3D mapping is performed using a "Simultaneous Localisation And Mapping" algorithm called GigaSLAM (K. Deng et al., 2025). GigaSLAM translates RGB images into a 3D map to develop the digital twin discussed in Section 13.3. Ultimately, the CV module must:

- perform pixel-wise segmentation under low-light, foggy, and variable lighting conditions
- operate within the onboard computing constraints
- integrate with the autonomy and swarm control modules to form a complete perception-to-action loop

11.2. Data strategy

Edlyn

Data forms the foundation of any deep learning model. Its performance is highly dependent on the quality and diversity of its training data as this is where it gains information from. This section outlines the acquisition, processing, and augmentation techniques used to create a robust dataset for training and validating the model.

Data acquisition

A dedicated data acquisition campaign will be conducted using a drone equipped with the onboard 4K RGB camera at a typical operating range of 3 m, such that an image covers 1 m^2.

This enables realistic conditions when flying to be fed to EFInet-2D. As planned in Chapter 17, this will be conducted in the detailed design phase. The following considerations are included:

- **Variation:** Data should include a variety of circumstances, both for lighting (e.g., low-angle sunlight, overcast skies, and nighttime) and temporal characteristics (flights conducted at different times of day). This improves generalisation and reduces reliance on consistency in lighting, considering the dim winter conditions and icing forms.
- **Collection size:** A total of ~4000 images will be collected, covering a wide range of blade angles, surface textures, and lighting conditions. This size is informed by prior work (Hacıefendioğlu et al., 2022) that achieved >96% segmentation accuracy using datasets with fewer than 2000 annotated images. However, since this model will be bigger (detailed in Section 11.3), a larger amount of training data is needed to support EFInet-2D.
- **Image resolution:** Images will be cropped and downsampled to frames of 224×224 in line with VGG-19 requirements while preserving spatial detail of icing regions.

Data pre-processing

As this is a supervised learning task, labels must be provided for each pixel in every image. Each frame will be pixel-annotated with classes: 0 = background, 1 = clean turbine, 2 = iced turbine. Hence, each image will be coupled with a 224×224 matrix of labels. This tedious task of labelling can be performed and managed on the CVAT [1] data annotation platform.

Furthermore, to give the model more information to learn, the size of the training dataset can be artificially increased through data augmentation. In this pursuit, copies of the images can be created but with layers of image manipulation, such as by adding photometric variations in the brightness and contrast, adding environmental overlays such as brightness shifts, fog overlays, noise, and blur (Shorten & Khoshgoftaar, 2019). Data will be split into training, validation, and test sets of 70%, 20%, and 10%, respectively. The test set will be used as unseen data to evaluate EFInet-2D with integrity.

11.3. EFInet-2D model architecture *Edlyn*

EFInet-2D is designed as a semantic segmentation network that classifies each pixel in a given image into one of the three aforementioned classes (Long et al., 2015). A transfer-learning approach (Yosinski et al., 2014) will be taken by extending a pre-trained convolutional neural network (CNN) model. This is to leverage knowledge already gained from training on extremely large datasets and adapt it to a specified task with a niche dataset.

While previous works in ice detection on wind turbines opt for U-net (an encoder-decoder style model (Ronneberger et al., 2015)) as the backbone model (Hacıefendioğlu et al., 2022), this implementation explores the novel use of VGG-19 (Simonyan & Zisserman, 2015) for segmentation in this domain. VGG-19 has shown high accuracy (~ 96%) in classifying iced turbine images (Kreutz et al., 2020), indicating that it can learn features of ice well. This can be credited to its large size. Furthermore, studies show that VGG-19 can outperform U-Net in segmentation, particularly in learning fine textures and contours (like turbine edges and ice) (Chanda et al., 2024). This novel approach is needed to combat the risk of bad weather and blurry images in operation, as the reports suggest that only high-quality images were used. However, its resource footprint necessitates a memory-efficient decoder design.

The VGG-19 layers up to the last convolutional layer will provide the encoder functionality and will be extended with a lightweight decoder module to bring the final output size to a matrix

[1] https://www.cvat.ai/

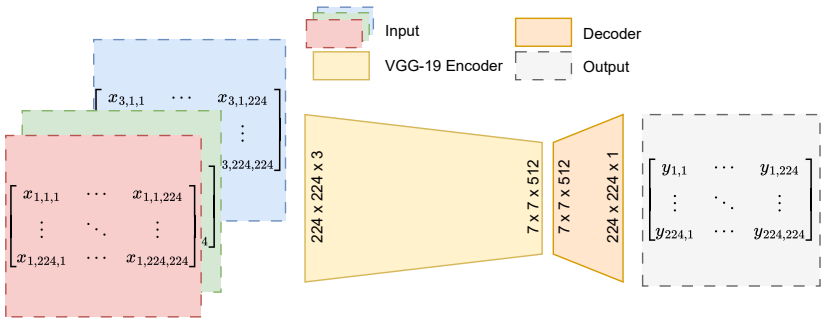

Figure 11.1: *EFInet-2D architecture*

of 224×224. An illustration of EFInet-2D's layers, along with the size of the tensors, is given in Figure 11.1. Hence, the layers of the final model are as follows:

Encoder (VGG-19): The RGB image is processed as a 3D input matrix of $x_{i,j,k} \in [0, 255]$. The encoder uses the convolutional blocks of the VGG-19 network pre-trained on ImageNet (J. Deng et al., 2009). These extract hierarchical spatial features, compressing the preprocessed image of $224 \times 224 \times 3$ dimensions to a $7 \times 7 \times 512$ feature map. In early training epochs, these layers are frozen to preserve the pre-trained model state. Later, they are fine-tuned for task-specific adaptation.

Decoder: The decoder layers must be trained from scratch. They are a lightweight upsampling pipeline that progressively restores spatial resolution through transposed convolutions and upsampling. The last layer uses a Softmax activation to assign probabilities of the three classes to each spatial coordinate (Lecun et al., 1998). From this, the class with the maximum probability is assigned to each pixel, as $y_{i,j} \in \{0, 1, 2\}$. Hence, the latent representation is expanded back to $224 \times 224 \times 1$.

Furthermore, as this task is inherently a classification of each pixel, the loss function must suit its probabilistic nature. Hence, the binary cross entropy loss is used (Ruby & Yendapalli, 2020), along with Adaptive Moment Estimation (Adam) optimiser (Kingma & Ba, 2014). Training of this model can be conducted on various platforms, provided that CUDA[2] and graphic processing unit (GPU) functionality are available. Online resources for this include Kaggle[3] and AWS[4]. The TU Delft also has a high-power computer as an available resource[5].

This preliminary architecture can only go this far in detail. There are still numerous hyperparameters that have to be optimized for, including learning rate, number of hidden layers, number of hidden units for these layers, dropout probability, and coefficients for regularization. This will be conducted by a grid search.

11.4. Evaluation metrics *Edlyn*

Evaluation metrics are needed to select the best hyperparameter configuration of the model, which is defined by 2 aspects: assessing segmentation quality and validating deployability within the drone system. It is important to look beyond accuracy as a singular metric to give a holistic evaluation of EFInet-2D. In safety operations such as this, it is more favourable to predict a threat (ice) that is not there than to bypass an imminent one. Thus, model architecture and thresholds are optimised to minimise them, even at the cost of increased false positives.

[2]https://developer.nvidia.com/cuda-zone
[3]https://www.kaggle.com/
[4]https://aws.amazon.com/
[5]https://www.tudelft.nl/dhpc/system

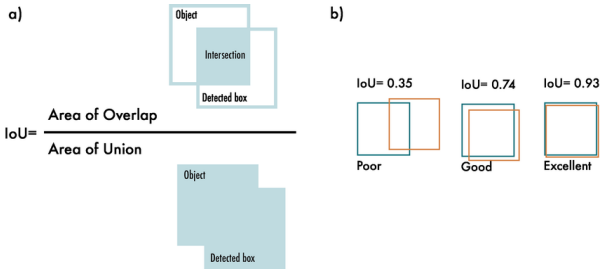

Figure 11.2: *Illustration of IoU (Terven et al., 2023)*

The most common metric for the segmentation task is intersection over union (IoU) per class. IoU is calculated per class and is useful for assessing the overlap quality between predicted and ground truth regions as shown in Figure 11.2. Based on the illustration, an IoU of at least 0.7 should be targeted. Hacıefendioğlu et al. (2022) have achieved a score of 0.8 in this aspect. A high IoU for the "ice" class is a priority, as this directly impacts the reliability of de-icing actions. The dice coefficient (F1 Score for segmentation) complements IoU by emphasising the harmonic mean between precision and recall (Milletari et al., 2016). This is especially beneficial in cases of class imbalance, which is expected in scenarios where ice forms sparsely on large turbine surfaces.

In addition, more operational metrics include latency and model footprint as EFInet-2D operates in an embedded context. Similar models run for ~30 ms on a drone-sized onboard computer (Yang et al., 2025). For the operations designed, leeway is given up to 50 ms. Beyond conventional accuracy, it is necessary to monitor memory usage and power consumption during inference, ensuring computation sustainability. These metrics define whether a model is deployable onboard or must be redesigned for a lighter inference head.

11.5. 3D Integration

Michal, Edlyn

The integration of the CV module into the system of this mission, encompassing all the drones in the swarm and the ground station, is a pivotal part of the design. The 2D output of the CNN model will be translated to actionable spatial data in 3D coordinates relative to the wind turbine thanks to a 30 FPS RGB camera feed that is passed to the ground station and allows for the creation of a 3D high fidelity map of the area, guiding the perception of the autonomous drone.

To create this map, a SLAM algorithm is used. Also known as Simultaneous Localisation And Mapping, SLAM is a class of algorithms that allows autonomous systems such as robots or drones to understand the environment they are in and where they are located within it. There are various types of SLAM algorithms, starting from classical algorithms (for example ORB-SLAM by Mur-Artal and Tardos (2017)) to algorithms that leverage machine learning for depth perception, feature extraction, and similar tasks that improve the capabilities of the model (for example DROID-SLAM[6]).

From all the existing SLAM algorithms, GigaSLAM (K. Deng et al., 2025) stands out for its RGB-only input and its ability to scale to kilometre-scale maps. GigaSLAM estimates the pose of the camera based on image features, estimates the depth of various sections of the image, and finally generates a combination of Gaussian primitives (Zhou et al., 2024) that best explain the observed pixels. All parts and algorithms (using `ZoeDepth` as depth perception network) used in its pipeline are likewise open-source and business-friendly. The map can now be used to generate a digital twin.

[6]https://github.com/princeton-vl/DROID-SLAM

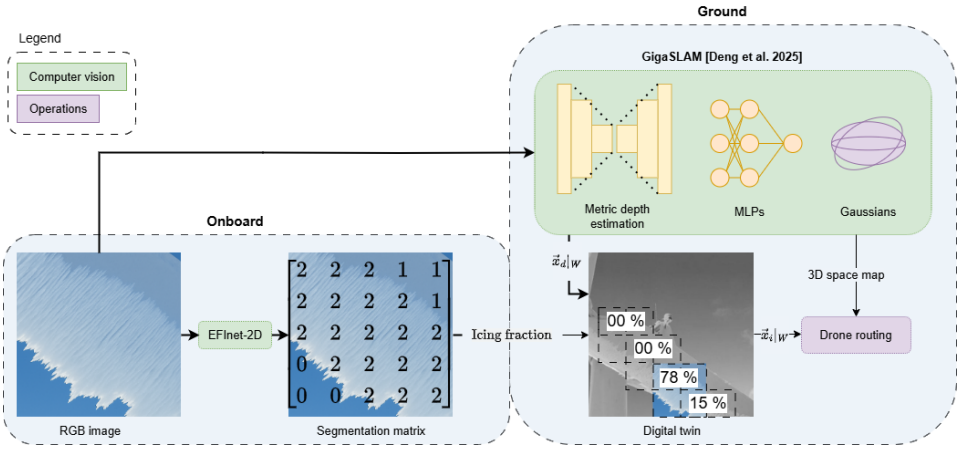

Figure 11.3: *Computer vision integration*

As the drone approaches a wind turbine, it begins scanning its surface at a rate of 1 frames per second (fps). Each image is processed onboard, and the information regarding ice coverage is passed on to the ground station. The ice coverage percentage is matched with the location of the wind turbine extracted from the SLAM-based map. This information is used to build the digital twin (Allen, 2021). The digital twin is used to keep track of the de-icing progress and to plan and continuously adapt drone routing (see Section 13.3), forming a complete perception-action loop. A detailed explanation on the dataflow pipeline and integration with other subsystems is given in Chapter 12.

11.6. Hardware selection

Edlyn

The hardware components function to create input for the computer vision model and facilitate computation. They are selected to satisfy operational conditions and the computational demand of the onboard deep learning model. The primary components include a single camera mounted on a gimbal, lighting and an onboard processor. Together, the components ensure high-fidelity image capture, robust real-time analysis and modular integration with ground command.

- **Camera:** SIYI A8 Mini[7] with global shutter and HDR capability, mounted on a 3-axis gimbal for stabilisation. It is suitable for low-light, foggy, and dynamic conditions. Integration with ArduPilot[8] allows for camera pose logging, which can then be used for photogrammetric reconstruction. It fulfils requirements `USER-S-VIS-1.1, 2.3, 3.1` with regard to its resolution, field of view and speed. However, its operation temperature only goes down to -10°C, missing the -30°C operational requirement. Hence, a separate heater must be considered for it, leading to the rise of `USER-S-VIS-9.1`.
- **Lighting:** An integrated LED flash synchronised with the camera improves image contrast under dark or foggy conditions. It is lightweight, small and cheap, while providing ~ 150 lumens of brightness [9]
- **Onboard Computer:** NVIDIA Jetson Orin NX 16GB[10] (more than the 8GB mandated by `USER-S-ACC-4.1`), chosen for its CUDA-accelerated processing, TensorRT compatibility, and sufficient memory for heavy segmentation models.

Hence, the following breakdown is produced, aligning with the mass, power, and cost budgets

[7] https://shop.siyi.biz/products/siyi-a8-mini-gimbal-camera
[8] https://ardupilot.org/
[9] https://nl.aliexpress.com/item/1005003322811459.html
[10] https://www.nvidia.com/en-us/autonomous-machines/embedded-systems/jetson-orin/

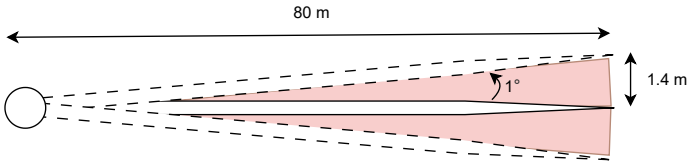

Figure 11.4: *Uncertainty propagation of wind turbine dimensions*

as prescribed in Chapter 5. The combined payload remains under 500 g and draws <30 W, ensuring compatibility with the design.

Table 11.1: *Computer vision module specifications*

Item	Dimensions [mm]	Mass [g]	Price [€]	Nominal power [W]
Camera + mounting	55 × 55 × 70	95	200	5
Light	68 × 50 × 49.5	81	30	2
Computer	69.6 × 45	300	600	25
Total		476	623	30

11.7. Limitations and recommendations *Edlyn*

A discussion with an engineer from SpectX Delft[11] highlighted the high risk of uncertainty in pose data. Considering that a wind turbine blade can be very long, even a 1° orientation deviation can result in a 1.4 m deviation at the tip of the blade, as illustrated in Figure 11.4. Thus, high-fidelity location and orientation data must be fused with image outputs to ensure centimetre-level targeting accuracy.

The main limitation of the current system lies in its dependence on accurate pose estimates from the GigaSLAM model. Misalignment between pose data and image timestamps can lead to incorrect targeting, and must be time synchronised to provide accurate data. Furthermore, the current model is decoupled from the control module, and relies on a ground station for de-icing planning. By decoupling the perception and actuation process, immediate spraying is traded-off for more robust resource management. Hence, the time synchronisation and accuracy must be validated in progressively realistic scenarios.

To address these issues, future development should focus on tighter integration between perception and control. This would allow real-time triggering of de-icing chemicals based on immediate CV feedback. These approaches are made feasible by the onboard computer's reserved capacity. Hence, in the design improvement phase of the system's future plans (Chapter 17), a real-time, closed-loop visual servoing system using onboard models to directly detect and spray ice will be implemented, eliminating the need for the current digital twin setup.

[11] https://www.spectx.nl/

12

Software and hardware integration

Edlyn, Josephine, Max

Visual tools are required for clear visualization of coupled and decoupled subsystems on the drone. This is a crucial step in systems integration. As such, the interfaces between different modules will be explained from a hardware perspective in Section 12.1, software in Figure 12.4, and communications perspective in Section 12.4.

12.1. Hardware integration

Josephine, Edlyn

The hardware diagram shows the architecture of the drone system. It is divided into a main module, de-icing module and camera module. Within each module different components are shown. The main module is the core of the drone, integrating most of the critical subsystems. It includes sensors, communication system, power & propulsion systems, the computer and the chemical system. The heat exchanger in the main module distributes thermal energy throughout the whole module and therefore shows no specific arrows, but the background of the module is given a light yellow colour, implying that it heats all components. The de-icing module is responsible for dispersing the chemicals during the de-icing operation. This is done via a physical connection between the chemical system in the main module. Lastly, the camera module is responsible for detecting and therefore visualising the ice coverage on the wind turbine. The camera module however, is attached to the main module, according to the drone's design, where the camera is attached to the main module

Furthermore, arrows indicate the relationships between blocks. Red dashed arrows indicate that a block provides power to another block. Blue line indicate that one block sends data to another block. Lastly, green dotted lines indicate that the block provides a physical input to another block, this can be for example de-icing chemicals or heat. This structure enables the drone to perform all its operations in an efficient and safe way.

12.2. Software integration

Edlyn

The software block diagram outlines the logical architecture of the drone system, particularly how different software modules interact with each other to perform a mission autonomously. The system is divided into two main components, the onboard and ground based modules. It also shows how physical agents interact with the software architecture. Hence, the software block diagram is included in Figure 12.2

The onboard computer runs on the Ubuntu 20.4[1] operating system. The main control system on the computer is the ArduPilot[2] autopilot, a widely adopted open-source software for UAVs, which manages core functionalities such as flight stabilization, waypoint navigation, and camera control. All of the computer vision models is implemented with Python packages including PyTorch and NumPy, optimized for GPU acceleration using CUDA[3]. The other embedded

[1] https://releases.ubuntu.com/focal/

[2] https://ardupilot.org/

[3] https://developer.nvidia.com/cuda-zone

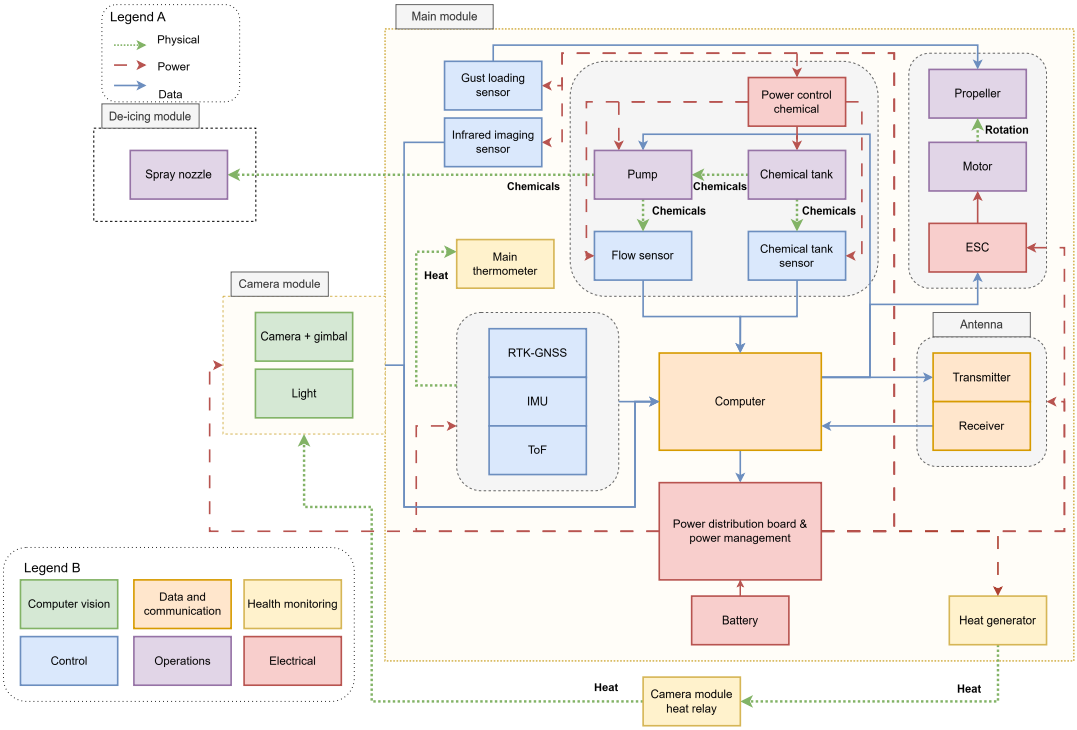

Figure 12.1: *Hardware block diagram*

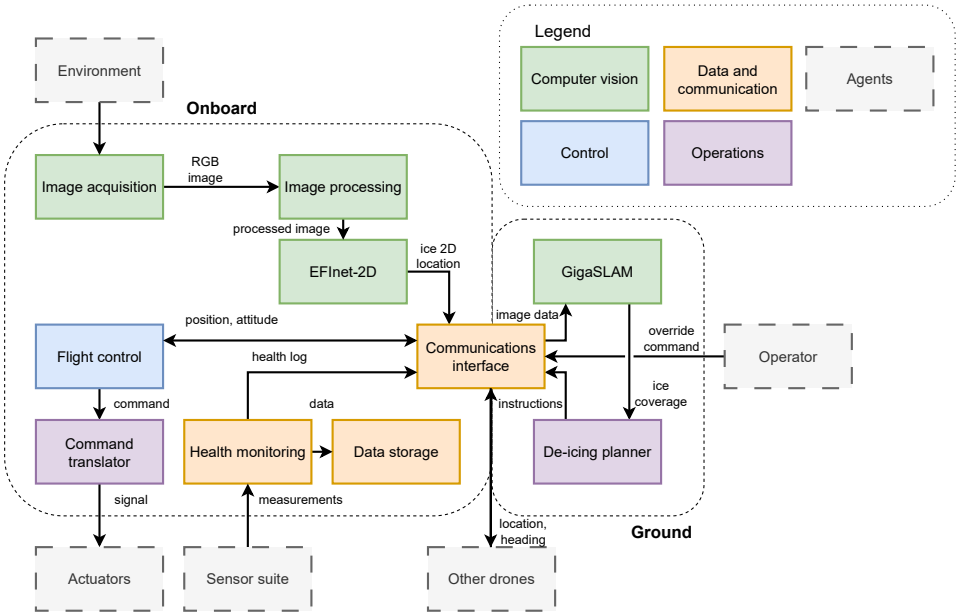

Figure 12.2: *Software block diagram*

systems function in C. On the ground station, a digital twin of the turbine is maintained using GigaSLAM (Chapter 11). This also integrates the de-icing planner, path-finding algorithms, and scheduling logic for coordinated swarm operation

The software architecture makes room for inputs and outputs. While each drone is capable of executing the mission independently, the system allows for human-in-the-loop intervention via override commands from the operator. Furthermore, communication between drones is conducted via FANET (Chapter 13). The command translator module bridges software and hardware by converting processed float outputs into discrete actuator-level control signals.

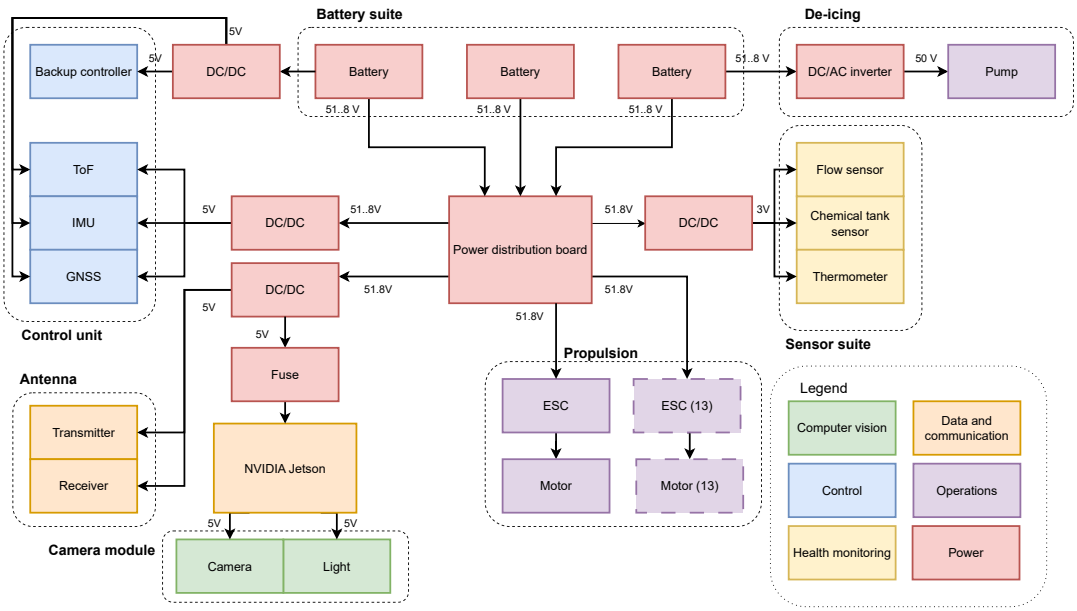

Figure 12.3: *Electric block diagram*

12.3. Electrical block diagram *Maxim, Edlyn*

The drone's electrical architecture is organised around four main components the power system, propulsion system, control sensors and health monitoring.

The power module consists of three different batteries connected in parallel. Each of these batteries produces an output voltage of 51.8V as stipulated in Chapter 5. The power distribution board then receives this voltage and distributes to the the different sections. The propulsion module is taken as part of the operations, getting power directly supplied by the power distribution board without the need of any conversion. Firstly, the power is delivered to the electronic speed controllers (ESCs) which is then used to determine the required voltage per motor. There is a total of 14 motors with their corresponding ESCs.

A voltage of 3V is allocated for health monitoring, requiring a DC to DC converter. A similar process is used for the control sensors. To protect the NVIDIA Jetson which is powered at 5V, a fuse has been placed as a fail safe mechanism. The NVIDIA Jetson then powers the camera and the camera light.

12.4. Data handling and communications *Edlyn*

The communication flow and data handling diagram presents a comprehensive flow of information through different software elements in the drone's system. It is centered around the onboard computer. This system manages both high-throughput and low-frequency data streams. The different arrows represent different data rates, ranging from 1 bps to >10 Mbps. There are six major modules in the aspect, which are computer vision, control, data and communication, operations, health monitoring and power. Each module performs specialized tasks while contributing to the system-wide perception-action loop necessary for autonomous de-icing. Hence, the diagram is given in Figure 12.4.

The primary functional chain in the system is ice detection and control. The CV inference initiates the loop.The rest of this chain is detailed in Chapter 11. EFInet-2D outputs the coordinates of ice within the frame of the picture, in a segmentation map (Float[224,224]). To map this into 3D coordinates on the wind turbine, the picture is transmitted to the ground

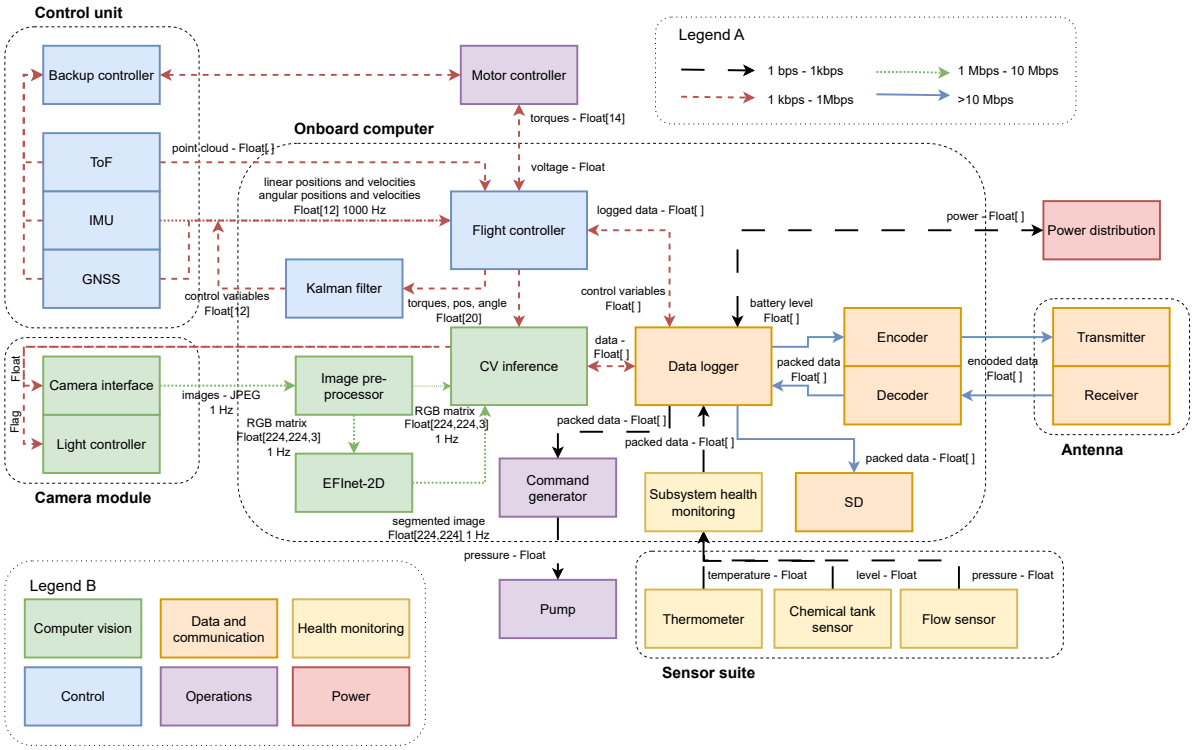

Figure 12.4: *Communication flow and data handling block diagrams*

station as detailed in . The speed of this loop is mostly governed by the output rate of the computer vision, which is estimated to be ~ 50 ms per image.

The control module is responsible for real-time state estimation and actuation. It takes inputs of location and orientation from sensors, and monitors for potential obstacles. A backup controller provides fault tolerance by enabling return-to-launch (RTL) protocols in the event of onboard computer failure, in line with `INS-M-SAFE-2.2`. This redundancy is critical for safety, particularly in autonomous or semi-supervised swarm operations.

The data and communication module handles external interfacing, sending, receiving and aggregating data. It should work at a very high rate for quick processing, and possibly handling large data, inline with `USER-S-COMM-1.1, 2.1, 3.1, 5.1`. The sensor data is managed by subsystem health monitoring, that can produce error messages if critical readings are obtained. All output from the sensors are backed up on an onboard SD unit, ensuring traceability.

13

Operations and logistics

Maxim, Josephine, Leonardo

This chapter details out the operational flow and the logistics of the drones mission. Section 13.1 describes operations in terms of mission stages, a block diagram is included for clarity. Moreover, Section 13.2 covers the logistics, detailing upon the battery operation, logistics plan, sensors in navigation and inter drone communication. Lastly, to get a better understanding of the drones operations, its functions are described in a functional flow and breakdown diagram in Section 13.4. Also, Table 13.1 gives a indication of the mission time for different phases of the drones flight time

Table 13.1: *Time indication for different mission steps*

Mission step	**Time (s)**
Horizontal transit to turbine	133
Vertical climb to inspection altitude	56
Ice detection	100
Chemical spray application	252
Post-deicing inspection	26
Decent to safe altitude	56
Horizontal transit to ground station	133
Total Time	**756**

The time estimates above are directly derived from Subsection 4.5.3 with the vertical and horizontal distances respectively (168m and 1000m) as well as the velocities (3m $s^{-}1$ and 7.5m $s^{-}1$)

13.1. Mission operation

Josephine,Leonardo

This section gives an outline of the full operational workflow. The process consists of several coordinated stages, starting with a mission request and ending with post-mission evaluation. Each stage is designed to ensure that the de-icing process is efficient, safe and specifically tailored to the conditions of the wind farm. An overview of the stages can be found in Figure 13.1.

S1 - Mission request

The mission starts by a specific wind turbine company requesting a de-icing operation as a consequence of having wind turbines operating in areas prone to ice storms, which can lead to losses in power output of the wind turbines or can affect the structure of the wind turbine. This step is considered external to our solution.

S2 - Mission Planning & Analytics

After receiving a request, the team will start gathering all the data needed to make an accurate flight plan. This includes ice coverage predictions, wind farm sizing, including the number of

wind turbines and the size of wind turbines and the supervisory control and data acquisition (SCADA) system. All these factors will ultimately lead to the optimum swarm size and the optimum amount of chemicals needed to remove all the ice. This modularity aspect of the swarm of drones is accounted for in the market analysis. In a mission setting this information is treated as a "mission plan"

S3 - Mobilisation

As soon as the mission plan is finished, a transportation logistics plan will be constructed specifying the amount of trucks and equipment needed in order to transport all the equipment. Moreover a truck based ground control station (GCS) carrying all of the drones, chemicals and servicing tools are dispatched to the turbine site. It is important to mention that the de-icing operation will start as soon as the meteorological icing is finished as stated in Subsection 2.1.2. A detailed plan on the path optimization from wind turbine to wind turbine is in Subsection 13.2.4.

S4 - Site Set-up & Pre-Flight

Upon arriving at the specific area assigned in the logistics plan, the drones will be mobilised. This consists of making sure all the drones are fully charged by checking their batteries. Next is loading de-icing fluid through a connection between the chemical and operations trucks. Other pre-flight checks will be performed including hardware, software, sensor and communication checks (INS-M-SAFE-2.3 The drone shall undergo a self-diagnostic check before each mission, completed in <30 seconds).

The preflight procedure includes the ground station providing turbine-specific geometry and orientation data such as: hub, height, blade angle and yaw position.

S5- Launch

When all drones are ready and pre-flights have been performed, the first wave of drones will autonomously take off and approach the respective blade section. Each drone has its designated section on the drone where two blades will have three drones operating on it at once and one will have two drones.

S6 - On-Blade ice mapping

As soon as all the drones are in the air and they have moved to their respective blade section, they will proceed to scan the blade with their RGB camera. Continuously, computer vision will be used to detect the ice coverage. Every drone will send their results of the computer vision on the ice coverage to the ground control station. The ground control will collect all the data and will make a prediction on how much chemicals are needed per section as a result of the ice coverage data. In addition, the ground control will create a digital twin of the wind turbines to making a de-icing plan to assess how the ice coverage is divided among the wind turbine. The digital twin will be used to make a de-icing plan.

S7 - Targeted spray application

In accordance with the ice map created during ice inspection, the drones will proceed to performing the de-icing operation. The payload system will be initialized by starting up the pump and continuously the chemicals will be sprayed on the respective wind turbine section.

S8 - Post-spray verification

After the drone is finished spraying the chemicals it carries, a second scanning operation is conducted during and after the spray application. This will result in new ice-maps. They will be compared to the ice-maps constructed before de-icing application to verify the success of the

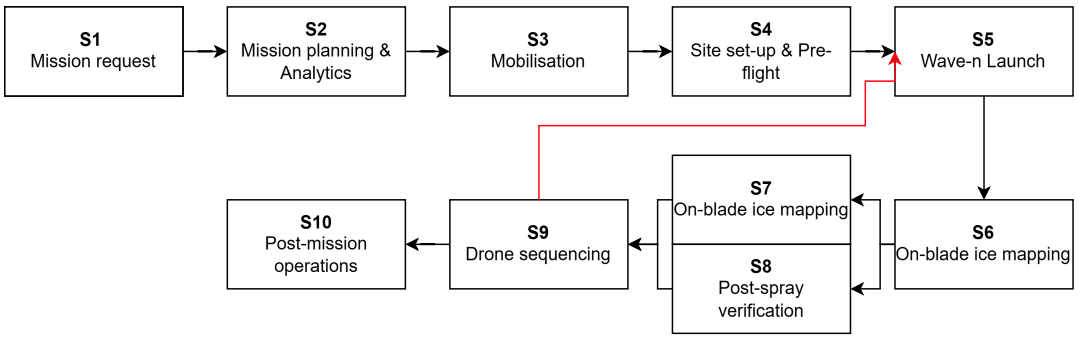

Figure 13.1: *Mission operation block diagram*

de-icing operation.

S9 - Drone sequencing

Additionally, two situations can occur after having performed the de-icing operation. The first situation is that the drone needed all their payload in order to perform the de-icing operation. In this case the drone will return back to the ground. On the ground an operator will switch the battery of the drone to recharge. Also, the operator will connect the tube coming from the truck with chemicals to the drone and continuously the drone will be refuelled with de-icing fluid. As soon as the drone is refuelled and recharged, it will take off again from the ground station platform to continue its de-icing plan.

The other situation would be that the drone is still left with an amount of chemicals after de-icing its assigned blade section. In order to perform the de-icing operation as efficient as possible the drone will have to move to another section according to the flight plan created by the digital twin on the blade where another drone is operating to 'help' de-icing. Since, it is a possibility that in the flight plan it is estimated that some blade section will need more chemicals to completely de-ice the section and some will need less. The drones will communicate with each other in order to not overlap spraying areas and to not crash into each other. Continuously, the drone will start performing the de-icing operation again on the other blade section. The drone will then also return to the ground station and will also recharge and refuel to go up again and continue the de-icing process according to the de-icing plan.

S10 - Post-Mission Operations

As soon as all ice is removed, the last wave of drones will return back to the ground station. Any required maintenance operations on the drones will be performed. Also, all data will uploaded and a performance report will be generated. This will be used to assess how the operations went and the data will be used in order to optimize consequent de-icing operations. An important function to note is the fact that the drone possesses a backup controller which connects to a battery when the main controller malfunctions. (INS-M-SAFE-2.2 All critical failures (propulsion, power, communication) shall trigger automated failsafe landing.)

13.2. Logistics

Josephine, Maxim, Leonardo

Moreover, this section will go over all the logistics considering the operation. This will be first explained in terms of the battery, then the ground station. Also, the sensors included in the drone related to the operations will be described and the section will end with an explanation on the inter drone communication architecture

13.2.1. Battery

In order to make the operation fast and smooth, the battery must be designed to allow for easy removal and assembly.

The handle located on top of the battery, will make it easy to lift up the battery and to reposition it. Moreover, it will make it easy to remove the battery once installed into the drone. This will allow for a quick switch in battery, once the battery has ran out, allowing the drone to continue its de icing mission with minimum time delay in switching battery.

The black lines on the side of the battery are the slot guides. These were integrated onto the battery in order to provide a way to secure the battery in place. They are designed to match the battery with the grooves located inside the drone.

Now taking a look at the back of the battery, it is important to have a latch system on the battery. This way even when the drone is tilting the chance of the battery slipping off is negligible. The battery will be equipment with a spring-loaded latch, the button on the back will trigger the switch mechanism so the battery can be securely fitted.

13.2.2. Charging station

In order to find the number of batteries needed per drone some calculations can be made. Each drone needs three 44,000mAh batteries to fly. By observing similar batteries, such as the ones used in the DJI Flycart 30 [1], the charging power of the batteries can be taken as approximately 5700W. For a first order estimate, it can then be assumed that a 44,000mAh, 51.8V battery takes 24 minutes ($(44\text{Ah} \cdot 51.8\text{V})/5700\text{W} \cdot 60\text{min} = 24\text{min}$) to recharge. Considering that the mission time of a drone is 13.6 minutes (see parameter 3.18 in Section A.1), each drone will fly two times before the first set is fully charged. Each drone, therefore, needs three sets of three batteries.

The required generator size is computed by multiplying the charging power (5700W) by the number of batteries charging at any given time. Since two sets of three batteries are charging for each of the 8 drones that brings the total to roughly 274kW. This can be achieved by using a D250 GC (60 Hz) Generator Set(250KW)[2]. As a first order estimate, the batteries can be charged for up to two times the length of the mission flight time of 13.6 minutes. Leaving 30 seconds to physically change the battery, the maximum charging time of a battery is 26 minutes. This reduces the required power draw to 5260W, bringing the total power required to just over 250kW. Thus, coming to the conclusion that one generator will be sufficient.

13.2.3. Ground station operations

Main truck

To ensure the delivery of all the necessary equipment to the wind turbine site efficiently, a transportation plan has been developed. To summarise, the items which have to be delivered to the site are:

- 8 unmanned aerial vehicles (UAVs)
- 72 high-capacity batteries
- 1 diesel generator

In order to complete this operation a large tilt trailer (90 m^3) from ENPEK will be used. The vehicle offers the following specifications, its dimensions are 13.6m x 2.4m x 2.7m and the load

[1] https://www.dji.com/ch/flycart-30/specs

[2] https://www.clevelandbrothers.com/products/106460-d250-gc

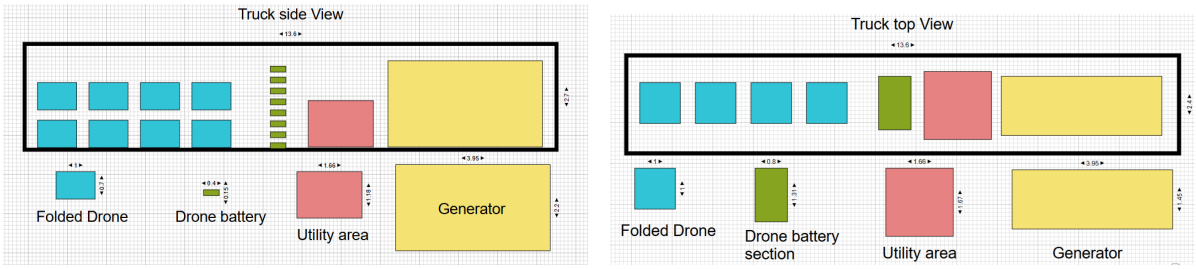

(a) *Truck side view* **(b)** *Truck top view*

Figure 13.2: *Side-by-side views of the truck*

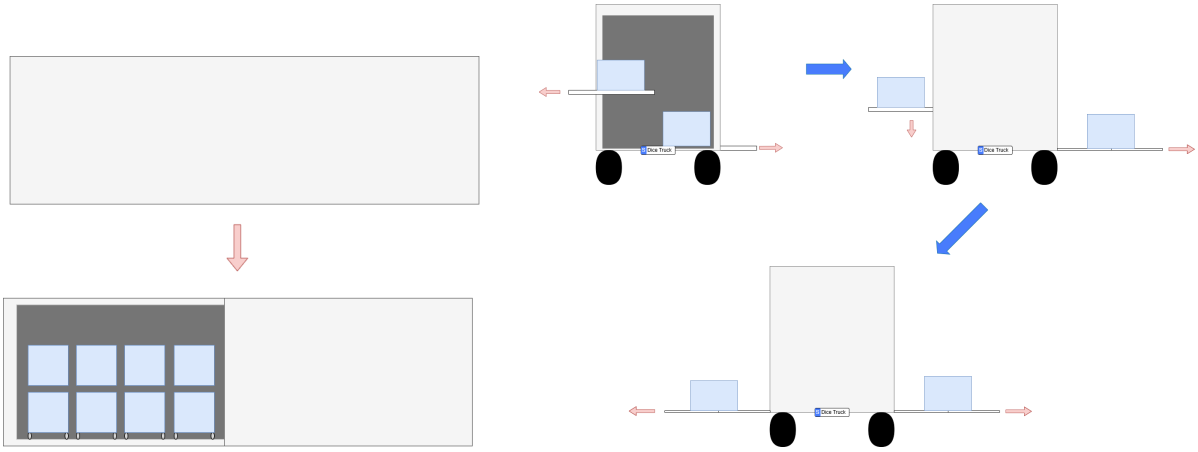

(a) *Sliding door side view of truck* **(b)** *Deployment of floor view from the back of truck*

Figure 13.3: *Truck deployment sequence, a) provides a aside view of the truck b) shows the truck from a back view*

capacity is 24 000 kg [3]. Taking into account both the volume and weight constraints of the truck, leads to the possible configuration shown in Figure 13.2a. The folded drone dimensions were taken from the design footprint. To account for the extra protective packaging, foam inserts will be added to provide safety. A margin of 20 mm to 30 mm will be added to each side, increasing the dimensions of the drone on all axes. This foam will also be applied to the drone batteries but on a smaller scale. However, the generator will not have any protective foam and is bolted to the ground below it. Also, space is allocated for the storage of extra components, maintenance tools, etc. The drones as demonstrated in Figure 13.2a are positioned on two separate elevated platforms. This arrangement prevents contact between drones and would simplify both loading and unloading procedures.

A maximum load check for 1 generator (3055 kg), 8 drones (100 kg each), and 72 batteries (10 kg each) is performed and leads to a total mass of 4575 kg, well below the 24 000 kg limit. Moreover, in order to provide a fast deployment time, the truck container will be equipped with a sliding door on the sides of the truck. This door will slide backwards, allowing clear access to the drone. Furthermore, the two separated floors for the drones mentioned previously will, in reality, function like a lift-gate. This lift gate will be supported by the sides of the truck and deploy the drones outward. This can be visualised in Figure 13.3. In order to account for the extra moment created by the drones extending outwards, both floors will be extended at the same time. An in-depth structural analysis of these lift gates will not be conducted, but Railgate Series Gate (n.d.) provides a similar solution and has a maximum capacity of 900 kg, which will easily surpass the needed requirement of 400 kg.

[3] https://www.enpeks.rs/truck-dimensions.html

(a) *Ground area next to wind turbine in Stor-Rotliden.* **(b)** *Same area with components marked.*

Figure 13.4: *Ground area next to wind turbine in Stor-Rotliden (images from Google Maps).*

Chemical truck
From the case study of Stor-Rotliden it was found that in order to de-ice the whole wind farm approximately 26000L of de-icing liquid would be needed. In order to transport all these liquid two Sinotruk Howo (20000L) trucks will be used. Using two smaller trucks makes it easier to navigate non-paved roads.

Ground station
It is worth noting how the ground station will be arranged near the wind turbine. It is important to investigate how all these truck will be able to fit next to the wind turbine. Again looking at Stor-Rotliden, using satellite images from google maps it can be seen that each turbine has a dedicated section. Exploring the most limiting one shown in Figure 13.4a. A sanity check will be performed to verify that all necessary components can fit within this area. The surface areas of the active components at the ground station are calculations can be found in Appendix B: Hence, the total area required by all components is

$$A_{\text{components}} = 137.36\,\text{m}^2 \ll A_{\text{site}} = 918\,\text{m}^2,$$

All components can comfortably fit within the available area. Even though it has been demonstrated that all the components could fit into the ground station. In order to provide a rapid operation time, the generators will stay within the truck. Then the truck container will be equipped with a sliding door so that the drone can be charged while the generators stays inside. The drone will be deployed with the lift gate system. A possible configuration of this is shown in Figure 13.4a.

13.2.4. Shortest path finder

In order to de-ice the wind turbines farm in the quickest way possible an optimal path must be determined. The goal is to find an efficient traversal method which ensures that each turbine is visited at least once.

To do this, graph theory would be used, where each road will be modelled as a node and the number of wind turbines on that road would be its corresponding weight. A "junction" node will be placed where these roads intersect and their weight will be set to zero. The algorithm's objective would be to minimise the total travel time which is directly correlated with the number of wind turbines it visits. Based on satellite data there are two possible starting points from the north of the park or the south of the park. Using a depth first search (DFS) algorithm ensuring that all turbines will be visited. The algorithm keeps count of the total cost of the travel, which will in turn help to provide a total time estimation for the task.

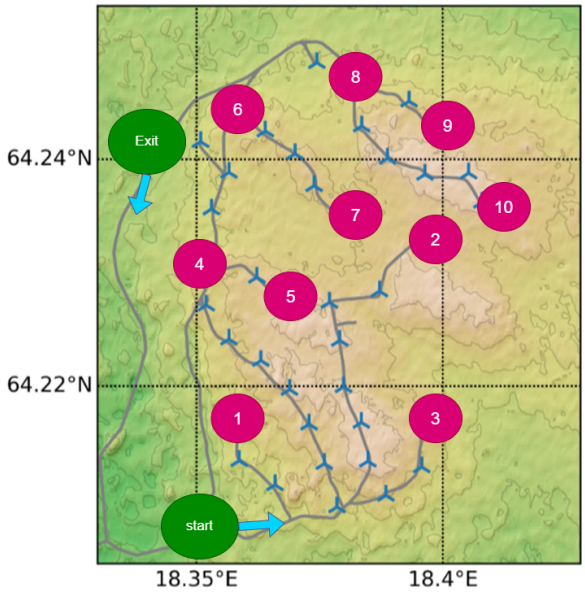

Figure 13.5: *Shortest path in order to vist all wind turbines*

The DFS was implemented onto the given graph using the networkx python library (Hagberg et al., 2008). The following results were then collected to create Figure 13.5, which will provide a more visual result. Where the number in the nodes represent the order and not the weight. The total cost generated by this path was 64. The mean distance between wind turbines is approximately $500m$ meaning that the total travelling distance in order to de-ice all the turbines will be $32km$, roughly translating to an hour of travel time (assuming a mean velocity of $30kph$). Moreover, the code is easily abatable so it can easily be changed for a new wind farm by modifying the coordinates and number of nodes/junctions.

13.2.5. Navigation sensors in operation

Important factors to be considered when the drones are in the air is that they must know their position accurately in order to accurately position themselves to de-ice the wind turbine properly. The RTK-GNSS in combination with the IMU-9DOF sensor will be the key players in defining the drones position accurately. The RKT-GNSS provides a centimeter level positioning and accuracy and therefore enables precise drone localization (USER-S-ACC-2.1, 2.2: Horizontal ±0.2 m and vertical ±0.1 m accuracy). The IMU sensors are responsible for measuring its attitude. It must ensure accurate attitude control for stable imaging and chemical spray alignment. Another important thing for the drone when it is manoeuvring through the air is that it must avoid bumping into the wind turbine, other drones or other obstacles. This is important in order to avoid damage on the wind turbine as well as on the drone itself. The Time-of-flight (ToF) sensors are responsible for this and will provide short-range obstacle detection. 20 ToF sensors will work in parallel to make sure they will cover the whole drone in performing obstacle detection. Five sensors will be placed on each side of the drone. Since the time-of-flight sensors have a field of view of 27 degrees and a maximum range of four meters [4], this number of sensors is chosen for the drone to perform 360°horizontal obstacle detection (PUBL-M-SAFE-2.3 The drone shall feature horizontal 360° obstacle detection within a 3-meter range.).

13.2.6. Inter drone communication

Since the chosen design will consist of a swarm of drones, an important aspect is how the drones will communicate with each other. After performing a literature search on how drones in a

[4]https://www.st.com/resource/en/datasheet/vl53l1x.pdf

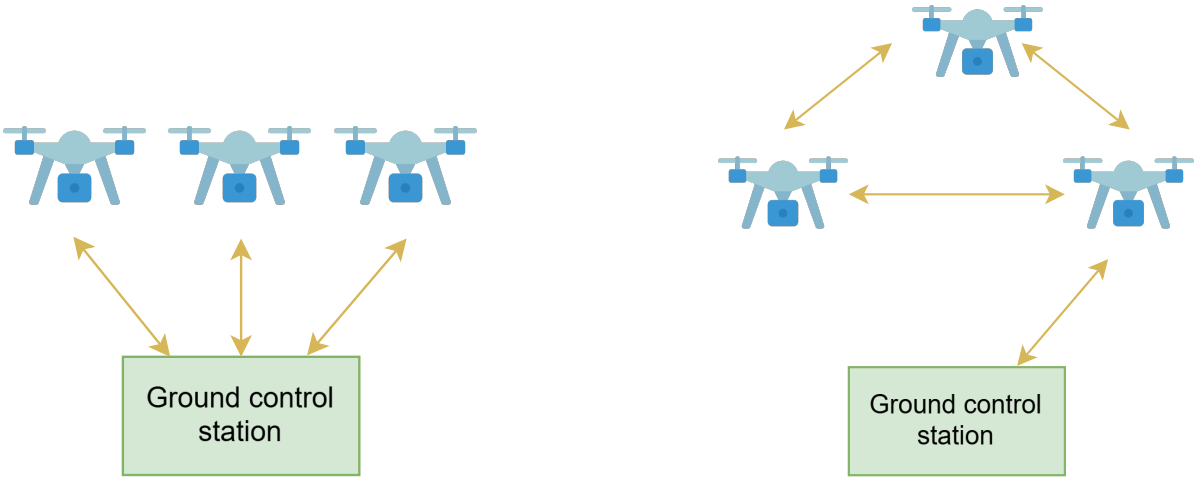

(a) *Infrastructure based architecture* **(b)** *FANET based architecture*

Figure 13.6: *Two situations for communication architecture of drone swarm*

swarm typically communicate, it became clear that mainly two types of architecture can be used (Campion et al., 2018). The first type is an infrastructure-based architecture and is visualised in Figure 13.6a. A ground control station is present to receive telemetry information from all the drones in the swarm and send commands back to each UAV. Using this type of architecture will make the drone semi-autonomous as the drones are fully reliant on a ground control. Additionally, since this type of communicating architecture is dependent on a ground control station it will cause a lack of system redundancy. In case of failure to any operations of the ground control station the whole swarm of drones will be affected. Additionally the operation area is limited to the communication coverage of the infrastructure. Also, there will be a lack of distributed decision making. The second type of communication architecture is using a flying ad-hoc network architecture (FANET) (Bekmezci et al., 2013) and is visualised in Figure 13.6b. This architecture works by every drone being part of a communication network. This network will allow real-time UAV-to-UAV and UAV-to-GROUND communication. In this architecture, nodes are dynamically assigned and reassigned based on dynamic routing algorithms. In this way a subset of the drones can communicate with the ground control station, while all drones constitute an ad hoc network (Bekmezci et al., 2013). Consequently, the UAVs can communicate with each other and the ground control station. The main advantages of using this architecture includes a distributed decision making and it will provide redundancy in the communication network. Also, another advantage of this method is that nodes can join and leave the network dynamically, which increases the scalability of the swarm.

Since, scalability is an important aspect of the project, since it is required to be able to decide the optimum amount of drones within the swarms based on the specific mission, the FANET option is the preferred choice to be used as the communication infrastructure. Also, the fact that FANET will provide redundancy in the communication infrastructure is very beneficial. Therefore, FANET will be used as the communication infrastructure in the swarm of drones. As stated by Bekmezci et al. (2013), in order to incorporate FANET accurately into the drones, they must be equipped with a GNSS and IMU sensors to communicate its position accurately to the other drones in the network. Since these are also the sensors chosen for the position determination, FANET will be sufficient to implement. The ground control will be mainly used to assess ice coverage data from all the drones and communicate that with the drones in the network as stated earlier. The UAV-to-UAV communication will be important for the drones to avoid moving into each other and to avoid disrupting each others path.

13.3. Digital twin strategy *Michal*

As mentioned in Section 11.5, the computer vision module, combined with a SLAM algorithm is used to build a digital twin of the wind turbine. A digital twin (Allen, 2021) is a reduced order digital counterpart of a real life system that can be used for process optimization, design exploration, and predictions amongst other things. Here, the digital twin will mainly be used for drone routing although it opens the doors to many more opportunities in the future. Firstly, it is necessary to understand the components of the digital twin.

Firstly, to model the wind turbine as a reduced-order system, each blade (since those, and not the hub, are of interest) is modelled as 10 sections (this is selected as an early estimate that balances resolution with computational complexity). Each section is defined by its centroid (x_i, y_i, z_i) and area in m^2. Furthermore, as explained in Section 11.5 each section (or node) is assigned a value from 0 to 100 representing the icing coverage. Knowing the effective spraying rate Subsection 4.5.8, translating the icing coverage into a time necessary to de-ice is trivial. In addition, the origin of the wind turbine is stored as a point (x_0, y_0, z_o) in the SLAM map. Therefore, the position of each section of the wind turbine is known in the SLAM map as well. The last missing piece is the position of the ground station. By definition this one is known or can relatively easily be measured either by GNSS or simply by logging the drone position when it is at the ground station. The next step is routing.

13.3.1. Drone routing

The goal of drone routing is to determine the path that each drone should take (taking into account constraints such as battery life or spraying time) such that the makespan (the longest flight time) of all drones is minimized. This is a k-TSP problem, also called a multiple travelling salesman problem. There exist various options to solve it. One possible and popular way to solve such problem is through the use of a Guided Local Search, or GLS for short, metaheuristic [5] algorithm. GLS algorithms combine a local search with a penalty system that allows them to escape local optima and approach the global optimum. One implementation is through Google's OR-Tools [6]. Figure 13.7 shows the most important parts of a GLS algorithm. Starting from a greedy [7] seed, the optimizer minimizes the cost function (the length of the makespan as mentioned before) by performing various operations on nodes such as swapping routes and others, until it reaches a global optimum. A classical gradient descent would stop here, however, the GLS algorithm modifies the gradient by searching for the most costly arcs (also called features) and punishing them, making them appear less optimal. As such, a new gradient is observed and the optimiser can continue further. This loop of punishment and optimisation is continued until a set timer lapses or a number of loops is reached. The output of this is a sequence of points that each drone must follow and the expect time it will take them. With this, the ice perception module provides actionable data and forms a complete perception-action loop.

Limitations and further work

Certainly, there are a number of limitation to this method. Here is a list of limitation and possible solution to be implemented in a future stage.

- The current method (see Figure 13.8 and Figure 13.9) exists only in 2D although making it 3D appears to be trivial.
- Implementing a check for de-icing fluid usage is likewise simply the addition of one more dimension of constraints and is relatively simple.

[5] https://en.wikipedia.org/wiki/Metaheuristic
[6] https://developers.google.com/optimization?hl=fr
[7] https://en.wikipedia.org/wiki/Greedy_algorithm

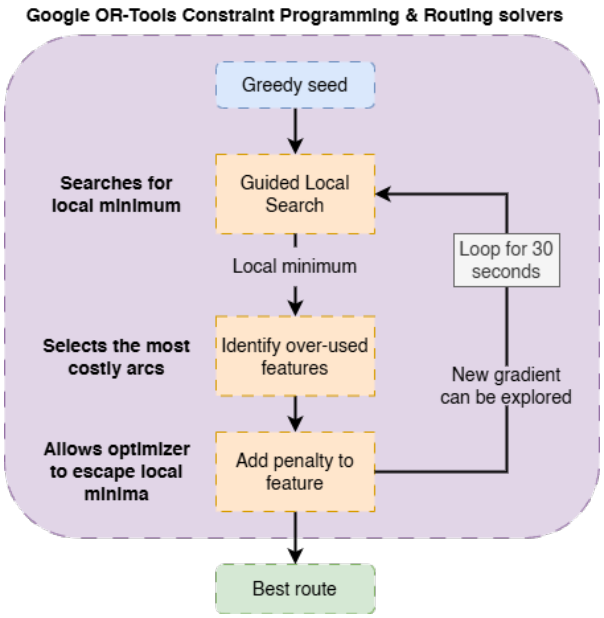

Figure 13.7: *Main route optimisation steps implemented using Google's OR-Tools. Guided Local Search allows the optimiser to escape local optima.*

- A structure that will allow the drones to refuel is considered too and is expected to be implementable in the short term through the use of internal methods in OR-Tools.
- Implementing collision avoidance in routing is slightly more complicated. One possible solution to prevent collision is to block any two drones from passing at the same turbine in a given time frame, say 30 seconds. This reduces (although it does not fully prevent the risk of a collision).

13.4. Functional overview of drone system *Josephine*

Another clear way of representing the operation of the system is by showing the functions the drone must perform throughout its lifecycle. This is crucial for understanding how different subsystems interact and to visualise the operational flow of the drones. Additionally, the functional diagrams helped identify parallel processes, iterative loops, and conditional behaviours. This can be done in two ways

First, by representing the functions in a functional flow diagram, we describe the logical order and interdependencies of the functions that need to be performed. The functional flow diagram first shows, on a high level, the mission phases and continuously breaks these down into detailed subfunctions. Additionally, it details the functions that will be performed for every mission phase. The mission phase starts by designing the actual drone and ends with its decommission phase. What can also be noticed in the diagram is that, mainly in the operation phase, functions will be performed in parallel. This is indicated by an AND block. Also, it could be the case that within a subfunction, the next function could have two possibilities, based on a specific condition. This is indicated with an OR block, and the specific condition is specified in the arrows. Also, it can be the case that after performing a specific function, the drone will have to iterate back to a previous function. In this case, the specific number of the function is represented in a block. Colours are used to indicate function hierarchy levels. Furthermore, each block includes the specific subsystem or hardware responsible for executing the function

Secondly, the functional breakdown structure shows a hierarchical representation of the functions and therefore does not represent a specific order of the functions. The functions

are consistent with the functional flow diagram. Again, the mission phases are shown on the highest level, and the tree flows down to all the specific functions required in each phase.

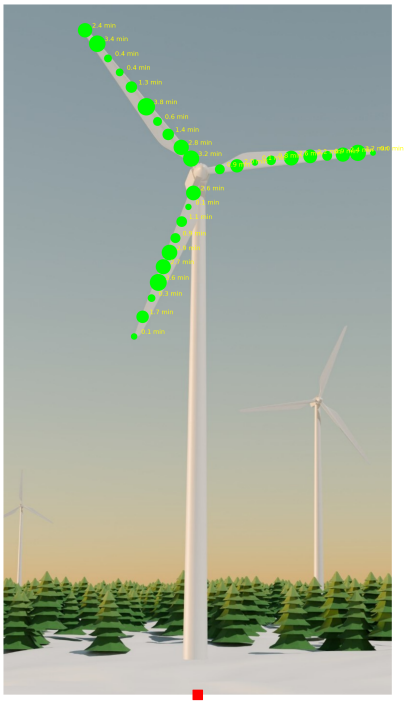

Figure 13.8: *Wind turbine digital twin showing a random icing pattern. The size of the green nodes is proportional to the icing fraction. The yellow text is the estimated service time.*

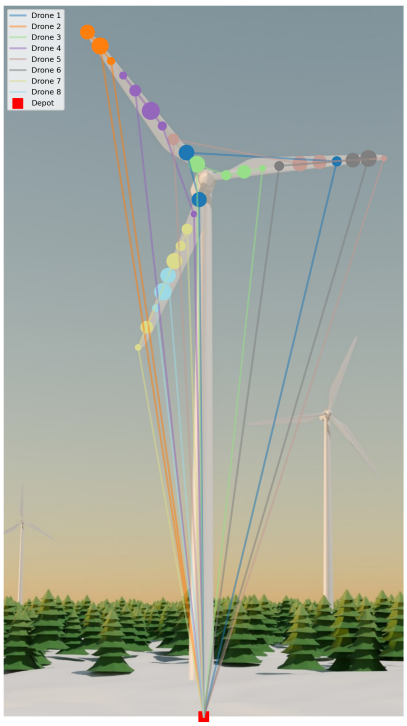

Figure 13.9: *Optimal drone routes overlaid over a wind turbine image. Each colour represents the path of one drone. The red square is the depot from which all the drones start.*

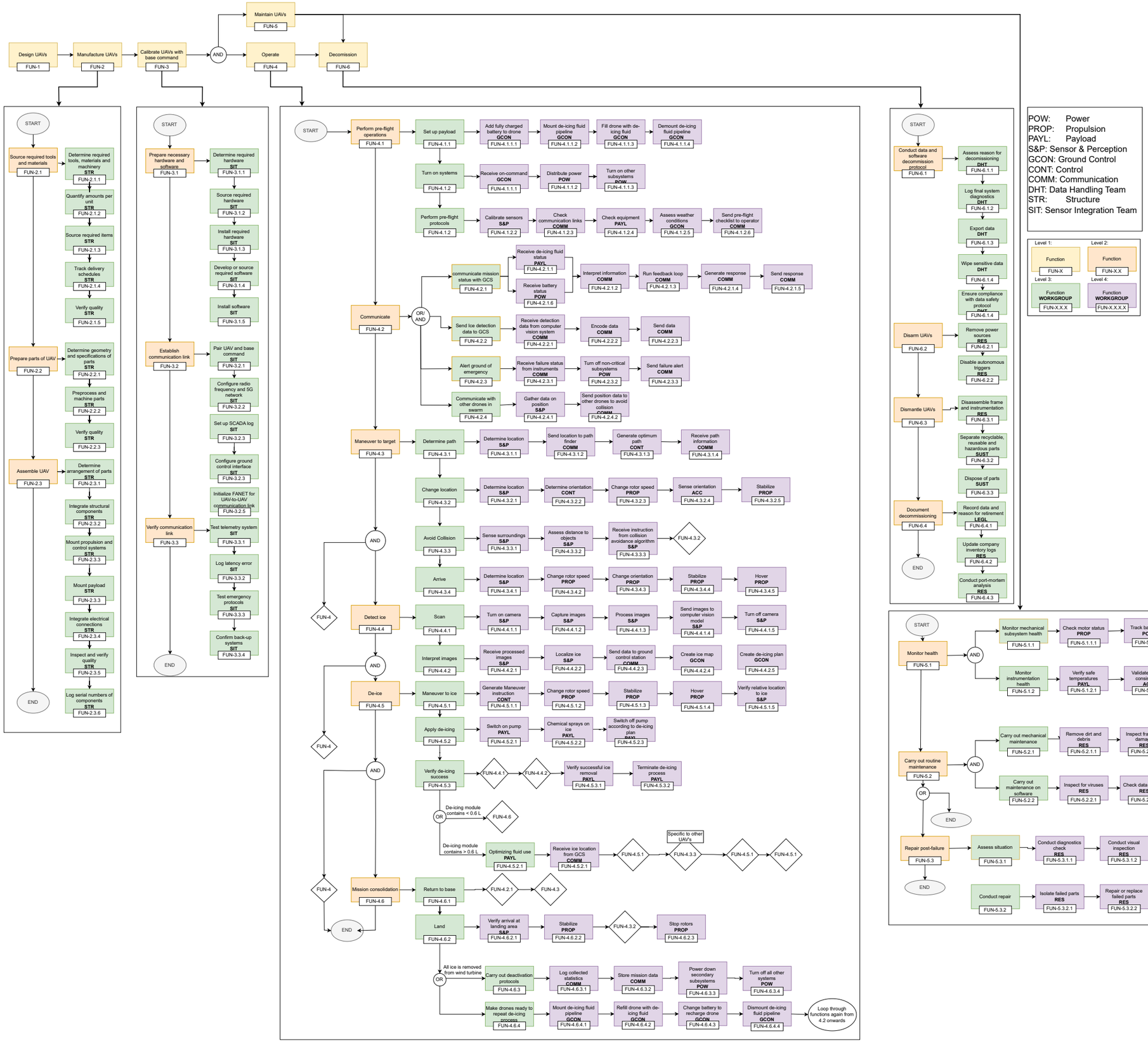
Maintain UAVs
FUN-5
Design UAVs
FUN-1
Manufacture UAVs
FUN-2
Calibrate UAVs with base command
FUN-3
AND
Operate
FUN-4
Decomission
FUN-6
START
Source required tools and materials
FUN-2.1
Determine required tools, materials and machinery
STR
FUN-2.1.1
Quantify amounts per unit
STR
FUN-2.1.2
Source required items
STR
FUN-2.1.3
Track delivery schedules
STR
FUN-2.1.4
Verify quality
STR
FUN-2.1.5
Prepare parts of UAV
FUN-2.2
Determine geometry and specifications of parts
STR
FUN-2.2.1
Preprocess and machine parts
STR
FUN-2.2.2
Verify quality
STR
FUN-2.2.3
Assemble UAV
FUN-2.3
Determine arrangement of parts
STR
FUN-2.3.1
Integrate structural components
STR
FUN-2.3.2
Mount propulsion and control systems
STR
FUN-2.3.3
Integrate electrical connections
STR
FUN-2.3.4
Inspect and verify quality
STR
FUN-2.3.5
Log serial numbers of components
STR
FUN-2.3.6
END
START
Prepare necessary hardware and software
FUN-3.1
Determine required hardware
SIT
FUN-3.1.1
Source required hardware
SIT
FUN-3.1.2
Install required hardware
SIT
FUN-3.1.3
Develop or source required software
SIT
FUN-3.1.4
Install software
SIT
FUN-3.1.5
Establish communication link
FUN-3.2
Pair UAV and base command
SIT
FUN-3.2.1
Configure radio frequency and 5G network
SIT
FUN-3.2.2
Set up SCADA log
SIT
FUN-3.2.3
Configure ground control interface
SIT
FUN-3.2.3
Initialize FANET for UAV-to-UAV communication link
FUN-3.2.5
Verify communication link
FUN-3.3
Test telemetry system
SIT
FUN-3.3.1
Log latency error
SIT
FUN-3.3.2
Test emergency protocols
SIT
FUN-3.3.3
Confirm back-up systems
SIT
FUN-3.3.4
END
START
Perform pre-flight operations
FUN-4.1
Set up payload
FUN-4.1.1
Add fully charged battery to drone
GCON
FUN-4.1.1.1
Mount de-icing fluid pipeline
GCON
FUN-4.1.1.2
Fill drone with de-icing fluid
GCON
FUN-4.1.1.3
Demount de-icing fluid pipeline
GCON
FUN-4.1.1.4
Turn on systems
FUN-4.1.2
Receive on-command
GCON
FUN-4.1.1.1
Distribute power
POW
FUN-4.1.1.2
Turn on other subsystems
POW
FUN-4.1.1.3
Perform pre-flight protocols
FUN-4.1.2
Calibrate sensors
S&P
FUN-4.1.2.2
Check communication links
COMM
FUN-4.1.2.3
Check equipment
PAYL
FUN-4.1.2.4
Assess weather conditions
GCON
FUN-4.1.2.5
Send pre-flight checklist to operator
COMM
FUN-4.1.2.6
Communicate
FUN-4.2
OR/ AND
communicate mission status with GCS
SIT
FUN-4.2.1
Receive de-icing fluid status
PAYL
FUN-4.2.1.1
Receive battery status
POW
FUN-4.2.1.6
Interpret information
COMM
FUN-4.2.1.2
Run feedback loop
COMM
FUN-4.2.1.3
Generate response
COMM
FUN-4.2.1.4
Send response
COMM
FUN-4.2.1.5
Send Ice detection data to GCS
FUN-4.2.2
Receive detection data from computer vision system
COMM
FUN-4.2.2.1
Encode data
COMM
FUN-4.2.2.2
Send data
COMM
FUN-4.2.2.3
Alert ground of emergency
FUN-4.2.3
Receive failure status from instruments
COMM
FUN-4.2.3.1
Turn off non-critical subsystems
POW
FUN-4.2.3.2
Send failure alert
COMM
FUN-4.2.3.3
Communicate with other drones in swarm
FUN-4.2.4
Gather data on position
S&P
FUN-4.2.4.1
Send position data to other drones to avoid collision
COMM
FUN-4.2.4.2
Maneuver to target
FUN-4.3
Determine path
FUN-4.3.1
Determine location
S&P
FUN-4.3.1.1
Send location to path finder
COMM
FUN-4.3.1.2
Generate optimum path
CONT
FUN-4.3.1.3
Receive path information
COMM
FUN-4.3.1.4
Change location
FUN-4.3.2
Determine location
S&P
FUN-4.3.2.1
Determine orientation
CONT
FUN-4.3.2.2
Change rotor speed
PROP
FUN-4.3.2.3
Sense orientation
ACC
FUN-4.3.2.4
Stabilize
PROP
FUN-4.3.2.5
AND
Avoid Collision
FUN-4.3.3
Sense surroundings
S&P
FUN-4.3.3.1
Assess distance to objects
S&P
FUN-4.3.3.2
Receive instruction from collision avoidance algorithm
S&P
FUN-4.3.3.3
FUN-4.3.2
Arrive
FUN-4.3.4
Determine location
S&P
FUN-4.3.4.1
Change rotor speed
PROP
FUN-4.3.4.2
Change orientation
PROP
FUN-4.3.4.3
Stabilize
PROP
FUN-4.3.4.4
Hover
PROP
FUN-4.3.4.5
FUN-4
Detect ice
FUN-4.4
Scan
FUN-4.4.1
Turn on camera
S&P
FUN-4.4.1.1
Capture images
S&P
FUN-4.4.1.2
Process images
S&P
FUN-4.4.1.3
Send images to computer vision model
S&P
FUN-4.4.1.4
Turn off camera
S&P
FUN-4.4.1.5
AND
Interpret images
FUN-4.4.2
Receive processed images
S&P
FUN-4.4.2.1
Localize ice
S&P
FUN-4.4.2.2
Send data to ground control station
COMM
FUN-4.4.2.3
Create ice map
GCON
FUN-4.4.2.4
Create de-icing plan
GCON
FUN-4.4.2.5
De-ice
FUN-4.5
Maneuver to ice
FUN-4.5.1
Generate Maneuver instruction
CONT
FUN-4.5.1.1
Change rotor speed
PROP
FUN-4.5.1.2
Stabilize
PROP
FUN-4.5.1.3
Hover
PROP
FUN-4.5.1.4
Verify relative location to ice
S&P
FUN-4.5.1.5
Apply de-icing
FUN-4.5.2
Switch on pump
PAYL
FUN-4.5.2.1
Chemical sprays on ice
PAYL
FUN-4.5.2.2
Switch off pump according to de-icing plan
PAYL
FUN-4.5.2.3
FUN-4
AND
Verify de-icing success
FUN-4.5.3
FUN-4.4.1
FUN-4.4.2
Verify successful ice removal
PAYL
FUN-4.5.3.1
Terminate de-icing process
PAYL
FUN-4.5.3.2
OR
De-icing module contains < 0.6 L
FUN-4.6
De-icing module contains > 0.6 L
Optimizing fluid use
PAYL
FUN-4.5.2.1
Receive ice location from GCS
COMM
FUN-4.5.2.1
FUN-4.5.1
Specific to other UAV's
FUN-4.3.3
FUN-4.5.1
FUN-4.5.1
FUN-4
Mission consolidation
FUN-4.6
Return to base
FUN-4.6.1
FUN-4.2.1
FUN-4.3
END
Land
FUN-4.6.2
Verify arrival at landing area
S&P
FUN-4.6.2.1
Stabilize
PROP
FUN-4.6.2.2
FUN-4.3.2
Stop rotors
PROP
FUN-4.6.2.3
All ice is removed from wind turbine
OR
Carry out deactivation protocols
FUN-4.6.3
Log collected statistics
COMM
FUN-4.6.3.1
Store mission data
COMM
FUN-4.6.3.2
Power down secondary subsystems
POW
FUN-4.6.3.3
Turn off all other systems
POW
FUN-4.6.3.4
Make drones ready to repeat de-icing process
FUN-4.6.4
Mount de-icing fluid pipeline
GCON
FUN-4.6.4.1
Refill drone with de-icing fluid
GCON
FUN-4.6.4.2
Change battery to recharge drone
GCON
FUN-4.6.4.3
Dismount de-icing fluid pipeline
GCON
FUN-4.6.4.4
Loop through functions again from 4.2 onwards
START
Conduct data and software decommission protocol
FUN-6.1
Assess reason for decomissioning
DHT
FUN-6.1.1
Log final system diagnostics
DHT
FUN-6.1.2
Export data
DHT
FUN-6.1.3
Wipe sensitive data
DHT
FUN-6.1.4
Ensure compliance with data safety protocol
DHT
FUN-6.1.4
Disarm UAVs
FUN-6.2
Remove power sources
RES
FUN-6.2.1
Disable autonomous triggers
RES
FUN-6.2.2
Dismantle UAVs
FUN-6.3
Disassemble frame and instrumentation
RES
FUN-6.3.1
Separate recyclable, reusable and hazardous parts
SUST
FUN-6.3.2
Dispose of parts
SUST
FUN-6.3.3
Document decommissioning
FUN-6.4
Record data and reason for retirement
LEGL
FUN-6.4.1
Update company inventory logs
RES
FUN-6.4.2
Conduct port-mortem analysis
RES
FUN-6.4.3
END
POW: Power
PROP: Propulsion
PAYL: Payload
S&P: Sensor & Perception
GCON: Ground Control
CONT: Control
COMM: Communication
DHT: Data Handling Team
STR: Structure
SIT: Sensor Integration Team
Level 1:
Function
FUN-X
Level 2:
Function
FUN-X.X
Level 3:
Function
WORKGROUP
FUN-X.X.X
Level 4:
Function
WORKGROUP
FUN-X.X.X.X
START
Monitor health
FUN-5.1
AND
Monitor mechanical subsystem health
FUN-5.1.1
Check motor status
PROP
FUN-5.1.1.1
Track battery life
POW
FUN-5.1.1.2
Detect overheating
PROP
FUN-5.1.1.3
Check battery health
POW
FUN-5.1.1.4
Detect performance decrease in rotor
PROP
FUN-5.1.1.4
Communicate health status
COMM
FUN-5.1.1.5
Monitor instrumentation health
FUN-5.1.2
Verify safe temperatures
PAYL
FUN-5.1.2.1
Validate sensor consistency
ACC
FUN-5.1.2.2
Validate sensor accuracy
ACC
FUN-5.1.2.3
Check de-icing liquid levels
PAYL
FUN-5.1.2.4
Monitor de-icing performance
PAYL
FUN-5.1.2.5
Communicate status
COMM
FUN-5.1.2.6
Carry out routine maintenance
FUN-5.2
AND
Carry out mechanical maintenance
FUN-5.2.1
Remove dirt and debris
RES
FUN-5.2.1.1
Inspect frame for damage
RES
FUN-5.2.2.2
Lubricate moving joints
RES
FUN-5.2.2.3
Replace worn out parts
RES
FUN-5.2.2.4
Tighten fasteners
RES
FUN-6.2.5
Use cleaning agents on sensitive parts
RES
FUN-6.2.6
Recalibrate instrumentation
RES
FUN-6.2.6
Log maintenance information
RES
FUN-6.2.6
Carry out maintenance on software
FUN-5.2.2
Inspect for viruses
RES
FUN-5.2.2.1
Check data storage
RES
FUN-5.2.2.2
Export data to base server
RES
FUN-5.2.2.3
Update software
RES
FUN-5.2.2.4
Verify integration with updated software
RES
FUN-6.2.5
OR
END
Repair post-failure
FUN-5.3
Assess situation
FUN-5.3.1
Conduct diagnostics check
RES
FUN-5.3.1.1
Conduct visual inspection
RES
FUN-5.3.1.2
Determine failed parts
RES
FUN-5.3.1.3
Assess severity
RES
FUN-5.3.1.4
END
Conduct repair
FUN-5.3.2
Isolate failed parts
RES
FUN-5.3.2.1
Repair or replace failed parts
RES
FUN-5.3.2.2
Recalibrate repaired systems
RES
FUN-5.3.2.3
Update maintenance log
RES
FUN-5.3.2.4

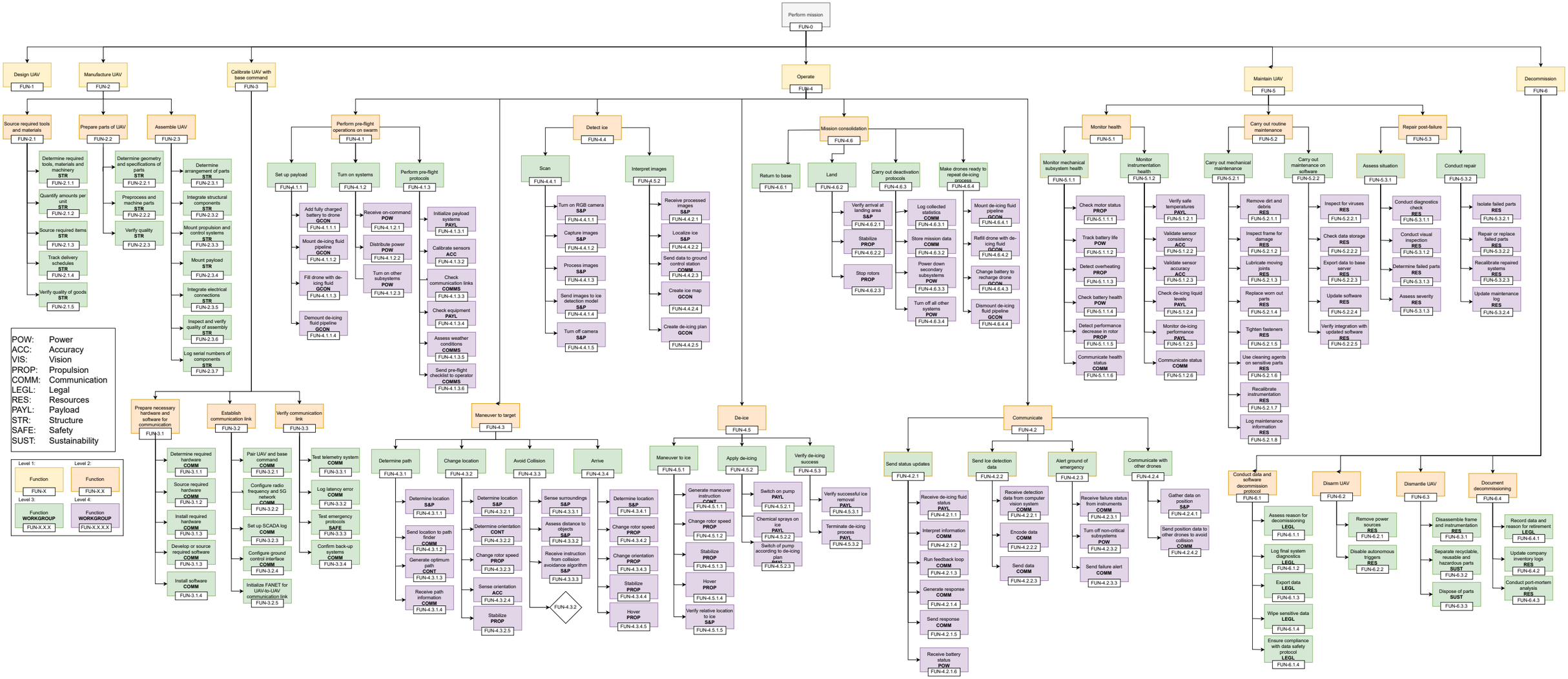
Perform mission
FUN-0
Design UAV
FUN-1
Manufacture UAV
FUN-2
Calibrate UAV with base command
FUN-3
Operate
FUN-4
Maintain UAV
FUN-5
Decommission
FUN-6
Source required tools and materials
FUN-2.1
Prepare parts of UAV
FUN-2.2
Assemble UAV
FUN-2.3
Determine required tools, materials and machinery STR
FUN-2.1.1
Quantify amounts per unit STR
FUN-2.1.2
Source required items STR
FUN-2.1.3
Track delivery schedules STR
FUN-2.1.4
Verify quality of goods STR
FUN-2.1.5
Determine geometry and specifications of parts STR
FUN-2.2.1
Preprocess and machine parts STR
FUN-2.2.2
Verify quality STR
FUN-2.2.3
Determine arrangement of parts STR
FUN-2.3.1
Integrate structural components STR
FUN-2.3.2
Mount propulsion and control systems STR
FUN-2.3.3
Mount payload STR
FUN-2.3.4
Integrate electrical connections STR
FUN-2.3.5
Inspect and verify quality of assembly STR
FUN-2.3.6
Log serial numbers of components STR
FUN-2.3.7
POW: Power
ACC: Accuracy
VIS: Vision
PROP: Propulsion
COMM: Communication
LEGL: Legal
RES: Resources
PAYL: Payload
STR: Structure
SAFE: Safety
SUST: Sustainability
Level 1:
Function
FUN-X
Level 2:
Function
FUN-X.X
Level 3:
Function WORKGROUP
FUN-X.X.X
Level 4:
Function WORKGROUP
FUN-X.X.X.X
Perform pre-flight operations on swarm
FUN-4.1
Set up payload
FUN-4.1.1
Turn on systems
FUN-4.1.2
Perform pre-flight protocols
FUN-4.1.3
Add fully charged battery to drone GCON
FUN-4.1.1.1
Mount de-icing fluid pipeline GCON
FUN-4.1.1.2
Fill drone with de-icing fluid GCON
FUN-4.1.1.3
Demount de-icing fluid pipeline GCON
FUN-4.1.1.4
Receive on-command POW
FUN-4.1.2.1
Distribute power POW
FUN-4.1.2.2
Turn on other subsystems POW
FUN-4.1.2.3
Initialize payload systems PAYL
FUN-4.1.3.1
Calibrate sensors ACC
FUN-4.1.3.2
Check communication links COMMS
FUN-4.1.3.3
Check equipment PAYL
FUN-4.1.3.4
Assess weather conditions COMMS
FUN-4.1.3.5
Send pre-flight checklist to operator COMMS
FUN-4.1.3.6
Detect ice
FUN-4.4
Scan
FUN-4.4.1
Interpret images
FUN-4.4.2
Turn on RGB camera S&P
FUN-4.4.1.1
Capture images S&P
FUN-4.4.1.2
Process images S&P
FUN-4.4.1.3
Send images to ice detection model S&P
FUN-4.4.1.4
Turn off camera S&P
FUN-4.4.1.5
Receive processed images S&P
FUN-4.4.2.1
Localize ice S&P
FUN-4.4.2.2
Send data to ground control station COMM
FUN-4.4.2.3
Create ice map GCON
FUN-4.4.2.4
Create de-icing plan GCON
FUN-4.4.2.5
Mission consolidation
FUN-4.6
Return to base
FUN-4.6.1
Land
FUN-4.6.2
Carry out deactivation protocols
FUN-4.6.3
Make drones ready to repeat de-icing process
FUN-4.6.4
Verify arrival at landing area S&P
FUN-4.6.2.1
Stabilize PROP
FUN-4.6.2.2
Stop rotors PROP
FUN-4.6.2.3
Log collected statistics COMM
FUN-4.6.3.1
Store mission data COMM
FUN-4.6.3.2
Power down secondary subsystems POW
FUN-4.6.3.3
Turn off all other systems POW
FUN-4.6.3.4
Mount de-icing fluid pipeline GCON
FUN-4.6.4.1
Refill drone with de-icing fluid GCON
FUN-4.6.4.2
Change battery to recharge drone GCON
FUN-4.6.4.3
Dismount de-icing fluid pipeline GCON
FUN-4.6.4.4
Monitor health
FUN-5.1
Carry out routine maintenance
FUN-5.2
Repair post-failure
FUN-5.3
Monitor mechanical subsystem health
FUN-5.1.1
Monitor instrumentation health
FUN-5.1.2
Carry out mechanical maintenance
FUN-5.2.1
Carry out maintenance on software
FUN-5.2.2
Assess situation
FUN-5.3.1
Conduct repair
FUN-5.3.2
Check motor status PROP
FUN-5.1.1.1
Track battery life POW
FUN-5.1.1.2
Detect overheating PROP
FUN-5.1.1.3
Check battery health POW
FUN-5.1.1.4
Detect performance decrease in rotor PROP
FUN-5.1.1.5
Communicate health status COMM
FUN-5.1.1.6
Verify safe temperatures PAYL
FUN-5.1.2.1
Validate sensor consistency ACC
FUN-5.1.2.2
Validate sensor accuracy ACC
FUN-5.1.2.3
Check de-icing liquid levels PAYL
FUN-5.1.2.4
Monitor de-icing performance PAYL
FUN-5.1.2.5
Communicate status COMM
FUN-5.1.2.6
Remove dirt and debris RES
FUN-5.2.1.1
Inspect frame for damage RES
FUN-5.2.1.2
Lubricate moving joints RES
FUN-5.2.1.3
Replace worn out parts RES
FUN-5.2.1.4
Tighten fasteners RES
FUN-5.2.1.5
Use cleaning agents on sensitive parts RES
FUN-5.2.1.6
Recalibrate instrumentation RES
FUN-5.2.1.7
Log maintenance information RES
FUN-5.2.1.8
Inspect for viruses RES
FUN-5.2.2.1
Check data storage RES
FUN-5.2.2.2
Export data to base server RES
FUN-5.2.2.3
Update software RES
FUN-5.2.2.4
Verify integration with updated software RES
FUN-5.2.2.5
Conduct diagnostics check RES
FUN-5.3.1.1
Conduct visual inspection RES
FUN-5.3.1.2
Determine failed parts RES
FUN-5.3.1.3
Assess severity RES
FUN-5.3.1.3
Isolate failed parts RES
FUN-5.3.2.1
Repair or replace failed parts RES
FUN-5.3.2.2
Recalibrate repaired systems RES
FUN-5.3.2.3
Update maintenance log RES
FUN-5.3.2.4
Prepare necessary hardware and software for communication
FUN-3.1
Establish communication link
FUN-3.2
Verify communication link
FUN-3.3
Determine required hardware COMM
FUN-3.1.1
Source required hardware COMM
FUN-3.1.2
Install required hardware COMM
FUN-3.1.3
Develop or source required software COMM
FUN-3.1.3
Install software COMM
FUN-3.1.4
Pair UAV and base command COMM
FUN-3.2.1
Configure radio frequency and 5G network COMM
FUN-3.2.2
Set up SCADA log COMM
FUN-3.2.3
Configure ground control interface COMM
FUN-3.2.4
Initialize FANET for UAV-to-UAV communication link
FUN-3.2.5
Test telemetry system COMM
FUN-3.3.1
Log latency error COMM
FUN-3.3.2
Test emergency protocols SAFE
FUN-3.3.3
Confirm back-up systems COMM
FUN-3.3.4
Maneuver to target
FUN-4.3
Determine path
FUN-4.3.1
Change location
FUN-4.3.2
Avoid Collision
FUN-4.3.3
Arrive
FUN-4.3.4
Determine location S&P
FUN-4.3.1.1
Send location to path finder COMM
FUN-4.3.1.2
Generate optimum path CONT
FUN-4.3.1.3
Receive path information COMM
FUN-4.3.1.4
Determine location S&P
FUN-4.3.2.1
Determine orientation CONT
FUN-4.3.2.2
Change rotor speed PROP
FUN-4.3.2.3
Sense orientation ACC
FUN-4.3.2.4
Stabilize PROP
FUN-4.3.2.5
Sense surroundings S&P
FUN-4.3.3.1
Assess distance to objects S&P
FUN-4.3.3.2
Receive instruction from collision avoidance algorithm S&P
FUN-4.3.3.3
FUN-4.3.2
Determine location S&P
FUN-4.3.4.1
Change rotor speed PROP
FUN-4.3.4.2
Change orientation PROP
FUN-4.3.4.3
Stabilize PROP
FUN-4.3.4.4
Hover PROP
FUN-4.3.4.5
De-ice
FUN-4.5
Maneuver to ice
FUN-4.5.1
Apply de-icing
FUN-4.5.2
Verify de-icing success
FUN-4.5.3
Generate maneuver instruction CONT
FUN-4.5.1.1
Change rotor speed PROP
FUN-4.5.1.2
Stabilize PROP
FUN-4.5.1.3
Hover PROP
FUN-4.5.1.4
Verify relative location to ice S&P
FUN-4.5.1.5
Switch on pump PAYL
FUN-4.5.2.1
Chemical sprays on ice PAYL
FUN-4.5.2.2
Switch of pump according to de-icing plan PAYL
FUN-4.5.2.3
Verify successful ice removal PAYL
FUN-4.5.3.1
Terminate de-icing process PAYL
FUN-4.5.3.2
Communicate
FUN-4.2
Send status updates
FUN-4.2.1
Send Ice detection data
FUN-4.2.2
Alert ground of emergency
FUN-4.2.3
Communicate with other drones
FUN-4.2.4
Receive de-icing fluid status PAYL
FUN-4.2.1.1
Interpret information COMM
FUN-4.2.1.2
Run feedback loop COMM
FUN-4.2.1.3
Generate response COMM
FUN-4.2.1.4
Send response COMM
FUN-4.2.1.5
Receive battery status POW
FUN-4.2.1.6
Receive detection data from computer vision system COMM
FUN-4.2.2.1
Encode data COMM
FUN-4.2.2.2
Send data COMM
FUN-4.2.2.3
Receive failure status from instruments COMM
FUN-4.2.3.1
Turn off non-critical subsystems POW
FUN-4.2.3.2
Send failure alert COMM
FUN-4.2.3.3
Gather data on position S&P
FUN-4.2.4.1
Send position data to other drones to avoid collision COMM
FUN-4.2.4.2
Conduct data and software decommission protocol
FUN-6.1
Disarm UAV
FUN-6.2
Dismantle UAV
FUN-6.3
Document decommissioning
FUN-6.4
Assess reason for decomissioning LEGL
FUN-6.1.1
Log final system diagnostics LEGL
FUN-6.1.2
Export data LEGL
FUN-6.1.3
Wipe sensitive data LEGL
FUN-6.1.4
Ensure compliance with data safety protocol LEGL
FUN-6.1.4
Remove power sources RES
FUN-6.2.1
Disable autonomous triggers RES
FUN-6.2.2
Disassemble frame and instrumentation RES
FUN-6.3.1
Separate recyclable, reusable and hazardous parts SUST
FUN-6.3.2
Dispose of parts SUST
FUN-6.3.3
Record data and reason for retirement LEGL
FUN-6.4.1
Update company inventory logs RES
FUN-6.4.2
Conduct port-mortem analysis RES
FUN-6.4.3

Part IV:

Vol. 4 | Performance, Testing & Verification

14

Verification & validation

Patryk

Verification and validation of the design is a vital step towards proving the validity of the design. The procedure follows a V-shape framework for V&V, as previously planned in the midterm report. In Section 14.1, the verification of software, models, and systems is discussed, in Section 14.2, validation of the model and system is developed and in Section 14.3, the tests for verification and validation are created.

14.1. Verification

Patryk

The purpose of establishing a comprehensive verification strategy is to ensure that the system meets the required capabilities. This section focuses on verifying that all the requirements specified for the mission are complied with. In Subsection 14.1.1 the code verification is conducted and in Subsection 14.1.2 the sensitivity analysis is performed.

14.1.1. Model and code verification

During the design process, multiple models were developed for the aircraft and its subsystems. These models were mostly developed using computational methods specified in programming languages. To ensure the high quality of the models, the accuracy of the code needs to be verified. The verification of the models is carried out in three ways: unit testing, system integration testing, and sensitivity analysis.

Code verification

The code is verified in a bottom-up manner. The process begins with unit testing of the most fundamental functions of the software and is followed by higher levels of system integration until a full software integration test. The unit tests are conducted using separate functions of the code, where an input is run through the function and the output is compared against the expected result. A similar testing structure is used in the integration tests, but the inputs are run through multiple functions and the final output is compared with the expected result. By testing each elementary function and their integration at different levels, a comprehensive verification of the code can be established. In the V&V Appendix C, Table C.1 provides a compliance matrix for the unit tests, and Table C.2 demonstrates a compliance matrix for the specified system and corresponding integration tests. Also in Appendix C, Table C.3 shows that the unit testing conducted for the software comprehensively verifies the functionality of the code by examining the coverage of unit tests across the entire code domain tested by that file.

Sensitivity analysis

During design, some parameters for the systems are defined, but it is not true that those are the definite values for the final design. They can vary slightly due to uncertainties of assumptions made, models developed, or manufacturability within precision. Another issue is that the design might need to be altered slightly in the future due to stakeholder needs evolving.

For this reason, an important verification step to consider is the sensitivity of the design. By varying the most important parameters for each model, the sensitivity of each model and its

accuracy can be obtained. For all subsystems for which models were developed, such sensitivity analysis was conducted.

For drone sizing, the sensitivity analysis can be found in Subsection 5.2.5, for aeroacoustic design in Section 8.7, and for the flight dynamics model in Section 10.2. From drone sizing analysis, it can be observed that the main independent variables of flight time and payload mass influence greatly the required battery capacity, weight and the number of rotors required. The design possesses a limit of how much the flight time or payload mass can be changed for a suitable configuration to be developed. This means, as mentioned in Subsection 5.2.5, that when tweaking the parameters of design, the limits of the drone need to be considered carefully.

The noise map model sensitivity analysis shows that changing important parameters still produces accurate results. Varying the weighing matrices of the controller of flight dynamics resulted in large sensitivity of the Q and R matrices. As mentioned in Section 10.2, increasing the R weights leads to slower responses to disturbances and small rate of changes in thrust. Altering Q weights influences how quickly and using what state variables the system responds to disturbances. The sensitivity analysis of control shows that it is vital to fine-tune the gain weighing matrices for ensuring smooth and robust response to disturbances.

During the feasibility study of the design, a financial model was established for planning out operations. The model had also a sensitivity analysis developed, which can be seen in detail in Subsection A.0.1. From this analysis, it can be concluded that every variable used in modelling, when varied, causes a significant change in the profit margins. From this fact, it can be said that the choice of the financial model for operations has to be chosen with much consideration and high confidence. Failing to meet the operational goals can lead to large malperformance of the mission.

14.1.2. System verification

In order to ensure that the system performs within expected capabilities, the system must meet all requirements. At this stage of the project, compliance with multiple requirements can be verified, but the verification of some requirements requires the development of a prototype. Therefore, some requirements have verification plans and procedures developed for them. There are four methods of verification used to verify compliance with the requirements: Inspection, Analysis, Demonstration, and Test.

Inspection is used when compliance can be determined through simple qualitative observation of the system. Analysis is conducted when the system must be verified with either theoretical calculation or derivation. Demonstration is a less formal way of showing the capabilities of the system with some non-rigorous measurements. A test is a formal demonstration, where many variables need to be controlled and precise measurements taken.

During the design process, the analysis is conducted primarily. Inspection can be performed on subsystems or the integrated system after prototype development. Demonstrations and test require a prototype and testing campaigns for the prototype, they are developed in Section 14.3

The verification procedures and requirement compliance for each of the requirements (shown in Appendix D) were collected into Tables C.4 through C.6, which are located in Appendix C. The requirement ID is given in the first column, followed by the type of verification and the verification strategies performed for each requirement. The tables also indicate whether the requirements are met by the current design and if verification has already been conducted. All cases of non-compliance are discussed in detail, while for the cases that lack of verification stem from the previously mentioned early stage of the project, when no prototype was available for testing.

The non-compliance of requirements is caused by the early stage of the project, which makes it

impossible to determine if the product will comply with some requirements in the future. One group of such requirements are those that need operational data to verify their compliance, such as USER-M-SAFE-2.1, USER-M-SUST-3.1 and USER-M-SAFE-2.2. To quantify the performance of the actual design on those requirements, statistical data from the mission operations is needed.

Non-compliance is also caused by the fact that there is no satisfactory documentation made at the design stage of the project, as for requirements ENV-M-SUST-3.2, MANU-S-STR-4.3 and ACIN-S-COMM-4.1. Those documents are planned to be developed when the design is more converged and ready for production.

Another such issue is produced by requirement USER-M-LEGL-3.1, which requires compliance with EASA regulations, but under conditions of "Specific" category, the regulations are very specific to the design. This makes the process of certification pushed back to the later stages of design.

For requirements EMPL-M-RES-2.1 and EMPL-M-RES-2.2, a customer is required along with a business projection, compliance cannot be decided until the operation phase. The last group of requirements are USER-M-SAFE-2.2 and USER-S-ACC-2.1, which point currently not implemented autonomous navigation and obstacle avoidance control systems.

14.2. Validation *Patryk*

Validation confirms that the system meets stakeholder goals in real-world use and answers the broader question of whether the right system has been built to satisfy stakeholder needs and mission objectives. This section outlines the project's comprehensive validation strategy and activities currently undertaken for model validation. In Subsection 14.2.1 the models built for design are validated and in Subsection 14.2.2, the system developed is validated against stakeholder needs.

14.2.1. Model validation

In order to develop the design of the system, several models were used to approximate drone's parameters. The models are built on analytical or numerical methods that are established using assumptions. It is vital to validate both the models and assumptions on which the models are based. Extensive validation shows that, assumptions are good approximations of the real world and the models are accurate in comparison to higher fidelity models. The models which need to be validated are the drone sizing estimation, noise model and drone flight dynamics model.

Drone sizing

The model used for drone sizing is based on statistical and analytical methods. In order to use analytical formulas for sizing components, some assumptions are necessary to be introduced first. For the structure that integrates the components, rigid body mechanics are assumed. This is a valid assumption due to the fact that conservative values of mass and size are taken using safety factors. An assumption made for the battery sizing is that the battery sizing follows the Peukert's Law as stated by Galushkin et al. (2020). Peukert's law is a good approximation at high discharge currents; therefore, it is a valid assumption. A limitation of this method is that it is simplified to be temperature invariant. Another assumption taken is that the thrust of rotors that are coaxial is reduced by 15% in comparison to separate rotors (Tamburrini et al., 2024).

The sizing of the drone is validated by developing component geometries through CAD modelling and analysing loads on the structure through FEM. CAD modelling validates the component size and mass calculations. This allows to remove the rigid body simplification in order to analyse structure deflections. Implementing CFD calculations on the coaxial rotors would allow validation of the thrust loss assumption. At the current stage of the design, CAD

modelling was conducted for shape validation. For future project development it is planned to conduct FEM calculations on the drone structure and CFD on lifting surfaces.

Noise model
For creation of a noise map, Xrotor the open source program was used. The method and it's limitations are extensively explained in Chapter 8. In simplified terms the Xrotor method focuses on estimating the noise caused by a singular rotor under a fixed wing configuration, rather than the integrated drone system. Therefore, the main assumption taken for use of this model is that the main influence for noise is caused by rotors and neglect the effect from the orientation of the motor. The interference with drone structure and spraying noise are also neglected.

The method of validation for the Xrotor method is explained extensively in Section 8.4, using the analytical formula of far-field theory. In future project development it is aimed to conduct higher fidelity model validation through creating a full system CFD analysis and eventually a more robust noise prediction for the prototype during operation.

Drone flight control
To model the dynamics of the model, a linearized version of equations of motion based on Newtonian mechanics and Euler's law of rotation was chosen, as shown in Equation 10.2 from Chapter 10. This is considered a valid assumption for the intended operation case (hover), as justified by Heng et al. (2015).

In order to validate the use of the model discussed in Section 10.2 for the chosen mission profile, several assumptions need to be made. First assumptions are related to the flight conditions. Due to the flight profile being performed in level hover and close to the Earth surface, than a flat Earth and small aircraft angles assumptions can be made. For the purpose of control analysis, the drone is considered as a rigid body. The deflections found in the structural analysis in Chapter 7 do not require a different assumption. For short time period stability analysis, the aircraft is assumed to have constant mass. From these assumptions, it follows that the aircraft has constant drag and moment coefficients. For the controller design, the delay in information transfer between sensors and actuators is neglected. The noise from the sensors is modelled as Gaussian white noise.

In order to validate the model itself, a higher fidelity model needs to be developed. The most relevant simplifications to be removed during validation processes would be: treating the drone as a LTI system and modelling sensors as controller measurements with added white noise. This would result in a non-linear model of drone dynamics with proper sensor data introduced for error estimation. Due to time constraints, this validation method was not conducted, therefore it is postponed to later stages of the design. Comparing against such model at hover trim point would result in an accurate analytical validation method. Furthermore, once a prototype is developed, the control and stability behaviour can be measured and assessed with the model used for simulating the control of the system.

14.2.2. System validation
The system and all of its integrated sub-assemblies need to evaluated to determine whether they fulfil the stakeholder needs and mission objectives. In order to demonstrate that the finished drone system is able to satisfy stakeholders, several testing strategies need to be developed.

Mission-level validation
For safety requirements, a field trial can be conducted under real wind and icing conditions, monitored by safety observers using a checklist. To validate deployment efficiency, a simulated setup, deployment, and mission execution from the ground station to task completion can be conducted. The planned mission profile of the drone can also be submitted for review by a

certified UAV expert, EASA regulatory experts, or wind turbine companies to get a professional opinion, ensuring legality in European airspace.

Subsystem-level validation
This section validates that each core subsystem complies with the stakeholder requirements determined in the previous chapters. The aerodynamics of the drone can be simulated and tested to validate the operational requirements set initially. These include the payload the drone can carry and the endurance of the aircraft.

Environmental validation
The conditions in which the drone will perform its de-icing task are harsh; thus, validation is key, especially in offshore and winter environments. A cold test can be performed on the fully built drone structure using the climate chamber facility at the Netherlands Aerospace Centre (NLR). Wind tests can also be conducted on the drone structure to validate its stability under wind conditions. This can be done using the Low Speed Wind Tunnel facility at TU Delft. For environmental validation of the drone structure, a humidity test can additionally be performed to simulate fog conditions using the facilities at NLR (Arendsen & Centre, 2024).

Stakeholder-aligned validation
The following methods can be used for validation of business and regulatory goals. Market research analysts can be contacted to assess project feasibility and returns for stakeholders. Moreover, financial predictive models based on service revenue, maintenance costs, and deployment savings can be used to calculate the return on investment (ROI). A regulatory readiness review can be performed to align the design with the EASA Specific Operations Risk Assessment framework and confirm regulatory compliance.

14.3. Testing campaign *Patryk*

The V&V testing should be conducted such that separate unit tests can be conducted simultaneously, optimising testing cost and time. This section focuses on developing testing campaigns for an optimal testing strategy. Inspection activities are the easiest to fit into any type of testing done, as most of the time they include very quick and qualitative measurements of mission performance. Therefore, those would be introduced into tests of the prototype. For activities involving document inspection, this would be done by the compliance engineer in the design certification stage. Detailed financial analysis and compliance with regulation analysis will be performed as the design enters the preproduction stages.

In the project development timeline it is planned to develop a testing prototype, after finalised design and before entering production. The need for verifying the capabilities of the drone and validating the design creates a need for the development of physical prototype testing in the future of the project. It is considered in low detail, due to the maturity of the design. The testing plan follows the same structure as all of the verification and validation procedures, going from the detail into a more integrated architecture.

14.3.1. Module tests
Some of the functions performed by the done can be tested within smaller modules. The tests that mostly related to subsystem requirements on functionality and performance. The modules are created using systems performing a certain capability. These modules are:

- Power module - system relating to power storage and distribution.
- Control module - system responsible for flight manoeuvring and state control of all the subsystems.

- Vision module - system responsible for detecting ice.
- Propulsion module - system responsible for torque generation.
- Communication module - system responsible for the transfer of information between systems.
- Structure module - system responsible for load-bearing capabilities of aircraft.
- De-icing module - system responsible for the de-icing of wind turbines.

Those modules can allow for testing of respective subsystem requirements specified in Table C.4 - C.6. In this way, by integrating the modules for higher-level integration requirement testing, the concept of the design is validated. Using the separate modules, the assumptions used for modelling can be validated on real-world data. Some of the tests conducted for validation of modules relate to stakeholder requirements. For vision module requirement `USER-S-VIS-2.1` states that 95% of ice needs to be detected. In communication module requirement `ENV-M-SUST-2.6` creates a need for possible over-the-air updates. Lastly, in de-icing module `USER-S-PAYL-3.1` requires for 90% of ice removal. Testing such real-life operational capabilities of the system's modules acts as a validation to the stakeholders of the design meeting their needs. The final test conducted after the theoretical design process closure is building a flying prototype. This prototype would be the integration of all the systems in a way that they are supposed to interact. Creating such a system allows for validating the product with real-world performance data. This test also allows for demonstration to the stakeholders to account for their possibility in changing requirements.

14.3.2. Testing cost

As with any part of a design project, it is important to consider the costs of verification and validation. The costs mainly vary between V&V stages. The cost is assessed mostly in the price of testing and the time taken for testing. For software verification, the only cost present is the high amount of time that is required to test the software, due to student labour not incurring any costs. Test development is the most time-consuming component of that process. It can be approximated as around 10 hours per module. Modelling and analysis tests also do not come with any financial cost, but rather a development time cost. Another time commitment is validating the assumptions made for the model through analysis of model, its assumptions and comparison to a high-fidelity model or a test. For this task has varying time-commitments depending on subsystem tested. Testing developed for after the project design stage is not time-relevant as much as cost-relevant. This is because the design team is not involved in building the prototype in the future. According to the requirement `INV-M-RES-1.1`, the prototype development cost shall not exceed 500000€ (FY2025). This target is treated as the budget for developing all the module tests, including those of less project integration. Another cost to consider is the cost of testing facilities of NLR's climate chamber (Arendsen & Centre, 2024) and wind tunnel at TU Delft for environmental validation. Due to the collaboration of TU Delft with NLR and between faculties, the cost of testing facilities might be reduced, but should still be considered for the prototype testing plan.

15

Risk assessment

Maxim, Likun

Risks are one of the most important factors to understand during the design process, as even a small but likely risk with serious consequences can alter the final design and might lead to the failure of the entire mission. Therefore, it is essential to conduct a thorough risk assessment prior to the detailed design and operation phases, to ensure mature preparation and minimise the impact of potential risks on the final outcome.

In this chapter, the risk assessment from the previous report is revisited. First, in Section 15.1, the criteria for risk assessment are defined, including the fundamental concepts and the methodology applied in the subsequent analysis. Next, Section 15.2 presents a detailed evaluation of the potential risks associated with each subsystem and operation with different colour codes. This section also assesses the likelihood and consequence of each risk, which may influence key design decisions. Subsection 15.2.1 outlines the mitigation strategies, contingency plans, and potential design impacts for the previously identified risks, besides a second evaluation of likelihood and consequence demonstrates how the mitigation measures alter the risk profile. Finally, in Subsection 15.2.2, two two-dimensional matrix maps are shown to provide an better overall visualization of risk likelihood versus consequence.

15.1. Risk assessment criteria definition

Maxim, Likun

To provide a standardized evaluation of different risks, the risk assessment criteria must be predefined. These criteria will primarily cover two key aspects to quantify the risks. First, the likelihood of risk occurrence will be assessed and categorized into five levels, ranging from 0% to 100%, as shown below:

- **Very Low:** $P < 5\%$
- **Low:** $5\% \leq P < 20\%$
- **Moderate:** $20\% \leq P < 50\%$
- **High:** $50\% \leq P < 80\%$
- **Very High:** $P > 80\%$

Secondly, the consequence of each risk event is quantified using qualitative levels that describe the extent to which project performance may be affected:

- **Insignificant:** No real operational impact, at most a minor inconvenience.
- **Marginal:** Minor technical performance degradation or only a secondary mission objective is affected.
- **Moderate:** Noticeable but still manageable, reduction in technical performance.
- **Critical:** The perform ability of the primary mission is questionable.
- **Catastrophic:** Mission failure or significant non-achievement of performance requirements.

Using these two dimensional assessment the risk statements can be clearly structured that specify the failures to meet the project's functional goals or performance requirements. Each

risk statement is scored against both scales, resulting in a two dimensional risk matrix which will be discussed in Section 15.2.

15.2. Subsystem and operational risks assessment *Maxim, Likun*

In a bottom-up design process, the development always starts with subsystem design. In this case, eight different subsystems have been considered, including de-icing, payload, structural, aerodynamics, propulsion, power, control, and manufacturing. Each of these subsystems carries potential risks during the design phase. Table 15.1 lists all technical risk statements, along with their assigned likelihood and consequence classes, demonstrating a structured list across subsystems and operation. The abbreviations used in the tables are explained as follows. TR stands for Technical Risk, DICE for the De-icing Subsystem, STR for the Structure Subsystem, AERO for the Aerodynamics Subsystem, PROP for the Propulsion Subsystem, POW for the Power Subsystem, CTRL for the Control Subsystem, MANU for the Manufacturing and Supply Chain Subsystem, and OP for the Operation Subsystem.

Table 15.1: *Technical Risk Statements by Subsystem.*

Risk ID	Risk Statement	Likelihood	Consequence
	De-icing		
TR-DICE-1	The drone cannot detect ice with sufficient accuracy due to unfavourable weather conditions.	High	Moderate
TR-DICE-2	Incomplete ice removal due to uneven ice thickness.	Moderate	Moderate
TR-DICE-3	Chemical fluid freezing at -30°C when standing still.	Low	Catastrophic
	Structures		
TR-STR-1	Structural material becomes brittle and cracks at temperatures down to –30°C.	Moderate	Critical
TR-STR-2	Leakage of de-icing chemicals due to small cracks.	Low	Critical
TR-STR-3	Corrosion or loosening at bolted joints in high humidity environments.	Moderate	Moderate
	Aerodynamics		
TR-AERO-1	Propeller stall under sudden gusts, leading to temporary loss of lift.	Moderate	Critical
TR-AERO-2	Aerodynamic interference between rotors in multicopter causing unpredictable flow patterns and instability.	High	Moderate
TR-AERO-3	Noise emissions exceeding regulatory limits during operation.	Moderate	Marginal
	Propulsion		
TR-PROP-1	Motor failure or thrust imbalance, leading to an unwanted moment around the centre of gravity or not enough thrust generation.	Low	Critical
TR-PROP-2	Dust and moisture can get into the motor bearings, increasing friction and reducing lifespan.	Low	Moderate
	Power		
TR-POW-1	Environmental conditions may reduce battery life.	High	Moderate

Risk ID	Risk Statement	Likelihood	Consequence
TR-POW-2	Electronic power systems degrade rapidly due to extreme cold.	Moderate	Marginal
TR-POW-3	Power imbalance, some drone batteries may run down faster than others, causing a loss in coordination.	Moderate	Moderate
	Control		
TR-CTRL-1	The drone does not meet the communication range required.	Low	Moderate
TR-CTRL-2	Signal loss in remote or obstructed environments.	Moderate	Critical
TR-CTRL-3	Signal loss due to weather-induced signal noise.	Moderate	Moderate
TR-CTRL-4	Flight instability due to high winds.	Moderate	Critical
TR-CTRL-5	Sensor limitations due to fog, snow, or reflective surfaces.	Moderate	Marginal
	Manufacturing & Supply Chain		
TR-MANU-1	Unwanted manufacturing conditions lead to additional wear of the drone	Low	Moderate
TR-MANU-2	Delays in the supply chain for drone system production.	Low	Moderate
TR-MANU-3	Inaccuracies in the bolt may lead to bad connection between components.	Low	Marginal
	Operation		
TR-OP-1	Communication interference during swarm operation.	High	Marginal
TR-OP-2	Wake interference between drones in a swarm.	Moderate	Critical
TR-OP-3	Suboptimal de-icing liquid utilisation during operation.	High	Marginal
TR-OP-4	Position offset causing swarm to deviate from expected position.	Moderate	Marginal
TR-OP-5	Drone lands in the wrong assigned area during battery replacement.	Low	Marginal
TR-OP-6	Loss of GPS signal or GNSS spoofing near metallic turbine, resulting in navigation drift or flight instability.	Low	Critical

15.2.1. Post risks analysis

This section presents an overview of the previously identified risks, along with the corresponding mitigation strategies, contingency plans, and design impacts. It also includes a second evaluation of the risks after implementing the mitigation strategies. The mitigation strategies aim to reduce the probability of risk occurrence, while the contingency plans provide fallback actions to ensure operational continuity in the event of failure. Additionally, design impacts are considered to reflect their influence on decision-making and the required engineering actions.

For the manufacturing subsystem, design impacts are marked as not applicable. At the current stage, it is assumed that the manufacturing process will proceed as expected and will not influence the actual system design. The complete content is summarized in Table 15.2, which provides a clear subsystem and operational risk management framework to support robust analysis for deployment in extreme weather environments.

Table 15.2: *Combined Risk Management by Subsystem*

Risk ID	Mitigation Strategy	Contingency Plan	Design Impacts	Likelihood	Consequence
De-icing					
TR-DICE-1	Combine RGB and infrared imaging sensors to minimise extreme-weather impact, such as fog and rain.	Abort the mission temporarily and climb to a higher altitude or upwind zone for better visibility, retry detection and if still fail to detect, return to the ground station.	Specify the number of redundant imaging sensors and determine a minimum detection confidence threshold for pausing or retrying operations.	Low	Moderate
TR-DICE-2	Scan entire blade pre-flight with high-resolution mapping and dynamically adjust spray rate.	Change to manual control to redo the de-icing with real-time visual operation.	Collect and analyse spray data to obtain overspray rates, train models to choose better mapping and spray adjustments.	Low	Moderate
TR-DICE-4	Integrate internal heating elements to prevent freezing at –30°C.	Stop de-icing operation and return to the ground station for maintenance.	More complex mechanism design and non-standing liquid causing heavier sloshing, which may also affect the control subsystem.	Low	Marginal
Structures					
TR-STR-1	Integrate internal heating elements to maintain material ductility at –30°C.	Interrupt the operation, put the drones in the enclosure heating zone.	Required low-temperature composite formulations or heating design.	Low	Critical
TR-STR-2	Apply self-sealing techniques from aircraft fuel tanks to all chemical enclosures.	Use waterproof adhesive tape for a temporary solution.	The thickness of the structure needs to be carefully considered, and self-sealing components will incur more weight cost.	Very low	Critical

Risk ID	Mitigation Strategy	Contingency Plan	Design Impacts	Likelihood	Consequence
TR-STR-3	Apply protective coating for bolted joints	Replace the fastener or add auxiliary reinforcement tools such as tape or instant glue.	Select corrosion-resistant coatings for fasteners, but this will lead to heavier weight and may influence aerodynamic performance.	Low	Moderate
Aerodynamics					
TR-AERO-1	Install gust-loading sensors and active blade-pitch control to maintain stall margin.	Reduce airspeed and hover stably until gust subsides and if stall still exists descend to lower altitude.	Required more complex control system and mechanism in propulsion design.	Low	Critical
TR-AERO-2	Optimize rotor spacing via CFD and switch operation rotors via dynamic spacing controls.	Switch off the interfered rotors to physically increase the spacing separation.	The spacing in between rotors are strictly limited which may also limit the structure design.	Moderate	Moderate
TR-AERO-3	Design low-noise propellers and cover the propeller with protected shell to minimise the noise spread .	Reduce the rpm and if noise still exceeds limits, return for quieter propeller installation.	Require investigation on low-noise airfoil geometry and acoustic dampening materials which lead to more limitations in material chosen.	Low	Marginal
Propulsion					
TR-PROP-1	Perform pre flight motor balancing check.	Apply the emergency landing procedure, and once the drone has landed replace the faulty motor.	Additional algorithms had to be added and tested into the final design.	Very low	Moderate
TR-PROP-2	Apply dust repellent, water resistant lubricants when the drones are landed between each wind turbine.	Activate automatic thrust calibration routine in FC. Once on the ground, replace the affected motor or ESC.	The motors were placed in a symmetrical manner and the set of co-axial rotors were rotating in opposite direction from each other.	Very low	Moderate
Power					

Risk ID	Mitigation Strategy	Contingency Plan	Design Impacts	Likelihood	Consequence
TR-POW-1	Incorporate active thermal management including heaters, insulation for battery packs.	Use other batteries in rotation if one gets damaged.	A heating element has been added to the drone design in order for the payload system to be better protected against cold weather.	Low	Moderate
TR-POW-2	Incorporate the same thermal management for the power electronics.	Use excess thrust until the landing station is reached.	A heating element has been added to the drone design in order for the payload system to be better protected against cold weather.	Moderate	Marginal
TR-POW-3	Incorporate a battery management for each battery which has a reading of the current and voltage	Change the battery rotation to minimize the chance that one drone is constantly with three faulty batteries, reducing uncertainty.	A high number of batteries have been used per drone, a total of three, that way if a battery runs down faster there are still two others to make up for it.	Low	Moderate
Control					
TR-CTRL-1	Fit high-gain directional antenna to extend communication range.	When the signal is lost the emergency landed protocol will be triggered that way, the drone will not go further away	A larger communication device was used with its corresponding software.	Very low	Moderate
TR-CTRL-2	Add secondary backup communication link, such as cellular.	Same protocol as TR-CTRL-1	A larger communication device was used with its corresponding software.	Low	Critical
TR-CTRL-3	Select hardware which is specificity altered to fit the specific weather conditions	Same protocol as TR-CTRL-1	A FANET communication system is placed in order to have an extended reach.	Low	Moderate

Risk ID	Mitigation Strategy	Contingency Plan	Design Impacts	Likelihood	Consequence
TR-CTRL-4	Have a high thrust to weight ratio of 2.2 so that high winds will be resisted.	Attempt a reset of the affected motor circuit once, then land immediately if the reset fails.	This influenced the number of rotors and the size of the motors to be placed in the drone.	Low	Critical
TR-CTRL-5	Enclose sensors within a polarized, protective transparent housing to guard against fog/snow.	Activate the landing plan, then clean the sensor's protective transparent box with a cleaning cloth.	A transparent box which could fit all the sensors was designed and integrated as part of the payload.	Low	Marginal
Manufacturing & Supply Chain					
TR-MANU-1	Implement manufacturing practices such as cleaning procedures, regular sanitation audits, and component surface inspections.	Replace damaged parts with parts stored in the truck.	Not applicable	Very low	Moderate
TR-MANU-2	Maintain a safety stock buffer, and perform regular supplier performance reviews	Use a backup drone stored in the warehouse.	Not applicable	Very low	Moderate
TR-MANU-3	Keep spare bolts and have regular quality control checks	Replace faulty bolts with new ones before takeoff or after landing.	Not applicable	Very low	Marginal
Operation					
TR-OP-1	Assign a unique communication channel to each drone.	Switch to a predefined backup frequency band or wired link, if interference still exists, change to manual control.	Require the communication system to support multi-frequency control, necessitating more advanced hardware.	Moderate	Marginal

Risk ID	Mitigation Strategy	Contingency Plan	Design Impacts	Likelihood	Consequence
TR-OP-2	Enforce a minimum separation distance between drones to prevent zone conflicts.	Increase drone spacing and reduce airspeed, if wake interactions still exists, pause the swarm mission and resume with less units.	Define minimum drone-spacing constraints in the flight planner and integrate path-planning algorithms into the control system.	Low	Critical
TR-OP-3	Implement a dynamic protocol that monitors fluid levels and reassigns drones with remaining de-icer to nearby tasks.	Trigger a conserve mode that control spray rate, if fluid usage still exceeds expectations, return to the ground station for refill and redeploy.	Introduce an adaptive routing algorithm in the mission control software and communication architecture to support real-time data exchange between drones and the ground station.	Moderate	Marginal
TR-OP-4	Implement inter drone communication to calibrate and maintain separation distances.	Implement onboard collision avoidance and correction algorithm, if offset cannot be corrected, halt swarm advance and wait for manually intervention.	Require pre-mission algorithm training and more precise detection sensors.	Low	Marginal
TR-OP-5	Deploy onboard visual landing aids to guide each drone to its designated touchdown zone.	Abort the landing procedure, climb to a safe hover altitude, then restart landing sequence to the correct assigned pad.	Equip the RGB system with a rotating mechanism for downward-facing ability and train algorithms for landmark detection.	Very low	Marginal
TR-OP-6	Activate inter drone links to mitigate wind turbine signal interference.	Activate the inertial navigation backup system.	Integrate multiple navigation sensors into the autopilot and implement logic to prioritize among their outputs.	Very low	Critical

15.2.2. Risk maps

To assess the risk level (R) of each statement, likelihood (P) and consequence (C) classes are each assigned values from one to five, with higher numbers indicating greater likelihood or severity of consequence.

Based on the risk assessment in Section 15.2, two risk maps have been generated. These maps are presented as heat maps, where increasing red intensity indicates higher risk levels. Figure 15.1a illustrates the risk levels prior to the implementation of mitigation strategies, while Figure 15.1b shows the outcomes after mitigation. As can be clearly observed, the risk indicators have shifted toward the left bottom corner of the matrix, demonstrating that the mitigation strategies are effective in reducing the overall risk levels.

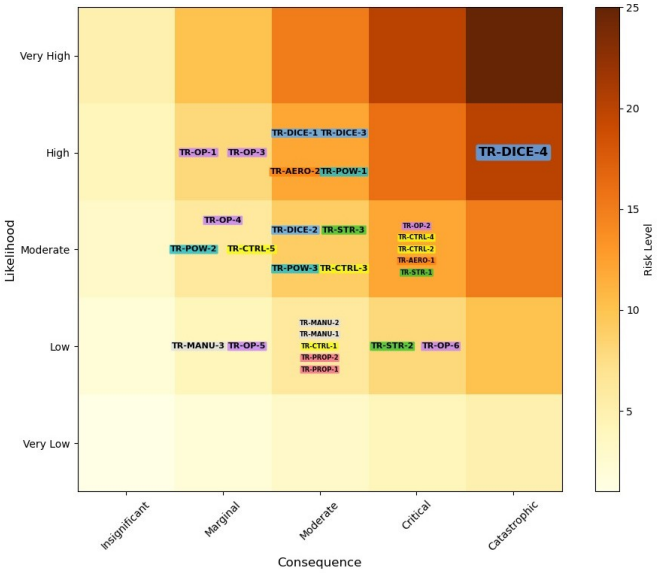

(a) *Before mitigation*

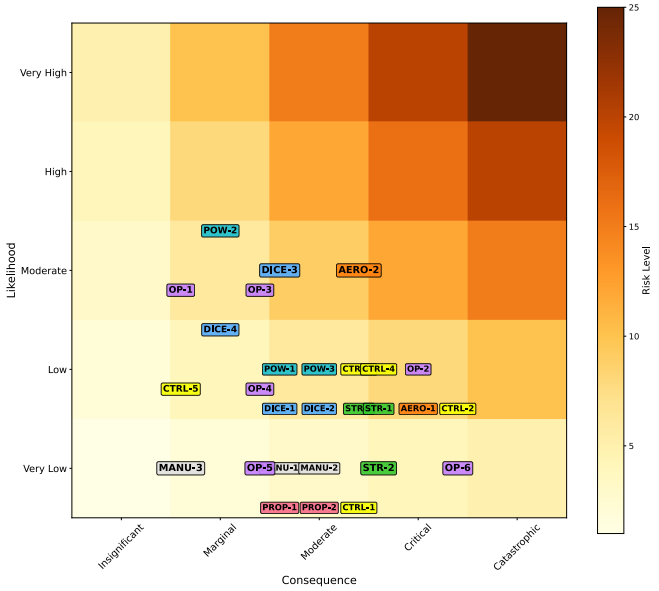

(b) *After mitigation*

Figure 15.1: *Heat-map risk matrices for all subsystems and operation: (a) before and (b) after mitigation strategies*

15.2.3. Reliability, availability, maintainability, and safety (RAMS) characteristics

This section is made to evaluate the drone under the RAMS criteria. This will ensure that the drone will compile with the operational and safety requirements.

Reliability

First, looking at the reliability according to the requirement USER-S-PAYL-3.1, the drone must be able to remove 90% of the ice in the affected zone. Using a solution chemical de-icer made up of 60% propylene glycol and 40% de-ionised water as industry stranded (Struk, 2017). Along side the chemical de-icer, the onboard computer vision system has a detection rate of 96% based on Chapter 11 . Combining these two factors the overall drone system is capable of reliably meeting the 90% removal requirement. In cases of errors there is a list of mitigation strategies to ensure the completion of the mission.

Availability

The availability references to the proportion of time the drone is mission-ready compared to its down time (maintenance or logistics). Mathematically it is usually expressed as:

$$\text{Availability} = \frac{\text{Uptime}}{\text{Uptime} + \text{Downtime}}$$

However, according to the financial statement (see Chapter 4), The drone needs to be mission ready 10 times a year. The time of performed mission depends on weather conditions. Thus, meaning that even if drone requires a large maintenance time it can be scheduled in such a way that will not affect the mission. Furthermore, under risk TR-MANU-2 there will always be a spare drone in the warehouse in case of a drones malfunction.

Maintainability

The drone carries a battery with an incorporated monitoring device which is used to flag when maintenance is required. Once a certain threshold is reached the drone is signalled to return back to the ground station for further inspection. The operator will then intervene and perform the necessary maintenance process. In accordance with USER-S-STR-2.1, the system shall operate effectively in temperatures as low as -30°C.

Safety

When conducting the mission, safety is of the utmost importance. Following requirements USER-M-SAFE-2.1 and USER-M-SAFE-2.2 the drone must under no circumstances collide against the wind turbine structures or nearby flying drones. In order to ensure this requirement is met, Time of Flight (ToF) sensors were included in the drone's payload which are able to locate obstacles in proximity. Moreover, under USER-M-SAFE-2.3 the drone shall incorporate an emergency landing protocols which activates within 3 seconds of detecting a system failure.

16

Sustainable development strategy

Hew

This chapter outlines the sustainability development strategy behind the de-icing drone project, focusing on minimising environmental impact, while maximising operational efficiency. It includes a life cycle assessment spanning manufacturing, operations, and end-of-life, evaluates noise emissions, and proposes recommendations for improving sustainability. In Section 16.1 the life cycle assessment of the drone is conducted and in Section 16.2 the limitations and recommendations for the sustainability are given.

16.1. Life cycle assessment

Hew

Understanding and minimising the environmental footprint of the de-icing drone system is essential for ensuring its long-term sustainability and regulatory compliance. This section presents a Life Cycle Assessment (LCA) covering the full span of the drone's development and deployment, from material sourcing and manufacturing to operational logistics and end-of-life considerations. Each stage is evaluated for its primary environmental concerns, with mitigation strategies proposed to reduce negative impacts. This structured approach supports the integration of sustainability into the design, production, and operation of the system.

16.1.1. Drone manufacturing

The goal of performing an LCA on the manufacturing process of the drone is to evaluate the environmental impacts of the drone manufacturing process to guide sustainable material and design choices. It begins with raw material sourcing, followed by manufacturing. Next, LCA proceeds to the assembly process and finally the storage and deployment of the product. This LCA process is based on the production plan presented in Section 7.4. First, a thorough investigation of the primary environmental concern from each of the steps in the production plan is performed, followed by suggestions for better quantifying and scaling these impacts. In the end, improvement strategies are provided to help mitigate these concerns. Table 16.1 shows all the above summarised.

16.1.2. End-of-Life considerations and material sustainability

At the end of the drone's operational life, the responsible disposal and recovery of its components is critical to reduce long-term environmental impact. The carbon fibre airframe poses a recycling challenge due to its thermoset matrix. Carbon fibre has high embodied energy due to the carbonisation process and is non-biodegradable (Meng et al., 2017). Since limited recycling options exist for now, such as thermal or mechanical processes, which are energy-intensive, this has to be taken into account when coming up with a strategy to tackle this. Additionally, scrap carbon fibre generated during manufacturing is difficult to repurpose. Thus, some recommendations and suggestions are:

- Minimise material offcuts via efficient computer numerical control (CNC) nesting and digital design optimisation.
- Use modular, separable designs to make disassembly for recycling more efficient (Duflou

Table 16.1: *Life Cycle Assessment Summary for Deicing Drone Production*

Production Step	Primary Environmental Concern	LCA Assessment Focus	Sustainability Mitigation Strategy
Buy COTS Components	High embodied energy, packaging waste	Assess supplier energy mix and transport footprint	Prioritise suppliers using renewable energy and minimal packaging
Outsourced Manufacturing	Energy use and material scrap from machining	Include embedded emissions from subcontractors	Engage with low-emission manufacturers; optimise material usage
Quality Check (COTS/Structures)	Negligible (inspection tools/electricity)	Not significant	Maintain efficient test protocols to avoid unnecessary rework
RMA Parts	Transport emissions, material loss	Quantify reverse logistics and scrappage rates	Implement stricter quality control before procurement to reduce returns
Surface Finish	VOC emissions, chemical disposal	Model chemical emissions and worker exposure risk	Switch to water-based coatings or low-VOC alternatives
Assembly	Electricity use, minor tool emissions	Not significant	Use efficient assembly tools and minimise idle operation
Disassemble	Wasted materials, added emissions	Assess rate and impact of rework loops	Improve first-pass assembly quality through training
Storage	Continuous energy consumption (lighting/temperature)	Estimate energy demand and duration of storage	Use energy-efficient storage systems and time-bound inventory rotation

et al., 2008).

- Use reclaimed or recycled material where feasible, particularly in non-load-bearing structures.
- Design a recycling manual as per requirement ENV-M-SUST-3.2 to better facilitate the disassembly process of the drone.

16.1.3. Biodegradability of de-icing chemical agents

Although chemical agents are necessary due to their commercial readiness (and low TRL level of alternatives), the strategy still aims to maximise sustainability by selecting the most biodegradable options. For the de-icing solutions, the viable options are ethylene glycol, propylene glycol, non-chloride salts (potassium formate considered currently) and ethanol. Outside of the high toxicity danger of ethylene glycol, all the others are fully biodegradable and a suitable option. To minimise the environmental impact, the biochemical oxygen demand (BOD) and chemical oxygen demand (COD) should be evaluated. Those indicators provide the required amount of oxygen needed to break down the pollutants present in water through biochemical and chemical processes. Based on the selection of ethylene glycol as the de-icing agent to be used, the environmental impact can be quantified in order to paint a better picture of how each de-icing operation affects the surrounding environment. Equation 16.1 shows how the total BOD load can be calculated for 26kg of de-icing agent used for a single de-icing operation(Staples et al., 2001) in accordance with the operations profile shown in Chapter 13.

$$\mathrm{BOD_{load}} = m_{\mathrm{EG}} \times \mathrm{BOD_{specific}} = 26\,\mathrm{kg} \times 600\,\frac{\mathrm{g\ O_2}}{\mathrm{kg\ EG}} = 15{,}600\,\mathrm{g\ O_2} = 15.6\,\mathrm{kg\ O_2} \tag{16.1}$$

This equates to 15.6 kg of oxygen in a receiving water body, which is enough to severely deplete dissolved oxygen levels, leading to anoxic conditions that can be lethal to aquatic life. However,

the acute toxicity of ethylene glycol is relatively low, which results in falling under the following criterion:

$$LC_{50,acute} > 10{,}000\,mg/L$$

While ethylene glycol has a relatively high biodegradation rate, with 90% to 100% degradation within the time frame of 24 hours to 28 days, it is worth noting that this rate will decrease for anaerobic or cold environments.

16.1.4. Battery production and disposal

The de-icing drone utilises high-capacity Diamond Ultra-Low Temperature Series semi-solid-state lithium-ion (Li-ion) batteries(decided in Chapter 5, specifically configured in 14S arrangements with a capacity up to 128 747.7 mA h. However, while these batteries offer excellent energy density and thermal stability, they also present significant sustainability challenges throughout their life cycle.

The production of lithium-ion batteries involves energy-intensive processes and the extraction of finite resources such as lithium, cobalt, and nickel. Mining these raw materials is associated with environmental degradation, water pollution, and high carbon emissions. Additionally, semi-solid-state designs, although safer and more temperature-resilient, often use advanced polymer or ceramic-based electrolytes, complicate end-of-life recycling and increase environmental handling challenges. Disposal poses additional challenges. If not properly handled, end-of-life batteries can lead to hazardous chemical leakage, fire risk, and heavy metal contamination of soil and groundwater. From a LCA perspective, battery production is one of the highest contributors to the drone's overall embodied carbon footprint (Dunn et al., 2012). Key impact areas include:

- Greenhouse gas emissions from raw material extraction and cell manufacturing
- Energy consumption during cell assembly and temperature conditioning
- Toxicity potential from electrolyte leakage or thermal degradation

To mitigate these impacts, the following strategies are recommended:

- Sourcing from certified sustainable suppliers that use ethical mining practices and incorporate recycled materials into cathode production.
- Implementing a battery end-of-life recovery program in partnership with certified e-waste or lithium recycling facilities.
- Monitoring battery health in real time using onboard battery management systems (BMS) to prevent early degradation and extend usable life, which helps to fulfil requirement `ENV-M-SUST-2.4`, which is that the battery has to last more than 1000 cycles
- Designing modular battery enclosures that allow for easier disassembly, inspection, and cell-level replacement, thus reducing overall waste.

16.1.5. Ground station trucks and logistics

The ground station plays a crucial role in supporting the drone de-icing operations. While ground support infrastructure is essential for operational effectiveness, it also introduces additional environmental burdens related to fuel use, emissions, and logistical complexity. The remoteness of the target wind farm also adds another dimension of complexity when developing suitable strategies to ensure the sustainability of operations, as transportation options for such conditions are limited.

The primary environmental impact of the ground station stems from the operation of diesel-powered trucks, which contribute significantly to greenhouse gas (GHG) emissions. Frequent deployment in cold or mountainous regions often requires engine idling for heat, further increasing fuel consumption and local air pollution. Moreover, the logistics involved in transporting the drone, payloads, and de-icing fluid over long distances amplify the overall carbon footprint. Manufacturing and retrofitting the trucks themselves also carry embedded emissions, particularly from materials such as aluminium, steel, and electronics for communication and telemetry systems. In a full LCA, ground logistics contribute primarily to the operational emissions phase, depending on the frequency, distance, and duration of deployments. Key environmental impacts include:

- Fossil fuel combustion (CO_2, NO_x emissions)
- Resource depletion from truck fabrication and battery banks
- Noise and environmental disruption in sensitive regions

Recommended mitigation strategies to reduce these impacts include:

- Transitioning to hybrid or electric trucks for drone transportation and on-site power supply, where infrastructure permits.
- Implementing route optimisation algorithms to reduce travel distance, idling time, and fuel consumption.
- Using modular and compact ground stations, co-locating ground stations with renewable energy sources
- Scheduling operations in clusters or batches to reduce unnecessary repositioning between missions.

16.2. Limitations and recommendations *Hew*

There are some limitations to achieving sustainability in the drone life cycle. The sustainability aspect of this project is limited by the fact that almost all chemicals still produce pollution to some extent. While the immediate solution is to deploy a different method for de-icing, advanced non-chemical methods such as ultrasonic or vibration-based de-icing are still currently at a low technology readiness level (TRL) and thus are not yet deployable. Furthermore, de-icing operations, which are highly reliant on the weather conditions, may induce limitations when optimal de-icing operations are planned. Table 16.2 shows these limitations as well as some recommendations on how to tackle these issues.

Table 16.2: *Sustainability Limitations and Recommendations for the De-icing Drone*

Limitation	Recommendation
All available chemical de-icing agents have an environmental impact, particularly in aquatic ecosystems	Continue material research to identify or develop less toxic, biodegradable de-icing alternatives.
Advanced non-chemical methods such as ultrasonic or vibration-based de-icing are at a low TRL and not deployable at scale	Monitor and collaborate with research institutions working on next-generation de-icing methods. Plan for future integration as TRL increases.
Weather-dependence and operational downtime in extreme storms or icing conditions	Include weather forecasting integration and adaptive mission planning in software systems as per requirement ENV-M-SUST-2.6 to reduce failed flights and unnecessary emissions.

Part V:

Vol.5 | Implementation Logistics

17

Project development strategy

Josephine

This chapter provides a structured view of the most important development activities that must be performed after the DSE in order to ensure that the drones will come into service. In order to visualise this a project design and development logic diagram and a Gantt chart are constructed. These diagrams help translating ideas into a clear plan. Since a design process requires a lot of work and therefore a lot of time, it is crucial to have a broad overview of the tasks that still need to be performed in all stages of the design process. They ensure consistency and traceability throughout the project and help the design process in translating realistic and achievable goals to detailed actions.

Project design & development logic

This diagram shows a logical order of major activities that must performed after finishing the DSE. It is represented as a block diagram with each block showing a distinct action or development step. The activities are connected by arrows showing the temporal progression and the dependencies between tasks. It may also be the case that functions are performed in parallel. The diagram is structured as follows. It starts by the end of the DSE and the diagram ends at the end-of-life phase of a drone. An important phase in the diagram includes the detailed design phase, that will end with a design for a prototype to be manufactured. After a prototype is structured, several flight tests will be performed to make sure the drone works individually, as intended. When flight tests fail, the diagram shows an iteration back to the final design to make design improvements, based on an analysis of the failure conditions. If the test flights succeed, the process continues with performing tests with a swarm of drones. When all tests are performed successfully, the design is finished and certification must be obtained. As soon as certification is received the drones can going to service. At the same time several marketing campaigns will be performed in order to sell the drone and increase popularity.

Gantt chart

With a clear description of the required activities that need to be performed in the phases after the DSE, a required time can be assigned to it. This is done via a Gantt Chart. The Gantt chart shows all the activities that need to be performed until the drones can go into service. The activities are consistent with the project design and development logic diagram. On the horizontal axis, the dates are given in months. This is different than for the project Gantt chart, since the post-DSE activities require more time. Also, an estimated duration is assigned to every task in order to clearly show what the lines in the Gantt chart represent. For the activities concerning performing marketing campaigns and bringing the drones into service, a dashed line is represented, which indicates that these activities are ongoing as soon as the drones will be in service. Arrows in the Gantt chart indicate dependencies between tasks.

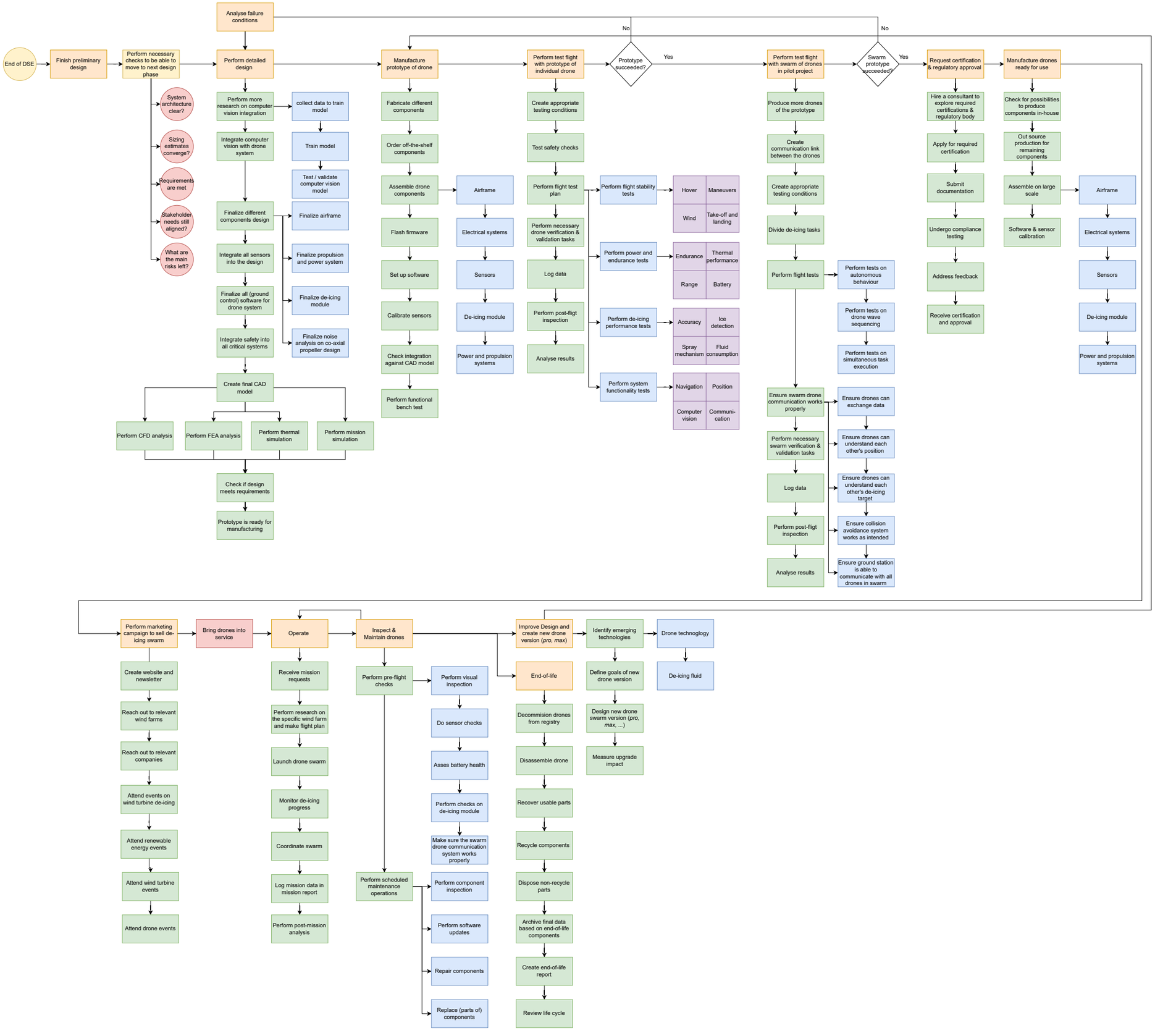
End of DSE
Finish preliminary design
Perform necessary checks to be able to move to next design phase
System architecture clear?
Sizing estimates converge?
Requirements are met
Stakeholder needs still aligned?
What are the main risks left?
Analyse failure conditions
Perform detailed design
Perform more research on computer vision integration
collect data to train model
Train model
Test / validate computer vision model
Integrate computer vision with drone system
Finalize different components design
Finalize airframe
Finalize propulsion and power system
Finalize de-icing module
Finalize noise analysis on co-axial propeller design
Integrate all sensors into the design
Finalize all (ground control) software for drone system
Integrate safety into all critical systems
Create final CAD model
Perform CFD analysis
Perform FEA analysis
Perform thermal simulation
Perform mission simulation
Check if design meets requirements
Prototype is ready for manufacturing
No
Manufacture prototype of drone
Fabricate different components
Order off-the-shelf components
Assemble drone components
Airframe
Electrical systems
Sensors
De-icing module
Power and propulsion systems
Flash firmware
Set up software
Calibrate sensors
Check integration against CAD model
Perform functional bench test
Perform test flight with prototype of individual drone
Prototype succeeded?
Yes
Create appropriate testing conditions
Test safety checks
Perform flight test plan
Perform flight stability tests
Hover
Maneuvers
Wind
Take-off and landing
Perform power and endurance tests
Endurance
Thermal performance
Range
Battery
Perform necessary drone verification & validation tasks
Log data
Perform post-fligt inspection
Analyse results
Perform de-icing performance tests
Accuracy
Ice detection
Spray mechanism
Fluid consumption
Perform system functionality tests
Navigation
Position
Computer vision
Communi-cation
No
Perform test flight with swarm of drones in pilot project
Swarm prototype succeeded?
Yes
Produce more drones of the prototype
Create communication link between the drones
Create appropriate testing conditions
Divide de-icing tasks
Perform flight tests
Perform tests on autonomous behaviour
Perform tests on drone wave sequencing
Perform tests on simultaneous task execution
Ensure swarm drone communication works properly
Ensure drones can exchange data
Perform necessary swarm verification & validation tasks
Ensure drones can understand each other's position
Log data
Ensure drones can understand each other's de-icing target
Perform post-fligt inspection
Ensure collision avoidance system works as intended
Analyse results
Ensure ground station is able to communicate with all drones in swarm
Request certification & regulatory approval
Hire a consultant to explore required certifications & regulatory body
Apply for required certification
Submit documentation
Undergo compliance testing
Address feedback
Receive certification and approval
Manufacture drones ready for use
Check for possibilities to produce components in-house
Out source production for remaining components
Assemble on large scale
Airframe
Electrical systems
Sensors
De-icing module
Power and propulsion systems
Software & sensor calibration
Perform marketing campaign to sell de-icing swarm
Create website and newsletter
Reach out to relevant wind farms
Reach out to relevant companies
Attend events on wind turbine de-icing
Attend renewable energy events
Attend wind turbine events
Attend drone events
Bring drones into service
Operate
Receive mission requests
Perform research on the specific wind farm and make flight plan
Launch drone swarm
Monitor de-icing progress
Coordinate swarm
Log mission data in mission report
Perform post-mission analysis
Inspect & Maintain drones
Perform pre-flight checks
Perform visual inspection
Do sensor checks
Asses battery health
Perform checks on de-icing module
Make sure the swarm drone communication system works properly
Perform scheduled maintenance operations
Perform component inspection
Perform software updates
Repair components
Replace (parts of) components
Improve Design and create new drone version (*pro*, *max*)
End-of-life
Decommision drones from registry
Disassemble drone
Recover usable parts
Recycle components
Dispose non-recycle parts
Archive final data based on end-of-life components
Create end-of-life report
Review life cycle
Identify emerging technologies
Define goals of new drone version
Design new drone swarm version (*pro*, *max*, ...)
Measure upgrade impact
Drone technoglogy
De-icing fluid

Post-DSE Gantt Chart D-ice

TASKS	Duration	July 2024	August 2025	September 2025	October 2025	November 2025	December 2025	January 2026	February 2026	March 2026	April 2026	May 2026	June 2026
End of DSE													
1. Perform detailed design	~12 weeks												
1.1 Perform more research on computer vision integration	~3 weeks												
1.1.1 Collect data to train model													
1.1.2 Train model													
1.1.3 Test / validate computer vision model													
1.2 Integrate computer vision with drone system	~1 week												
1.3 Finalize different components design	~2 weeks												
1.4 Integrate all sensors into the design	~1 week												
1.5 Finalize all (ground control) software for drone system	~1 week												
1.6 Integrate safety into all critical system	~1 week												
1.7 Create final CAD model	~1 week												
1.8 Perform CFD analysis	~1 week												
1.9 Perform FEA analysis	~1 week												
1.10 Perform thermal simulation	~1 week												
1.11 perform mission simulation	~1 week												
1.12 Check if design meets requirements													
1.13 prototype is ready for manufacturing				★									
2. Manufacture prototype of drone	~5 weeks												
2.1 Fabricate different components	~2 weeks												
2.2 Order of-the-shelf components	~2 weeks												
2.3 Assemble drone components	~2 weeks												
2.3.1 Airframe													
2.3.2 Electrical systems													
2.3.3 Sensors													
2.3.4 De-icing module													
2.3.5 Power and propulsion systems													
2.4 Flash firmware	~1 day												
2.5 Set up software	~2 days												
2.6 Calibrate sensors	~2 days												
2.7 Check integration againt CAD model	~1 days												
2.8 Perform functional bench test	~2 days												
3. Perform test flights with prototype of individual drone	~4 weeks												
3.1 Create appropriate testing conditions	~1 week												
3.2 test safety checks	~2 days												
3.3 Perform flight test plan	~1 weeks												
3.3.1 Perform flight stability tests													
3.3.2 Perform power and endurance tests													
3.3.3 Perform de-icing performance tests													
3.3.4 Perform system functionality tests													
3.4 Perform necessary drone verification & validation tasks	~1 week												
3.5 Log data	~1 week												
3.6 Perform post flight inspection	~2 days												
3.7 analyse results	~1 week												
4. Perform test flights with swarm of drones	~7 weeks												
4.1 Produce more drones of the prototype	~2 weeks												
4.2 Create communication interface between the drones	~1 week												
4.3 Create appropriate testing conditions	~3 days												
4.4 Divide de-icing tasks	~1 day												
4.5 Perform fligth tests	~2 weeks												
4.5.1 Perform tests on autonomous behaviour													
4.5.2 Perform tests on wave sequencing													
4.5.3 Perform tests on simultaneous task execution													
4.6 Ensure swarm drone communication works properly	~1 week												
4.6.1 Ensure drones can exchange data													
4.6.2 Ensure drones can understand each other's position													
4.6.3 Ensure drones can understand each other's de-icing target													
4.6.4 Ensure drones will not collide													
4.6.4 Ensure ground station is able to communicate with all drones in the swarm													
4.7 Perform necessary swarm verification & validation tasks	~1 week												
4.8 Log data	~2 weeks												
4.9 Perform post-flight inspection	~2 days												
4.10 Analyse results	~1 week												
5. Request certification and regulatory approval	~8 weeks												
5.1 Hire a consultant to explore required certifications & regulatory body	~2 weeks												
5.2 Apply for required certification	~1 week												
5.3 Submit documentation	~1 week												
5.4 Address feedback	~2 weeks												
5.5 Receive certification and approval	~2 weeks												
6. Manufacture drones for use	~8 weeks/ swarm												
6.1 Check possibilities to produce components in-house & produce in house	~3 weeks												
6.2 Out source production for remaining componentns	~3 weeks												
6.3 Assemble on large scale	~4 weeks/ swarm												
6.3.1 Airframe													
6.3.2 Electrical systems													
6.3.3 Sensors													
6.3.4 De-icing module													
6.3.5 Power and Propulsion													
6.4 Software & sensor calibration	~1 week												
7. Perform marketing strategies to sell drone	*ongoing*												
7.1 Create website and news letter													
7.2 Reach out to relevant wind farms													
7.3 Reach out to relevant companies													
7.4 Attend events on wind turbine de-icing													
7.5 Attend renewable energy events													
7.6 Attend wind turbine events													
7.7 Attend drone events													
8. Bring drones into service	*ongoing*											★	

18

Conclusion

Patryk

The design report for the wind turbine de-icing drone provides a comprehensive explanation and justification of the design steps taken. It is achieved by performing extensive economical and technological analysis, while employing rigorous systems engineering guidelines. Using the research knowledge mission needs and operation plans are drafted, which define the requirements for the project design. The developed requirements act as a guideline for designing aircraft systems. Multiple methods are used for aircraft design, such as modelling, theoretical analysis or research-based approximations. The converged design of systems is integrated and displayed in block diagrams for visualisation of system interfaces. To ensure high quality of the design work conducted, arguments supporting validity of design are given. This is done mostly in form of verification and validation strategies, supported with risk and sustainability assessments. In the end, the implementation of the design to the market application was analysed and assessed.

The final design results in a innovative approach to performing wind turbine de-icing using drone architecture. The key strength that distinguishes the mission design from the market is its employment of autonomous drone swarm for de-icing. The application of computer vision for ice-detection and 3D mapping, and control for autonomous navigation and de-icing, cuts down significantly on costs of human labour. Swarm coordination integrated with the ground operations plan allows the mission to distinguish itself through profitable service time. From the perspective of the aircraft platform, an innovative structural design of U-shape heptacopter is employed. This allows clearance for the de-icing spraying mechanism while still maintaining the symmetry in the x-axis and moment stability in hover while spraying. These design shining points allow the project design to stand out as a novel and sustainable take on the chemical de-icing in the drone market.

When concluding the design report for the mission, it has to be emphasised that the design of the drone is not finalised. Enough evidence was established throughout the report to produce a feasible design for the mission needs and objectives, however as can be seen by the compliance matrix in Subsection 14.1.2 not all of the requirements are complied with yet. Those requirements are either unrealistic to be met currently and need to be renegotiated with the stakeholder or need to be proven as complied with through future operation. In addition, not every method and system concept is sufficiently validated yet. For this reason it is recommended to conduct further design work in increasing complexity of the models in order to validate the design. An important consideration for further work on the design is to keep in mind the sensitivities of the systems given in Subsection 14.1.1, as several systems change their performance considerably with change in design parameters.

Limitations & Recommendations

All of the design methods, whether it is modelling, simulation or analysis possess their limitations stemming from assumptions taken for simplifying the design process. Another reason for limitations can be the limited domain of applications for the used method. Hence,

future work is outlined.

The market analysis, which acts as a design model for mission's operation, was developed using a case study of a single wind farm location. This limits the ability to replicate the exact mission profile for other wind farm use cases. Therefore, the method needs to be validated in the future against using the mission with different operations profiles of other wind farms. The analysis considers only primary financial variables, such as profits and expenses, which is recommended to be expanded in the future by other variables such as taxes, interests or liquidity.

The drone sizing was done using statistical and analytical methods done with iteration. This creates a limitation of comparing the model parameters against existing products on the market, while the project develops an unconventional aircraft. For this reason, it is recommended to conduct component based structural and performance analysis, such as FEM, CFD and motor dynamics analysis. In the pre-production state all of the design has to be validated by producing a prototype.

Following the recommendation of conducting computational fluid dynamic (CFD) analysis on the structure for configuration design, it is also beneficial to conduct noise CFD to ensure compliance with noise requirement `USER-M-SUST-2.3` (as given in Appendix D). Current methods are limited due to not including the influence of structure on the noise of rotors.

The drone control at current design stage is limited by the assumptions taken to streamline the model design process. A major limitation of the design is that the drone dynamics are approximated as linear. In the future a model has to be established that treats the system as non-linear, which requires non-linear control. Currently the controller employed is incapable of autonomous trajectory planning, but is capable of trajectory tracking (Heng et al., 2015). Therefore to ensure high autonomy of the aircraft the currently unused in control loop time-of-flight (ToF) sensor needs to be used and artificial intelligence model-informed robot path planning strategies need to be developed. As the last stage of control design, it is necessary to integrate coordinated control of the drone swarm to provide highly efficient de-icing.

Currently, the computer vision is used exclusively for its primary mission - ice detection. The integration of computer vision with the drone navigation is currently not implemented. This greatly limits the ability of the aircraft to operate autonomously. Coupling the computer vision with control architecture will also allow for real time ice detection and spraying without human intervention.

Current design work as shown in this section acts more as a proof of concept for the autonomous capabilities of the used drone platform. The design currently provides a low level of autonomy, which the report acknowledges, through planning out the in-air operations for control and computer vision in Chapter 13 and Chapter 11 respectively.

Statement on the use of AI

Artificial intelligence tools were used in this report only for auxiliary purposes. GitHub Copilot was used to assist with coding. ChatGPT was used to support LaTeX formatting and to locate academic sources. AI was not used to generate any academic content in this report.

Acknowledgments

The authors would like to thank Dr. Xuerui (Sherry) Wang (PhD), Hafiz Ghazali Bin Muhammad Amri (MEng.), Direnc Atmaca (MSc.) for their continuing support.

References

Stoyanov, D., Nixon, J., & Sarlak, H. (2021). Analysis of derating and anti-icing strategies for wind turbines in cold climates. *Applied Energy*, *288*, 116610. 10.1016/j.apenergy.2021.116610

Vattenfall, Martinez, B., & Trombe, P. (2016). *Benchmark study of icing forecasts do they add value?* https://windren.se/WW2016/2_1_1_Martinez_Benchmark_study_of_icing_forecasts_Do_they_really_add_a_value.pdf.

Gao, L., & Hu, H. (2021). Wind turbine icing characteristics and icing-induced power losses to utility-scale wind turbines. *Proceedings of the National Academy of Sciences*, *118*(42). https://doi.org/10.1073/pnas.2111461118

International Cloud Atlas Volume I: Manual on the Observation of Clouds and other Meteors. (1975). World Meteorological Organization.

Yirtici, O., Ozgen, S., & Tuncer, I. H. (2019). Predictions of ice formations on wind turbine blades and power production losses due to icing. *Wind Energy*, *22*(7), 945–958. https://doi.org/10.1002/we.2333

Lehtomäki, V., & Task, I. W. (2016). *Wind energy in cold climates available technologies-report* (tech. rep.). Task 19, Tech. Rep., IEA 2018. 2018. Available online: https://community ...

Quayson-Sackey, E., Nyantekyi-Kwakye, B., & Ayetor, G. K. (2025). Technological advancements for anti-icing and de-icing offshore wind turbine blades. *Cold Regions Science and Technology*, *231*, 104400. https://doi.org/https://doi.org/10.1016/j.coldregions.2024.104400

Li, H., Hu, Q., Jiang, X., Yu, Z., Shu, L., Li, C., & Qiu, Z. (2022). Review on anti-icing and de-icing techniques of wind turbine blades. *Proceedings – Int. Workshop on Atmospheric Icing of Structures*, *14*, 15.

Habibi, H., Cheng, L., Zheng, H., Kappatos, V., Selcuk, C., & Gan, T.-H. (2015). A dual de-icing system for wind turbine blades combining high-power ultrasonic guided waves and low-frequency forced vibrations. *Renewable Energy*, *83*, 859–870. https://doi.org/10.1016/j.renene.2015.05.025

Fraunhofer IFAM. (2023). Drones protect wind turbines from ice [Accessed: 2025-04-29]. *Fraunhofer Research News*. https://www.ifam.fraunhofer.de/en/press-releases/drones-protect-wind-turbines-from-ice.html

Wisson Robotics. (2025). Drone de-icing solution [Accessed: 2025-04-29]. https://www.wissonrobotics.com/en/Drone-De-icing-Solution.html

Sae ams 1424/1a-2023: Deicing/anti-icing fluid, aircraft sae type i glycol (conventional and nonconventional based) (2023rd ed.) [Foundation specification AMS 1424 with category specification AMS 1424/1A for aircraft de/anti-icing fluids]. (2023). SAE International. https://doi.org/10.4271/AMS1424/1

Xu, P., Zhang, D., & Li, A. (2025). The de-icing method using synthesized envelope modulation signals from resonance low-frequency and ultrasonic signals. *Applied Acoustics*, *231*, 110411. https://doi.org/10.1016/j.apacoust.2024.110411

Damodaran, A. (2025, January). *Margins by sector (us)*. https://pages.stern.nyu.edu/~adamodar/New_Home_Page/datafile/margin.html

The Wind Power. (2025). *Stor-rotliden (sweden) - wind farms*. https://www.thewindpower.net/windfarm_en_10483_stor-rotliden.php

Vattenfall. (2011). *Power plants: Stor-rotliden*. https://powerplants.vattenfall.com/stor-rotliden/

Kgi-Admin. (2022). Power plant profile: Stor-rotliden, sweden. https://www.power-technology.com/data-insights/power-plant-profile-stor-rotliden-sweden/?cf-view

Rinker, J., & Dykes, K. (2018). *Windpact reference wind turbines* [NREL/TP-5000-67667]. https://www.nrel.gov/docs/fy18osti/67667.pdf.

Clausen, N.-E., Wadham-Gagnon, M., Wallenius, T., Cattin, R., Ronsten, G., Klintström, R., Durstewitz, M., Baring-Gould, I., Byrkjedal, Ø., Krenn, A., & Guodian United Power Technology. (2014, February 11). *Site ice classification*. https://windren.se/WW2014/06_02_027_Site%20ice%20classification%20-%20case%20studies%20and%20recommendations.pdf

Cattin, R. (2016). *Validation of the IEA Task 19 Ice Classification*. Retrieved May 15, 2025, from https://winterwind.se/wp-content/uploads/2016/02/3_3_3_Cattin_Validation_of_the_IEA_Task_19_ice_site_classification.pdf

VTT Technical Research Centre of Finland. (2015). *Vtt public wice atlas*.

IEA Wind TCP. (2018, October). *Available technologies for wind energy in cold climates*. https://iea-wind.org/wp-content/uploads/2021/09/Lehtomaki-et-al.-2018-Available-Technologies-for-Wind-Energy-in-Cold-Climates-report-2-nd-edition-2018.pdf

Vestas. (2011). *Vestas v90 1.8-2.0mw*. https://www.ledsjovind.se/tolvmanstegen/Vestas%20V90-2MW.pdf

U.S. Department of Transportation & Federal Aviation Administration. (2023, August). *Ground deicing program*. https://www.faa.gov/other_visit/aviation_industry/airline_operators/airline_safety/deicing/23-24_General_Information.pdf

Caterpillar Inc. (2025). *D250 gc, c9, 60hz, 250 ekw spec sheet*. https://emc.cat.com/pubdirect.ashx?media_string_id=LEHe2023-

Ember. (2025, May 5). *European electricity prices and costs | ember*. https://ember-energy.org/data/european-electricity-prices-and-costs/#datasets

Torenbeek, E. (1982, January 1). *Synthesis of subsonic airplane design*. https://doi.org/10.1007/978-94-017-3202-4

Raymer, D. (2018, August 2). *Aircraft design: A conceptual approach, sixth edition*. https://doi.org/10.2514/4.104909

Roskam, J. (1989, January 1). *Preliminary sizing of airplanes*. http://ci.nii.ac.jp/ncid/BA33849300

Delbecq, S., Budinger, M., Ochotorena, A., Reysset, A., & Defay, F. (2020). Efficient sizing and optimization of multirotor drones based on scaling laws and similarity models [Publisher: Elsevier BV]. *Aerospace Science and Technology*, *102*, 105873. https://doi.org/10.1016/j.ast.2020.105873

Budinger, M., Reysset, A., Ochotorena, A., & Delbecq, S. (2020). Scaling laws and similarity models for the preliminary design of multirotor drones [Publisher: Elsevier BV]. *Aerospace Science and Technology*, *98*, 105658. https://doi.org/10.1016/j.ast.2019.105658

Biczyski, M., Sehab, R., Whidborne, J. F., Krebs, G., & Luk, P. (2020). Multirotor Sizing Methodology with Flight Time Estimation [Publisher: Wiley]. *Journal of Advanced Transportation*, *2020*, 1–14. https://doi.org/10.1155/2020/9689604

Gatti, M. (2017). Complete Preliminary Design Methodology for Electric Multirotor. *Journal of Aerospace Engineering*, *30*(5), 04017046. https://doi.org/10.1061/(ASCE)AS.1943-5525.0000752

Biczyski, M., Sehab, R., Whidborne, J. F., Krebs, G., & Luk, P. (n.d.). Multirotor sizing methodology with flight time estimation. *Journal of Advanced Transportation*, *2020*(1), 9689604. https://doi.org/10.1155/2020/9689604

Carhart, S., Cooper, D., Gaitan, L., Kaliterna, M., Lama, S., Rogel-Herrera, P., & Yabe, Y. (2020). Heavy lift drone.

Evro, S., Ajumobi, A., Mayon, D., & Tomomewo, O. S. (2024). Navigating battery choices: A comparative study of lithium iron phosphate and nickel manganese cobalt battery technologies. *Deleted Journal*, 100007. https://doi.org/10.1016/j.fub.2024.100007

Galushkin, N. E., Yazvinskaya, N. N., & Galushkin, D. N. (2020). A critical review of using the peukert equation and its generalizations for lithium-ion cells. *Journal of The Electrochemical Society*, *167*(12), 120516. https://doi.org/10.1149/1945-7111/abad69

Traub, L. W. (2013). Validation of endurance estimates for battery powered UAVs. *The Aeronautical Journal*, *117*(1197), 1155–1166. https://doi.org/10.1017/S0001924000008757

Villeneuve, E., Karmouch, E., & Boulerice, X. (2022). Development of a small and transportable de-icing/anti-icing drone-mounted system. part 1: System design. *Drone Systems and Applications*, *10*(1), 155–177. https://doi.org/10.1139/dsa-2021-0036

Struk, P. (2017). How to take it off, section: Fluid application procedures. *A Pilot's Guide to Ground Icing, Module IV - De-Icing Operations*.

Haddaoui, M. (2019). Development of a propeller source noise model. https://api.semanticscholar.org/CorpusID:198323693

Afari, S. (2019). *Prediction of noise associated with an isolated uav propeller* [Master's thesis]. EmbryRiddle Aeronautical University. https://commons.erau.edu/edt/463/

Mark Drela, H. Y. (2011). Xrotor user guide (plain-text documentation). *Massachusetts Institute of Technology*. https://web.mit.edu/drela/Public/web/xrotor/xrotor_doc.txt

Gutin, L. (1948, October). *On the sound field of a rotating propeller* (NACA Technical Memorandum NACA–TM–1195). National Advisory Committee for Aeronautics (NACA), Langley Aeronautical Laboratory. Langley Field, VA, USA. https://ntrs.nasa.gov/citations/20030068996

Klein, P. (2017). Parametric modeling and optimization of advanced propellers for next-generation aircraft. https://api.semanticscholar.org/CorpusID:117374818

N.S.L.Elbers. (2021). *Assessment of an aircraft propeller noise model by verification and experimental validation* [Master's thesis]. Delft University of Technology. https://doi.org/10.4123/uuid:d566dd4b-b6ac-4b52-b05b-0e1391281936

T-MOTOR. (n.d.). NS26×8.5 Prop UAV Carbon Fiber Propeller. https://store.tmotor.com/product/ns26x8_5-prop-uav-carbon-fiber.html

Russo, N., Marano, A. D., Gagliardi, G. M., Guida, M., Polito, T., & Marulo, F. (2023). Thrust and noise experimental assessment on counter-rotating coaxial rotors. *Aerospace*, *10*(6). https://www.mdpi.com/2226-4310/10/6/535

Heng, X., Cabecinhas, D., Cunha, R., Silvestre, C., & Qingsong, X. (2015). A trajectory tracking lqr controller for a quadrotor: Design and experimental evaluation. *TENCON 2015 - 2015 IEEE Region 10 Conference*, 1–7. https://doi.org/10.1109/TENCON.2015.7372729

Pal, S. (2019). Ecg monitoring: Present status and future trend. In R. Narayan (Ed.), *Encyclopedia of biomedical engineering* (pp. 363–379). Elsevier. https://doi.org/10.1016/B978-0-12-801238-3.10892-X

Jahja, M., Farrow, D., Rosenfeld, R., & Tibshirani, R. J. (2019). Kalman filter, sensor fusion, and constrained regression: Equivalences and insights. *Proceedings of the 33rd Conference on Neural Information Processing Systems (NeurIPS)*.

Gonçalves da Silva, G., Bazanella, A., Lorenzini, C., & Campestrini, L. (2019). Data-driven lqr control design. *IEEE Control Systems Letters*, *3*(1), 180–185. https://doi.org/10.1109/LCSYS.2018.2868183

Dydek, Z. T. (2010, September). *Adaptive control of unmanned aerial systems* [Ph.D. Thesis]. Massachusetts Institute of Technology [Supervisor: Anuradha M. Annaswamy].

Deng, K., Zhang, Y., Yang, J., & Xie, J. (2025, June). GigaSLAM: Large-Scale Monocular SLAM with Hierarchical Gaussian Splats [arXiv:2503.08071 [cs]]. https://doi.org/10.48550/arXiv.2503.08071

Hacıefendioğlu, K., Başağa, H. B., Yavuz, Z., & Karimi, M. T. K. (2022). Intelligent ice detection on wind turbine blades using semantic segmentation and class activation map approaches based on deep learning method. *Renewable Energy*, *182*, 1–16. https://doi.org/10.1016/j.renene.2021.10.025

Shorten, C., & Khoshgoftaar, T. M. (2019). A survey on image data augmentation for deep learning. *Journal of Big Data*, *6*(1), 60. https://doi.org/10.1186/s40537-019-0197-0

Long, J., Shelhamer, E., & Darrell, T. (2015). Fully convolutional networks for semantic segmentation. *2015 IEEE Conference on Computer Vision and Pattern Recognition (CVPR)*, 3431–3440. https://doi.org/10.1109/CVPR.2015.7298965

Yosinski, J., Clune, J., Bengio, Y., & Lipson, H. (2014). How transferable are features in deep neural networks? *Proceedings of the 28th International Conference on Neural Information Processing Systems - Volume 2*, 3320–3328.

Ronneberger, O., Fischer, P., & Brox, T. (2015). U-net: Convolutional networks for biomedical image segmentation. In N. Navab, J. Hornegger, W. M. Wells, & A. F. Frangi (Eds.), *Medical image computing and computer-assisted intervention – miccai 2015* (pp. 234–241). Springer International Publishing.

Simonyan, K., & Zisserman, A. (2015). Very deep convolutional networks for large-scale image recognition. *International Conference on Learning Representations*.

Kreutz, M., Alla, A. A., Eisenstadt, A., Freitag, M., & Thoben, K.-D. (2020). Ice detection on rotor blades of wind turbines using rgb images and convolutional neural networks [53rd CIRP Conference on Manufacturing Systems 2020]. *Procedia CIRP*, *93*, 1292–1297. https://doi.org/10.1016/j.procir.2020.04.107

Chanda, M., Mazumder, O., Patwary, M., & Paul, S. (2024). Is the vgg-19 road segmentation method better than the customized unet method?, 994–1000. https://doi.org/10.1109/AIC61668.2024.10730836

Deng, J., Dong, W., Socher, R., Li, L.-J., Li, K., & Fei-Fei, L. (2009). Imagenet: A large-scale hierarchical image database. *2009 IEEE Conference on Computer Vision and Pattern Recognition*, 248–255. https://doi.org/10.1109/CVPR.2009.5206848

Lecun, Y., Bottou, L., Bengio, Y., & Haffner, P. (1998). Gradient-based learning applied to document recognition. *Proceedings of the IEEE*, *86*(11), 2278–2324. https://doi.org/10.1109/5.726791

Ruby, U., & Yendapalli, V. (2020). Binary cross entropy with deep learning technique for image classification. *International Journal of Advanced Trends in Computer Science and Engineering*, *9*. https://doi.org/10.30534/ijatcse/2020/175942020

Kingma, D., & Ba, J. (2014). Adam: A method for stochastic optimization. *International Conference on Learning Representations*.

Milletari, F., Navab, N., & Ahmadi, S.-A. (2016). V-net: Fully convolutional neural networks for volumetric medical image segmentation. *2016 Fourth International Conference on 3D Vision (3DV)*, 565–571. https://doi.org/10.1109/3DV.2016.79

Terven, J., Cordova-Esparza, D., Ramirez-Pedraza, A., & Chavez-Urbiola, E. (2023). Loss functions and metrics in deep learning. A review. arXiv 2023. *arXiv preprint arXiv:2307.02694*.

Yang, J., Zhang, Y., Fan, W., Wang, J., Zhang, X., Liu, C., Liu, S., & Xue, L. (2025). A novel lightweight multi-scale feature fusion segmentation algorithm for real-time cervical lesion screening. *Scientific Reports*, *15*(1), 6343. https://doi.org/10.1038/s41598-025-89596-8

Mur-Artal, R., & Tardos, J. D. (2017). ORB-SLAM2: An Open-Source SLAM System for Monocular, Stereo and RGB-D Cameras [arXiv:1610.06475 [cs]]. *IEEE Transactions on Robotics*, *33*(5), 1255–1262. https://doi.org/10.1109/TRO.2017.2705103

Zhou, Y., Wu, S., & Yan, L.-Q. (2024, September). Unified Gaussian Primitives for Scene Representation and Rendering [arXiv:2406.09733 [cs]]. https://doi.org/10.48550/arXiv.2406.09733

Allen, B. D. (2021). Digital Twins and Living Models at NASA.

Gate, T. (n.d.). Cobalt Truck equipment. https://cobalttruck.com/products/product-info/tommy-gate-liftgates

Hagberg, A., Swart, P. J., & Schult, D. A. (2008). *Exploring network structure, dynamics, and function using networkx* (tech. rep.). Los Alamos National Laboratory (LANL), Los Alamos, NM (United States).

Campion, M., Ranganathan, P., & Faruque, S. (2018). A review and future directions of uav swarm communication architectures. *2018 International Conference on Computing, Networking and Communications (ICNC)*, 377–383.

Bekmezci, I., Sahingoz, O. K., & Temel, Ş. (2013). Flying ad-hoc networks (fanets): A survey. *Ad Hoc Networks*, *11*(3), 1254–1270.

Tamburrini, R., et al. (2024). Master thesis and internship [br]-master's thesis: Design of a coaxial counterrotating rotor for an emergency drone [br]-internship.

Arendsen, P., & Centre, R. N. .-. N. A. (2024). *Cold testing has become hot* (tech. rep.). NLR - Royal Netherlands Aerospace Centre. https://www.nlr.org/wp-content/uploads/2025/03/E2043_Cold-Testing-has-become-hot-1.pdf

Meng, F., McKechnie, J., Turner, T., & Pickering, S. (2017). Energy and environmental assessment and reuse of fluidised bed recycled carbon fibres. *Composites Part A: Applied Science and Manufacturing*, *100*, 206–214.

Duflou, J. R., Seliger, G., Kara, S., Umeda, Y., Ometto, A., & Willems, B. (2008). Efficiency and feasibility of product disassembly: A case-based study. *CIRP annals*, *57*(2), 583–600.

Staples, C. A., Williams, J. B., Craig, G. R., & Roberts, K. M. (2001). Fate, effects and potential environmental risks of ethylene glycol: A review. *Chemosphere*, *43*(3), 377–383.

Dunn, J. B., Gaines, L., Sullivan, J., & Wang, M. Q. (2012). Impact of recycling on cradle-to-gate energy consumption and greenhouse gas emissions of automotive lithium-ion batteries. *Environmental science & technology*, *46*(22), 12704–12710.

(2025). https://www.flyeye.io/drone-calculators-thrust-to-weight-ratio/

Miles, M., & Prior, S. D. (2025). Investigation of the performance of unequal co-axial rotors. *Drones and Autonomous Vehicles*, *2*(1).

A

Financial analyses

A.0.1. Sensitivity Analysis

Parameter	Value [€/MWh]	Profit margin	Unit
MWh price	30	-16.6	%
	60	10.2	%
	90	19.2	%
	120	23.7	%

Table A.1: *Profit margin sensitivity to MWh price*

Parameter	Value [m^2]	Profit margin	Unit
Turbine area	300	27.0	%
	600	11.0	%
	900	-5.0	%
	1200	-21.1	%

Table A.2: *Profit margin sensitivity to turbine area*

Parameter	Value [–]	Profit margin	Unit
No. de-icings	3	32.7	%
	6	22.4	%
	9	12.1	%
	12	1.8	%

Table A.3: *Profit margin sensitivity to number of de-icings*

Parameter	Value [€]	Profit margin	Unit
Drone price (total)	25 000	11.2	%
	50 000	8.6	%
	100 000	3.5	%
	125 000	0.9	%

Table A.4: *Profit margin sensitivity to total drone price*

Parameter	Value [€]	Profit margin	Unit
Battery cost (/battery)	1 000	13.3	%
	2 000	8.6	%
	3 000	4.0	%
	4 000	-0.7	%

Table A.5: *Profit margin sensitivity to battery cost*

Parameter	Value [L/m^2]	Profit margin	Unit
De-icing fluid use	0.5	13.0	%
	1.0	8.6	%
	1.5	4.3	%
	2.0	0.0	%

Table A.6: *Profit margin sensitivity to de-icing fluid use*

Parameter	Value [€/L]	Profit margin	Unit
Fluid cost	0.2	14.0	%
	0.5	9.0	%
	0.8	4.0	%
	1.1	-1.0	%

Table A.7: *Profit margin sensitivity to fluid cost*

Parameter	Value [%]	Profit margin	Unit
SG&A / Revenue	10	13.3	%
	20	8.6	%
	30	4.0	%
	40	-0.6	%

Table A.8: *Profit margin sensitivity to SG&A / Revenue*

Parameter	Value [%]	Profit margin	Unit
Wind-farm ROI	10	21.2	%
	20	15.2	%
	30	10.0	%
	40	5.6	%

Table A.9: *Profit margin sensitivity to wind-farm ROI*

Parameter	Value [%]	Profit margin	Unit
Yearly loss	5	-73.3	%
	10	-3.1	%
	11	3.3	%
	12	8.6	%

Table A.10: *Profit margin sensitivity to yearly power loss*

A.1. Financial analysis parameters

To make it easier to follow the whole process of the financial analysis and be able to replicate it, Table A.11 to Table A.13 provide all the parameters that were used, alongside their values or sources (be it external or through intermediate computations).

Table A.11: *Comprehensive cost-benefit model for drone-based wind-turbine de-icing (sections 1–3). "[!]" marks critical inputs used in the sensitivity analysis.*

#	Parameter	Value	Unit	Type	Formula	Source
1. Wind-farm overview						
1.1	MWh price [!]	56.61	€ / MWh	Input	–	(Ember, 2025)
1.2	Yearly production	200 000	MWh / yr	Input	–	(Vattenfall, 2011)
1.3	Yearly loss	12	%	Input	–	(VTT Technical Research Centre of Finland, 2015; IEA Wind TCP, 2018)
1.4	Yearly revenue	11 322 000	€ / yr	Intermediate	1.1 × 1.2	–
1.5	Turbine power	2	MW	Input	–	(The Wind Power, 2025)
1.6	Turbine number	40	–	Input	–	(Vattenfall, 2011)
1.7	Turbine area [!]	644	m^2	Input	–	Subsection 4.5.1
2. Baseline icing losses						
2.1	Energy loss	27 273	MWh (total)	Intermediate	(1.2 / (1–1.3)) × 1.3	–
2.2	Missed revenue	1 543 909	€ (total)	Intermediate	2.1 × 1.1	–
3. Drone operational properties						
3.1	Number of de-icings [!]	10	events / yr	Input	–	(Clausen et al., 2014)
3.2	Spraying rate	5	L / min	Output	–	Optimization
3.3	Payload	21	kg	Output	–	Optimization
3.4	Travel distance (vertical)	169	m	Input	–	(Vestas, 2011)
3.5	Velocity (vertical)	3	m / s	Input	–	Subsection 4.5.1
3.6	Travel distance (horizontal)	1 000	m	Input	–	Subsection 4.5.1
3.7	Velocity (horizontal)	7.5	m / s	Input	–	Subsection 4.5.1
3.8	Travel time	133	s	Intermediate	3.6 / 3.7	–
3.9	Time to climb	56	s	Intermediate	3.4 / 3.5	–
3.10	Detection time	126	s	Input	3.11 / 2	Subsection 4.5.1
3.11	Spraying time	252	s	Intermediate	3.3 / 3.2 × 60	–
3.12	Time to descend	56	s	Intermediate	3.4 / 3.5	–
3.13	Travel time	133	s	Intermediate	3.6 / 3.7	–
3.14	Time to refuel	60	s	Input	–	Subsection 4.5.1
3.15	Operational safety margin	10	%	Input	–	Subsection 4.5.1
3.16	Effective spraying fraction	28	%	Intermediate	3.11 / (Σ(3.8;3.14)(1+3.15))	–
3.17	Effective spraying rate	1.40	L / min	Intermediate	3.2 × 3.16	–
3.18	Mission time	13.6	min	Intermediate	Σ(3.8;3.14)/60	–
3.19	Flight time	12.6	min	Output	Σ(3.8;3.14)–3.14/60	–

Table A.12: *Cost-benefit model (sections 4–6). "[!]" marks critical inputs used in the sensitivity analysis.*

#	Parameter	Value	Unit	Type	Formula	Source
4. Drone costs						
4.1	Drone price (total) [!]	50 000	€	Input	–	Subsection 4.5.1
4.2	Operational lifetime	5	years	Input	–	Subsection 4.5.1
4.3	Number of drones	8	–	Output	–	Optimization
4.4	Yearly drone cost (total)	80 000	€ / yr	Intermediate	(4.1 / 4.2) × 4.3	–
4.5	Number of batteries (/drone)	3	–	Input	–	Subsection 4.5.1
4.6	Number of battery sets (/drone)	3	–	Input	–	Subsection 4.5.1
4.7	Battery cost (/battery) [!]	2 000	€	Input	–	Foxtech Diamond[1]
4.8	Battery cost (total)	144 000	€	Intermediate	4.7 × 4.6 × 4.5 × 4.3	–
5. De-icing downtime cost						
5.1	Time to clean (drone / turbine)	7.7	h / turbine	Intermediate	1.7 / 3.17 / 60	–
5.2	Time to clean (all drones / turbine)	1.0	h / turbine	Intermediate	1.7 / (3.17 × 4.3) / 60	–
5.3	Time to clean (one drone, total)	306	h (total)	Intermediate	(1.7 × 1.6)/(3.17)/60	–
5.4	Time to clean (all drones, total)	38	h (total)	Intermediate	(1.7 × 1.6)/(3.17 × 4.3)/60	–
5.5	Downtime (total)	7 850	h / yr	Intermediate	3.1 × 5.2 × (1.6(1.6+1))/2	–
5.6	Additional missed revenue	444 399	€ (total)	Intermediate	5.5 × 1.1	–
6. De-icing fluid cost						
6.1	Fluid type	Propylene Glycol	–	Input	–	Chapter 3
6.2	De-icing fluid use [!]	1	L / m^2	Input	–	(U.S. Department of Transportation & Federal Aviation Administration, 2023)
6.3	Fluid cost [!]	0.52	€ / L	Input	–	Subsection 3.3.3
6.4	Total liquid volume	257 600	L	Intermediate	6.2 × 1.6 × 1.7 × 3.1	–
6.5	Total fluid cost	133 952	€ (total)	Intermediate	6.4 × 6.3	–

Table A.13: *Cost-benefit model (sections 7–8). "[!]" marks critical inputs used in the sensitivity analysis.*

#	Parameter	Value	Unit	Type	Formula	Source
7. Ground station and SG&A cost						
7.1	Operational lifetime (ground)	5	years	Input	–	Subsection 4.5.1
7.2	Diesel generator cost	50 000	€	Input	–	CAT D250 GC[2]
7.3	Diesel fuel cost (/L)	1.49	€	Input	–	Cargopedia[3]
7.4	Diesel consumption	73.3	L / h	Input	–	(Caterpillar Inc., 2025)
7.5	Diesel fuel cost (total)	41 823	€	Intermediate	7.3 × 7.4 × 5.4 × 3.1	–
7.6	Trailer cost	50 000	€	Input	–	Norstar Company[4]
7.7	Tank truck	50 000	€	Input	–	Sinotruck HOWO[5]
7.8	Number of tank trucks	2	–	Input	–	Section 13.2
7.9	SG&A / Revenue [!]	20	%	Input	–	Finlistics[6]
7.10	Sales, General & Administrative	143 287	€	Intermediate	7.9 × (2.2 – 5.6 – 8.4)	–
7.11	Total cost (incl. SG&A)	225 110	€	Intermediate	(7.7 × 7.8+7.6)/7.1+7.5+7.10	–
8. Financial outcome						
8.1	Wind-farm ROI [!]	33	%	Input	–	Subsection 4.5.1
8.2	Additional revenue (wind farm)	383 075	€ / yr	Intermediate	2.2 – (2.2/(1+8.1))	–
8.3	% of additional revenue	3.4	%	Intermediate	8.2 / 1.4	–
8.4	Profit from de-icing (operator)	133 373	€ / yr	Output	2.2 – 4.4 – 4.8 – 5.6 – 6.5 – 7.11 – 8.2	–
8.5	Margin (operator)	18.6	%	Output	8.4 / (2.2 – 5.6 – 8.2)	–

1: https://store.foxtech.com/diamond-hvt-12s-66000/ 2: https://www.machinerytrader.com/listing/auction-results/245254465/caterpillar-d250gc-stationary-generators-power-systems 3: https://www.cargopedia.net/europe-fuel-prices 4: https://norstarcompany.com/blog/how-much-does-a-truck-trailer-cost/ 5: https://sinotruk-intl.en.made-in-china.com/product/YQgRuSKPvIkT/China-Sinotruck-HOWO-20000-Liters-Heavy-Special-Water-Tanker-Truck-6X4-Watering-Cart-Transport-Sprinkler-Spray-Water-Tank-Bowser-Truck-290HP-336HP.html 6: https://finlistics.com/metric-of-the-month-selling-general-and-administrative-sg-a-as-a-percentage-of-revenue/

B

Drone Sizing

B.1. Thrust-to-weight ratio

The thrust-to-weight (T/W) ratio is a design choice driven by the mission profile and informed by literature on heavy-lift drones. For missions requiring careful, slow flight, a T/W ratio of at least 1.5 is common Biczyski et al., n.d. However, D-ICE's mission profile includes gust loads during de-icing, meaning it needs extra thrust capacity to maintain control. This pushes the reasonable design range to somewhere between 1.5 and 2.2. 2.2 is selected as a conservative estimate for the drone. 2025

Hovering is the most demanding phase of our mission, and coaxial rotors are typically used in such applications (e.g., DJI FlyCart 30, DJI Agras T50). Coaxial setups double the number of rotors in the same footprint, increasing available thrust. However, they also introduce aerodynamic interference between the upper and lower rotors.

This interference means that thrust is not doubled. To reduce the interference effects the vertical spacing between the two rotors should be at least 20% of the propeller diameter. Even with this precaution, coaxial configurations experience an average thrust loss of about 15% (17% more power required for the same thrust).Tamburrini et al., 2024; Miles and Prior, 2025.

B.2. Thrust filtering

During the propeller selection procedure a parameter used to decipher the optimum propeller is two specific thrust point: **Thrust at hover and Thrust at wide open throttle (WOT)**. The formula used to select for the propellers hover is:

$$T_h = \frac{W_{TO}}{n_{rotor}} \tag{B.1}$$

Where T_h, W_{TO} and n_{rot} Thrust at hover, takeoff-weight and number of rotors respectively. For the wide-open throttle:

$$T_{WOT} = r_t T_h \tag{B.2}$$

Where T_{WOT} and r_t are WOT thrust and thrust to weight ratio.

B.3. Databases

Two databases were utilized to ensure an informed component selection. The first being for propellers and the second for motors. Both of these were extensively pre-processed to integrate into the loop.

Firstly, the data for the propellers were sourced from a US-based propeller manufacturer, APC propellers [1]. For application in this method, 2 separate datasets were combined, resulting in 231 models occurring in both. The first included extensive simulation-based performance data, including thrust values, power, torque and coefficients for angular velocities of rates 1000 to

[1] https://www.apcprop.com/?v=796834e7a283

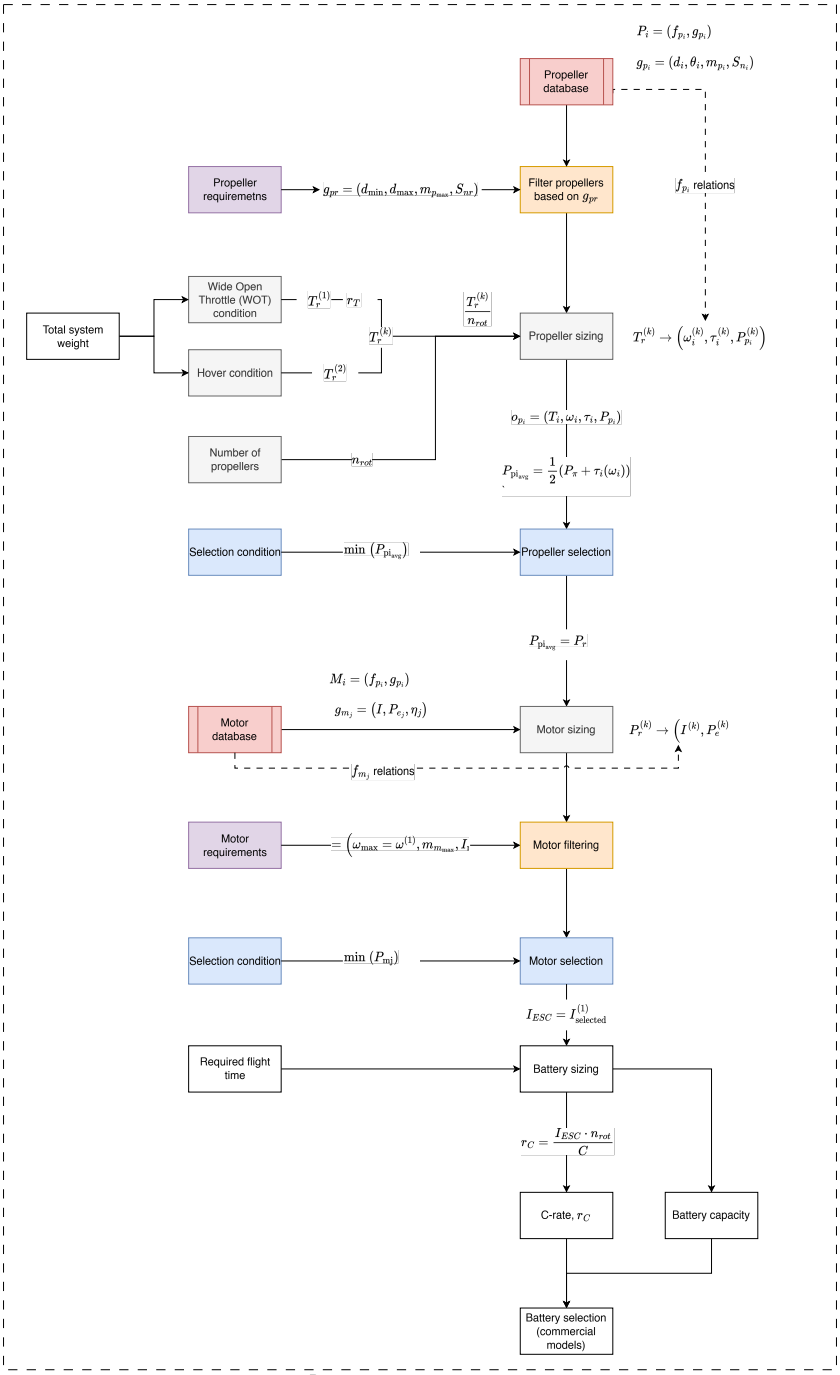

Selection based on minimum power required for hover P_{hover}

23000 RPM in increments of 1000 RPM. A second data sheet included physical dimensions of propellers. There were combined to enabling filtering of options based on dimensional requirements before performance-based selection. Furthermore, an additional performance dataset was available for validating the simulated data.

The motors were also from a selection provided by DriveCalc [2], which offered detailed performance characteristics and dimensional aspects of the motors. These motors are a collection from various manufacturers. In some cases, the current rating of the motor was considered as that for a recommended Electronic Speed Controller (ESC) to be paired with it.

Both databases provide empirical data grounded in real-world applications. However, similar to

[2] http://www.drivecalc.de/

the limitations noted by Biczyski et al., the databases remain restrictive. Particularly for the case that the drone is in a higher weight class, larger propeller options capable of supporting 100 kg in total are scarce. In future iterations, it would be recommended to source wider databases. Nevertheless, the flexibility of this method allows it to accept custom-designed component data, thereby extending its applicability beyond the standard database limitations. The following histograms demonstrate the distributions of propellers according to their diameter and the motor voltage rating available in the database. The histograms importance will manifested in future work, where an expanded database (higher voltage motors and large-diameter propellers)would be used for iterations in the design.

(i) Eight unfolded drones: $A_{\text{drone (each)}} = (2\,\text{m}) \times (2\,\text{m}) = 4\,\text{m}^2$,
$A_{\text{drones (total)}} = 8 \times 4\,\text{m}^2 = 32\,\text{m}^2$.

(ii) One large generators: $A_{\text{gen (each)}} = (3.95\,\text{m}) \times (1.45\,\text{m}) = 5.7\,\text{m}^2$,

(iii) One large truck: $A_{\text{truck1}} = (20\,\text{m}) \times (2.4\,\text{m}) = 48\,\text{m}^2$.

(iv) Two smaller trucks: $A_{\text{truck2 (each)}} = (5.7\,\text{m}) \times (2.496\,\text{m}) = 25.8336\,\text{m}^2$,
$A_{\text{truck2 (total)}} = 2 \times 25.8336\,\text{m}^2 = 51.6672\,\text{m}^2$.

C

Verification & Validation Strategies

Code Verification

The tables presented in this section act as a support to the code verification section in Subsection 14.1.1.

Table C.1: *The unit test compliance matrix for the design code.*

Test ID	Test name	Inputs	Expected Output	Compliance	Description
		Drone Sizing Estimation			
UT-DS-01	test_returns_best_motor	conditions, state	motor list	Yes	Returns the correct motor
UT-DS-02	test_skips_invalid_resistance	conditions, state	empty list	Yes	Returns expected empty list
UT-DS-03	test_no_valid_motors	conditions, state	empty list	Yes	Returns expected empty list
UT-DS-04	test_metadata_loading	data file	data frame	Yes	Initializes the data frame with correct data
UT-DS-05	test_filter_metadata	data frame	data frame	Yes	Returns a filtered data frame
UT-DS-06	test_interp_model_at_thrust	data frame, chosen_thrust	series	Yes	Returns a series at the given thrust
UT-DS-07	test_load_performance_curves	model list	performance data curves	Yes	Returns the expected performance data curves
UT-DS-08	test_best_prop_full_at_thrust_fails_if_thrust_out_of_range	data frame, thrust	exception	Yes	Correctly returns an exception when thrust out of range
UT-DS-09	test_battery_initialization	self.battery	dictionary	Yes	All the global variables initialized for the battery are initialized correctly
UT-DS-10	test_ncells_valid	number of cells	valid	Yes	Valid number of cells is produced
UT-DS-11	test_ncells_invalid	number of cells	invalid	Yes	Invalid number of cells is produced
UT-DS-12	test_voltage_valid	voltage	valid	Yes	Valid voltage is produced
UT-DS-13	test_voltage_invalid	voltage	invalid	Yes	Invalid voltage is produced
UT-DS-14	test_power_valid	power	valid	Yes	Valid power produced
UT-DS-15	test_power_invalid	power	invalid	Yes	Invalid power produced
UT-DS-16	test_capacity_valid	capacity	valid	Yes	Valid capacity produced
UT-DS-17	test_capacity_invalid	capacity	invalid	Yes	Invalid capacity produced
UT-DS-18	test_peukert_valid	peukert exponent	valid	Yes	Valid peukert exponent produced
UT-DS-19	test_peukert_invalid	peukert exponent	invalid	Yes	Invalid peukert exponent produced
UT-DS-20	test_Rt_valid	hour-rating	valid	Yes	Valid hour-rating produced
UT-DS-21	test_Rt_invalid	hour-rating	invalid	Yes	Invalid hour-rating produced
UT-DS-22	test_set_capacity	new_capacity	self.entry	Yes	New capacity is correctly recalculated
UT-DS-23	test_get_capacity	None	capacity	Yes	Function gets the capacity
UT-DS-24	test_min_rc	(5,5)	25/capacity/1000	Yes	The values for min_rc match
UT-DS-25	test_simplified_discharge	None	capacity/1000*power*voltage	Yes	The correct value is called
UT-DS-26	test_discharge_time	None	time difference (1)	Yes	The time difference match with expectation
UT-DS-27	test_required_capacity	24	required_capacity	Yes	Required capacity is correct for provided value
UT-DS-28	test_extend_df	motor and meta data dataframe	motor and meta data dataframe	Yes	Extends the dataframe sucessfully
		Stability and Control			
UT-CS-01	test_initialization	None	self.variables	Yes	The global variables are initialized correctly
UT-CS-02	test_build_state_space	global variables	A,B,C,D	Yes	Expected state-space model is built
UT-CS-03	test_compute_lqr	A, B	K, S, E	Yes	Expected gains are produced
UT-CS-04	test_lqr_controller	x, x_ref, u_ref	u	Yes	Input vector is calculated as expected
UT-CS-05	test_simulate_runs	X0, x_ref	times, X, U_sim	Yes	The simulation runs as expected
UT-CS-06	test_plot_6DOF_time_response	times, X, U_sim, frame_iterate, N_arms, max_thrust, X0, X_refs, arm_length, wind_vectors, wind_forces, wind_torques, dt	plot	Yes	The plot is created as expected and is verified visually
		Noise			
UT-NS-01	test_correction_factor	x_data, y_data	quadratic coefficients	Yes	The quadratic coefficients are calculated as expected

Table C.2: *The integration test compliance matrix for the design code.*

Test ID	Test name	Integrated functions	Input	Expected Output	Compliance	Description
		Drone Sizing Estimation				
IT-DS-01	test_find_best_propeller	filter_metadata + load_performance_curves + + best_prop_full_at_thrust	conditions, mass	series	Yes	It is an integrated function that returns that returns the expected series for a propeller
IT-DS-02	test_load_best_battery	required_capacity + set_capacity + + discharge_time + min_rc	conditions, p_req, n_rotors, I_ESC	battery series	Yes	Returns the series with best battery as expected
IT-DS-03	test_run_loop	full integration	conditions, output_dir, tol, max_iters	state	Yes	The full run is acting as expected
		Stability and Control				
IT-CS-01	test_compute_lqr_state_space_integration	build_state_space + compute_lqr	global variables	K,S,E	Yes	Integrates from initialization till LQR calculation
IT-CS-02	test_simulate_with_lqr	full integration	global variables	times, X, U_sim	Yes	Full integration run acts as expected

Table C.3: *The coverage of unit tests for software used in modelling.*

File	Statements	Miss	Coverage
control_main.py	121	6	95%
control_plot.py	169	7	96%
battery.py	117	9	92%
MotorDatabaseHandling.py	87	5	94%
PropDatabaseHandling.py	161	10	94%

System Verification

The tables presented in this section act as a support to the system verification section in Subsection 14.1.2.

Table C.4: *Compliance and verification matrix for project requirements (Part 1/3)*

ID	Verification Type	Verification Strategy	Compliance	Verified
USER-S-VIS-2.1	Test	Run the ice detection model through a labelled testing dataset, that the model wasn't trained on and calculate the model accuracy	✓	X
USER-S-PAYL-3.1	Demonstration	Demonstrate through a standard mission operation, the drone is able to de-ice at least 90% of the prototype turbine	✓	X
USER-M-RES-2.1	Demonstration	Demonstrate that the prototype drone is able to de-ice the turbine in a single operation	✓	X
USER-S-STR-2.1	Test	The drone is put in a testing environment (cooler) and checked for sustained operation, including the spraying payload.	✓	X
USER-S-POW-5.2	Analysis, Test	Develop a model of the drone dynamics response due to wind loads. It is validated by drone at MTOW being put in a low-speed wind tunnel and checked for stability of flight within 12m/s of wind	✓	✓
USER-M-SAFE-2.1	Test	A substitute structure is used for testing, where it is put under the impact of the deicing and possibly, simulated, light collisions of aircraft with the structure	X	X
USER-M-SUST-3.1	Test	Conduct operational testing over a representative sample of missions	X	X
USER-M-SAFE-2.2	Test	Conduct tests of MTOW aircraft with example obstacles in the way of the target and the aircraft shall avoid them over a representative mission cycle number	X	X
USER-M-SAFE-2.3	Demonstration	Demonstrate that the aircraft at MTOW can perform an emergency landing in the desired time.	✓	X
USER-M-SUST-2.1	Analysis	Analyse academic literature for the deicing agent's biodegradability	✓	✓
USER-M-SUST-2.2	Demonstration	Apply a volt- and amp meters to the electrical circuit of the drone and run the circuit at the highest power draw for the duration of the mission operation. Calculate the energy consumed during that time and check compliance with the requirement.	✓	X
USER-M-SUST-2.3	Analysis, Test	Develop a model for noise caused by the system. To validate, run the propulsion and de-icing module in an echo chamber, while taking measurements of sound emission intensity at a distance decided.	✓	✓
USER-S-STR-3.1	Demonstration	Measure the weight of all the components of the drone with a scale.	✓	X
INV-M-RES-4.1	Analysis	Analyse the cost of components summed together into the drone system in manufacturing, while assuming a low level of production automation and no economies of scale.	✓	✓
INV-M-RES-1.2	Analysis	Simulate financial model with OPEX tracking using existing market models and software	✓	X
USER-M-LEGL-3.1	Analysis	Perform a documentation review and create compliance checklist	X	X
USER-S-ACC-4.1	Test	Perform a timed setup test to ensure deployment time requirements are met	✓	X
USER-M-RES-1.1	Test	Perform range flight test with telemetry logging	✓	X
USER-S-COMM-3.1	Test	Perform communication link test using remote telemetry	✓	X
USER-S-VIS-2.1	Test	Perform lab test with HDR chart/datasheet	✓	X
USER-S-VIS-1.1	Test	Calibrate camera settings and perform test image analysis	✓	X
USER-S-VIS-3.1	Test	Perform video test and frame analysis	✓	X
USER-S-COMM-2.1	Test	Perform range test with telemetry log	✓	X
USER-S-VIS-2.3	Test	Perform a FOV measurement using a test chart	✓	X
USER-S-POW-3.1	Test	Perform timed charging test with battery log	✓	X

Table C.5: *Compliance and verification matrix for project requirements (Part 2/3)*

ID	Verification Type	Verification Strategy	Compliance	Verified
USER-S-PROP-2.1	Test	Perform propulsion system test in climate chamber simulating operational climate	✓	X
USER-S-PROP-1.1	Test	Perform thrust step response test with force sensor using high speed DAQ system	✓	X
USER-S-PROP-3.1	Test	Perform flight test with GPS or onboard velocity logging	✓	X
ENV-M-SUST-2.2	Analysis	Perform chemical analysis or Safety Data Sheet review of the de-icing agent	✓	✓
ENV-M-SUST-2.4	Analysis	Perform data sheet validation according to manufacturer specs or accelerated lifecycle test	✓	✓
ENV-M-SUST-3.1	Demonstration	Perform hands-on assembly and disassembly trial	✓	X
ENV-M-SUST-2.6	Test	Perform a simulated Over-the-Air (OTA) update test	✓	X
USER-S-PROP-4.1	Analysis, Test	Develop a model of the drone dynamics response due to wind loads. To validate, perform tethered thrust test or real flight acceleration measurement.	✓	✓
USER-S-STR-2.1	Test	Perform Accelerated life testing or FEM fatigue simulation	✓	X
USER-S-STR-3.1	Inspection	Perform a physical weigh-in at the end of the design and assembly process to visually verify	✓	X
ENV-M-SUST-3.2	Analysis	Perform documentation audit and usability walk-through to prospective customers	X	X
USER-S-PAYL-3.1	Test	Flow rate test using graduated cylinder and stopwatch using a lab bench with controlled fluid system	✓	X
USER-S-PAYL-3.2	Inspection	Perform visual inspection paired with fill volume measurement	✓	X
USER-S-POW-3.2	Test	Perform electrical test for over-voltage cut-off	✓	X
USER-S-POW-4.1	Test	Measure input vs output power during operation	✓	X
MANU-S-STR-4.1	Analysis	Use CAD software based part count and perform Design for Manufacturability (DFM) review	✓	✓
MANU-S-STR-4.2	Analysis	Perform a part spec sheet review and a Bill Of Materials (BOM) audit	✓	✓
MANU-S-STR-4.3	Analysis	Perform design review and component certification	X	X
USER-S-POW-5.1	Test	Perform full flight test under load and calculate endurance	✓	X
USER-S-ACC-4.1	Test	Hardware verification and performance profiling	✓	X
USER-S-ACC-2.1	Test	Field testing with GPS-based flight logs compared to known coordinates	✓	X
USER-S-ACC-2.2	Test	Altitude sensor calibration against laser altimeter or drone barometric altimeter test over a controlled height range	✓	X
USER-S-COMM-1.1	Test	Inject command signals and measure return telemetry latency using oscilloscope or logging software	✓	X
USER-S-COMM-3.1	Test	Run communication tests in various conditions (weathered, obstructed) and log package delivery rate	✓	X
GOV-M-LEGL-1.1	Inspection	Verify if each component is CE certified through research	✓	✓
GOV-M-LEGL-2.1	Analysis	Through research of academic material, determine if the materials chosen are RoHS-compliant	✓	✓
GOV-M-LEGL-3.2	Test	Conduct a test flight, while logging the activity and verifying its correct storage	✓	X
GOV-M-LEGL-3.3	Analysis	Verify that the material has SDS rating lower than 1, using literature	✓	✓
GOV-M-LEGL-3.4	Inspection	Verify by inspection that the payload compartment is double-walled and test the seal with pressurised liquid	✓	X
INS-M-SAFE-2.2	Test	Perform unit testing and integration testing of the fail-safe logic	✓	X
INS-M-SAFE-2.3	Demonstration	Run the self-diagnostic software on the prototype drone and measure runtime	✓	X
ACIN-S-COMM-4.1	Inspection	Ensure system documentation is provided in required formats and contains the required content	X	X
PUBL-M-SAFE-2.1	Inspection	Inspect the propulsion system if it has guards fully covering the sides of the propellers.	✓	X
PUBL-M-SAFE-2.2	Test	Unit test the software, detection model and sensors for detection of unexpected flying objects and return policy to the ground station.	✓	X
PUBL-M-SAFE-2.3	Test	Test the object detection system in a controlled environment, introducing an object from different directions at different distances around 5 meters.	✓	X
INV-M-RES-1.2	Analysis	Analyse the total development cost of the mission over three years to verify compliance.	✓	✓
EMPL-M-RES-1.1	Inspection	Inspect the project planning to verify the 5-year scope and funding allocation.	✓	✓
EMPL-M-RES-1.2	Analysis	Perform documentation review of project planning deliverables.	✓	✓
EMPL-M-RES-2.1	Inspection	Review partnership agreements, such as MOUs.	X	X
EMPL-M-RES-2.2	Analysis	Perform market adoption report and service log trend analysis.	X	X

Table C.6: *Compliance and verification matrix for project requirements (Part 3/3)*

ID	Verification Type	Verification Strategy	Compliance	Verified
USER-S-POW-1.1	Test	Perform bench test with power meter .	✓	X
USER-S-POW-2.1	Demonstration	Perform telemetry or power draw logging during communication test.	✓	X
USER-S-ACC-1.1	Test	Perform environmental test with known ice targets followed by ROC curve analysis.	✓	X
USER-S-PROP-1.2	Test	Perform static thrust test using load cell or thrust stand.	✓	X
USER-S-ACC-3.1	Test	Perform closed-loop thrust control test with sensor feedback.	✓	X
USER-S-PROP-5.1	Analysis, Test	Develop a model of the drone dynamics response due to wind loads. To validate, perform a free-flight test with motion tracking using OptiTrack, for example.	✓	✓
IND-S-STR-4.1	Test	Perform a number of field tests with time keeping.	✓	X
IND-S-STR-3.1	Test	Perform static load test or structural simulation.	✓	X
IND-S-PAYL-1.1	Test	Perform climate chamber test and wind tunnel test according to set requirements.	✓	X
IND-S-PAYL-1.2	Test	Perform lab test according to IP67 standards and obtain certification.	✓	X
IND-M-SAFE-2.1	Demonstration	Perform field trial and staffing observation.	✓	X
IND-M-RES-1.1	Analysis	Perform documentation audit of data flow and encryption.	✓	✓
USER-S-ACC-2.1	Test	Perform flight simulations and do flight log comparisons, validate with test flights.	X	X
USER-S-COMM-5.1	Test	Conduct functional tests to confirm that drones can exchange messages in a simulated or real swarm deployment.	✓	X
USER-S-POW-6.1	Test	Measure total energy consumed during a full mission using power logging equipment and verify against defined thresholds.	✓	X
USER-S-ACC-3.3	Test	Perform system-level testing under controlled conditions with simulated icing and environmental variation to assess sensor and actuation performance.	✓	X
USER-S-STR-5.1	Inspection	Review CAD models and perform physical inspection to confirm the presence of load-bearing structural components and their material properties.	✓	X
MANU-S-STR-4.3	Analysis	Verify method and material via spec sheet and process certification.	✓	✓
MANU-S-STR-4.4	Inspection	Inspect mechanical fasteners on the built platform and confirm compliance with joint design in technical drawings.	✓	X
USER-S-PAYL-5.1	Demonstration	Measure the temperature of the computer during a test operation.	✓	X
USER-S-PAYL-5.2	Demonstration	Measure the temperature of the de-icing liquid during a test operation.	✓	X
USER-S-VIS-9.1	Demonstration	Measure the temperature of the camera during a test operation.	✓	X

D

Requirements

This appendix displays the collected requirements for the entirety for the mission.

Table F.1: *The requirements for the project design.*

ID	Requirement	Type
USER-S-VIS-2.1	The system shall detect icing with at least 95% (2σ) accuracy using computational vision.	Driving
USER-S-PAYL-3.1	The de-icing process shall remove at least 90% (2σ) of ice from the affected area in a single operation.	Standard
USER-M-RES-2.1	The system shall cover at least 1 wind turbine (2σ) per deployment	Standard
USER-S-STR-2.1	The system shall operate effectively in temperatures as low as -30 °C.	Standard
USER-S-POW-5.2	The system shall operate effectively while subject to wind speeds up to 12 m/s.	Standard
USER-M-SAFE-2.1	The system shall not cause structural damage to wind turbines.	Standard
USER-M-SUST-3.1	System uptime shall be at least 95% with a failure rate of less than 1 per 100 missions.	Standard
USER-M-SAFE-2.2	The system shall have collision avoidance systems with at least a 99% success rate in obstacle detection.	Standard
USER-M-SAFE-2.3	The system shall have emergency landing protocols activates within 3 seconds of detecting system failure.	Standard
USER-M-SUST-2.1	The system shall use biodegradable chemical de-icing agents.	Standard
USER-M-SUST-2.2	The system shall have a energy consumption that does not exceed 5 kWh per mission.	Standard
USER-M-SUST-2.3	The system shall have noise emissions below 85 dB at 10 meters.	Standard
USER-S-STR-3.1	The mass of the drone shall be under 100 kg.	Standard
INV-M-RES-4.1	The system shall be designed to be manufacturable at a unit cost below €30 000 (FY2025) in mass production (100 pieces).	Standard
INV-M-RES-1.2	Maintenance costs shall be under €2 500 (FY2025) per year per drone.	Key
USER-M-LEGL-3.1	The system shall comply with EASA regulatory requirements for autonomous drone operations.	Standard
USER-S-ACC-4.1	Deployment time of the system shall be under 15 minutes per turbine.	Standard
USER-M-RES-1.1	The system shall have an operational range of at least 1km from the base station.	Standard
USER-S-COMM-3.1	The system shall allow remote monitoring and control via cellular network.	Standard
USER-S-VIS-2.1	Any and all cameras shall have a dynamic range larger than 70 dB.	Standard

Table F.1: *The requirements for the project design.*

ID	Requirement	Type
USER-S-VIS-1.1	Any and all cameras shall have a resolution of at least 1920x1080 pixels.	Standard
USER-S-VIS-3.1	Any and all cameras shall be rated for taking at least 25 frames per second.	Standard
USER-S-COMM-2.1	The communication subsystem shall maintain a two-way command-and-telemetry link at at least 1 km line-of-sight	Standard
USER-S-VIS-2.3	The camera shall have a horizotal FOV of at least 80 °	Standard
USER-S-POW-3.1	The battery shall restore 80% of its charge within 30 minutes.	Standard
USER-S-PROP-2.1	The propulsion subsystem shall be able to withstand tempetures between -30 and 45°C.	Key
USER-S-PROP-1.1	The thrust set point shall measure an output change within <21ms	Driving
USER-S-PROP-3.1	The horizontal cruise velocity shall be able to go to up to 5m/s	Driving
ENV-M-SUST-2.2	The de-icing method shall not involve substances classified under EU REACH Annex XVII	Driving
ENV-M-SUST-2.4	The drone's battery shall support at least 1000 charge cycles before needing replacement	Driving
ENV-M-SUST-3.1	At least 90% of the drone's structural and electronic components shall be removable using standard tools in under 30 minutes by a technician with basic drone training.	Standard
ENV-M-SUST-2.6	The system software shall support over-the-air updates to extend operational life and reduce electronic waste	Standard
USER-S-PROP-4.1	The propulsion system unit shall be able to generate at least 1 m/s^2 to counter gusts.	Driving
USER-S-STR-2.1	The fatigue life of the structure shall exceeded 150 per deployment	Driving
USER-S-STR-3.1	the empty airframe mass shall not exceeded 10 kg	Driving
ENV-M-SUST-3.2	A disassembly manual shall be provided to support certified recycling facilities.	Standard
USER-S-PAYL-3.1	the payload of the de-icing spray shall have at least a flow rate of 5L/min	Driving
USER-S-PAYL-3.2	The tank shall hold more than 20 L de icing fluid	Driving
USER-S-POW-3.2	The batteries shall include overcharge protection	Standard
USER-S-POW-4.1	The subsystem shall achieve at least 85% energy efficiency during operation	Standard
MANU-S-STR-4.1	The drone structure shall consist of no more than 50 unique parts, all manufacturable using standard 3- or 5-axis CNC machining or injection molding.	Standard
MANU-S-STR-4.2	All fasteners shall conform to ISO metric standards to avoid custom fabrication.	Key
MANU-S-STR-4.3	Assembly time for one unit shall not exceed 8 hours using semi-automated processes.	Driving
USER-S-POW-5.1	The drone shall have an endurance of at least 10 minutes	Standard
USER-S-ACC-4.1	The inboard computer shall have at least 8GB of ram	Standard
USER-S-ACC-2.1	The onboard positioning system shall deliver horizontal accuracy ≤ ±0.2 m	Driving
USER-S-ACC-2.2	The onboard positioning system shall deliver vertical accuracy ≤ ±0.1	Standard

Table F.1: *The requirements for the project design.*

ID	Requirement	Type
USER-S-COMM-1.1	The communication subsystem shall sustain a round-trip command-to-acknowledgement latency of ≤ 100 ms	Driving
USER-S-COMM-3.1	The communication subsystem shall have a packet loss with ≤ 1%	Standard
GOV-M-LEGL-1.1	All electronic components shall be CE-certified for electromagnetic compatibility.	Driving
GOV-M-LEGL-2.1	All materials used in the drone shall be RoHS-compliant.	Driving
GOV-M-LEGL-3.2	The system shall log all flight activity, including location and time stamps, for at least 6 months to support regulatory audits.	Driving
GOV-M-LEGL-3.3	The applied material shall have an SDS rating of 1 or lower and must be non-toxic and non-flammable.	Standard
GOV-M-LEGL-3.4	Chemical storage onboard shall be contained in a double-walled, sealed compartment.	Standard
INS-M-SAFE-2.1	The drone shall include a parachute or controlled descent system capable of limiting impact energy to <69 J in the event of failure.	Standard
INS-M-SAFE-2.2	All critical system failures (e.g., propulsion, power, communication) shall trigger an automated failsafe landing.	Driving
INS-M-SAFE-2.3	The drone shall undergo a self-diagnostic check before each mission, completed in less than 30 seconds.	Driving
ACIN-S-COMM-4.1	The manuals shall be provided in both PDF and HTML format and must include hardware diagrams, safety protocols, and software architecture.	Driving
PUBL-M-SAFE-2.1	Exposed rotors shall be equipped with guards to reduce injury risk during landing or emergency descent.	Driving
PUBL-M-SAFE-2.2	The system shall automatically abort the mission and return to home if an unexpected moving object is detected within 3 meters.	Driving
PUBL-M-SAFE-2.3	The drone shall feature horizontal 360° obstacle detection within a 3-meter range	Standard
INV-M-RES-1.2	The total cost of project development and deployment shall not exceed 500,000€ (FY 2025) over the first year.	Standard
EMPL-M-RES-1.1	The project shall be planned for a minimum duration of 5 years with funding allocated to support operations throughout.	Standard
EMPL-M-RES-1.2	The project shall include a 5-year roadmap with at least two planned system upgrades or expansions.	Standard
EMPL-M-RES-2.1	The project shall secure at least two commercial or governmental partners within 2 years of launch.	Standard
EMPL-M-RES-2.2	The project shall grow its serviced wind turbine count by at least 15% annually during years 1–3.	Standard
USER-S-POW-1.1	The payload subsystem shall consume no more than 700 W mean power	Driving
USER-S-POW-2.1	The communication and control subsystem shall consume no more than 50 W mean power	Driving
USER-S-ACC-1.1	The ice-detection sensor shall detect ice layers ≥ 2 mm thick on metal and composite surfaces at a distance of 2 m with ≥ 95 % probability of detection	Driving
USER-S-PROP-1.2	The propulsion system shall have a minimum thrust of at least 1500 N at sea level	Driving

Table F.1: *The requirements for the project design.*

ID	Requirement	Type
USER-S-ACC-3.1	The propulsion subsystem shall maintain output thrust within ±0.5 N of the commanded thrust level	Driving
USER-S-PROP-5.1	The propulsion subsystem shall recover from a sudden 1 m horizontal displacement caused by wind disturbance and return to its hover position in less than 2 seconds	Driving
IND-S-STR-4.1	All payload modules shall be replaceable within 10 minutes by one technician using standard tools.	Standard
IND-S-STR-3.1	The platform shall maintain structural integrity under all payload configurations up to 40 kg.	Standard
IND-S-PAYL-1.1	The system payload shall be operable in humidity levels up to 100%.	Driving
IND-S-PAYL-1.2	All payload modules shall be IP67 rated for water and dust protection.	Standard
IND-M-SAFE-2.1	The system shall reduce the need for human presence in de-icing operations to 2 people.	Driving
IND-M-RES-1.1	Data handling shall comply with GDPR when storing operator and flight data.	Standard
USER-S-ACC-2.1	The drone shall use autonomous navigational algorithms to determine the optimal path it should take	Driving
USER-S-COMM-5.1	The design shall allow drones to communicate with each other and operate in a swarm	Driving
USER-S-POW-6.1	The power subsystem shall use a semi-solid battery	Driving
USER-S-ACC-3.3	The de-icing payload shall use chemical de-icing method	Driving
USER-S-STR-5.1	The drone(s) shall be in non-tethered multicopter configuration(s)	Key
MANU-S-STR-4.3	The anti-corrosive coating shall be applied using liquid spray painting	Driving
MANU-S-STR-4.4	Subsystem parts shall be connected using bolted joints	Driving
USER-S-PAYL-5.1	The on-board computer shall have sufficient heat generation to maintain at least -10°C.	Standard
USER-S-PAYL-5.2	The de-icing liquid tank shall be kept at a temperature of 60°C throughout the duration of the mission.	Standard
USER-S-VIS-9.1	The camera shall be kept at a temperature higher than -10°C.	Standard